Production of $K^{\pm}$ and ϕ-Mesons in Ag+Ag-Collisions at 1.58 A GeV

Dissertation
zur Erlangung des Doktorgrades
der Naturwissenschaften

vorgelegt beim Fachbereich Physik
der Johann Wolfgang Goethe-Universität
in Frankfurt am Main

von
Marvin Kohls
aus Darmstadt

Frankfurt 2023
(D30)

vom Fachbereich Physik der

Johann Wolfgang Goethe-Universität

als Dissertation angenommen.

Dekan:
Prof. Dr. Roger Erb

Gutachter:
Prof. Dr. Joachim Stroth
Prof. Dr. Christoph Blume

Datum der Disputation:
24.10.2023

What cannot be known hollows the mind. Fill it not with guesswork.

Galadriel, Rings of Power

Abstract

This work focuses on the investigation of K^+, K^- and ϕ-meson production in Ag(1.58 A GeV)+Ag collisions, respectively, at a centre of mass energy of $\sqrt{s_{\mathrm{NN}}} = 2.55$ GeV. The energetically cheapest channel for direct K^+ production in binary NN-collisions $NN \rightarrow N\Lambda K^+$ lies at exactly this energy. For the remaining K^- and ϕ-meson, an excess energy of $\sqrt{s_{\mathrm{exc}}^{K^-}} = 0.31$ GeV and $\sqrt{s_{\mathrm{exc}}^{\phi}} = 0.34$ GeV has to be provided by the system. This makes these particles an excellent probe for effects inside the medium.
K^+ ($|u\bar{s}\rangle$) and K^- ($|\bar{u}s\rangle$) mesons can be reconstructed directly as they possess a $c\tau \approx 3.7$ m [47]. Using the $\approx 3.3 \times 10^9$ recorded Ag(1.58 A GeV)+Ag $0-30\%$ most central collision events, all reconstructed K^+ and K^- within the detector acceptance are investigated for their kinematical properties and their particle production rates compared to a selection of existing models.
This work describes how the events are selected to obtain pure Ag(1.58 A GeV)+Ag collisions, from which the charged Kaons can be extracted. Furthermore, the detailed steps are elaborated with which the particle identification is performed. Finally, it is discussed how extracting the $K^{\pm}$ count rates from the reconstructed mass spectra is performed by subtracting a background estimated by an interpolation algorithm. The 1.34×10^7 K^+ and 1.21×10^5 K^- reconstructed this way are analysed in their multiplicities as a function of transverse mass and rapidity.
Furthermore, the $\phi \rightarrow K^+K^-$ channel is investigated. This work describes how the daughter particles are selected from the sample of $K^{\pm}$ candidates in the reconstructed mass spectra and how additional constraints minimise the amount of background. Using another background estimation method explained in this work, a total of 5.67×10^3 ϕ-mesons are reconstructed for further analysis. With these multiplicities, for the first time in this energy region, it is possible to investigate the particle production yields in three distinct intervals of collision centrality for the $0-30\%$ most central events. This allows for a multidifferential view of strange hadron production mechanisms by comparing different excitation functions between measured data and model predictions from statistical hadronisation models and transport models, utilising observations from [3] and [119]. The reconstruction of the Ξ^--Baryon multiplicities in [125] offers an excellent opportunity for a test of the SHM ansatz of strangeness canonical radii as a mechanism for strangeness suppression, as it contains two-fold open strangeness at an excess energy of $\sqrt{s_{\mathrm{exc}}^{\Xi^-}} = 0.70$ GeV. It is shown, that the same choice of R_C for a singular parameterisation fails to simultaneously describe the ϕ/Ξ^- and ϕ/K^- ratios.
The observation of a universal scaling of strange hadron production rates as function of $\langle A_{\mathrm{part}} \rangle$ holds true also for Ag(1.58 A GeV)+Ag collisions with a slope parameter of $\alpha = 1.50 \pm 0.03$, which is consistent with $\alpha = 1.45 \pm 0.06$ obtained from Au(1.23 A GeV)+Au collisions. Furthermore, this global parameter α is consistent with the slopes extracted from individual fits. This enables a discussion on the question, whether strangeness is produced in $s\bar{s}$-pairs, followed by a percolation process along the overlapping pion clouds of the nucleons participating in the collision, only forming final hadronic states below a certain nuclear density threshold.
As for Au(1.23 A GeV)+Au, also in Ag(1.58 A GeV)+Ag collisions a significant difference in the obtained T_{Eff}-parameter between K^+ and K^- is observed. By taking into account the substantial contribution of the $\phi \rightarrow K^+K^-$ feed-down ($\approx 15\%$) to the K^- transverse mass spectra, this work shows that the softening of the spectrum can, to a large extend, be explained by this effect.

Kurzfassung

Diese Arbeit konzentriert sich auf die Untersuchung der K^+-, K^-- und ϕ-Mesonenproduktion in Ag(1.58 A GeV)+Ag-Kollisionen bei einer Schwerpunktsenergie von $\sqrt{s_{\mathrm{NN}}} = 2.55$ GeV. Der energetisch günstigste Kanal für die direkte K^+-Produktion in binären NN-Kollisionen $N \rightarrow N\Lambda K^+$ liegt bei genau dieser Energie. Für die verbleibenden K^- und ϕ-Mesonen muss eine Überschussenergie von $\sqrt{s_{\mathrm{exc}}^{K^-}} = 0.31$ GeV und $\sqrt{s_{\mathrm{exc}}^{\phi}} = 0.34$ GeV vom System bereitgestellt werden. Dies macht diese Teilchen zu einer ausgezeichneten Sonde für Effekte im Inneren des Mediums. K^+ ($|u\bar{s}\rangle$) und K^- ($|\bar{u}s\rangle$) Mesonen können direkt rekonstruiert werden, da sie ein $c\tau \approx 3.7$ m [47] besitzen. Anhand der $\approx 3.3 \times 10^9$ aufgezeichneten Ag(1.58 A GeV)+Ag $0-30\%$ zentralsten Kollisionsereignisse werden alle innerhalb der Detektorakzeptanz rekonstruierten K^+ und K^- auf ihre kinematischen Eigenschaften und ihre Teilchenproduktionsraten im Vergleich zu einer Auswahl bestehender Modelle untersucht.
Diese Arbeit beschreibt, wie die Ereignisse ausgewählt werden, um reine Ag(1.58 A GeV)+Ag-Kollisionen zu erhalten, aus denen die geladenen Kaonen extrahiert werden können. Darüber hinaus werden die detaillierten Schritte erläutert, mit denen die Teilchenidentifikation durchgeführt wird. Schließlich wird erörtert, wie die Extraktion der $K^{\pm}$-Zählraten aus den rekonstruierten Massenspektren durch Subtraktion eines durch einen Interpolationsalgorithmus geschätzten Untergrunds erfolgt. Die auf diese Weise rekonstruierten 1.34×10^7 K^+ und 1.21×10^5 K^- werden in ihren Multiplikationen als Funktion der transversalen Masse und der Geschwindigkeit analysiert. Darüber hinaus wird der $\phi \rightarrow K^+K^-$ Kanal untersucht. In dieser Arbeit wird beschrieben, wie die Tochterteilchen aus der Stichprobe der $K^{\pm}$-Kandidaten in den rekonstruierten Massenspektren ausgewählt werden und wie zusätzliche Beschränkungen die Menge des Untergrunds minimieren. Unter Verwendung einer anderen Methode zur Abschätzung des Hintergrunds, die in dieser Arbeit erläutert wird, werden insgesamt 5.67×10^3 ϕ-Mesonen rekonstruiert.
Mit diesen Multiplizitäten ist es zum ersten Mal in diesem Energiebereich möglich, die Ausbeute der Teilchenproduktion in drei verschiedenen Intervallen der Kollisionszentralität für die $0-30\%$ zentralsten Ereignisse zu untersuchen. Dies ermöglicht eine multidifferentielle Betrachtung der Produktionsmechanismen seltsamer Hadronen durch den Vergleich verschiedener Anregungsfunktionen zwischen gemessenen Daten und Modellvorhersagen aus statistischen Hadronisierungsmodellen und Transportmodellen unter Verwendung von Beobachtungen aus [3] und [119]. Die Rekonstruktion der Ξ^--Baryonen-Multiplizitäten in [125] bietet eine ausgezeichnete Gelegenheit für einen Test des SHM-Ansatzes der kanonischen Seltsamkeitsradien als Mechanismus zur Seltsamkeitsunterdrückung, da sie zweifach offene Seltsamkeit bei einer Überschussenergie von $\sqrt{s_{\mathrm{exc}}^{\Xi^-}} = 0.70$ GeV enthalten. Es wird gezeigt, dass die gleiche Wahl von R_C für eine singuläre Parametrisierung nicht in der Lage ist, die ϕ/Ξ^- und ϕ/K^- Verhältnisse gleichzeitig zu beschreiben.
Die Beobachtung einer universellen Skalierung der Produktionsraten seltsamer Hadronen als Funktion des $\langle A_{\mathrm{part}} \rangle$ gilt auch für Ag(1.58 A GeV)+Ag-Kollisionen mit einem Steigungsparameter von $\alpha = 1.50 \pm 0.03$, der mit $\alpha = 1.45 \pm 0.06$ aus Au(1.23 A GeV)+Au-Kollisionen konsistent ist. Außerdem stimmt dieser globale Parameter α mit den Steigungen überein, die aus den individuellen Fits extrahiert wurden. Dies ermöglicht eine Diskussion der Frage, ob Seltsamkeit in $s\bar{s}$-Paaren erzeugt wird, gefolgt von einem Perkolationsprozess entlang der sich überlappenden Pionenwolken der an der Kollision beteiligten Nukleonen, wobei nur finale hadronische Zustände

unterhalb einer bestimmten Kerndichteschwelle gebildet werden.
Wie bei Au(1.23 A GeV)+Au wird auch bei Ag(1.58 A GeV)+Ag-Kollisionen ein signifikanter Unterschied in den erhaltenen T_{Eff}-Parametern zwischen K^+ und K^- beobachtet. Unter Berücksichtigung des erheblichen Beitrags des $\phi \to K^+K^-$ feed-downs ($\approx 15\%$) zu den K^- transversalen Massenspektren zeigt diese Arbeit, dass die Aufweichung des Spektrums zu einem großen Teil durch diesen Effekt erklärt werden kann.

Contents

1. Introduction

The standard model of particle physics contains the theories of the electroweak and the strong interactions. The three fundamental forces are transmitted by exchange particles - the strong interaction by the massless gluon, the electromagnetic interaction by the massless photon and the weak interaction by the $W^{\pm}$ and Z^0 bosons. The dynamical mediation of forces by the exchange particles is coupled to the corresponding charge of each interaction, the colour charge (strong), the electric charge (electromagnetic) and the weak charge (weak). The forces themselves act between the different groups of fermions - the leptons and the quarks - being particles of half-integer spin, as listed in table 1.1.

Fermions	**Family**			**Electr. Charge**	**Colour Charge**
	1st	**2nd**	**3rd**		
Quarks	u	c	t	+2/3 e	r,g,b
	d	s	b	−1/3 e	r,g,b
Leptons	e^-	μ^-	τ^-	−1 e	none
	ν_e	ν_μ	ν_τ	0	none

Table 1.1.: Groups and families of fermions according to the standard model of particle physics (taken from [106]).

The Higgs-Boson (H) plays a crucial role as well. It is the only known fundamental scalar particle. The coupling of a fermion to a Higgs-Boson is always proportional to its mass, which is why it plays a central role in the generation of current masses.
Three quark flavours are of importance to this work: up (u), down (d) and strange (s). They are listed, with their corresponding quantum numbers, in table 1.2. Here, B stands for the baryon number, J for the spin, I for the isospin with the third component I_3 and S for the strangeness quantum number. The electric charge is given in table 1.1. For all quantum numbers with a designated sign, the sign flips for the corresponding antiquark.

Flavour	**B**	**J**	**I**	**I_3**	**S**
u	+1/3	1/2	1/2	+1/2	0
d	+1/3	1/2	1/2	−1/2	0
s	+1/3	1/2	0	0	−1

Table 1.2.: Quark flavours relevant to this work with their corresponding quantum numbers as taken from [106]. More information is in the text.

In all three interactions, energy, momentum, angular momentum, electromagnetic and colour charge, as well as baryon- and lepton-number, are conserved. For the strong and electromagnetic interaction, I_3 and strangeness are conserved, while the isospin I is only conserved in the strong interaction.
In heavy ion collisions, the properties of strongly interacting matter are studied. The theory of strongly interacting matter is quantum chromodynamics, briefly elaborated in the following section.

1.1. Quantum Chromodynamics

Quantum chromodynamics (QCD) describes the interaction of quarks and gluons, which form the fundamental building blocks of all hadronic matter. Each quark possesses one of the colours - red, green or blue - or a corresponding anticolour, while each gluon carries a colour and its anticolour to remain colour-neutral. Every system of quarks and gluons has to be overall colour neutral. This means that, for baryons, each quark has to have one of the three colours, while mesons always contain a colour-anticolour-pair. Therefore, it is not possible to observe free quarks, an effect which is known as *confinement* and reflected by the leading order of the running coupling constant of the strong interaction [106]

$$\alpha_s(Q^2) = \frac{12\pi}{(33 - 2n_q) \cdot \ln\left(Q^2/\Lambda^2_{\mathrm{QCD}}\right)} \tag{1.1}$$

depending on the momentum transfer Q^2. Furthermore, n_q denotes the number of quark flavours present and $\Lambda_{\mathrm{QCD}} \approx 200$ MeV [50] is the QCD scale parameter, which also gives the order of the u and d constituent quark masses.
In a static system, the further apart, e.g., a $q\bar{q}$-pair the larger the coupling constant as the momentum transfer is lower. As gluons carry colour charge, they can couple to each other, which leads to the formation of flux tubes or strings in the gluon field between the bound quarks, creating a field of the form [29]

$$V(r) = -\frac{\alpha}{r} + \sigma \cdot r \ . \tag{1.2}$$

Here, r describes the distance between two quarks and σ represents the elasticity constant representing the string of gluons between them. Consequently, the QCD potential increases linearly with increasing distance and two quarks can only be separated by breaking the flux tube due to forming a new $q\bar{q}$-pair. In return, following the Heisenberg uncertainty principle

$$\hbar \leq \Delta x \cdot \Delta p \tag{1.3}$$

smaller distances between quarks within a common system also reduce the coupling constant due to an increase in the momentum transfer. Using equation 1.3, one can, furthermore, argue that the localisation of the constituent quarks due to confinement within a sphere of $r \approx 1$ fm [116] leads to a constituent quark momentum of $p \approx 200$ MeV/c within the nucleon. This way, $\approx 2/3$ of the nucleon mass is phenomenologically accounted for by the localisation of constituent quarks.
When overlapping the contents of many hadrons, a system of quasi-free (*asymptotically free*) quarks and gluons is created. This medium of quasi-free quarks and gluons is called a *Quark Gluon Plasma* (QGP), which can be effectively described as a purely thermal medium creating $q\bar{q}$-pairs and gluons which recombine to form hadrons at sufficiently small temperatures. Accordingly, this medium can be attributed to thermodynamical properties like a temperature T (and chemical potentials μ) following the composition of the created matter. Some theoretical calculations for the phase transition between confined matter and QGP yield a critical temperature of $T_c \approx 151 \pm 3 \pm 3$ MeV [27], which is in accordance with experimental findings [22]. The phase transition is a crossover with (nearly) massless u, d and s quarks. More details can be found in [50].
At high temperatures and vanishing baryo-chemical potentials μ_B, the quarks and gluons behave quasi-free ($p \propto T \gg \Lambda_{QCD}$) as the high densities within the medium shield them from any interaction beyond the Debye length $r_D \propto 1/(\alpha_s T)$ [50]. However, at low temperatures and high

baryo-chemical potentials, the nature of the created medium is not yet fully understood. The known properties of compressed baryonic matter are discussed further in section 1.2.
Another important finding is the absence of chiral symmetry breaking in the QGP, which is elaborated further in the following section.

1.1.1. Chiral Symmetry Breaking

Chirality describes the association of the spin of a quark with its momentum. Right-handed, or positive chiral, quarks have aligned spin and momentum orientations. Left-handed, or negative chiral, quarks have an opposite orientation of spin and momentum. Both states, energetically, exist with the same probability. In mathematical terms, assuming massless u and d quarks, this splits the quark interaction term of the QCD Lagrangian into a left-handed and a right-handed term [40]

$$\bar{q}(x)(i\gamma_\mu D^\mu)q(x) \rightarrow \bar{q}_L(i\gamma_\mu D^\mu)q_L + \bar{q}_R(i\gamma_\mu D^\mu)q_R$$

with $q = \begin{pmatrix} u \\ d \end{pmatrix}$ the quark iso-spinor, γ_i the gamma-matrices containing the different iterations of the Pauli-matrices and D^μ the covariant derivative. The symmetry is given by the fact that a rotation of q by a unitary matrix U does not change the Lagrangian term. So a chirally symmetric particle is invariant under parity transformations. For mesons with massless u and d quarks, these rotations can act on the isospin, e.g., changing a π^+ into a π^-, or on an axial vector part rotating particle species into one another, e.g., $\pi \rightarrow \sigma$ [88]. The symmetry group is $\mathrm{SU}(2) \times \mathrm{SU}(2)$, where 2 stands for the two isospin components. Including the strange quark, q contains s as a third component and the symmetry group becomes $\mathrm{SU}(3) \times \mathrm{SU}(3)$. Nevertheless, the significantly higher current quark mass of the s-quark ($m_s \approx 95$ MeV/c^2[141]) in comparison to the u ($m_u \approx 2$ MeV/c^2[141]) and d ($m_d \approx 5$ MeV/c^2[141]) make the fundamental assumption of a negligible quark mass doubtable.

Chiral symmetry is broken if q_L and q_R states mix. In the case of spontaneous symmetry breaking, this means transforming a symmetric system (regarding a symmetry group) into a non-symmetric vacuum state. A representation of this process is, leaning the analogy on [40], a ball with an unstable balance on a local maximum of a radially symmetric distribution. Hereby, the ball represents a ground state of a particle. Any influence of a force leads to the ball rolling down the slope towards a local minimum. This breaks the system's symmetry, as the ball's direction of motion creates a distinguishable difference from the rest of the distribution. This is shown in figure 1.1 for the cases of a system without (a) and with the spontaneous breaking of the symmetry (b). The minimum value of the potential plus the local ground state energy breaks the global symmetry of the potential in this classical analogon.
An effective ansatz for determining the mass of particles from QCD is introducing a mean-field approach. The resulting massive quark condensate terms introduced into the Lagrangian are not invariant under the corresponding $\mathrm{SU}(2)_L \times \mathrm{SU}(2)_R$ symmetry group, which explicitly breaks the chiral symmetry of the system, introducing an asymmetry. This way, $q\bar{q}$-pairs with a finite mass are generated.
Massless scalar particles are produced if a continuous symmetry is spontaneously broken. For each broken symmetry, one scalar particle exists called a *Goldstone boson*. If an explicitly broken symmetry is spontaneously broken, the produced Goldstone bosons possess masses, typically remaining small. For the case of only u and d quarks included, the resulting Goldstone bosons are the pions.

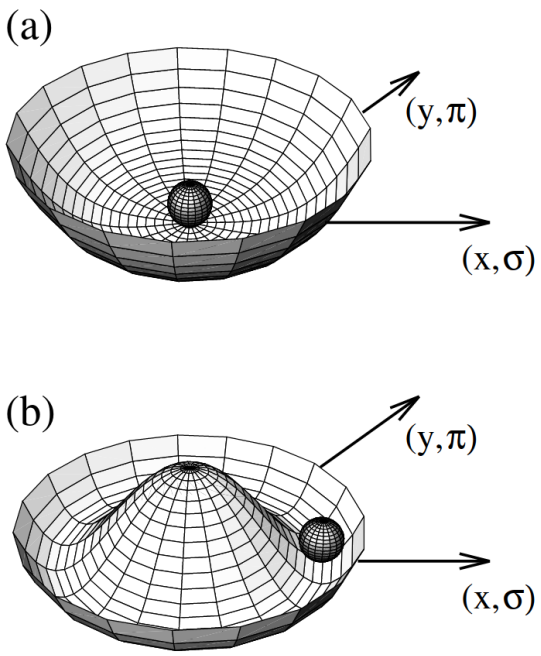

Figure 1.1.: Effective potentials for the cases of no spontaneous breaking of the symmetry (a) and a spontaneously broken symmetry (b) in the shape of a Mexican-hat-potential [88]. Each axis represents a certain particle state, indicating rotational symmetry in case (a) and broken rotational symmetry in case (b).

As QCD calculations on large scales are challenging to solve without using a numerical ansatz, the most common way of determining the properties of strongly interacting systems is lattice QCD which is discussed briefly in the following section.

1.1.2. Lattice QCD

The calculations of the non-perturbative QCD - on the scales of nucleon radii and larger - are complex due to the presence of self-interaction, the resulting number of large field components as well as the considerable value of the QCD coupling constant α_s compared to the coupling constant, e.g., of the electromagnetic interaction $\alpha_{\text{e.m.}} = 1/137$. Consequently, the large resulting values α_s^n for $n > 1$ make calculations complicated. To circumvent the emerging difficulties, a numerical lattice approach is chosen.
The basic idea is the subdivision of the continuous quantum field in a grid of quark and gluon configurations in typical spacetime lattice sizes of a few fm. Each of these grid cells is called a plaquette. Monte Carlo simulations are performed such that the number of quarks and antiquarks of each type is the same for each plaquette. However, they all contain a statistically independent field configuration. Then, the action [29]

$$S = \int d^4x \mathcal{L} \tag{1.4}$$

is calculated as the sum of all plaquette contour integrals. The expectation value of the corresponding observables is determined by averaging over all obtained values. Using this initial configuration, the values are varied to achieve lower values for S. This way, possible phase transitions are made visible by driving the entire system towards an equilibrated state. Spotting these phase transitions is part of an ongoing effort to map and understand the entire phase diagram of nuclear matter. The current state is briefly introduced in section 1.4.

1.2. Heavy Ion Collisions

To study the properties of QCD under extreme conditions, nuclei are accelerated and collided with one another. By comparing the kinematical distributions of the products of these collisions with model predictions, information about the dynamical processes within the strongly interacting matter can be retrieved. A fundamental parameter of any heavy-ion collision is the amount of overlap between the two nuclei. This overlap describes how head-on a collision occurred, defined via the *impact parameter* of the collision. It is abbreviated by the letter b, the distance between the centres of the cross-sections of the two nuclei, which is shown in figure 1.2. As it is not experimentally accessible, observables dependant on the impact parameter are used to estimate the collision centrality and, consequently, the size of the system created in the collision (see section 3.5.4).

Figure 1.2.: Impact parameter b of a collision between two identical nuclei A+A with the perspective along the beam axis.

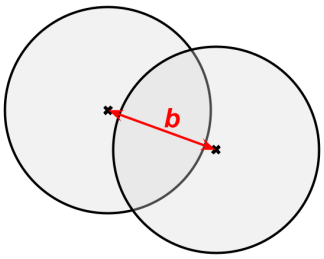

The cross-sections of the colliding nuclei in figure 1.2 are illustrated perpendicular to the beam axis. In a simplified manner, the overlap region between both cross-sections defines the reaction zone where the hadronisation processes occur.

A description commonly used in kinetic transport theories of heavy-ion collisions [79] is the superposition of large amounts of nucleon-nucleon (NN) collisions. In this picture, a fundamental observable is the available energy in a collision between a projectile and a target nucleon, $\sqrt{s_{\mathrm{NN}}}$. For HADES, a fixed-target experiment, the projectile describes the accelerated incoming nucleon while the target nucleon is at rest relative to the laboratory system. Correspondingly, the energy available in the centre of mass frame of the collision is defined as

$$\sqrt{s_{\mathrm{NN}}} = \sqrt{m^2_{\mathrm{projectile}}c^4 + m^2_{\mathrm{target}}c^4 + (E_{\mathrm{projectile}} + (m_{\mathrm{projectile}}c^2)) \cdot 2m_{\mathrm{projectile}}c^2}\ . \tag{1.5}$$

Before the collision, the two Lorenz-contracted nuclei move towards each other in the centre of mass frame (c.m.). Though the exact momenta of each nucleon within the nuclei is unknown, in many models, they are assigned the same velocity vector in magnitude and spatial orientation as the entire nucleus. When the nuclei collide, the nucleons of both nuclei scatter with each other according to their interaction cross-section. The resulting mean free path is defined as

$$\lambda_{\mathrm{m.f.p.}} = \frac{1}{\sigma_{\mathrm{tot}}\rho}$$

with the total interaction cross-section σ_{tot} and the medium density ρ. The total cross-section can be divided further into an *elastic* part σ_{el} and an *inelastic* part σ_{inel}, which leads to the formal definition $\sigma_{\mathrm{tot}} = \sigma_{\mathrm{el}} + \sigma_{\mathrm{inel}}$. Elastic reactions are scattering processes in which the number and intrinsic properties of the particles remain the same and only their respective momenta change, while the total momentum is conserved during the reaction. Inelastic reactions lead to the excitation of particles from their ground state, which affects the momenta as well as the

masses of the scattering particles.
Every nucleon participating in the scattering processes is called a *participant*. The nucleons which do not scatter are called the *spectators* of the collision. At beam energies of a few GeV, due to momentum conservation, a central bulk of compressed and mostly stopped baryonic matter forms.
Similar to the behaviour of a compressed volume of gas, the compressed baryonic matter undergoes a phase of expansion after reaching the maximum compression level, which can be subdivided into several stages. These stages are also depicted in figure 1.3, in which a simulation of the collision of two ^{107}Ag ions is shown. Each of the coloured spheres represents a particle.

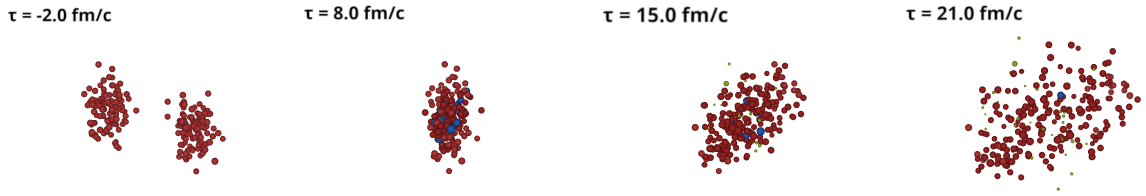

Figure 1.3.: Time evolution of a ^{107}Ag+^{107}Ag collision at 1.58 A GeV simulated by the UrQMD transport model (see section 1.3).

The two colliding nuclei start interacting at $\tau = 0$ fm/c and, represented by the second image in figure 1.3, reach a phase of maximum density, which is called a *fireball*, at around $\tau = 8$ fm/c, which is followed by the previously discussed expansion. While for temperatures around 150 MeV and vanishing nuclear net-density, a phase transition which realises quasi-free quarks within a chirally restored phase is predicted [87], at finite nuclear net-densities and moderate temperatures properties of the chiral condensate appear to determine hadronic properties. Phenomenologically this can be imagined by the nucleons forming a shell with enclosed valence quark content and a pion-cloud surrounding this shell [83]. When nuclei are compressed to nucleon densities $\rho > \rho_0$, the pion clouds of those nucleons strongly overlap, leading to the interaction of those $q\bar{q}$-pairs with one another and the formation of new mesonic states, depending on the available energy. This is schematically displayed in figure 1.4.

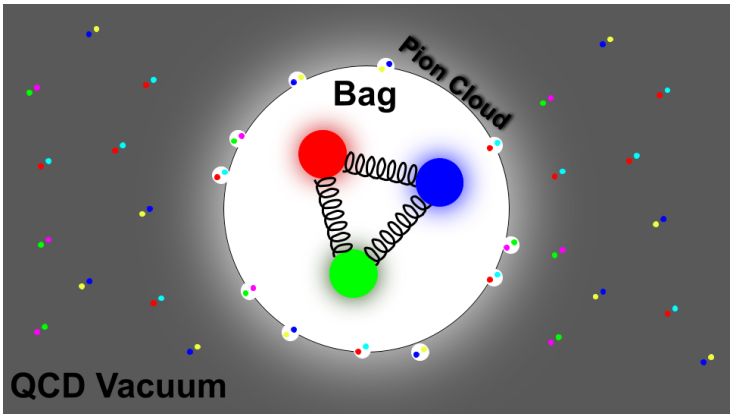

Figure 1.4.: Schematic depiction of the MIT bag model with the bag containing the valence quarks and the pion cloud surrounding it, interacting with the $q\bar{q}$-pairs produced in the QCD vacuum.

It is also a matter of ongoing debate whether those $q\bar{q}$-pairs are formed as a confined hadron or undergo a process of quark percolation [75].
Depending on the centrality of the collision, the following expansion of the collision system can manifest in different forms of collective motion. This collective motion is called flow and is described in section 1.2.2.
In the second stage, called the chemical freeze-out, the temperatures and densities of the system decrease sufficiently for inelastic processes to cease, which defines the final chemical composition of the produced particle spectrum with the exception of resonance and weak decays. The possible influence of quark exchange and coalescence mechanisms on the abundance of certain final state particles and light nuclei is of importance, as well. In the context of the K^- this is discussed in section 6.4.1.
In the final stage, the kinematic freeze-out, distances between the products of the collision increase sufficiently for elastic scattering processes to cease. After this stage, the kinematic distributions of all particles stay constant.

Photons and dileptons are direct probes for medium effects, as they do not take part in strong final state interactions. Furthermore, since vector mesons (ω,ρ^0,ϕ,...) possess decay channels into e^+e^- pairs, the reconstructed invariant mass spectrum (see section 4.2.2) of the dileptons is directly sensitive to the mass of the corresponding mother particles. Another important observable is the production of hadrons below their kinematic free nucleon-nucleon-interaction production threshold.

1.2.1. Strangeness Production at SIS18 Energies

A nucleus consists of protons and neutrons (nucleons) which in turn consist of gluons and quarks with flavours up and down. Other quark flavours either only exist as sea quarks indicated by the Feynman-graph displayed in figure 1.5

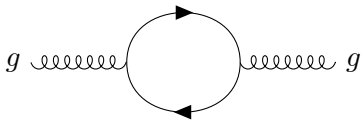

Figure 1.5.: Lowest order QCD diagram for virtual $s\bar{s}$ sea-quark production in the QCD vacuum.

or have to be produced by adding sufficient energy to the system and allowing for the emergence of a $q\bar{q}$-pair. In a QGP, this can happen either from the fusion of two gluons (figure 1.6)

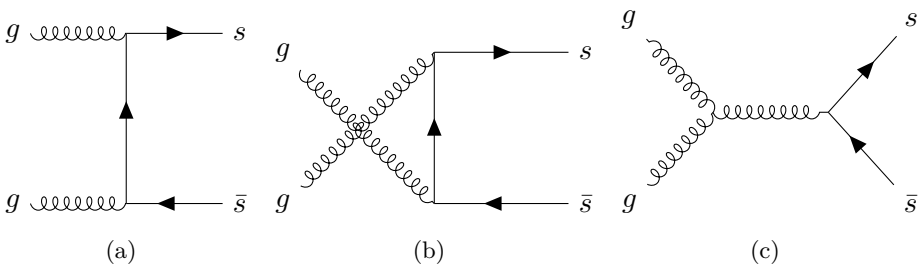

Figure 1.6.: Lowest order QCD diagrams for $s\bar{s}$ production via $gg \rightarrow s\bar{s}$.

or the fusion of two light quarks (figure 1.7) with a corresponding Q-value of $2m_s \approx 200$ MeV [47].
To produce strange hadrons in binary nucleon-nucleon interactions, looking at the asymptotic states only, the energy for the production of the entire hadron has to be provided. This includes

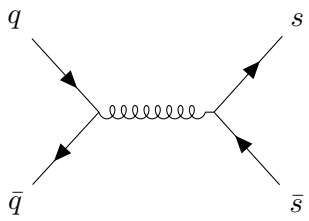

Figure 1.7.: Lowest order QCD diagrams for $s\bar{s}$ production via $q\bar{q} \rightarrow s\bar{s}$.

the current quark masses plus the energy necessary for the localisation of the constituent quarks. Consequently, in the picture of heavy-ion-collisions as a superposition of many NN interactions, the production of hadrons with strangeness quark flavour is expected to be strongly suppressed at energies of a few GeV. The energetically most favourable channel to produce strange hadrons is the binary nucleon-nucleon (NN) reaction

$$NN \rightarrow NK\Lambda$$

where, depending on the isospin of the nucleon, a K^0 ($|d\bar{s}\rangle$) or a K^+ ($|u\bar{s}\rangle$) emerges together with a Λ-Baryon ($|uds\rangle$) and a nucleon. An ^{107}Ag nucleus contains 47 protons and 60 neutrons, so isospin symmetry is nearly fulfilled. The Q-value of this associated production is $m_\Lambda + m_K - m_N \approx 670$ MeV [47]. The energetic threshold for this process is $\sqrt{s_{\mathrm{NN}}} = 2.55$ GeV, which coincides with the centre of mass collision energy of the analysed Ag(1.58 A GeV)+Ag events. The other two mesons relevant to this work are the K^- ($|\bar{u}s\rangle$) and the $\phi(1020)$ ($|s\bar{s}\rangle$). The latter is not considered a strange hadron, as the net strangeness is zero, which makes the ϕ-meson a particularly interesting probe. The energetically lowest production mechanisms for the generation of these mesons are

$$NN \rightarrow NNK^+K^-$$

with a threshold energy of $\sqrt{s_{\mathrm{NN}}} = 2.86$ GeV and

$$NN \rightarrow NN\phi$$

with a threshold energy of $\sqrt{s_{\mathrm{NN}}} = 2.90$ GeV. The corresponding mass of the $K^\pm$ is $m_{K^\pm} \approx 493.7$ MeV/c^2, while for the $\phi(1020)$ it is $m_{\phi(1020)} \approx 1019.5$ MeV/c^2 [141].
The assumption of isolated NN collisions is a simplified model description when discussing heavy ion collisions and dense nuclear matter. Assuming a proton charge radius of ≈ 0.88 fm [141] ($V = \frac{4}{3}\pi r^3 \approx 3$ fm^3) and an average ^{107}Ag radius of ≈ 4.5 fm [44] ($V \approx 382$ fm^3) it becomes apparent, that even without further compression not much space exists between the nucleons. However, for didactical purposes, this picture offers a good visualisation of medium interactions. In the picture of isolated nucleon-nucleon collisions, to accumulate sufficient energy in an interaction to surpass the energetic threshold for the production of mesons containing strangeness, an intermediate step via the production of resonances is needed. In this context, it means the excitation of a nucleon into a higher energetic state, e.g., via a Δ-resonance, of which $\Delta(1232)$ is the energetically lowest [141]. When a nucleon is excited to this state, it possesses a lifetime

$$\tau = \frac{\hbar}{\Gamma} \tag{1.6}$$

with the decay width Γ. The typical lifetime is a few fm/c. In the transport model picture (see section 1.3.1), the resonance can subsequently interact with other nucleons to obtain enough excitation energy to produce the strange hadrons previously discussed. For the production of a ΛK^+, this reads as

$$NN \rightarrow N\Delta$$

$$N\Delta \rightarrow N\Lambda K^+$$

As the $\phi(1020)$ has a $c\tau \approx 46$ fm [47], it barely leaves the fireball before it decays and is, therefore, classified as a resonance.
Another way to explain the production of hadrons below the energetic binary NN production threshold is off-shell production, as discussed in [53] and [62]. In this picture, the total width of the hadron states is modified inside the medium due to collisional broadening $\Gamma_{\text{collision}}$ which adds to the total width $\Gamma_{\text{total}} = \Gamma_{\text{vacuum}} + \Gamma_{\text{collision}}$ and depends on the baryon density and interaction cross-sections. For K^+, this effect is negligible, as the interaction cross section is $\sigma_{K^+N} \approx \sigma_{K^+N,\text{ elastic}} \approx 10$ mb and the velocities of the produced Kaons are also low [62]. The K^-N system, in contrast, couples strongly to the Λ- and Σ-hyperons, which leads to a shift of the K^- pole-mass inside the medium. This effectively lowers the energetic threshold for the production.

To summarise the chapter, strangeness production in heavy ion collisions at SIS18 energies is a sensitive probe to effects in the medium. The following section introduces several important experimental observables, which can be used to compare measured data to models as introduced in section 1.3 and draw conclusions about the properties of the created medium.

1.2.2. General Observables

To classify and interpret the data obtained from measurements, it is of the essence to define observables and correlate them to parameters obtained from models.
On the experimental side, the *event multiplicity* defines the overall number of produced particles per collision. As only charged particles can be directly detected, for most experiments, the term synonymously refers to the total number of charged particles detected per event. While the average number of emerging charged particles in heavy-ion collisions is phenomenologically found to be [29]

$$\bar{N}_{ch} \propto \left(\ln\left(\sqrt{s_{NN}}\right)\right)^2 \tag{1.7}$$

the charged particle multiplicity does not only vary with the collision energy s_{NN}. Furthermore, the previously introduced impact parameter plays a role as well. Several measurements in the low [7], intermediate [46] and high energy [31] regimes consistently show a difference in the particle production yield depending on the number of participating nucleons in a collision. Details on the classification by collision centrality are found in section 3.5.4.

Particles from heavy ion collisions typically reach significant fractions of the speed of light, making a relativistic description necessary. As a consequence, the energy E of a particle with mass m_0 and momentum p is given via [29]

$$E = \sqrt{(pc)^2 + (mc^2)^2}$$

Alternatively, by defining $\gamma = \frac{1}{\sqrt{1-\beta^2}}$, one arrives at $E = \gamma m$ and $p = \gamma\beta m$.
The phase space of the produced particles is defined by spanning a plane with a longitudinal and a transverse momentum axis, as figure Figure 1.8 indicates. In the longitudinal direction, the basic observable is called the *rapidity* of a particle, which is given via [29]

$$y = \tanh^{-1}(\beta) = \frac{1}{2}\ln\left(\frac{1+\beta}{1-\beta}\right) = \frac{1}{2}\ln\left(\frac{E+p_L}{E-p_L}\right) = \ln\left(\frac{E+p_L}{m_T}\right) \tag{1.8}$$

Here β is defined as the relativistic $\beta = v/c$, while E is the energy of the particle (cf. equation 1.5) and $p_L = p_z$ is the longitudinal momentum. For $\beta \to 1$ one arrives at $y \to \infty$, while $y \approx \beta$ is valid for small β.
The rapidity is additive under Lorentz transformations. Consequently, the shape of the rapidity distribution is also invariant under Lorentz transformations. A parallel shift can transform it between the centre of mass and the laboratory system. This is used in the presented analysis, where the final rapidity spectra are exclusively shown in the centre of mass system.
The designated value around $y = 0$ in the centre of mass frame is called the *midrapidity region* and corresponds to the central region of the collision zone in momentum space. This region is of considerable interest, as particles emerging from there, are either newly produced or undergo several rescattering processes changing their initial longitudinal momenta [57]. For the case of a fixed target experiment colliding ^{107}Ag+^{107}Ag ions at 1.58 A GeV, this value is found at $y = 0.82$ in the laboratory frame of reference. Analogously, one can define the projectile (y_P) and target (y_T) fragmentation regions. Those are the regions around the corresponding target and projectile rapidity values. The underlying idea is the fragmentation of the two colliding nuclei in the outer regions, leading to the emission of those fragments [29]. This also leads to several interpretations for spectra of the number of produced particles per unit of rapidity $\left(\frac{dN}{dy}\right)$. For particles with distributions peaking at a global maximum at midrapity, the dominant source is expected to be particle production or rescattering in the central region of the collision zone. For the case of two maxima located at target and projectile rapidity, the primary source is assumed to be fragmentation processes.
Ultrarelativistic particles are described in the frame of pseudorapidity η, as $E \approx p$. It estimates the resulting rapidity via the emission angle θ of the particle [29]

$$\eta = -\ln\left(\tan\left(\frac{\theta}{2}\right)\right)$$

In equation 1.8, m_T was already implicitly introduced, which stands for the *transverse mass*. This observable is directly depending on the *transverse momentum* $p_T = \sqrt{p_x^2 + p_y^2}$ via [29]

$$m_T = \sqrt{m_0^2 + p_T^2} \tag{1.9}$$

where m_0 denotes the rest mass of the corresponding particle. This way, m_T scales the p_T distribution with the particle's rest mass. This scaling proves helpful for the data presented in this work when applying fits and is thusly preferred over the p_T representation. More on this is found in chapter 5.

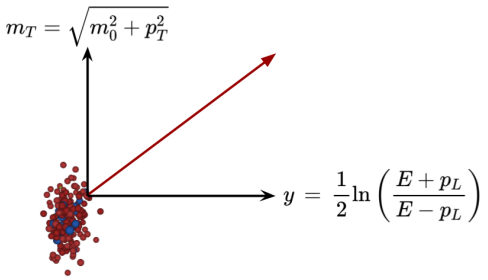

Figure 1.8.: Summary of the kinematic observables of a particle emitted from the collision zone.

Particle Flow

Another important observable is the collective emission or *flow* pattern of particle species from the collision zone. It is a measure of the collective expansion behaviour of the system. In general, the collective particle emission pattern is defined via [29]

$$E\frac{d^3N}{d^3p} = \frac{1}{2\pi}\frac{d^2N}{p_T dp_T dy}\left(1 + 2\sum_{n=1}^{\infty} v_n(p_T, y)\cos(n(\phi - \Psi_R))\right) \tag{1.10}$$

with the flow coefficients defined as the averages

$$v_n(p_T, y) = \langle\cos(n(\phi - \Psi_R))\rangle \tag{1.11}$$

and Ψ_R representing the position of the reaction plane. The angle ϕ represents the azimuthal emission angle of the particle. The reaction plane is spanned by the impact parameter vector and the collision (z) axis. A visual representation can be found in figure 1.9.

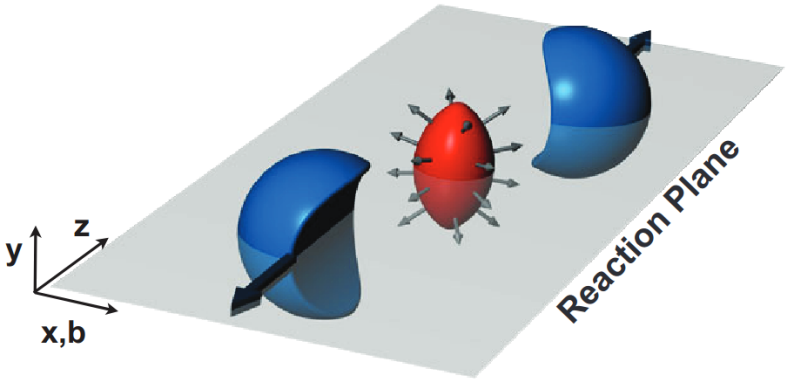

Figure 1.9.: Schematic of two colliding nuclei (blue) without stopping or Lorentz contraction considered [111]. The grey arrows indicate the collective behaviour (here, elliptic flow) of particles emerging from the central collision zone.

The most simple case can be observed for central collisions ($b = 0$) with a complete overlap of both nuclei. Here, the collision zone can be assumed to be spherical, and the resulting expansion isotropic ($v_n = 0$ for all n). No reaction plane can be defined, and the collective expansion is called *radial flow*. For collisions with $b > 0$, anisotropies in the emission pattern relative to the transverse plane may occur. Consequently, this is called anisotropic flow and means that $v_n \neq 0$ for these cases.
For symmetric collision systems, odd n results in opposite signs for the forward and backward directions of the collision system. For even Fourier harmonics, this is not the case. The flow pattern presented in figure 1.9 is the so-called *elliptic flow* v_2, which is dominant.
The first-order harmonic is called the *directed flow* and is characterised by $v_1 \neq 0$ as well as different signs for forward and backward directions. This can be understood in terms of momentum conservation: the directed flow of particles emitted from one nucleus results in an opposite flow of particles emitted from the other nucleus.

In the practical flow analysis, a direct reaction plane reconstruction is impossible, as the impact parameter is unknown. As a consequence, a so-called *event plane* is estimated by measuring the spatial orientation of the spectator particles [84]. More details on the flow analysis and results

for charged pions produced in Ag+Ag collisions at 1.58 A GeV can be found in [99].

1.3. Transport and Statistical Hadronisation Models

A commonly used description of heavy-ion collisions on a microscopic level is the time-evolution of a single particle density via the test particle method, taking into account repulsive interactions with the help of collision terms. This leads to the transportation of nucleons and the formation of hadronic resonances as well as mesons in the final state. This is how kinetic transport theory calculates and describes the obtained secondary particle spectra. Another way to describe final state particle yields is the assumption of an emission from an equilibrated source, whose thermodynamical parameters are constrained by fits onto measured particle spectra. This method is used for the statistical hadronisation models. Both approaches are introduced in the following subsections. A third way to model heavy ion collisions is through hydrodynamic modelling of the dense matter in a fluid-like way [80]. As these models are mainly used to describe collective behaviour, they are not discussed further.

1.3.1. Transport Models

Several transport models exist, which differ mostly in technical aspects [110]. They can be categorised into two groups:
Quantum Molecular Dynamics (QMD) models solve the relativistic transport equations numerically on an event-by-event basis as the interaction between Gaussian wave packets of finite width. This way, complete nucleons are scattered in QMD, which allows for detailed investigations of particle correlations and fluctuations.
Boltzmann-Uehling-Uhlenbeck (BUU) models determine the equations of motion from a density functional [138], which aims to describe the probability of a particle being found inside a certain part of the phase space [139]. The number of introduced test particles determines the degree to which stochastic processes happen and, thus, the abundance of fluctuations.
Despite the different approaches, similar equations of motion are obtained. The main differences can be traced back to deviations in the introduced potentials and formal definitions of, e.g., participants. As the results in chapter 6 are compared to UrQMD [30] and SMASH [135], which each represent one of the two groups, the following descriptions focus on the common fundamentals. In [62], a comparison of different transport approaches is performed with a focus on charged Kaons in the few GeV energy regime.

Initially, two spherical nuclei are generated according to a Woods-Saxon potential:

$$\frac{dN}{d^3r} = \frac{\rho_0}{\exp\left(\frac{r-r_0}{d}\right)+1} \ , \tag{1.12}$$

with the diffusiveness of the nucleus d. Also, other potentials can be used. The nucleons of both nuclei are then given the same momenta with opposite directions. Finally, the impact parameter for the collision is chosen randomly. Subsequently, the idea is solving the relativistic Boltzmann equation [135]:

$$p^\mu \partial_\mu f_i(x,p) + m_i F^\alpha \partial^p_\alpha f_i(x,p) = C^i_{\text{coll}} \ , \tag{1.13}$$

for the system of the two colliding nuclei, with the single particle distributions $f_i(x,p)$ for each particle species i as well as the long-range forces F^α, determined by the potentials, acting on them individually. Short-range interactions are described by the collision term C^i_{coll} of each particle. This ansatz allows obtaining each particle's complete phase space information at any

time during the collision. It solves the non-equilibrium dynamics of hadrons by resonance excitations and decay. These interactions are based on vacuum properties, i.e., fits on measured interaction cross sections where available. To solve the Boltzmann equation, it is crucial to define a collision criterion. For the case of UrQMD and SMASH, it is a geometric definition [135]. For each step, the collision criterion is checked, and if fulfilled, the scattering process is calculated.
If the decay width Γ of a particle exceeds 10 keV ($\tau \approx 6.5 \cdot 10^{-20}$ s), it is considered a resonance [135]. These resonances can undergo multi-scattering processes to accumulate significant energy compared to the ground state. Their decay is assumed to be the main source for strangeness production below the energetic free NN production threshold in the few GeV regime. Using this mechanism, Kaons (K^+,K^0) are produced via the channel already introduced in section 1.2.1:

$$NN \rightarrow NB^\star \rightarrow NYK \ ,$$

with the baryonic resonance $B^\star$ being a $N^\star$ or $\Delta^\star$ and the hyperon Y, either a Λ or a Σ [128]. Antikaons can be produced similarly via a baryonic resonance decaying into a $K\bar{K}$-pair or via a strangeness exchange reaction where a hyperon reacts with a pion:

$$\pi Y \rightarrow Y^\star \rightarrow \bar{K}N \ ,$$

though the latter is more unlikely as an additional hyperon resonance formation is needed before the fireball freezes out. In [119], it was found that about 25% of all K^- originate from a ϕ-meson decay. This introduces another important production mechanism in the channel:

$$NN \rightarrow NN^\star \ ,$$

$$N^\star \rightarrow \phi N \ ,$$

$$\phi \rightarrow K\bar{K} \ ,$$

The decay $N^\star \rightarrow \phi N$ has never been experimentally observed, which hints towards a rather small branching ratio. Preferably, direct $K\bar{K}$ and ϕ-meson production happens via the production and decay of a Δ-resonance as introduced in section 1.2.1. The branching ratios of the processes are obtained from experimental data.
Besides the (in-)elastic scattering processes, also other forces act on the particles in the collision. The one-particle Hamiltonian $H_i = \sqrt{\overrightarrow{p}_i^2 + m^2}$ is modified by adding a mean-field potential in the form of a Skyrme potential. This means that, depending on the local particle density, all particles feel an effective nuclear potential. The versions of the model used for later comparison do not contain further modifications due to an electromagnetic potential (Coulomb and Lorentz forces), as the modifications are in first-order negligible compared to the mean-field potential.
The predictions of different transport models for the Ag(1.58 A GeV)+Ag data presented in this work are shown in figure 1.10. More details on the differences between the models are found in [110]. Most transport models coincide for non-strange hadrons, while large deviations are visible for strange hadrons. In this context, by comparing the results, experimental measurements help to put constraints on the possible particle production mechanisms in the medium. Furthermore, by comparing the kinematic spectra, effects due to potentials can be isolated.

1.3.2. Statistical Hadronisation Models

One of the most fascinating observations is that simple concepts from statistical physics can describe many observations in heavy ion collisions. Assuming a radially symmetric, fully ther-

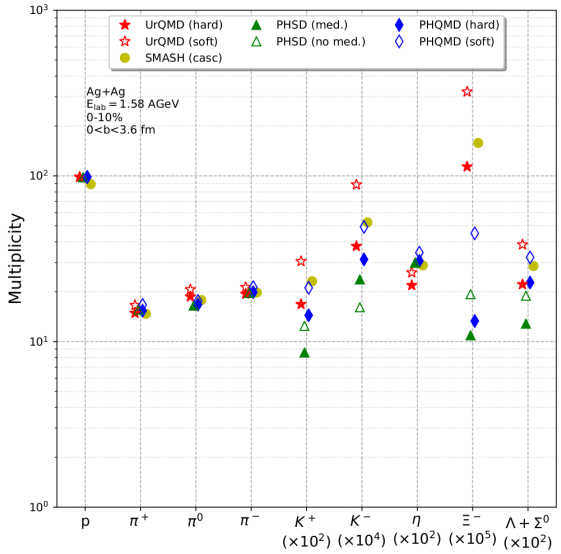

Figure 1.10.: Predictions for particle production yields from Ag(1.58 A GeV)+Ag collisions in different transport models [110].

malised hadron gas fireball, hadron yields are described surprisingly accurate throughout the collision energy scale. For a grand canonical ensemble including strangeness, the particle number density n_i of a particle species i is then defined as [62]:

$$n_i = \frac{N_i}{V} = g_i \int_0^\infty \frac{d^3p}{(2\pi)^3} e^{-(E_i - \mu_B B_i - \mu_S S_i)/T} \tag{1.14}$$

with the number of particles N_i per volume V. The energy $E_i = \sqrt{p^2 + m_i^2}$ is the single particle energy for the corresponding particle species. The temperature of the system T and the baryo-chemical potential μ_B are the two most decisive parameters for the discussion of the phase diagram of hadronic matter, as is elaborated in section 1.4. Correspondingly, μ_S is the strangeness chemical potential, while B_i is the baryon and S_i the strangeness number of particle species i. The spin-isospin degeneracy factor g_i represents the number of available spin and isospin states for otherwise identical particles of one sort.
This model can be fitted onto obtained particle yields and used to extrapolate to unmeasured yields for other particle species. Furthermore, these results can be used to extrapolate to other collision energies. This is used in chapter 6 to test the accuracy of the model predictions. The more particles are included in the initial fitting procedure, the better constrained the parameters.
However, as shown in [51], the model introduced with equation 1.14 only works with modifications in the few GeV energy regime. Average conservation of strangeness fails to describe the particle yields correctly. When introducing exact conservation of strangeness, the fit results coincide with data obtained from low-energy experiments. For charged Kaons, these modifications lead to equations of the form [62]:

$$n_{K^+} = g_{K^+} \int_0^\infty \frac{d^3p}{(2\pi)^3} e^{-E_{K^+}/T} \left[g_{K^-} \int_0^\infty \frac{d^3p}{(2\pi)^3} e^{-E_{K^-}/T} + g_\Lambda \int_0^\infty \frac{d^3p}{(2\pi)^3} e^{-(E_\Lambda - \mu_B)/T} \right] \tag{1.15}$$

$$n_{K^-} = g_{K^-} \int_0^\infty \frac{d^3p}{(2\pi)^3} e^{-E_{K^-}/T} \left[g_{K^+} \int_0^\infty \frac{d^3p}{(2\pi)^3} e^{-E_{K^+}/T} \right] \tag{1.16}$$

However, the assumption of a common freeze-out temperature for all particle species still contradicts the dynamical results obtained from transport calculations. Also, transport models need

to introduce in-medium masses for kaons to describe the experimental K^-/K^+-ratio. By itself, this poses no real contradiction, but the required freeze-out parameters for this ansatz would lie at $T \leq 34$ MeV and $\rho \leq 0.02\rho_0$ [133].
Two examples of thermal models are THERMUS [136] and Thermal-FIST [134]. They include ensemble options, quantum statistics and hadronic resonances. These frameworks are used to fit measured 4π particle production yields and to extrapolate for the particles not included in the fit. In [16], this is done with THERMUS for Ar(1.76 A GeV)+KCl data, where all quantum numbers are conserved grand canonically, while strangeness is conserved exactly. The resulting ratios between data (red points) and fit (blue lines) are shown in figure 1.11. The radius R_C

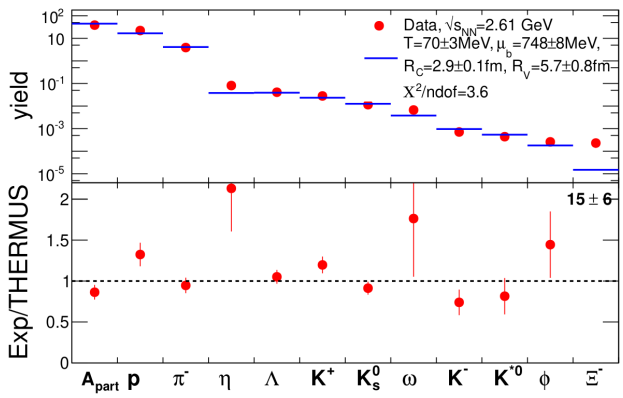

Figure 1.11.: Ratios between data (red points) and SHM fit (blue lines) for Ar(1.76 A GeV)+KCl data measured with HADES [16].

describes the microcanonical radius in which strangeness has to be exactly conserved, while R_V is the radius of the fireball volume at chemical freeze-out. This result shows that the model describes the data remarkably well, even for small systems in the few GeV energy regime. Nevertheless, some deviations, e.g., of the η and Ξ^-, hint towards the limits of this simple ansatz. Also, this model does only treat absolute particle production yields. This does not allow for drawing conclusions about the degree of thermalisation of the system.
It is, therefore, crucial to compare experimental hadron spectra with those predicted from a purely thermal fireball. In [78], a systematic comparison of transverse mass and rapidity spectra between HADES data and the THERMINATOR [85] Monte-Carlo generator is performed. A Siemens-Rasmussen model, describing the kinematic spectra and collective motion of particles emitted from an expanding source, is used for the description of the system with differentiation between local light quark ($\gamma_q = 1$) and strange quark ((γ_s)) equilibriums. Furthermore, baryon number, isospin 3-component and strangeness quantum number are conserved separately and recognised by a corresponding chemical potential. As a modification to this model, a Hubble-like expansion velocity distribution is applied, which means, that the expansion velocity of a particle is defined by $v(r) = \tanh(Hr)$ with a proportionality constant H. Also, resonance decays are included. The resulting distributions of protons and pions agree with experimentally determined transverse mass and rapidity spectra. Furthermore, the Δ-resonance can be identified as the dominant contribution to modifications of the thermal spectrum.

1.4. The QCD Phase Diagram of Nuclear Matter

Phase diagrams represent the different states of matter for different state variables of the system. In thermodynamics, temperature T is often plotted against another state variable representing pressure or density. This scheme can also be used for nuclear matter investigating the phases of matter as a function of T and the baryo-chemical potential μ_B, which is proportional to the density ρ. The higher the energy of the collision, the higher the temperature of the created

system. At the same time, the baryo-chemical potential is reduced as the colliding nuclei are increasingly Lorentz-contracted and the stopping power decreases strongly. This goes forth until the reaction zone consists only of particles created in the QGP and, consequently, possesses zero net-baryo-chemical potential. The experiments currently performed at the LHC, taking place at energies of several TeV, are close to this limit. This part of the QCD phase diagram resembles conditions of the early universe where, as it is expected, similar conditions were met as are emulated by the QGP stemming from high energy heavy-ion collisions.
In contrast, reducing the collision energy towards the few GeV energy regime leads to moderate temperatures of ≈ 100 MeV and an increasingly strong effect of stopping, meaning that colliding nuclei are (nearly) fully stopped along their path. More precisely, all nucleons participating in the multiple scattering processes resulting from the collision are slowed down before the created state of matter expands. The HADES experiment at the SIS18 accelerator facility at GSI in Darmstadt investigates these conditions.
Figure 1.12 depicts a collection of deduced chemical freeze-out points for experimental data. Each point represents the deduced point of a heavy-ion collision in which the chemical composition of the produced particle spectrum is determined.

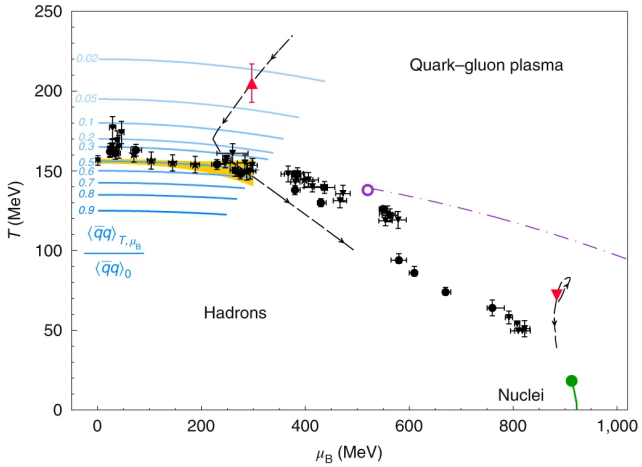

Figure 1.12.: Experimental mapping of the QCD phase diagram, as taken from [6]. More details can be found in the text.

The different utilised black markers are related to the different ensembles used for fitting the data (see section 1.3.2). For higher temperatures and low μ_B the smooth crossover region [33] is marked by the yellow band. A second-order QCD critical point is expected towards higher μ_B, but the exact location is not yet established. However, it is indicated by the purple dot, connected to a purple line representing a conjectured discontinuous first-order phase transition. The red triangle at $T \approx 200$ MeV and $\mu_B \approx 300$ MeV represents a data point measured by the NA60 collaboration [124]. Another red triangle at $T \approx 70$ MeV and $\mu_B \approx 900$ MeV represents a data point measured by the HADES collaboration [6]. For both cases, a black dashed line represents the predicted evolution of the fireball parameters [109][74][30], following the directions indicated by the arrows. For vanishing T and $\mu_B > 900$ MeV the green dot represents the critical endpoint [56] with the subsequent green line indicating a first-order liquid-gas phase transition for nuclear matter. The highlighted measurement by HADES also represents the first observation of dilepton emission from QCD matter under conditions resembling the expected conditions in binary neutron star mergers [6]. Figure 1.13 shows a direct comparison of the simulated density profiles between a binary neutron star merger and an Au+Au collision at 1.23 A GeV.

To determine the position of a measured freeze-out point in the phase diagram, the thermal hadronisation models introduced in section 1.3 are used. This, in return, leads to the physical

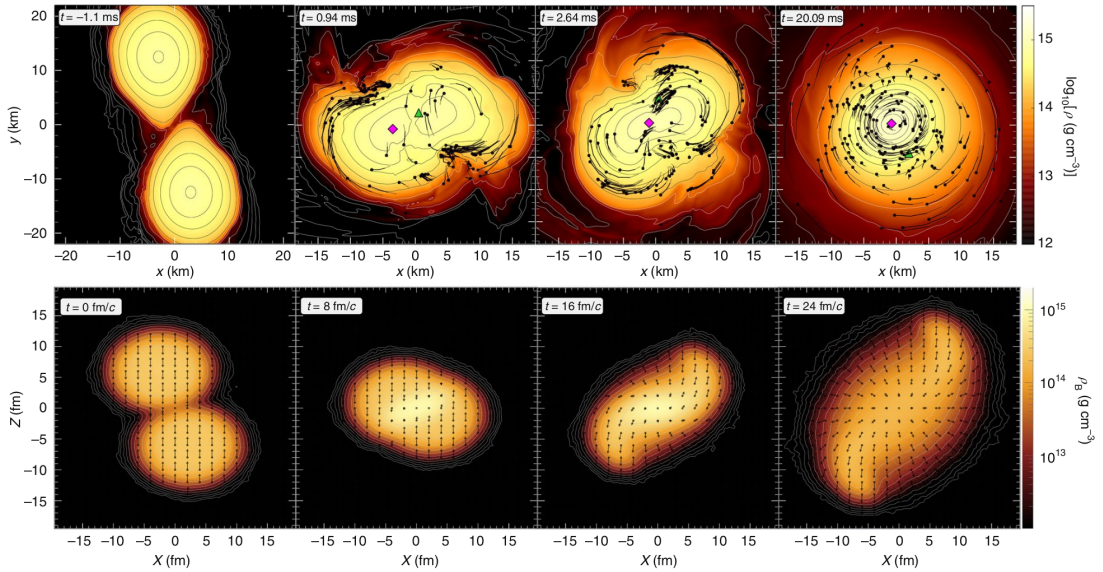

Figure 1.13.: Density profile comparison [6] between a binary neutron star merger system [98] and a heavy ion collision at the few GeV energy regime, based on [30]. Both colour-coded z-axes are depicted in the same density range.

implication of a thermally equilibrated fireball by assigning a single temperature and baryo-chemical potential to the entire system. For high-energy heavy-ion collisions with the formation of a QGP state, this model proves highly accurate [126]. At energies of a few GeV, this assumption proves to hold as well [16], which is an unexpected result for a system with large net-baryon densities. However, while for high-energy experiments the absolute yields are well described, the hadrons containing strangeness in the few GeV area pose a challenge to the statistical hadronisation models. Due to the low production rates, the strange hadron yields are a sensitive probe for medium effects, modelled via resonance production, different canonical ensembles and a different chemical potential μ_s. As it will be shown in section 6.3, there exist inconsistencies for strange hadrons at the few GeV regime. For the QGP there exist indications for a higher freeze-out temperature of strange hadrons, possibly due to lower cross-sections with the bulk matter [38], so the idea of a universal freeze-out temperature might be only approximately valid. In reality, a gradual phase transition might be realised instead. If this can be transferred to systems of dense nuclear matter, for rare probes, the resulting slight differences could significantly impact the accuracy of the description.

1.5. Previous Results and Motivation

The following sections introduce several topics and questions which this work focusses on.
The proximal goal of this work is the reconstruction and analysis of multidifferential particle production yields of charged Kaons and $\phi(1020)$-mesons produced in Ag+Ag collisions at a kinetic beam energy of 1.58 A GeV ($\sqrt{s_{NN}}$ = 2.55 GeV). As discussed in section 1.2.1, this collision energy corresponds to the free NN production threshold for K^+ and is well below the energetic thresholds for K^- and ϕ.

1.5.1. Charged Kaon Energy Excitation Function

One observable to understand the particle production mechanisms in more detail is the particle production rate dN/dy at midrapidity ($y_{c.m.} = 0$) as a function of collision energy $\sqrt{s_{\mathrm{NN}}}$. The results are, therefore, compared with the obtained rapidity density $\frac{dN}{dy}$ in $0-10\%$ most central Au+Au and Pb+Pb collisions measured with other experiments, as they are listed in the figures 1.14 for the K^+ and 1.15 for the K^-. Furthermore, the HADES Au+Au data [119] are also included. As Au+Au and Pb+Pb collisions have comparable numbers of participating nucleons, $\langle A_{\mathrm{part}} \rangle$, in this centrality range, a direct comparison of the results is possible without further corrections. For Ag+Ag collisions at 1.58A GeV, the average number of participating nucleons in $0-10\%$ most central collisions is nearly halved with 160.9 according to the Glauber Monte-Carlo model introduced in section 3.5.4. Consequently, the results are scaled by $(303.0/160.9)^{1.5}$, which is motivated by the scaling presented in section 6.5. Figure 1.14 shows the K^+ energy excitation function as a function of collision energy. Likewise, figure 1.15 does show the K^- energy excitation function as a function of collision energy. For both cases, the vertical grey line represents the individual threshold energies for the energetically cheapest production channel of the $K^{\pm}$ from binary NN-collisions (see section 1.2.1).

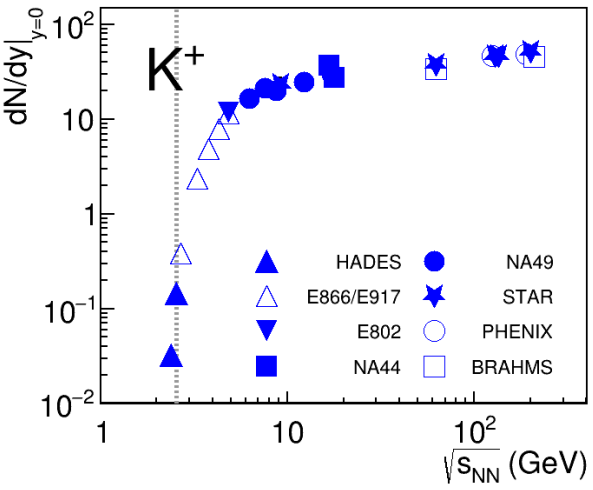

Figure 1.14.: K^+ production rate at midrapidity as a function of collision energy for central collisions [1][2][4][10][11][12][14][19][20][21][28][34][35][119]. The grey vertical line represents the free $NN \rightarrow NK^+\Lambda$ threshold energy of 2.55 GeV in the centre of mass frame.

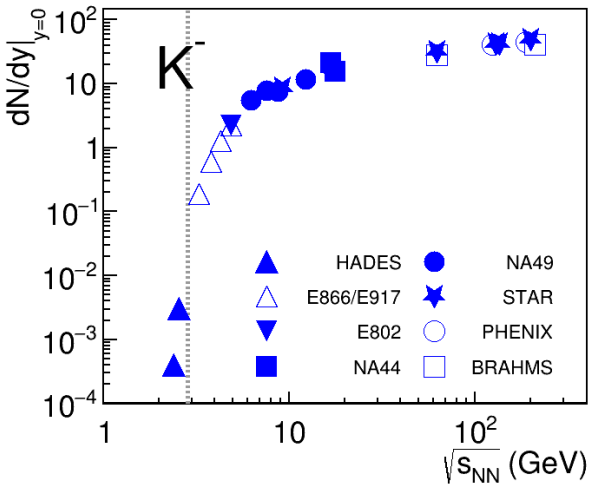

Figure 1.15.: K^- production rate at midrapidity as a function of collision energy for central collisions [1][2][4][10][11][12][14][19][20][21][28][34][35][119]. The grey vertical line represents the free $NN \rightarrow NNK^+K^-$ threshold energy of 2.86 GeV in the centre of mass frame.

These figures show the importance of the measurements performed at SIS energies, as previous results merely approached the energetic free NN reaction production threshold. At the same

time, the data taken by HADES can be used to shed light on medium interactions previously not accessible. As can be seen in figures 1.14 and 1.15, the results presented in this work also confirm previous data trends.

1.5.2. Particle Ratios

It has been observed that the K^-/K^+-ratio as a function of the incident beam energy can be described by a linear function [119] in the few GeV energy regime. This work aims to reconfirm this observation as well as perform a comparison with transport model results.
Another important finding of [119] is that in Au(1.23 A GeV)+Au collisions $\approx 25\%$ of all K^- originate from ϕ-meson decays, which is correlated with a steep rise of the ϕ/K^- ratio below the energetic free NN interaction production threshold for both particles. Figure 1.16 shows a selection of measurements for the ϕ/K^- ratio in the few GeV regime.

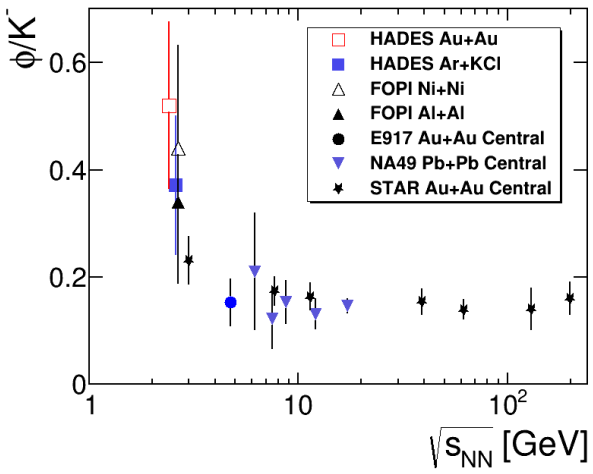

Figure 1.16.: ϕ/K^- ratio as a function of collision energy [3][9][13][15][66][81][105][119].

This work aims to confirm this observation with higher precision and test the predictions made by transport and statistical hadronisation models. In this context, one interesting observation is the indication of a rise in the ϕ/Ξ^--ratio seen by the STAR collaboration for Au+Au collisions at $\sqrt{s_{NN}} = 3$ GeV [3]. This contrasts with previous results obtained by the HADES collaboration for the Ar(1.76 A GeV)+KCl collision system [16]. Figure 1.17 shows the results from STAR and HADES measurements prior to this work.

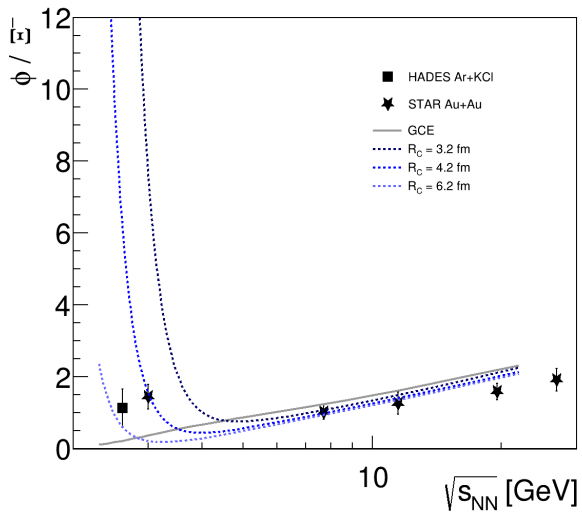

Figure 1.17.: ϕ/Ξ^- ratio as a function of collision energy [3][4][16]. GCE stands for grand canonical strangeness conservation, while the R_C-values represent different strangeness correlation radius parameterisations.

The indication of a rise in the STAR data is described by a THERMUS fit with a strangeness correlation radius $R_C = 4.2$ fm. In section 6.3, it is discussed whether the data presented in this work confirm this trend. Furthermore, the SHM fit parameterisation performed by STAR is tested for consistency regarding the ϕ/K^--ratio in section 6.4.

1.5.3. Universal $Mult/A_{\text{part}}$-A_{part} Scaling

The universal scaling of strange hadron production yields as a function of the number of participating nucleons within a collision, $\langle A_{\text{part}} \rangle$, seen in [119] proves to be a crucial observable in support for the quark percolation idea in the high-density phase of the collision. Moreover, the similar scaling of the ϕ-meson as well as the accordance of the K^- slope with a cocktail of thermal K^- and such from $\phi \rightarrow K^+K^-$ supports the idea of associated $s\bar{s}$-production and percolation as the underlying process for strange hadron production. These observations are, furthermore, indicated to be confirmed by the recent STAR data [140]. The observation is tested in section 6.5 if it holds true also for Ag(1.58 A GeV)+Ag collisions. Furthermore, a corresponding thermal K^- cocktail is compared with the measured transverse spectra to test the consistency with a purely thermal ansatz for the explanation of the difference in slope between K^+ and K^-.

1.5.4. Coulomb Effect for Charged Kaons

For positively charged pions and protons, an influence of the Coulomb interaction on the kinematic spectra is observed for different collision systems and energies measured with HADES [8][99]. If this effect can also be observed for K^+, it could explore the influence of an additional effective potential within the collision zone on the measured spectra. Section 6.8.2 elaborates on this possibility.

2. The HADES-Experiment

2.1. The Accelerator Facility at GSI

In south Hesse, near Darmstadt, Germany, the *GSI Helmholtzzentrum für Schwerionenphysik* is situated. Here the *Schwerionensynchrotron* (heavy ion synchrotron) SIS18 is accelerating heavy ions up to energies of a few GeV per nucleon since 1990 [101]. Its successor, the SIS100 accelerator is under construction at the moment. It will deliver the beam for the FAIR facility, which is also currently built. Figure 2.1 contains an overview of the whole accelerator facility.

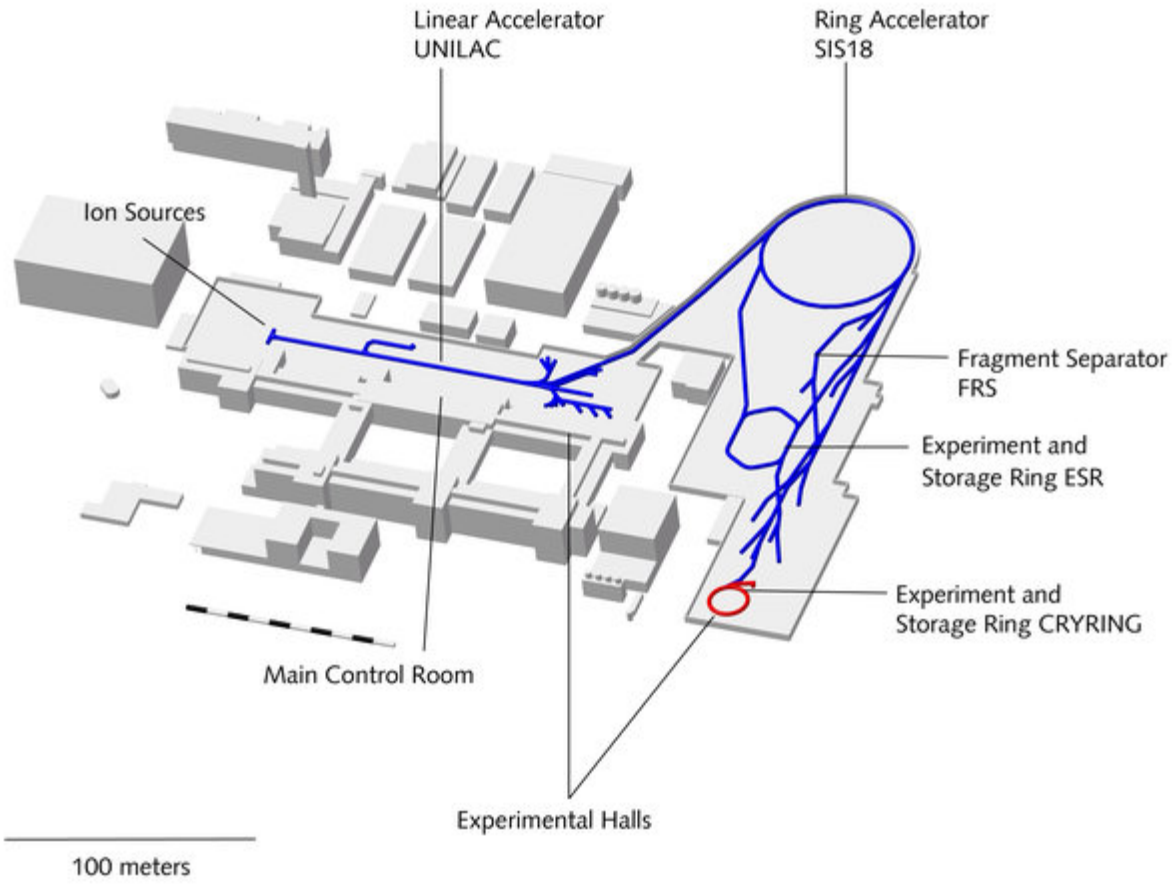

Figure 2.1.: Overview of the accelerator facilities at GSI [70].

The beam is produced in the ion source and undergoes a first linear acceleration in the UNILAC where low-energy experiments are situated. If necessary, the beam is then further delivered to and accelerated in the SIS18. From there, it is distributed to the experiments in the *Target Hall*.

The primary function of an ion source is to strip the shell electrons off the ion of interest. It can be a chemical compound or an individual element. At GSI, it is possible to accelerate a large variety of ions, as there are several ion sources present [121]. In general, ionisation is achieved with the help of a solenoidal magnetic field, in which an intense electron beam is circulating [29]. As this is not sufficient to completely ionise heavy ions, an additional stripping gas is used to ionise them in the UNILAC [121] after a first acceleration of the ions. The *UNiversal Linear ACcelerator* then accelerates the ions up to an energy of 11.4 A MeV [72].
After pre-acceleration in the UNILAC, the ions reach the SIS18, where they are further accelerated along a 2m long resonator and subsequently stored in the ring of 216 meters of circumference [73]. This way, accelerations of up to 90% of the speed of light, or 416000 circulations per second, are achieved. From the SIS18 storage ring the beam is then delivered to HADES and other experiments located in the target hall.

As part of the preparation for the commissioning of the new FAIR facility, the current physics agenda is performed under the scope of a *FAIR Phase-0* programme, using the SIS18 accelerator. The collision of ^{107}Ag-ions at 1.58 A GeV discussed in this thesis is part of this programme.

2.2. HADES

The *High-Acceptance Di-Electron Spectrometer* (HADES) is a fixed target experiment at GSI, specifically designed to investigate the properties of dense nuclear matter in an energy regime of a few A GeV. Compared to high-energy experiments, like at the LHC, the medium created in the most central collisions has a long lifetime. Besides the importance of investigations on properties of baryon-rich QCD matter, also astrophysical applications of these studies have become apparent over the last years (see [132] and section 1.4).
The general setup of HADES can be seen in figure 2.2 and consists of a system of tracking detectors in a polar angle area between 18° and 85° relative to the beam axis.

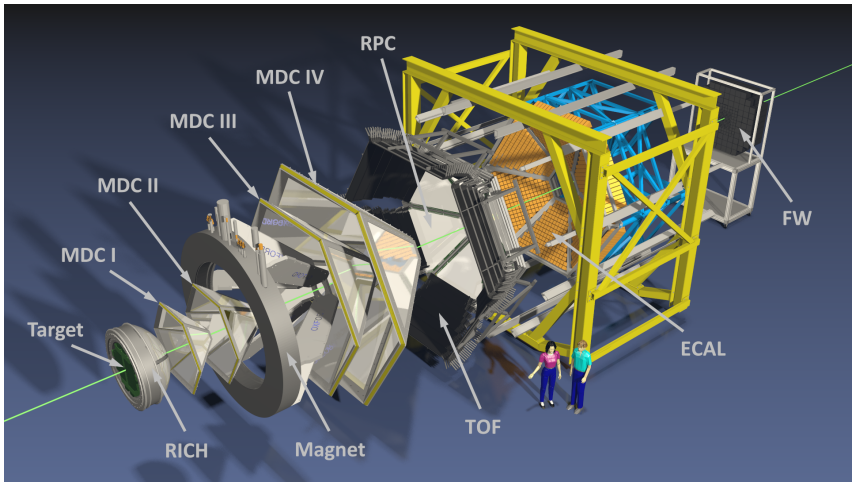

Figure 2.2.: Exploded 3D view on the HADES detector setup during the measurement series discussed in this thesis. The beam reaches the target, coming from the lower left side of the picture. A reaction is triggered, leading to the (produced) particles being tracked along their forward-boosted trajectories.

START and VETO are the trigger detectors along the beamline. The tracking detectors with an azimuthal angle coverage of nearly 360° are subdivided into six sectors of equal size. Restriction

to the forward direction is possible due to the nature of a fixed target experiment, where the (produced) particles experience a boost in the forward direction when transformed from the centre of mass to the laboratory system.

Charged particles traverse the inner detectors RICH and MDC I and II, after which their tracks are bent in the magnetic field of the toroidal magnet (see equation 3.4) proportionally to the corresponding Lorentz-force [89]:

$$\frac{d\vec{v}}{dt} = \frac{q}{m}(\vec{E} + \vec{v} \times \vec{B}) \tag{2.1}$$

Finally, the particles traverse the outer tracking detectors MDC III, IV and META, creating the stop signal for the time of flight measurement. Figure 2.3 depicts a cross-section of the HADES detector, which shows the actual dimensions of the compact setup.

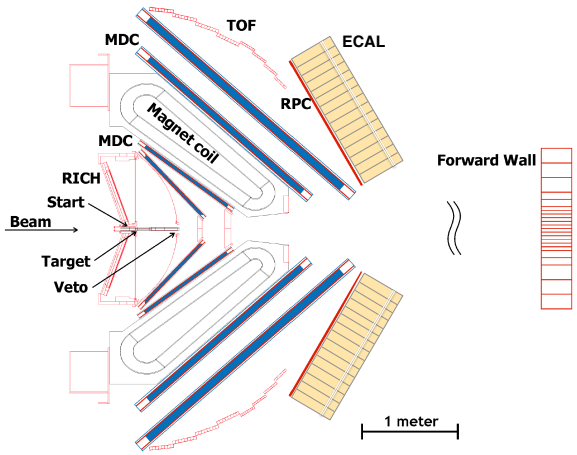

Figure 2.3.: Cross-section of the HADES experiment with the individual detector systems. A particle coming from the target zone is flying in forward direction, traversing the tracking detectors and, in its trajectory, bent by the magnet.

The following subchapters will discuss the individual subdetectors, emphasising those more relevant to the presented analysis.

2.2.1. START and VETO

The START and VETO systems are located before and behind the target respectively. START registers the start time signal of the incoming ion in-beam for the time of flight measurement. Hereby the trigger condition is such that no VETO hit is allowed for each START signal within a specific time range. This way, events with no reaction are not registered. Furthermore, events, where two ions passed the detector simultaneously and the correct time of the collision cannot be determined, are dismissed as well. Though the principle of a coincidence measurement is simple, a rate of up to 10^8 ions per spill [77] brings the challenge of high rates and material degradation due to radiation damage. The consequences of latter effect are discussed in section 3.5.2.
A Chemical Vapour Deposition (CVD) diamond strip counter was chosen for this task. More precisely, a single-crystal Chemical Vapour Deposition (scCVD) of 4.2×4.2 mm^2 surface area and 50 μm thickness was selected for START. A polycrystalline (pc) CVD of 9×9 mm^2 surface area and 100 μm thickness was chosen for the VETO detector [76]. They are both depicted in figure 2.4.
START is situated 72 cm in front of the target centre, and VETO 72 cm behind. While only one layer is used for VETO, the START detector consists of 2 layers with 16 stripes each. These gold stripes are used to resolve the beam position along the x- and y-directions.

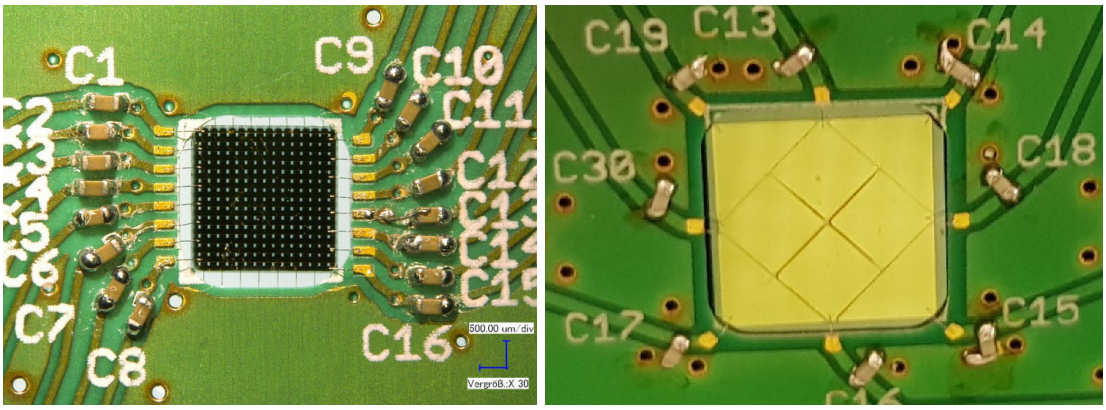

(a) START (b) VETO

Figure 2.4.: The scCVD diamond detector of START (left) and the pcCVD diamond detector of VETO (right) as taken from [125]. The size of VETO is slightly larger compared to START, as the beam widens over a distance of a few metres.

The choice of diamond detectors has several reasons. External atoms can not dope them because they have strong bonds inside the lattice structure. Furthermore, the energy to scatter an electron out of the lattice is 43 eV, which is much higher than e.g. silicon with 25 eV [89]. These facts make the material very radiation hard and crystals more useful than silicon as an in-beam detector. While scintillators are used instead of crystals for minimum ionising particle (MIP) beams, like protons and pions, crystals are preferred for heavy ions, as their electronic noise production is lower due to the large bandgap of 5.5 eV [77]. The high rates of the Ag-beam are also handled better by a crystal-based detection system due to the time resolution of $\sigma_{t_0} < 50$ ps [76]. In comparison: the scintillator-hodoscope used for the MIP beams reaches a time resolution of $\sigma_{t_0} \approx 300$ ps [77].

2.2.2. Target

For this beamtime, a segmented target of 15 natural silver foils was used, which consist of approximately 50 % ^{107}Ag and 50 % ^{109}Ag. A picture of the target in its carbon frame is shown in figure 2.5.

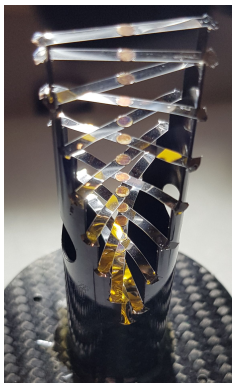

Figure 2.5.: The silver target with its 15 segments as used for the beamtime.

The segmentation was already used in previous beamtimes (see e.g. [119]) and aims at reducing the conversion of photons into lepton pairs inside the target region. In addition, the probability of other ions reacting in the same segment simultaneously, overlapping with the triggered event, is reduced.

2.2.3. RICH

The detector closest to the reaction zone is the *Ring Imaging Cherenkov* (RICH) detector. It uses the Cherenkov effect for the detection of relativistic $e^{\pm}$ with momenta of $0.1 \leq p \leq 1.5$ GeV/c [77]. For these electrons the propagation velocity v inside the C_4H_{10} isobutane gas of refraction index $n = 1.3518$ [93] is higher than the speed of light in the medium $\left(c' = \frac{c_0}{n}\right)$. Consequently, the passing $e^{\pm}$ polarizes the gas non-axisymmetric around its path. As a result, the actions of the polarized atoms do not cancel each other out and present a net polarization in the direction of motion of the charged particle. At the moment of relaxation of the polarized atoms, short electromagnetic pulses are produced, which can be detected as Cherenkov light [89]. This light is emitted in a cone in the direction of motion of the particle. The opening angle Θ of this cone is defined via [119]

$$\Theta = \arccos\left(\frac{c}{v \cdot n}\right) \tag{2.2}$$

These light cones are then reflected by a spherical mirror and detected as rings by Multi Anode Photomultipliers (MAPMTs) of the type Hamamatsu H12700C. Altogether 432 MAPMTs with a pixel-size of 5.8×5.8 mm^2 are arranged in 3×2 sub-arrays. As each MAPMT contains 64 channels, this results in a total of 27648 pixels. A depiction of the setup can be found in figure 2.6.

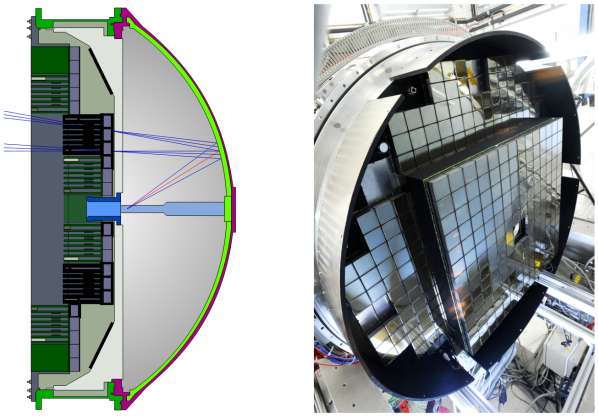

Figure 2.6.: Setup of the RICH detector as in [64], with the Cherenkov light paths indicated by the blue lines on the left side.

2.2.4. The Magnet Spectrometer

The magnet spectrometer consists of the *Mini-Drift Chambers* (MDCs) and the toroidal magnet between MDCs II and III (see figure 2.2 for reference). As a particle passes through the MDCs, which are filled with a Ar/CO_2 gas with a mixing ratio of 70/30, it ionises the gas, and the produced electrons and ions drift along the field lines. Those electrons are accelerated towards the anode wires, ionising more gas atoms on their way and leading to an avalanche of secondary ionisations. Furthermore, the total charge of the avalanche is proportional to the energy loss of the particle inside the drift cell, as the analogue signal is produced by the incoming electrons and the induced charge of the ions drifting away from the wire. The position of the intersection between the particle trajectory and the MDC plane is reconstructed by using the measured drift time and the drift velocity. In this way, the location of the intersection point between particle trajectory and MDC plane is determined as well as its energy deposit. Combining this information with the deflection of the particle trajectory due to the magnetic field, the momentum of the particle can be reconstructed (see section 3.1.4).

The Magnet

To ensure a sufficient momentum reconstruction resolution, the magnet is designed to produce a strong but locally confined field. Six coils are surrounding the beam axis, producing a toroidal field with a strength of up to 3.6 T, which is visualized in figure 2.7. Here the z-component represents the magnetic field strength in Tesla, obtained by systematically probing the field strength with Hall probes, while the x-axis represents the beam-axis and the y-axis the distance r to it.

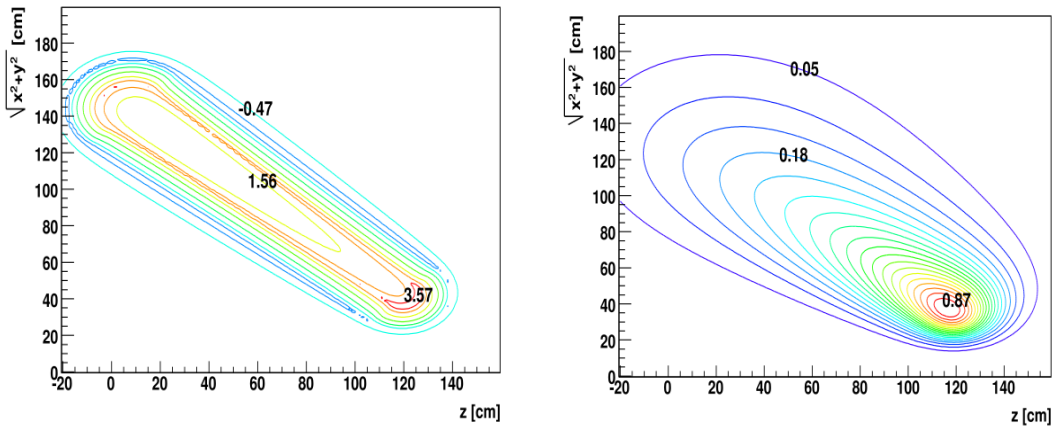

(a) Magnetic field map at $\phi = 30°$

(b) Magnetic field map at $\phi = 0°$

Figure 2.7.: Magnetic field maps for the case of the coil position at $\phi = 30°$ (a) and the space in between two coils at $\phi = 0°$ (b), as taken from [77]. Between two contour lines a step size of 0.24 T (a) and 0.046 T (b) was chosen.

This field distribution induces a transverse momentum kick p_k between 0.04 and 0.13 GeV/c [77] to charged particles crossing the magnetic field. In return, the path length through the field determines as $L \simeq 0.4$ m. A CAD sketch of the superconducting magnet, with a diameter of 3.56 m [77], can be seen in figure 2.8.

Figure 2.8.: The HADES superconducting magnet and its support ring, with a diameter of 3.56 m, seen in profile (left) and from the back (right) as taken from [77]. The previously mentioned structure of the six sections along the polar angle is prominently visible.

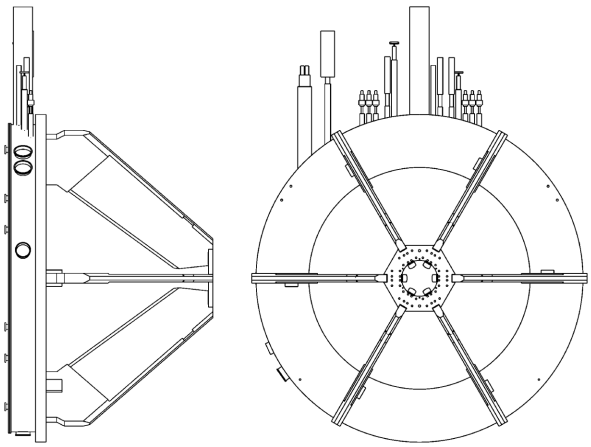

Each of the six coils has a throughput of 3464 A and consists of 140 turns [77]. Due to the resulting magnetic forces of 4.9×10^4 N per coil, a hexagonal plate connects the back end of the six coils, supporting the structure at the outer end around the beamline. An exemplary field map for a coil is seen in figure 2.7(a). Besides the structural support, the ring structure

on the large end of the coils also encapsulates nitrogen and helium cooling lines and electrical connections.

The Mini Drift Chambers

Overall the MDCs are a series of four consecutive planes of drift chambers of different sizes. Each plane consists of six sectors along the azimuthal direction ϕ. So overall, there are 24 trapezoidal chambers of 3-6 cm thickness [119]. Figure 2.9 shows the general arrangement of the MDC detectors inside the HADES setup.

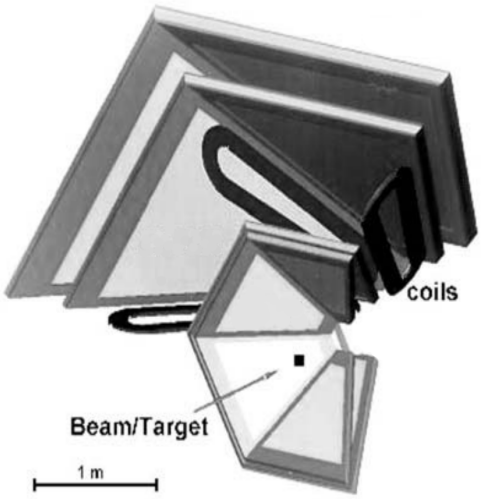

Figure 2.9.: The Mini Drift Chambers arranged before and behind the magnet, as taken from [77]. As for the magnet, the four layers and six sectors form the prominent feature.

Each chamber is filled with a mixture of 70% Ar and 30% CO_2, where the Argon serves as a counting gas. The addition of CO_2 as a quenching gas is made as it absorbs radiation from the recombination of electron-hole pairs. This prevents secondary ionisation processes, which could trigger secondary false signals.
The spatial arrangement of the drift chambers allows the azimuthal tracking coverage between 18° and 85° previously mentioned. To achieve a spatial resolution of less than 150 μm and reduce ambiguities in the track reconstruction for high multiplicity heavy-ion collisions, each chamber consists of six sense/field wire layers with different relative orientations. Those are depicted in figure 2.10 and chosen as ±0°, ±20° and ±40°.

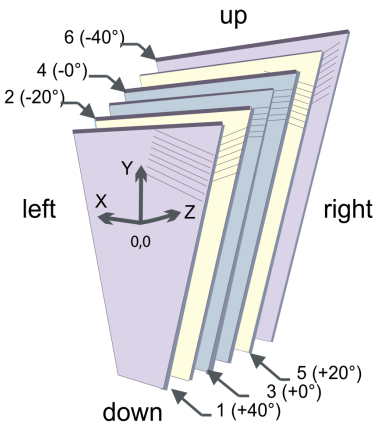

Figure 2.10.: Orientation of the wires between the six different stereo angle layers of an MDC, as taken from [77]. The varying orientation increases the resolution and decreases tracking ambiguities.

Those orientations are chosen to maximise spatial resolution in the direction of the momentum kick. In subdivision, each drift chamber contains about 1100 drift cells with active areas varying between 5×5 mm^2 in the first plane and increasing up to 14×10 mm^2 in the fourth and last plane, translating to active areas from 0.35 m^2 to 3.2 m^2 per chamber. Each drift chamber contains 6 planes of sense wires and 7 layers of field wires, which results in a total of 13 layers. The field wires separate the adjacent drift cells in each layer, while cathode wires of $80 - 100$ μm diameter separate the wire layers, orientated perpendicular to the sense and field wires. The position and orientation of sense and field wires, as well as the cathodes, can be seen in figure 2.11. While in operation, a negative potential of $U \approx 2000$ V is applied to the cathodes. Consequently, the electrons from the ionised gas drift towards the sense wire and, near the sense wire ($d \approx 50$ μm), produce an avalanche of secondary ionisations. As soon as these electrons reach the sense wire and their signal surpasses a certain threshold, the start time (leading edge) is taken. The stop time (trailing edge) is registered when the signal intensity falls below the threshold again.

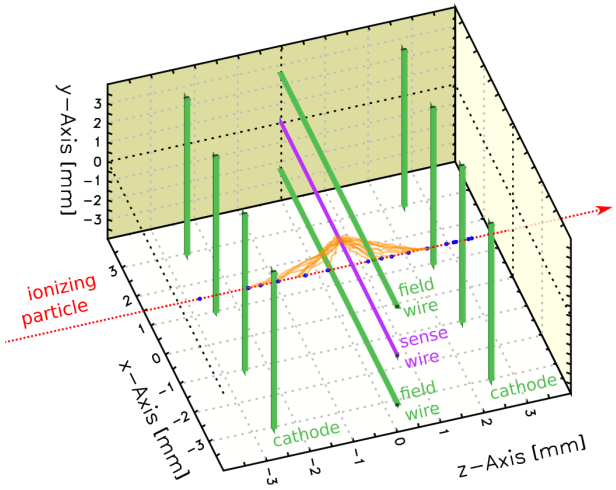

Figure 2.11.: Wire and field line arrangement inside the drift chambers, as taken from [137]. On its path (red) the charged particle ionises the gas so that the electrons (orange) start drifting towards the sense wire along the electric field lines (pink).

A drift chamber measures the closest distance of a track passing a drift cell to the sense/anode wire. This is done via the drift time of the produced electrons and ions along the electrical field lines in relation to the external start time signal [89]

$$x = \int_{t_{\text{start}}}^{t_{\text{end}}} v_D(t)dt \tag{2.3}$$

where t_{start} denotes the time of the ionisation process which statistically resulted in the shortest drift time and t_{end} is the time of the ion/electron detection. In return v_D stands for the drift velocity of the electrons produced by the ionisation processes. Hence, the time resolution of a drift chamber predominantly determines its position resolution.

To read out the signals from the approximately 27000 wires, analogue read-out boards for signal amplification, shaping and discrimination are mounted onto the frames. Those are connected to digitisation boards where the analogue signal converts into a *Time over Threshold* (ToT) measurement, as it can be seen in figure 2.12. It describes the first-order approximation that the time interval in which a pulse stays over the predefined threshold is proportional to the pulse height of a shaped pulse. Hereby the leading edge t_1 is registered when the signal surpasses the threshold and therefore is used as t_{end} for the position determination according to equation 2.3. The trailing edge t_2 is then defined as the point in time when the signal pulse falls below the

threshold again. Consequently, the ToT is defined as ToT $= t_2 - t_1$. With this correlation, the current information converts directly into time information.

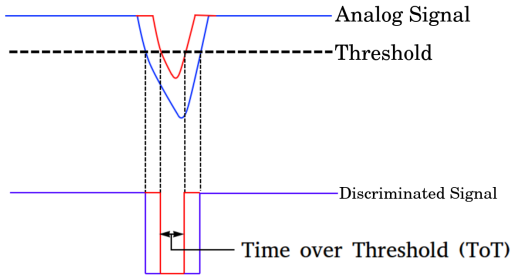

Figure 2.12.: The conversion process of an analogue electrical signal into a digital time over threshold information. Two times are measured - leading edge t_1 and trailing edge t_2. Together they encode the position and energy loss information.

While position determination is one of the tasks of the MDCs, another one is the measurement of the energy loss of a particle inside the chambers. As described in the Bethe-Bloch equation, the energy loss of a charged particle in a medium of known composition is mainly determined by its velocity and charge [89]

$$-\langle\frac{dE}{dx}\rangle = K\frac{Z}{A}\rho\frac{z^2}{\beta^2}\left[\frac{1}{2}\ln\left(\frac{2m_e c^2\beta^2\gamma^2 T_{\max}}{I^2}\right) - \beta^2 - \frac{\delta(\beta\gamma)}{2} - \frac{C(\beta\gamma, I)}{Z}\right] \tag{2.4}$$

A deeper discussion of all terms and variables is beyond the scope of this work but can be found in [89], [141], [45] and others. Nevertheless, the direct proportionality of the energy loss to the particle velocity (β) and charge (z) becomes apparent.

For small energies, the $1/\beta^2$ term dominates, while for large energies, the γ term dominates. In the intermediate region of $\beta\gamma = \frac{p}{mc} \approx 3 - 3.5$ or $\beta \approx 0.95$ [89] there is a minimum for the energy loss. Particles in this energy range are called *minimum ionising particles* or short MIPs. Figure 2.13 shows an example of a Bethe-Bloch curve for a positively charged muon in copper. The minimum ionising region is highlighted. One can see the $1/\beta^2$ dependency for low energies, which is motivated by the longer times between interactions $\Delta t \simeq \frac{d}{\gamma v}$ [89]. This time between interactions itself is proportional to the specific energy loss $\Delta E = \frac{(\Delta p)^2}{2m} \propto \frac{1}{v^2}$ [89], leading to the exponential drop in dE/dx towards the few GeV area.

The maximum energy deposition grows asymptotically with γ as a purely kinematic effect for energies higher than a few GeV. With relativistic effects becoming non-negligible, the transverse component of the electric field grows with γ, which increases the maximum impact parameter. This contributes directly to the maximum energy deposit $T_{\max}$ in equation 2.4.

The practical energy loss measurement in the HADES MDCs is performed with the previously introduced ToT as a measure for the energy loss of the charged particle. Protons have been used in [77] to measure the time over threshold for several incident angles and momenta in dependence on the distance from the sense wire. Knowing the particle type and momentum, as well as the drift gas and the track topology inside the cell, the ToT measurements can then be correlated with the energy loss via the Bethe-Bloch formula. Calculating the specific energy loss for each case and plotting the ToT against it, the distributions for the different incident angles can be described by the function [77]

$$\text{ToT} = f(dE/dx) = c_0 + c_1[\log_{10}(dE/dx + c_3)]^{c_2} \tag{2.5}$$

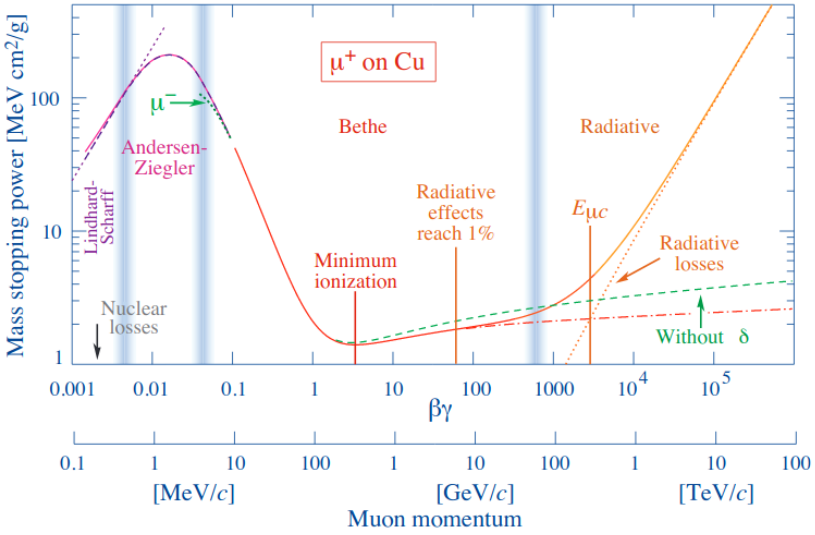

Figure 2.13.: Bethe-Bloch curve for the energy loss of a μ^+ in copper, plotted over $\beta\gamma$, as taken from [141].

with the fit-parameters c_0, c_1, c_2 and c_3. The resulting energy- or momentum-dependent energy loss curves are used for particle identification and background suppression in the scope of this work. An exemplary energy loss distribution for the HADES MDCs can be seen in figure 2.14.

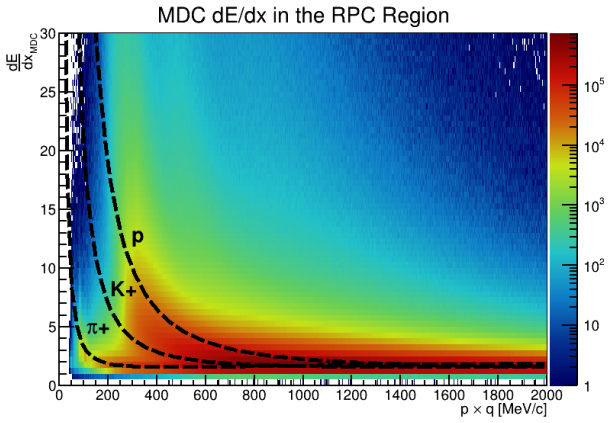

Figure 2.14.: Exemplary energy loss over momentum distribution for the HADES Mini Drift Chambers for a mass selection range of $200 < M < 800$ MeV/c^2. The dashed lines represent the corresponding theoretical Bethe-Bloch-Curves for the individual particles.

The lines drawn correspond to the theoretical Bethe-Bloch energy-loss curves for the corresponding particles in the $ArCO_2$ gas mixture. To calculate these curves, the energy loss in each of the constituent gases is taken into account according to the Bragg rule of additivity [48]. It states, that the energy loss of a particle passing a gas mixture is equal to the sum of the energy losses of the particle in each constituent gas, weighted with their mass proportions. Argon gas has a density of 1.662 kg/m^3 at a temperature of 20°C and 1 atmospheric pressure (1 atm) with a molar mass of ≈ 0.040 kg/mol [141]. This results in a molar density of ≈ 41.55 mol/m^3. For CO_2 the macroscopic density amounts to 1.842 kg/m^3 at a molar mass of ≈ 0.044 kg/mol. As the resulting ≈ 41.864 mol/m^3 are nearly identical with the molar density of Argon, one can assume volumetric proportions of the constituents following the molar proportions. The resulting proportions of the three elements in the gas mixture can be given as $\approx 69.475\%$ Argon, $\approx 22.192\%$ Oxygen and $\approx 8.333\%$ Carbon. The latter two fractions are calculated via the mass fractions of ≈ 0.727 for Oxygen and ≈ 0.273 for Carbon [141]. Utilising the mean excitation energies of 188 eV for Argon, 95 eV for Oxygen and 78 eV for Carbon [141], the specific energy

loss curve for each particle can be calculated as shown in figure 2.14.

The procedure on how to use the MDC energy loss information to perform particle identification and background suppression is further explained in chapter 4.1.3. Nevertheless, the minimum ionising attributes of the charged Kaons, Pions and Protons lead to a large area of overlap in the energy loss distributions due to the resolution capabilities. This reduces the separation power of energy loss as a particle selection criterion.

2.2.5. META

The *Resistive Plate Chambers* (RPC) and the TOF scintillation detectors are located behind MDC plane IV. As a combined detection system they are referred to as the **M**ultiplicity and **E**lectron **T**rigger **A**rray (META). Here the stop signal for the time-of-flight-measurement is generated when a particle is registered. Furthermore, the amount of detector hits registered is used for estimating the collision centrality of an event (see Section 3.5.4). The number of registered particles is also used for the trigger decision mechanism (see Section 2.2.8).
As it can be seen in figure 2.3, each of the sub-detectors covers a distinct angular range relative to the beam axis. RPC, as the inner-most META detector, ranges from 18° to 44°, while the TOF ranges from 44° to 88°. Both detectors are covered in the following sections.

RPC

The RPC detector is situated in the low polar angle region, consisting of 187 timing cells. In each layer, there are 31 rows and three columns. The widths range between 2.2 and 5 cm, while the lengths range between 12 and 52 cm. The size depends on the position along the polar direction. An exemplary sector paddle can be seen in Figure 2.15.

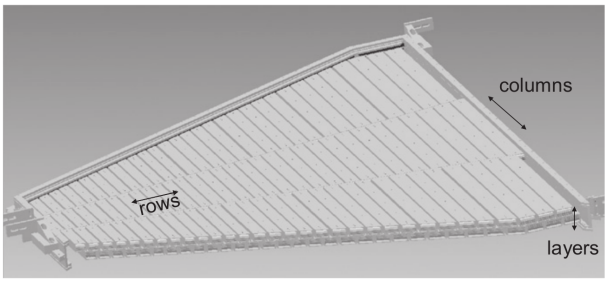

Figure 2.15.: An individual RPC sector, figure taken from [39]. Each sector consists of two overlapping layers of cells with a polar angle-dependent size.

The interior of one cell is a stack of alternating planes made from resistive glass and Aluminum. Between two glass insulation planes of 2 mm thickness, an Aluminum electrode of 2 mm thickness and a gas volume of 270 μm diameter are situated. This gas volume is filled with a mixture of 90 % Freon ($C_2H_2F_4$) and 10 % Sulfur Hexafluoride (SF_6) [90]. When a particle passes those layers, it ionises the gas in these small volumes. As a result, free charge influences a current in the Aluminum electrodes, which is read out as an electronic signal. An electric potential of around 6000 V is applied to each cell to increase the signal strength. Figure 2.16 shows the overall composition of such a cell with the different individual readout layers.

The RPC spatial resolution of one cell along the x-direction reaches its minimum at around 6 mm [55]. In an analysis of data presented in [43], the position resolution in full operation was found to be around 7-8 mm. In the case of the y-direction, the geometry of the cell determines the resolution. As the cell size depends on the position of the cell along y, position resolution here varies between 22 to 42 mm [90]. Due to the two detection layers, efficiencies of $\gtrsim 95\%$ are

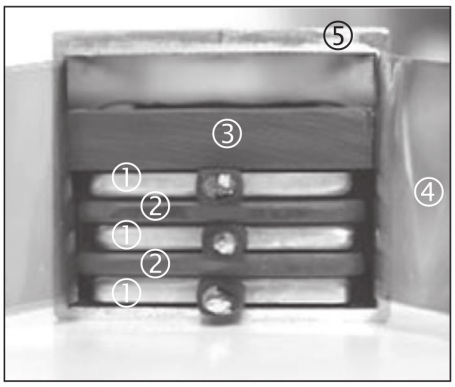

Figure 2.16.: Interior of an individual RPC cell, taken from [39]. The layers of Aluminum electrodes (1) and glass insulation (2) as well as a plastic pressure plate (3) and a kapton insulation (4) are highlighted. The whole cell is shielded by a 2 mm thick Aluminum tube (5).

achieved for MIPs. The time resolution σ_t of one cell has been determined to be 77 ps for one individual hit [42].

TOF

At polar angle values of $> 44°$, the TOF scintillation detector is located. Besides the subdivision into six sectors, each TOF sector is divided into eight modules. Each of these modules consists of a set of eight scintillator rods. Overall a total of 384 rods are built-in, each contained in a fibre case. The scintillation material is of the type BC408 [77].

Position and energy loss determination for a particle traversing a TOF rod is performed via a coincidence measurement between two Photomultiplier Tubes (PMTs) attached to the left and right of each scintillation rod. When a particle in the GeV energy regime crosses the material, the main contribution to the scintillation process is the excitation and spontaneous de-excitation of scintillator molecules. Due to this process, light is emitted inside the individual rod. As the scintillation material has a higher optical density than the surrounding air, the light is mainly reflected from the surface until it reaches the ends on both sides of the rod. There it is detected as a light pulse by the attached PMTs. The resulting time-integrated intensity is directly proportional to the deposed energy by the charged particle passing through the detector.

For optimal performance, the PMTs are connected to the rod via a material with a similar optical density to the scintillation material itself. These PMTs consist of a photocathode, several multiplier anodes and a signal anode. An outgoing signal shape can be parameterised by a rise time (time until the maximum is reached) and a decay time (time until the light pulse is below the detection threshold). For the time resolution, mainly the rise time plays a role, as it determines the time until the signal surpasses the threshold. The de-excitation time, in which new signals might be distorted, is typically a few ns and creates an afterglow. For the case of the TOF detector, this time is 2.1 ns [77].

To retrieve the spatial information along the rod, the time difference between the arrival of the light pulses at the left and the right end is read out. Thus the correlation between the spatial and the time information can be expressed by the displacement-time-law [77]

$$x = \frac{1}{2}\left(t_{right} - t_{left}\right) V_g$$

with V_g denoting the group velocity of the light pulse inside the detector material. Ultimately this leads to an x-position resolution σ_x of around 25 mm. In analogy to RPC, the resolution in y is determined by the rod diameter, which is around 20 mm for the 192 innermost ones and

30 mm for the same amount of outermost rods [18].

As previously mentioned, besides the coincidence with START for the time-of-flight measurement and the position determination, an energy loss measurement can be performed with the TOF detector. The deposed energy ΔE is directly proportional to the amplitudes a via [77]

$$\Delta E = k\sqrt{a_{right}a_{left}e^{L/\lambda_{at}}}$$

where k is a constant, λ_{at} is the attenuation time of the material and L is the rod length.
The detector system has thresholds for each rod applied. An incoming signal needs a finite time to reach this threshold and trigger the detection mechanism. Consequently, calculating the time-of-flight from the measured raw times results in a systematic offset. To avoid that, a so-called time-walk correction is applied to this detector, but also the RPC. For TOF, this correction is directly proportional to $\frac{1}{\sqrt{dE/dx}}$, as the time until a signal passes the threshold is mainly proportional to the amplitude. As can be seen in Section 4.1.7, this correction can also lead to systematic time-of-flight offsets.

2.2.6. ECal

The *Electromagnetic Calorimeter*, short ECal, is situated directly behind the META detector and ranges in the same polar angle range as the RPC detector. Figure 2.3 shows the localization in the detector cross-section. the main objective of this detector is the detection and identification of e^+, e^-, π^+ and π^-.
Beyond the subdivision into the six sectors, each sector consists of 163 modules of shielded lead glass connected with a PMT. One CEREN25 lead glass block has the dimensions of 92 × 92 × 420 mm. When a particle traverses the material, a shower of photons and hadrons is produced. The photons are directly registered by the PMTs, while the hadrons produce Cherenkov light and are observed indirectly. The resulting signal has a strength proportional to the particle's energy that crossed the detector.
During the Ag+Ag beamtime, only four out of six sectors were available. Consequently, ECal could not be included in this work's particle identification processes. More detailed information on the ECal detector can be found in [65].

2.2.7. Forward Wall

As it can be seen in figure 2.3, about 7 m behind the target, the *Forward Wall*, or short FW, is located. In contrast to most other subdetectors of the HADES experiment, the FW is not subdivided into sectors and is oriented perpendicular to the beam axis. The resulting polar coverage is in the range between 0.33° and 7.17° [125]. Each of the 288 quadratic BC408 scintillator modules, which make up the detector, is connected to a PMT. The detection principle this way directly compares to the previously discussed TOF detector (see section 2.2.5).

The system's primary purpose is the measurement of spectators from the collision zone. It allows for an independent determination of the centrality of a collision (see section 3.5.4) as well as a reconstruction of the event plane. Due to the nature of the fixed target experiment, the arriving particle density decreases with increasing polar angle. As a result, there are three different sizes of scintillators used. Around the centre, the FW has a hole of 8×8 cm^2, where the ion beam otherwise would cause substantial degradation and make the detection surface unusable in a short amount of time. Around that, five rings of overall 140 4×4 cm^2 scintillation modules follow. Those are followed by an overall of 64 modules of 8×8 cm^2 surface area, arranged in

two rings. Framing this setup, another three rings of 16×16 cm^2 modules form the outer edge of the detector, resulting in 84 modules in total.

2.2.8. Data Acquisition

In the *Data AcQuisition* system, short DAQ, all signals from the previously discussed detectors are collected and processed. A rudimentary interpretation of the data is performed, the trigger decision being an example.
First, the signals arrive at the *Front End Electronics* (FEE) of each detector. Next, the analogue signal is converted into a digital signal via the ToT method, and a global reference time is defined. Finally, this raw information is forwarded to a central hub and subsequently interpreted by the *Central Trigger System* (CTS). The CTS categorizes the measured events based on specific information, also called a first-level trigger decision. In the case of the Ag+Ag beamtime, this was the integrated number of META hits per event, which is correlated to the event centrality (see section 3.5.4). In this context, two trigger criteria were defined, which are called Physics Trigger or PT. For an event to be classified as PT3, at least an integrated number of 20 META hits have to be present. This trigger decision, in return, leads to a dismissal of mostly peripheral collision events. To not dismiss these peripheral collisions entirely, a PT2 decision is defined as a minimum amount of 5 META hits per event. Only every 32nd PT2 event without PT3 was written to a file for this beamtime. This was done as most events are PT2. Writing each PT2 event to files would increase the dead time of the detector and reduce the detection probability of a PT3 event. PT2 events are not included in any of the analysis results presented in the following chapters.

Finally, if an event fulfils the trigger criteria, the CTS creates a reference time signal for this event. This is used to correlate measurements from different subsystems in time, collect the data, and forward it to the computer farm. The incoming data stream is parallelised over eight *Event Builders* (EB), which write the events into separate *HADES List mode Data* (HLD) files and store them on local machines. The next trigger decision can only be taken after the FEEs sent the CTS the notification that the writing process is finished. More detailed information on the DAQ system can be found in [97].

2.3. Ag+Ag Beamtime Summary

In March 2019, HADES recorded a total of about 15×10^9 Ag+Ag collision events over the course of a month [94]. The measurement campaign was split into three parts as, besides the physics aspect, commissioning and calibration purposes were pursued. In table 2.1, the key data [102] for this beamtime is summarised.

Beam intensities of 1.3 - 3.5 MHz were reached during the beamtime. The primary purpose of the calibration run is the systematic investigation of detector performance and calibration. The production runs are physics motivated and describe the time the data was taken. Production run two was performed to compare the results with the previous HADES Au+Au beamtime (see e.g. [119]), which had the same beam energy but a different collision system size. The focus of this work lies on the production run 1. The beam energy in this run is directly at the threshold at which K^+ can be produced in free NN collisions, as described in section 1.2.1.

	Production Run 1	**Production Run 2**	**Calibration**
Beam Energy	1.58 A GeV	1.23 A GeV	1.23 A GeV
Magnet Current	3200 A	2500 A	200 A
Number of Events	13.68×10^9	1.32×10^9	0.26×10^9
Total File Size	334.52 TB	29.31 TB	5.75 TB
Duration	441.7 h	39.1 h	6.76 h
Mean Event Rate	8.6 kHz	9.4 kHz	10.5 kHz

Table 2.1.: Summary of the March 2019 beamtime. Besides the main data-taking period, another low-energy production run as well as a calibration run were performed.

3. Event Reconstruction

The HADES software framework HYDRA (**H**ADES s**Y**stem for **D**ata **R**eduction and **A**nalysis) builds upon the open-source software ROOT [112], developed at CERN in Geneva.
In general, the track and event reconstruction procedure is performed by global classes using the data provided by the readout classes of each subdetector. After reading out the detectors' raw data from the HLD files, calibration and reconstruction algorithms are applied, which are discussed in the following sections. All successfully reconstructed Ag+Ag event candidates, are stored in DST (**D**ata **S**ummary **T**ape) files. Those files' contents are mainly high-level physics observables necessary to perform analyses on the particle track level. This results in a reduced computational load when running analysis tasks.
For the algorithms to interpret the raw data provided by the subdetectors, the spatial orientation and location of each subdetector have to be known. To this purpose, the *photometric alignment* is used. More details on this procedure can be found in [117].

3.1. Track Reconstruction

Track reconstruction in HADES is typically split into track finding, combining the hits which belong together, and track filtering, to judge by the means of track quality criteria (χ^2-values) if a reconstructed track is a real track. In the first iteration, the clusters from the two inner MDC planes are used to estimate the reaction vertex (see section 3.2). Afterwards, the raw hit information of the MDC planes I and II as well as III and IV are used to create a straight line inner and an outer track segment each. Then, assuming a homogenous magnetic field projected onto a 2-dimensional kick-plane (see, e.g. figure 3.3), inner and outer track segments are assigned to each other. Combined, these track candidates are extrapolated towards the META-detector, where it is matched with a corresponding hit. Finally, there is a multi-layered approach of model fits to calculate the trajectory's momentum due to the bending in the magnetic field. In the following section, these steps are discussed in detail.

3.1.1. Initial track candidate search

Fired MDC drift cells are used to identify a track candidate. For this purpose, the wire layers of the inner MDCs are projected to one common projection plane. As the inner MDCs are not coplanar, the orientation of the projection plane is chosen such that the projections of the drift cells are of similar size. It is performed analogously for the outer MDCs - but as those are coplanar, the projection plane is simply defined as a plane centred between the two chambers. This procedure is depicted in figure 3.3. It is necessary to separately reconstruct *track-segments* for the projection plane of MDCs I and II, as well as for the projection plane of MDCs III and IV, as the toroidal magnet in between deflects particles according to the Lorentz-force with a deflection radius of [129]

$$R = \frac{mv}{qB}$$

Here R is the radius of the circle which a particle of the mass m and the velocity v as well as a charge q would describe inside a homogeneous magnetic field of the strength B. Knowing the magnetic field is constant, their $\frac{p}{q}$-ratio becomes the determining factor for the deflection. These

inner (MDCs I and II) and outer (MDCs III and IV) track segments will be later combined into a full *track candidate*.

Each projection plane spans an MDC x-y-position-plane. Once a cell is hit, its spatial distribution is projected onto that plane. Projecting the activated layers for each cell results in a distribution with a maximum if one cell per layer was activated. Figure 3.1 shows an example of such a projection for the inner MDCs. This maximum represents the intersection point of a straight track segment with the inner MDCs. The point of reference for the projection of the inner track segment onto the inner drift chambers is the reconstructed rection vertex along the beam-axis (see Cluster Vertex Finder in chapter 3.2). At the same time, the other dimensions are assumed to be centred around the target axis. The straight line is an approximation, as the

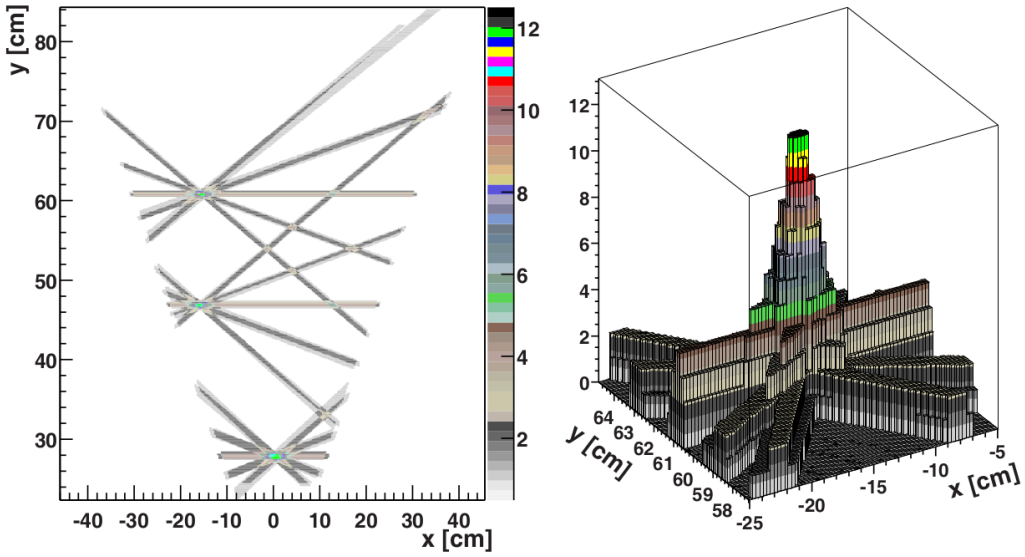

Figure 3.1.: Example of a projection-plane for a track candidate which created a signal in all 12 inner MDC layers [77]. The left plot shows the representation in the (x, y) coordinate system of the projection plane, while on the right, one can see the projection of the number of activated wires along the z-axis. The mean and width of the peak indicate the x-y-position of the intersection point between the inner track segment and the inner MDCs.

MDC layers closest to the magnet are not entirely field-free. Deviations from this straight track segment will be considered in the later stages of the tracking. To reconstruct the entire track and its momentum, the *kick-plane-method*, which is described in section 3.1.4, is used to represent the deflection of charged particles in a magnetic field. The intersection point of an inner MDC track segment with this kick-plane is used as the point of reference for the outer MDC track segment. Starting from this intersection point, the outer MDC track segment crosses the outer MDC projection plane in the (x, y)-position, again defined by the maximum of active wires (as seen in figure 3.1).
The time precision of drift chambers to measure the arrival of the electrons initiated by a charged particle depends on the gas mixture and the distance between the individual cathode and anode wires. For optimal spatial resolution, the angles of the wire planes have been adjusted to the direction of particle deflection. This means that the stereo angles are chosen such that the spatial precision of measuring the track interaction point with a chamber along the polar deflection is optimized. Nevertheless, they are also chosen so that ambiguities due to multiple hits per event

can be resolved.

3.1.2. MDC Drift Times

The reconstructed hits along the MDC planes can now be fitted with a corresponding model. Further improvement can be achieved as this fit is combined with the knowledge of the drift time information as well as the removal of left-right- and occupancy-related multi-hit-ambiguities. Drift time measurements for each cell geometry are interpreted in the context of GARFIELD simulations to achieve the latter. Combining these two efforts, a spatial resolution of 0.1-0.2 mm is reached [77].

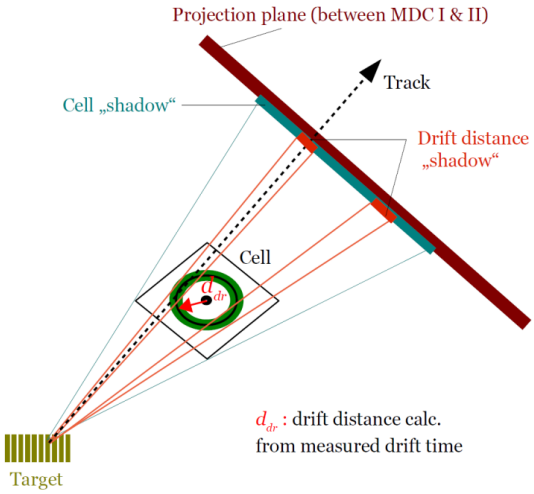

Figure 3.2.: Schematic showing the improvement of the position resolution due to the drift time interpretation as presented in [116]. The schematic is not drawn to scale.

Again a straight line fit is simultaneously performed on the hits of the track segment in both chambers. As the bending can be identified as a second-order effect [77], the approximation is justified in this stage.
A least-square minimization has to be performed on every activated drift cell along the track segment to reach the wanted resolution. The underlying function is given via

$$F = \sum_i \frac{(t^i_{\text{drift}} + t^i_{\text{shift}} + t^i_{\text{DT}})^2}{(\Delta t^i_{\text{DT}})^2} w_i \tag{3.1}$$

with the index i representing the activated drift cells along the fitted trajectory. The individual parameters of this function are determined by

- the simulated drift-time obtained from GARFIELD (t_{drift})
- the average deviation of all measured drift times of a track segment from the known correlation in $x - t$ space (t^i_{shift})
- the measured drift-time (t^i_{DT})
- the error of the drift-time measurement obtained from the GARFIELD simulations (Δt^i_{DT})

- and the weight factor w_i, representing a Tukey weight [114], to minimize the impact of outliers (evaluation from the difference between calculated and measured drift-time)

The last point is crucial, as the shift factor only takes global deviations into account. Individual time offsets or operational behaviours are not considered, which explains the necessity of individual weighting in case of insufficiently precise measurement.

3.1.3. Matching of Track Candidate and META-Hit

After successfully reconstructing the outer track segment, the corresponding META signal has to be assigned to reconstruct the time of flight for the particle. For that, the outer track segment is extrapolated as a straight line to the META detectors. As the outer track segment is already approximated by a straight line, so that, paired with the error from the META and MDC position measurement, it is not expected that this extrapolation points precisely to the real META hit point. Instead, a factor for the matching quality between the track segment and hit quantifies the association quality between registered hits and the extrapolated track. This parameter is called META matching quality and is given by a χ^2 measure, subsequently referred to as

$$\chi^2_{MM} = \sqrt{\left(\frac{dx}{\sigma_x}\right)^2 + \left(\frac{dy}{\sigma_y}\right)^2} \tag{3.2}$$

where dx and dy denote the deviation of the intersection of the extrapolated outer segment with the META plane from the measured META hit. In the meantime, σ_x and σ_y stand for the implied uncertainties of the position measurement. See chapter 2.2.5 for more information on the resolution of the META detectors. The result of equation 3.2 can be read as the distance between the intersection point of the track and the reconstructed META hit in units of standard deviations of the hit position.
This procedure is performed for all outer track segments and META hits alike. Pairs of track segments and hits are assigned so that both must lie within a range of 5 standard deviations for the resolution of the individual META hit. So it is also possible that hits and track segments are assigned to more than one individual match. The analysis takes this into account through a track sorting algorithm, which orders the tracks by predefined track quality criteria.

3.1.4. Momentum reconstruction

The physical foundation of momentum reconstruction is the fact, that charged particles undergo deflection if passing through a magnetic field. Assuming a magnetic field of strength $\overrightarrow{B}$ and a charged (q) particle of velocity $\overrightarrow{v}$, the Lorentz force acting on the particle is determined via $F = q(\overrightarrow{v} \times \overrightarrow{B})$. Consequently, the obtained reconstructed momenta are, in fact, momentum over charge ratios. This also translates into the masses calculated from the reconstructed momenta, which in return represent a mass over charge ratio.
As previously mentioned, there are three approaches to reconstructing a track and determining its momentum. The fastest method is the kick plane method. This gives a robust first estimate of the momentum.
Approximating the track with the so-called *spline* method delivers the second method of track reconstruction. In this iteration, reconstructed combinations of inner and outer track segments are fitted, and the momentum and the polarity are obtained to be used for later refinement.
The final step is then performed by the *Runge-Kutta* algorithm. Like the spline method, it is the standard for track reconstruction and, in comparison, achieves the highest precision.
Each algorithm is considered a step in refining the tracking by taking the output value of the previous iteration as a starting value.

Kick plane method

In the first iteration, the straight line approach is applied as mentioned in chapter 3.1.1. Here the deflection of a charged particle due to the toroidal magnet is substituted by an instantaneous change in direction (called *kick*) in the magnets' plane. For the classical case, one can describe this kick as [119]

$$\vec{p}_k = \vec{p}_{out} - \vec{p}_{in} = \int d\vec{p} = \int \vec{F} dt = \int q(\vec{v} \times \vec{B}) dt = -q \int \vec{B} \times d\vec{s} \tag{3.3}$$

In [115] it is shown that the original magnetic field can be replaced by another space-wise compressed field, which is stronger in magnitude and thusly creates the same deflection of a charged particle. Reducing this in the limit to a 2-dimensional plane, creates the introduced kick-plane, as it can be seen in figure 3.3. For HADES this is done with GEANT simulations (see chapter 3.7). To quantify this one can write the kick as the overall change in the momentum vector of the particle

$$|\vec{p_k}| = |\vec{p}_{out} - \vec{p}_{in}| = 2p \sin \frac{\Delta\theta_k}{2} \tag{3.4}$$

Here $\vec{p}_{in}$ and $\vec{p}_{out}$ represent the in- and outgoing momentum 3-vectors of the charged particle while $\Delta\theta_k$ is the deflection angle due to the kick-plane. To calculate this total deflection, one has to integrate the Lorentz force acting on the particle while it crosses the toroidal magnet

$$\Delta\theta_k = \frac{p}{q} \int_{l_{in}}^{l_{out}} B \sin\alpha dl = K(l_{out} - l_{in}) \tag{3.5}$$

with α the angle between the particle trajectory and the magnetic field and K a constant depending on the polar and azimuthal angle of the particle track segment. For HADES typically the factor $\sin\alpha \approx 1$ and the momentum-kick $|p_k| \approx \int B(l)dl$ is a function of the track length - so there is only a second order dependence on the momentum.

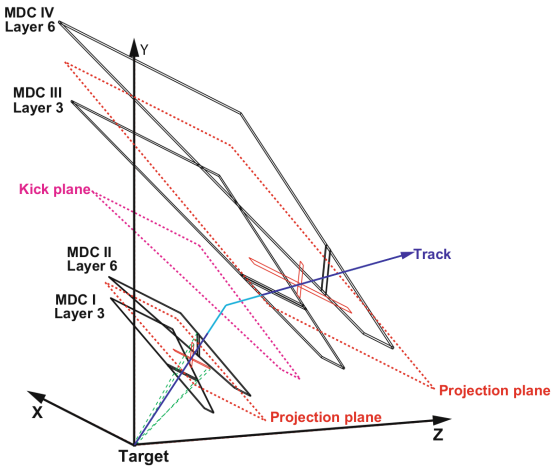

Figure 3.3.: Graphical representation of a fully reconstructed track candidate, as well as the projection planes and the magnetic field, condensed to a kick plane [77]. For the sake of simplicity, the MDC chambers are reduced to one layer each, though each chamber consists of 6 layers themselves.

This comes from the fact, that due to high momenta the overall deflection is small, which means that $\sin\frac{\Delta\theta_k}{2} \approx \Delta\theta_k$ and thusly $|p_k| \approx p\Delta\theta_k$.
Performing a Taylor-expansion on equation 3.5 and combining it with equation 3.4, one obtains

an expression for the overall momentum [115]

$$p = \frac{1}{2}\frac{p_{k_0}}{\sin\frac{\Delta\theta_k}{2}} + p_{k_1} + 2p_{k_2}\sin\frac{\Delta\theta_k}{2} \tag{3.6}$$

So in first order all parameters $p_{k_0}, p_{k_1}, p_{k_2}$ depend only on the intersection angle towards the magnetic field and can be obtained from an angle-dependent lookup-table.
The advantage of the kick-plane method is its universal usability even if only a META-hit is available instead of outer MDC information. In this case, the position measurement becomes dependent on the position resolution of either TOF or RPC (see chapter 2.2.5). Nevertheless, for this beamtime only tracks with outer MDC information are accepted. The initial implementation dates back to a setup, when outer MDC information was not yet used [90].

Spline method

A cubic spline minimization algorithm is used for initial full track reconstruction. As an input, the algorithm uses the *track-candidates'* hit point information, with inner and outer segments present, of the MDC layers. Furthermore, the first and second derivatives for these points are calculated and have to be met by the fit function representing the particles' trajectory.
In practical terms, each MDC is reduced to one plane so that for each track candidate, one global hit-point per MDC is provided. For the next step, the track-candidate is approximated with a function in the (z, r)-plane, where $r = \sqrt{x^2 + y^2}$. Figure 3.4 illustrates this cross-sectional plane. To map the deflection of the particle in the magnetic field, the part of the track between

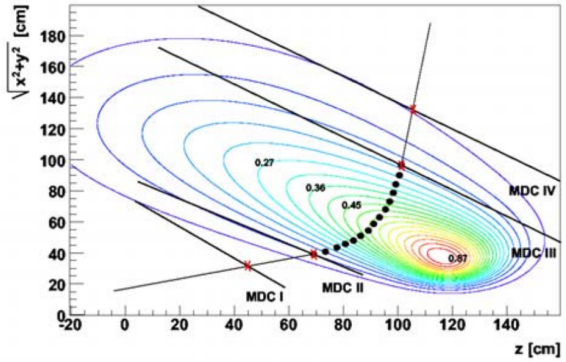

Figure 3.4.: Graphical representation of the spline fitting algorithm [77]. The number of intermediate points is reduced here to 15.

MDCs II and III is interpolated (for more details, see appendix A.2). As a preparation for the Runge-Kutta method, 50 equally separated points along the interpolated trajectory are chosen, with the corresponding derivatives being calculated.
Now for each point, the squared deviation $d^2 = (r_{spline} - r_{GEANT})^2$ for the spline r-value and the one obtained from GEANT is minimized. Here the latter one is directly momentum dependent, which results in a momentum value for each of the 50 points. The resulting momentum value from this method is then extracted from the average of these individual momenta. Systematic errors, meanwhile, are taken from the parameterized errors extracted from GEANT simulations. As a result, a relative momentum resolution of about 1 to 4.5% is achieved, also depending on the particle's momentum. Further information on this, as here previously referred to, can be found in [77].
Nevertheless, the interpolation between the inner and outer segments does not represent a phys-

ical trajectory. Instead, it represents the convergence point of a minimization algorithm, fitting a polynomial of degree n onto the track points so that the first and second derivatives of the points and the function match. Furthermore, this algorithm does not take uncertainties in the position measurement into account. Therefore, the uncertainties are taken from simulations, leading to further potential biases.

Runge-Kutta method

In the final step, the equations of motion for particles in a magnetic field are solved to determine the track-candidate-momentum. These second-order derivatives can only be solved numerically; the fourth-order Runge-Kutta algorithm is applied recursively. The idea is to extrapolate from one point to another, using the points from the spline interpolation between MDC II and III as a reference.
As an input, it receives the values for momentum and polarity from the previously used spline method, as well as vertex and direction from the initial track-segment fitter. Furthermore, the magnetic field map is used to obtain the spatial distribution of the magnetic field strength. With this input, the track parameters are iteratively optimized until they agree with the MDC hit points [77]. Finally, to quantify the quality of the final track candidate, it is estimated by a normalized χ^2_{RK} value, which is used to filter for the individual track quality in analyses performed on the data.
Like the previous methods, also this method does not take into account changes in energy and momentum, which occur due to scattering and energy loss of particles along their trajectory. It is assumed that a particle track has a constant momentum (vector). This leads to systematic shifts in the momentum resolution. For decay particles, which are reconstructed via their invariant mass distribution, this leads furthermore to potential shifts in their invariant mass.
A potential solution to this problem could be the *Kalman-Filter* approach. Like Runge-Kutta, it is an iterative minimization algorithm which uses a set of initial values for parameters of a given fit function onto the MDC track points. However, in contrast to Runge-Kutta, it iteratively updates the corresponding covariance matrix for each step of the minimization process, and this way also takes the errors of the position measurement into account [90]. This method is currently being implemented and will potentially serve as an addition to the Runge-Kutta method in future beamtimes.

3.2. Event Vertex Reconstruction

A triggered event is defined by a collision emitting a sufficient amount of particles into the active detector area, such that the readout electronics are triggered. Due to the segmented nature of the target, a precise reconstruction of the event vertices is crucial.
For this purpose, a sequence of three methods was implemented. Each method is based on the previous one, increasing the reconstruction accuracy with each step. The steps can be described as follows:

1. **Vertex position from cluster reconstruction:** the *cluster vertex finder* uses the information from MDCs I and II to perform a first estimation of the position of the reaction along the beam axis. As it is displayed on the right side of figure 3.1, a particle crossing the inner chambers creates a bunch of activated wires. Their intersection points can be identified as a *cluster* within a common projection plane of all layers in MDC I and II. Next, the resolution of the intersection points of the activated wires is determined. Random intersections are dismissed by requiring a threshold. Finally, the target segment

matching the point of highest resolution is selected as the target segment for the initial reaction. It is equivalent to a straight-line extrapolation to the target.

2. **Vertex position from inner track segments:** As soon as there is at least one fully reconstructed inner track segment present, it is extrapolated backwards to the target region. As in the inner track segment reconstruction, the applied method uses a straight line. Performed for all reconstructed inner track segments, clusters of tracks emerge in the vicinity of the initial reaction vertex. However, in contrast to the cluster vertex finder, the geometrical centre of gravity is used for the vertex reconstruction, which results in a non-discrete position distribution and a quantifiable error due to the distances of closest approach.

3. **Vertex position from particle candidates:** This represents the final and most precise position determination. The method performs the same operations as in the previous step but uses the fully reconstructed tracks for the extrapolation onto the beam axis. Therefore the χ^2 values of the reconstructed tracks also quantify the quality of the reconstructed vertex position.

The precision of all previous methods depends on the event multiplicity, as more reconstructed tracks per event result in a higher vertex reconstruction resolution.
Not every recorded event originates from a collision of two Ag-ions. The ion beam, delivered by the accelerator facility, can interact with materials other than the silver target, such as the frame for the target stripes. Additionally, detector inefficiencies can cause an insufficient reconstruction of single collision events (see section 3.5.2). Several criteria for the classification of events are used to ensure that only well-constructed collisions of silver ions are used for analysis purposes. The collection of these criteria is called *standard event-selection* and is used as subsequently described for all, except if explicitly described otherwise, analyses included in this work.

3.3. START Detector Calibration

Constant offsets are removed from the coincidence measurement between START and VETO by taking into account effects such as the length of cables between the detectors and the front-end electronics. With the goal of ps resolution and a signal propagation speed of ≈ 20 cm/ns, already cable-length differences in the mm scale give relevant delays.

In the first iteration, for all events, the START and VETO hits are used to calculate the delays between START- and VETO-hits for each START strip. This results in distributions peaking around a common value for each of the strips. The strip most activated by beam ions is then used for reference and the delay between it and each of the eight VETO pads is calculated for each event. This results in eight distributions, which are each fitted with a Gaussian. From these fits the most probable values are extracted and utilised as the offsets between the VETO pads. This is done similarly for the START strips, as the most activated VETO pad, number 4 in this case, is used to calculate the offsets between the different reconstructed start times for each START strip. Figure 3.5 shows the delays between both detectors for the case of different START strips concerning VETO pad 4 before (left) and after (right) the correction.
As this example shows, this correction removes a large proportion of the offsets. The presented correction enables a timing precision of approximately 110 ps, but the background and secondary structures can still be identified due to the change in performance of START caused by radiation damage. The implications of that are discussed further in section 3.5.2.
To further increase the precision, temperature changes and the variation of thresholds and

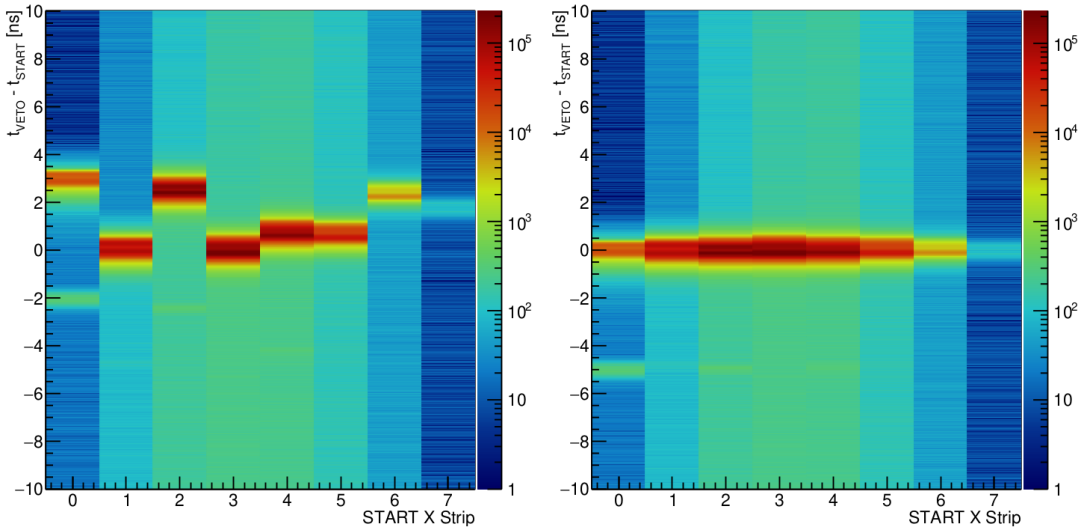

Figure 3.5.: Reconstructed delays between START strips (x-direction) and VETO pad 4 as taken from [125].

amplifications as a reaction to radiation damage are taken into account. This is done for each run by utilising π^- flight times. The π^- is chosen, as no sophisticated particle identification procedure is necessary. Most particles with a negative charge (identified by the track bending in the magnetic field) and momentum of $p > 300$ MeV/c are π^-. As the RPC detector possesses a better time resolution than TOF, only π^--tracks hitting the RPC detector are used. For each particle candidate selected this way, the nominal charged pion mass [141] is assigned so that β can be calculated from equation 3.7 using the reconstructed momentum. The time of flight is then calculated from the track length, and the difference between the measured and calculated flight time is plotted for all events of a run. As before, these run-wise distributions are fitted with a Gaussian and the offsets, represented by each most probable value, are corrected for. This concludes the START calibration and enables a final start time precision of $\sigma_t \approx 50$ ps.

3.4. Start Time Recalculation

To improve the measured time of flight precision for individual tracks, the actual START hit has to be identified for each event. As the beam intensities are large, each event possesses several START hit candidates within a time range of ± 25 ns around the reconstructed t_0 value. This start time is set to the initially assigned START hit. The hit information from the META detectors is then used to calculate the average time of flight of the three fastest particles per event. The reference distance between the collision vertex and META detectors is 2100 mm, the average distance between the target and META. One can justify this simplification by the fact that also for non-central events, $\pi^\pm$ event multiplicities are expected to lie at around $10^0 - 10^1$ per event. These, as well as the produced leptons, mostly have a β of approximately 1. Consequently, the bending of the track inside the magnetic field is minor and has no significant effect on flight time.

The determined average time of flight of the three fastest particles per event has to be around 7 ns. Consequently, the START hit closest to (-7 ± 2) ns is selected. Should there be no hit in this time window, the event gets discarded. Should there be two hits within a time window of ± 0.5 ns, they are assumed to be caused by the same ion and their t_0 is averaged.

For further improvement of the reconstructed start time, proton and pion tracks are used. Using

the reconstructed momenta (p) and the masses (m_0) known from [141], the expected velocities and time of flights can be calculated via [125]:

$$\beta = \frac{p}{\sqrt{p^2 + m_0^2}} \tag{3.7}$$

These are then compared to the flight times from the event with the previously reconstructed t_0 value. Should there be a systematic deviation from the expectation value, the START hit matching the expectation best is selected and finally assigned.

3.5. Event Selection and Classification

3.5.1. Event Selection

The following section describes the previously mentioned standard event selection and the applied methods to guarantee the highest possible purity for the Ag+Ag sample. In the analysis process, these standardized methods are called one after another by so-called *event-selection-flags* for each event in the data sample. Figure 3.6 shows the impact of these criteria on all collected data. The relative event yield is given in per cent.

Physics Trigger 3

This threshold is set for an event multiplicity of at least 20 META hits. Fulfilling this requirement, the event is called a PT3 triggered event (see also section 2.2.8). This criterion aims to suppress contamination, e.g. due to secondary reactions of Ag-ions with other materials, resulting in potentially reconstructed but unwanted events with low multiplicities. The disadvantage is the suppression of more peripheral collisions, where lower charged-particle multiplicities are produced. This condition is fulfilled for the $\approx 55\%$ most central Ag+Ag events at 1.58 A GeV.

Good START

The event must have a corresponding hit registered in the START detector. The *HParticleStart2HitFinder* uses events fulfilling this requirement and additionally calculates the average time of flight of the first three particles being detected in the META detector. This average flight time is further constrained into a time window of 5-9 ns. The basic assumption is that, especially for central collisions, mainly leptons and pions will contribute to this average, which results in a narrow distribution at around 7 ns. In section 3.5.2 further details are given.

Good Cluster Vertex

This criterion builds upon section 3.2 and the cluster vertex finder. A vertex is classified as accepted if the cluster vertex finder algorithm converges within the predefined position of the target along the beam axis ($-70 < \mathrm{Vert}_z < 0$ mm). To exclude events coming from reactions with the START detector, the cluster must be successfully assigned to one of the target stripes.

Good Candidate Vertex

In addition, to the successful cluster vertex reconstruction, this criteria requires that the vertex could also be reconstructed via the track candidates. The reconstructed vertex position must also possess a z-coordinate of > -70 mm, which corresponds to the beginning of the target region with the null point behind the last target stripe.

No Pile Up in START

To assure that one reaction of silver-ions is assigned to only one start time t_0, for each event, it is required that no additional START signal exists within a time window of -15 ns to 15 ns around the selected start time. Otherwise, the reconstructed momentum of a particle track would potentially be wrong due to an incorrectly assigned t_0 value. In the time window from -0.5 ns to 0.5 ns around the selected START hit additional START signals are allowed. This is done as crosstalk between START channels can appear and trigger a second time. Furthermore, the two START layers are treated independently, which can lead to two subsequent, independent t_0 values.

No VETO Signal

Here the events are removed, with a VETO signal within ± 15 ns around the START signal. Those are events in which the ions pass through the target segments without interacting with them. The criterion complements the one previously introduced, as it also removes events in which at least two ions passed START simultaneously, but one did not interact with the target region.

Good START to VETO

It is discarded if an event has a second registered START signal but no corresponding VETO signal in a time window of 15 ns to 350 ns after the selected START hit. This suppresses events where a second collision occurs while the previous one is not yet fully read out. Should another ion pass START in this time window, a VETO signal is demanded within ± 2 ns for the previous event to be accepted.

Good START to META

An event with a second registered START signal and more than 4 META hits within 7 ns to 12 ns after, in a time window from 80 ns to 350 ns after the selected START hit, is discarded. Though these additional tracks are in time distinguishable from the tracks of the actual event, they would increase the event multiplicity and, by that, the determined centrality (see chapter 3.5.4).

No Flashs in MDC

As the MDCs are operated at high voltages, there is a certain probability of electrostatic discharges, which are not necessarily correlated to particle tracks. Random static discharges can influence the precision of the track reconstruction. This way, only events are accepted with less than 20 fired wires with a time over threshold of fewer than 30 ns.

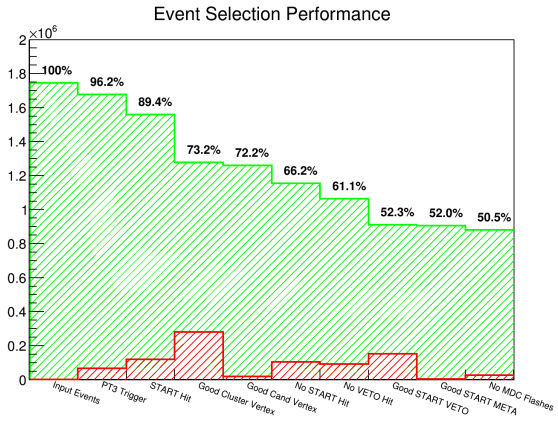

Figure 3.6.: Event selection criteria and their overall impact on the data. This graphic was created with a subsample of about 1.74×10^6 events. The green area represents the overall remaining fraction of events, while the red areas represent the relative amount of removed events per event selection step.

3.5.2. START Performance and the HParticleStart2HitFinder

During the data-taking period, the START detector was moved two times along the y-axis due to radiation damage. This chapter investigates the influence of mentioned material degradation on the t_0 reconstruction and the exclusion of track candidates with a wrong time of flight.
Figure 3.7 displays the number of registered beam ions for each START channel in the y-direction as a function of time - more precisely the day of the beamtime. As this shows evidently, the data-taking period can be subdivided into three periods in time, in each of which different channels of the START detector are used. The three distinct time intervals visible are the days 62-77, 77-81 and 81-87.

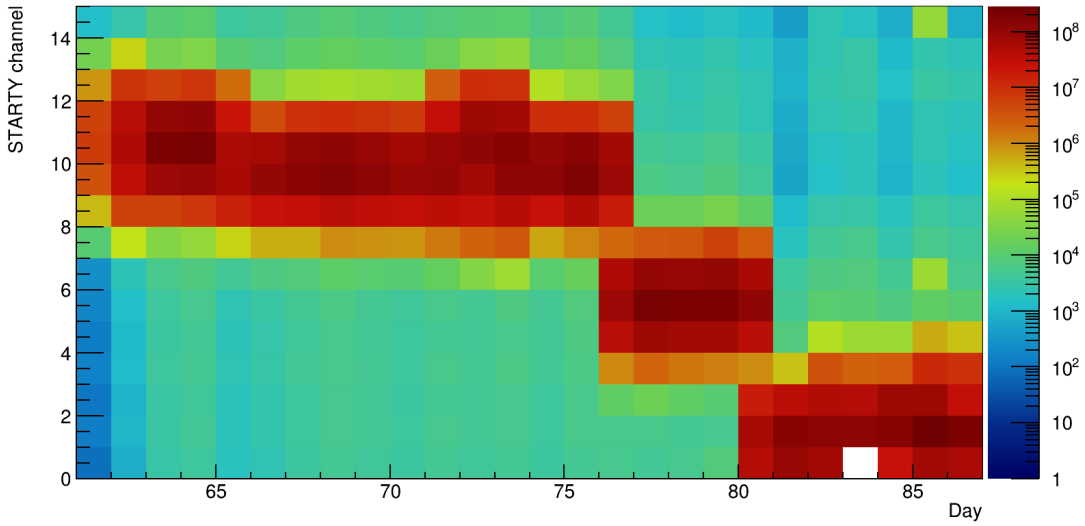

Figure 3.7.: Number of registered Ag-ion-hits along the y-axis of the START detector in relation to the days of beamtime. The three shifts of the detector can be seen.

Looking at the single-particle β vs $p \times q$ distributions for the different days of beamtime, as shown in figure 3.8, a large background towards lower particle β-p is observed for the early days (left side). Furthermore, a sharp cut-off at $\beta \approx 0.55$ can be seen. This background is less prominent in the third previously introduced time interval, which supports the idea that a large proportion of it is caused by incorrectly reconstructed times of flight due to wrongly assigned start times t_0.
Furthermore, the sharp cut-off of this structure suggests that particle tracks are assigned to the wrong time of flight until this surpasses a certain selection cut-off, which creates the edge

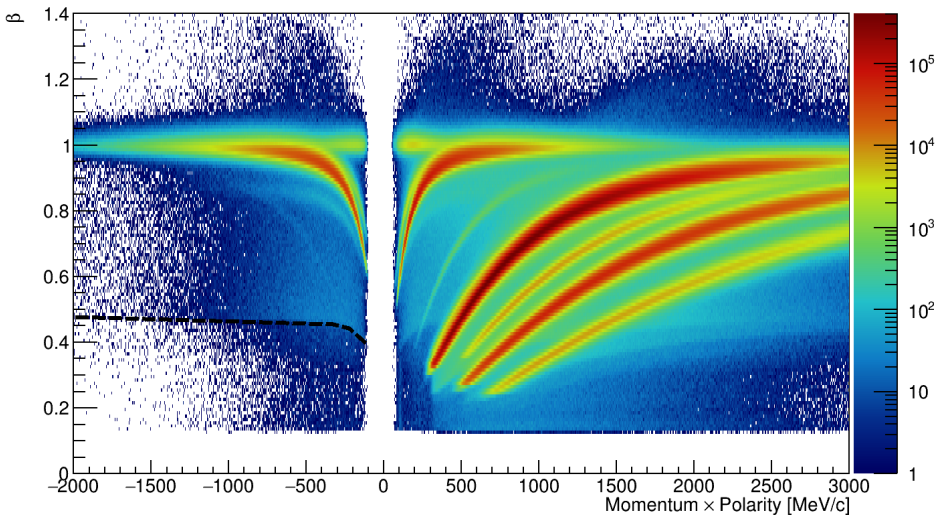

(a) Day 71

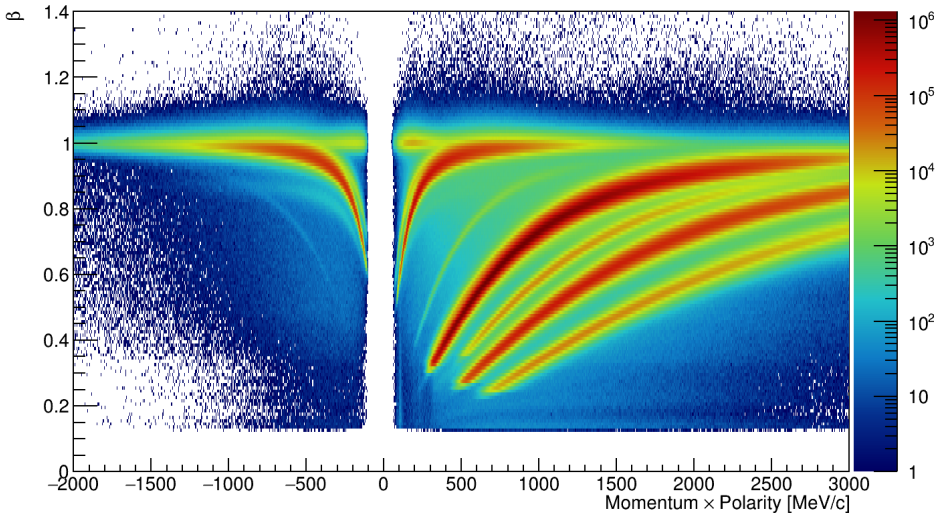

(b) Day 84

Figure 3.8.: β-momentum distribution for the RPC detector at different days of beamtime. For the days before the first shift (a) there is a clear structure visible around the K^--region, with a sharp cut-off at a β of around 0.55. In (b) the same distribution is shown for day 84 after the second shift.

marked in figure 3.8 (a).
Though the presented distributions represent only tracks associated with hits in the RPC detector, the same can be observed also for TOF. RPC was chosen for demonstration due to the better time resolution and clearer visibility of the effect.

As this background strongly overlaps with the K^- it directly contributes to the invariant mass spectrum of the ϕ-Meson in the $\phi \to K^+K^-$ channel, which can be seen in figure 3.9. More importantly, the background contribution to the single particle spectrum seems to be in the

same order of magnitude as the one from the $\phi \to K^+K^-$ channel.

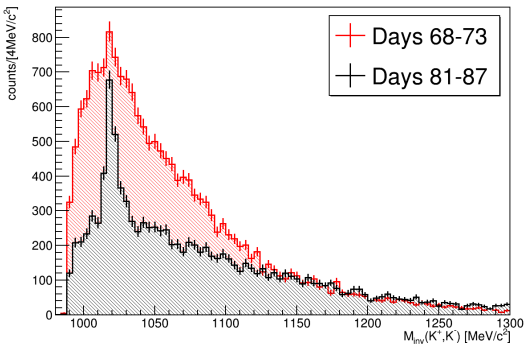

Figure 3.9.: Invariant K^+K^--pair-candidate mass distribution for different days of beamtime. For the days before the first shift of the START detector, the contamination in the low invariant mass region is prominent, while it reduces for the days after the second displacement.

One concludes, that the ϕ-meson, as a rare particle at kinetic beam energies of 1.58 A GeV, is a sensitive probe for calibration effects in the data in the order of magnitude of 10^{-4} to 10^{-5} per event. It is also important to suppress this background contribution to increase the signal-to-background ratio for the ϕ-meson analysis.

As part of the Good START event selection criterion, the *HParticleStart2HitFinder* routine is responsible for reconstructing the start time t_0 of an event. This function selects a START signal and then calculates the average flight time of the three fastest META hits per event. As, especially for central collisions, mainly electrons, muons and charged pions are expected in this category, with all of them having a comparable time of flight, a distribution with a peak at ≈ 7 ns is seen. This is displayed in figure 3.10, where the average time of flight of the three particle candidates with the lowest reconstructed time of flight per event is plotted for all accepted events.

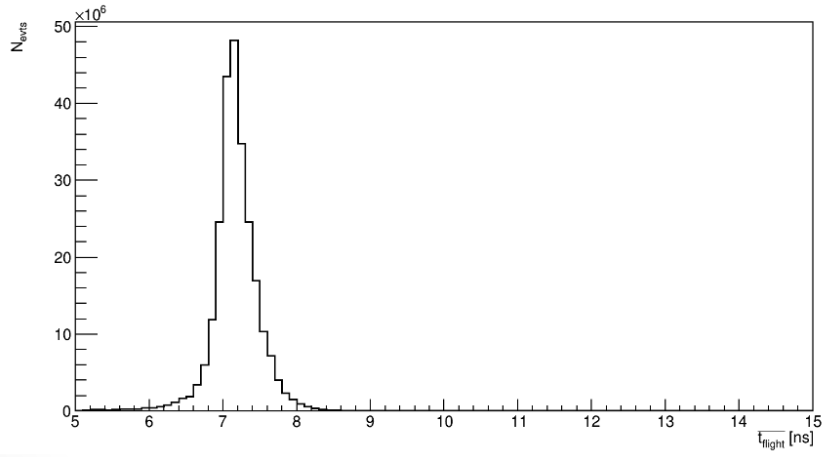

Figure 3.10.: Average time of flight of the three fastest reconstructed charged particle tracks per event. A narrow peak is visible with a mean value slightly higher than 7 ns.

The x-axis range represents the default time window in which events are accepted as part of the routine. This observable depends on the bending radius within the magnetic field, and this way, the $\frac{p}{q}$ ratio of the particle. So the higher the observed average time of flight value, the greater the charged particles' mass according to the momentum reconstruction [119]

$$\frac{s/t}{c} = \frac{v}{c} = \beta = \frac{p}{m} \cdot \frac{1}{\sqrt{\left(\frac{p}{m}\right)^2 + 1}} \tag{3.8}$$

The following working hypothesis is applied: Due to the inefficiency of START, the ion, which performs the initial reaction, is not detected. Subsequently, the multiplicity threshold for the trigger is surpassed, an event is created, and the signal of an ion passing earlier or later than the initial ion, also performing a reaction (e.g. Ag+C) and/or not triggering VETO, is used as a reference for the time of flight measurement. As this process is assumed to be happening due to material degradation, no correlation but a random distribution is expected within a particular time window. Translating this into the HParticleStart2HitFinder routine of using the average time of flight of the first three META hits per event as a selection criterion would mean a broad background distribution overlapping with the narrow peak at ≈ 7 ns.

A selection of events with ϕ candidates is performed to adjust the optimal setting for the time window to suppress the background. The average flight time of the three particle candidates with the highest βs per event is calculated for these events as displayed in figure 3.11.

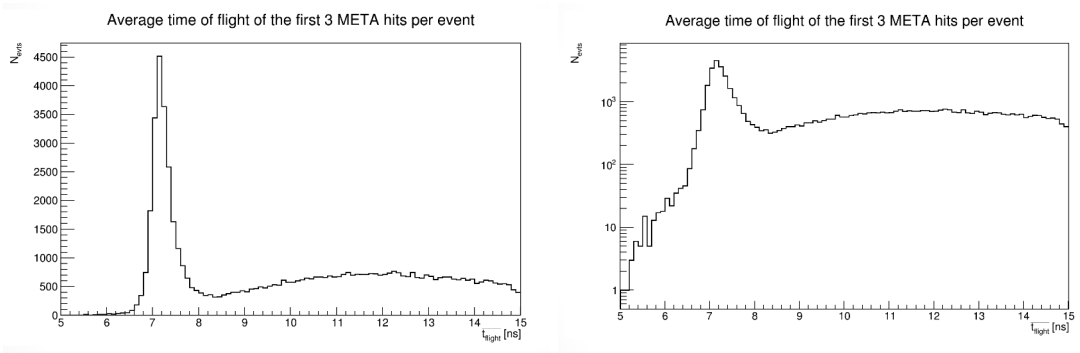

(a) Linear Scale (b) Logarithmic Scale

Figure 3.11.: Average time of flight of the three particle candidates with the highest β per event in linear (a) and in logarithmic scale (b). The broad secondary structure indicates a random distribution for the attribution of incorrect starting times.

These figures show a wide secondary structure overlapping with the main signal for correctly reconstructed starting times of Ag+Ag reactions. To find the optimal time window for the HParticleStart2HitFinder routine, the K^+K^- invariant mass spectrum is plotted and signal-to-background as well as significance extracted for different values of $\bar{t}_{\mathrm{ToF,max}}$. Table 3.1 shows the results of this analysis and underlines, that $\bar{t}_{\mathrm{ToF,max}} = 9$ ns appears to be the optimal value for the upper HParticleStart2HitFinder time-window-cutoff to strongly suppress the background under the $\phi(1020)$-meson peak.

While the S/B ratio continuously decreases for increasing values $\bar{t}_{\mathrm{ToF,max}}$, the significance reaches a maximum of around the value of 9 ns. Considering the findings from figure 3.11, a cut-off at 9 ns is reasonable, as no significant amount of correctly reconstructed events is removed from the sample. Overall this cut-off removes an additional 3% from all events.
The lower cut-off value $\bar{t}_{\mathrm{ToF,min}}$ is varied as well in the context of this analysis. However, as figure 3.11 already indicates, any effects are negligible within statistical uncertainties. This way, the lower cut-off value is kept at 5 ns.
To show the effectiveness of this new implementation a comparison of invariant mass spectra

$\bar{t}_{\mathbf{ToF,max}}$ [ns]	Signal/Background	Significance
8	1.338 ± 0.068	35.775 ± 1.184
9	1.119 ± 0.054	36.778 ± 1.206
10	0.933 ± 0.045	35.571 ± 1.222
11	0.746 ± 0.038	32.492 ± 1.249
12	0.511 ± 0.029	28.079 ± 1.289
13	0.382 ± 0.024	25.025 ± 1.304
14	0.310 ± 0.020	23.171 ± 1.319
15	0.285 ± 0.019	23.139 ± 1.333

Table 3.1.: The S/B ratio and the significance for different maximum values for the average time of flight criteria of the HParticleStart2HitFinder. All errors given here are purely statistical.

with and without this new $\bar{t}_{\mathrm{ToF,max}}$ cut-off-value is given in figure 3.12.

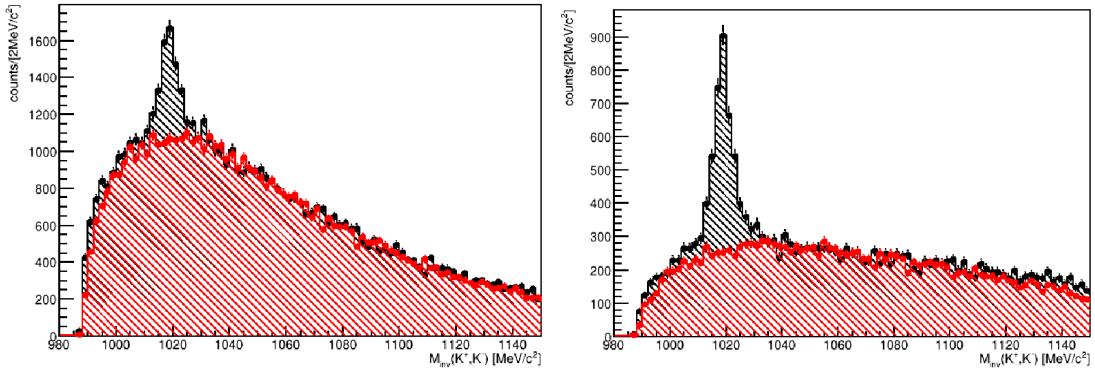

(a) $\bar{t}_{\mathrm{ToF}} < 15$ns (b) $\bar{t}_{\mathrm{ToF}} < 9$ns

Figure 3.12.: Invariant K^+K^--pair-candidate mass distribution (black) with the combinatorial background description via Mixed Event technique (red) with different maximum values for $\bar{t}_{\mathrm{ToF}}$. The power of the new implementation becomes apparent to the naked eye.

It can be seen that the modification of $\bar{t}_{\mathrm{ToF,max}}$ suppresses the background significantly and, after subtracting the mixed-event background (see section 4.3.1), increases the number of reconstructed $\phi(1020)$-mesons by $\approx 6\%$. As a consequence, it is implemented in the HParticleStart2HitFinder routine.

3.5.3. Sector Performance Selection

Static discharge in an MDC, which exceeds a certain safety limit, leads to a ramp-down of the HV supply for this chamber. After 30 seconds, this chamber is automatically ramped back up. During this time, large reconstruction inefficiencies occur, which affects the quality of the data. Consequently, the performance stability of all six sectors during the data-taking period is mapped. For each run, representing the time in which one HLD file was written, the average detection rate per event for the most abundant particles is observed sector-wise. Namely, those are $\pi^{\pm}$,$e^{\pm}$ and p. The particle selection for this criterion was performed with a 3 σ inclusion cut on the particle distribution in the β-momentum-plane. For the $e^{\pm}$ the successful reconstruction of a Cherenkov ring inside the RICH detector is required for a track candidate, as well as $\beta > 0.9$. Figure 3.13 shows the corresponding measured average particle multiplicities per run as a function of time.

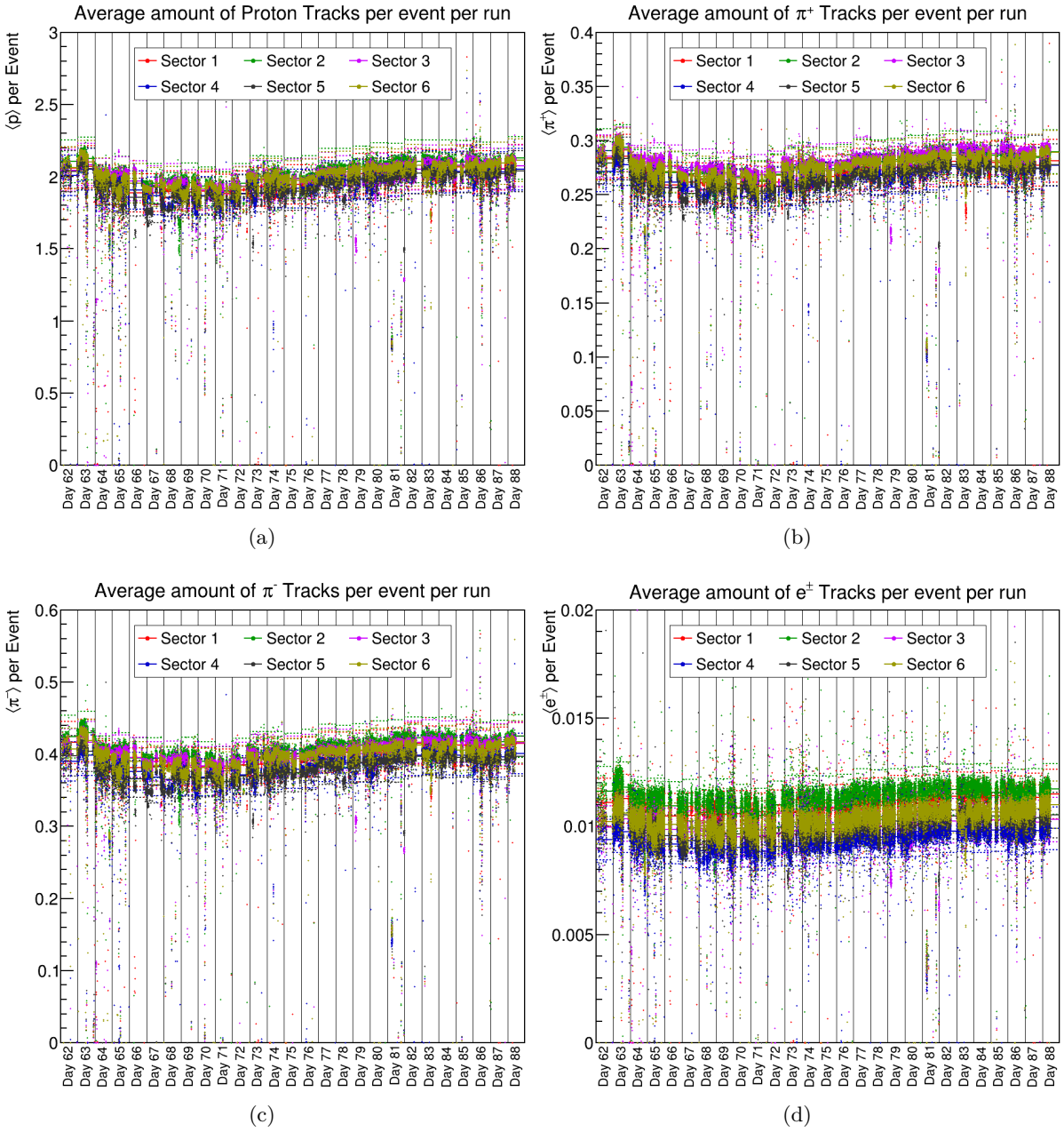

Figure 3.13.: Average measured event multiplicities for different particles during the beamtime [125]. For these most abundant particles, the distributions show a stable operation of the detector system during most of the beamtime.

A run is rejected if there is a significant deviation visible in one sector for the time window in which it was recorded. For hadrons, relative deviations of ±7% from the daily average

$$\langle M \rangle = \frac{\sum_{i=1}^{R} M_i}{R}$$

are accepted. Here, M denotes the multiplicity and R is the number of runs in the corresponding time interval. For the $e^{\pm}$, due to larger statistical uncertainties, ±10% are considered stable.

As the dotted lines, representing the allowed deviation limit from the daily average, underline, the system presents stable during the time. Overall this criterion leads to an additional removal of around 6.9% of all events.

3.5.4. Centrality Determination and Selection

The last step in the event classification and selection routine is the centrality selection. For HADES, a *Glauber Monte Carlo* approach is used to give an estimate for the centrality of a collision, as described in [5].
The goal of the procedure is to correlate the number of detected charged particles with the centrality of the collision. To achieve this, one makes use of the fact, that the centrality of a collision is directly proportional to the fraction of the total cross section σ_{AA} and the impact parameter b via

$$C = \frac{\int_0^b d\sigma/db'db'}{\int_0^\infty d\sigma/db'db'} = \frac{1}{\sigma_{AA}} \int_0^b \frac{d\sigma}{db'} db'$$

With sufficient knowledge of σ_{AA} one can furthermore set the impact parameter in relation to the observed particle multiplicity N in a way that the centrality can be estimated via

$$C \approx \frac{1}{\sigma_{AA}} \int_{N^{thr}}^\infty \frac{d\sigma}{dN'} dN'$$

with N^{thr} the multiplicity value for the lower edge of the centrality class.

Glauber models treat the collision of two nuclei as a superposition of collisions of their nucleons. Those are distributed randomly, according to a nuclear density profile

$$P(r) \propto r^2 \rho(r) = r^2 \frac{1 + w(r/R)^2}{1 + \exp\left(\frac{r-R}{a}\right)} \ .$$

In the case of a gold nucleus, as it is displayed in figure 3.14, the radius R is set to $R = 6.55$ fm, while $a = 0.52$ fm. Parameter w is used to describe nuclei with a density gradient and was set to $w = 0$ for this case.

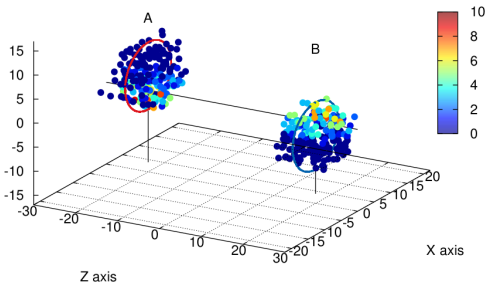

Figure 3.14.: Example for a spatial distribution of Au-nucleons before the collision, which is modelled by a Glauber Monte-Carlo model at an impact parameter of $b = 6$ fm as taken from [5]. The colour code represents the number of inelastic collisions the nucleon performs on its path.

To simulate the collision event, the nucleons are collectively moving along a straight-line trajectory (*Eikonal approximation*). The subsequent interactions on the nucleon level are taken into account individually.
In the Eikonal approximation, a nucleon is defined as a participant if at least one binary collision happens on its trajectory. So the size of the interaction volume also referred to as the system size, is directly proportional to the number of participants. Moreover, the average number of produced particles per event is, according to the *wounded nucleon model*, directly proportional

to the number of participants. This results from the correlation of the multiplicity of a nucleus-nucleus collision $N(\nu)$ to the number of individual nucleon-nucleon interactions ν, scaled by the average number of *wounded nucleons* N_w [41]

$$N(\nu) = (\nu + 1)N_w$$

Wounded nucleons are here described as nucleons that, on their trajectory, interact at least once inelastically. Hence, by simulating the collision of two nuclei as the interactions between the individual nucleons, the final particle multiplicities can be estimated independent of the number of participating nucleons and the impact parameter b.
Many collisions are statistically sampled and fitted onto measured data. As a result, *centrality classes* can be defined in intervals of event multiplicities, which allows performing a system size-dependent analysis using the observed charged-particle multiplicity.
Practically, the decision of whether a collision between two nucleons is taking place is determined by their distance

$$d_{ij} = \sqrt{\Delta x^2 + \Delta y^2}$$

as it should be smaller than the radius defined by the inelastic nucleon-nucleon cross-section

$$d_{ij}^2 \leqslant \frac{\sigma_{inel}^{NN}}{\pi}$$

Nevertheless, one expects a certain amount of event-by-event fluctuations for the correlation between the number of participants and the event multiplicity. This effect can be taken into account by sampling the number of charged particles per participant from a *Negative Binomial probability Distribution* (NBD) and fitting it onto the measured data. An NBD represents a purely random distribution for each trial, determining the probability of r successes from a fixed number of n trials before a defined number of k failures (for more details, see e.g. [37]). Using this ansatz, the proportionality $\langle N_{ch} \rangle = \mu \cdot \langle N_{part} \rangle$ for the charged particle multiplicity is obtained, with μ the mean value of the random distribution. Additionally, non-linear multiplicity-dependent inefficiencies, like secondary particle production in the material, are taken into account by a phenomenological efficiency function $\epsilon(\alpha) = 1 - \alpha \cdot N_{part}^2$.
In figure 3.15 the results for the Glauber Monte Carlo calculations of Ag+Ag collisions at 1.58 A GeV are summarized for the event characterization by centrality percentile. These results are used throughout the analysis for the event characterization.

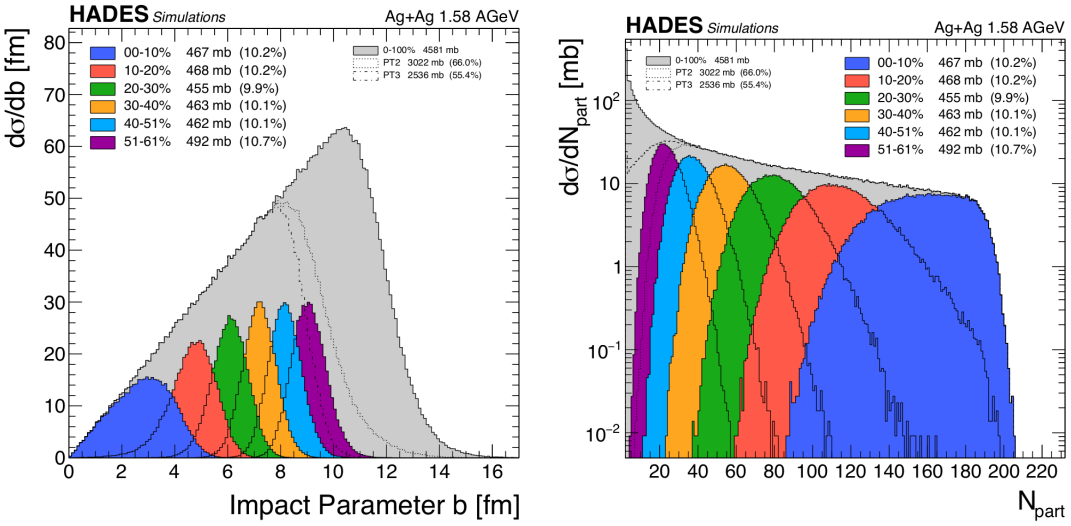

(a) Centralities for different impact parameters

(b) Centralities for different N_{part}

Figure 3.15.: Event centrality characterisation, according to the Glauber Monte Carlo Model, for Ag+Ag collisions at 1.58 A GeV for simulated UrQMD events (a) and data (b).

3.6. Track Selection and Classification

3.6.1. Track Sorter

The *HParticleTrackSorter* uses all particle tracks, whose straight-line extrapolations intersect with the META detector within a $\mu \pm 3\sigma$ around the hit and iteratively sorts them by predefined criteria. Those are adjusted for different particle species. In the case of charged hadron candidates the following criteria have to be met to be accepted:

1. For the inner MDC tracklet $\chi^2 \geq 0$, so that the fitting algorithm converged for the inner track segment.

2. For the outer MDC tracklet $\chi^2 \geq 0$ so that the fitting algorithm converged for the outer track segment.

3. Furthermore, a META hit has to exist.

4. The overall $\chi^2_{RK} > 0$ for the entire track.

5. A maximum value of $\chi^2_{RK} = 1000$ must not be exceeded for the entire track

6. χ^2_{MM} must lie within 0 and 3

7. From a predefined lookup table, it is queried if the used META cell should not be used

8. If $\beta < 0$ or the time of flight is greater than 60 ns, the track is discarded

Afterwards, an exclusion of double hits is performed. The final step is a sorting algorithm, which uses the χ^2_{RK} values of the tracks connected to one META hit to sort them and select the track with the lowest value.

3.6.2. Hadron Selection

Before the application of any particle identification methods, all fully reconstructed particle candidates of an event are pre-filtered for charged hadron candidates. To be accepted as such, a track has to

- possess a successfully reconstructed inner and outer MDC track segment, an assigned META hit, an inner track segment $\chi^2 > 0.$ and a $\chi^2_{RK} > 0.$
- have a track quality of $\chi^2_{RK} < 1000.$
- be in a range of $0. < \chi^2_{MM} < 3.$
- not have a hit inside a META cell which was excluded from the sample
- have a $\beta > 0.$
- have a time of flight of fewer than 60 ns.

A particle is considered a hadron candidate from the primary vertex if these criteria are met. These criteria form a loose preselection for the data from the DSTs. Additionally, to these general constraints, selection criteria on the reconstructed particle mass are applied to specifically select the charged Kaon area. While analyses of abundant particles, like protons and $\pi^{\pm}$, use identification methods in the β-momentum-plane, where the particle distributions are fitted, and all entries within a $\pm 2\sigma$ range are accepted, the charged Kaon event multiplicity is too low to do so. As it is orders of magnitude below proton and $\pi^{\pm}$ event multiplicities, the charged Kaons have to be extracted by describing the background below the mass peak with an appropriate fitting method and subtracting this background. The preselection is done via a wide mass constraint of $200. < M < 800.$ MeV/c^2. The proton and/or charged pion tails dominate the resulting mass distribution. The final preselection constraint is the particle charge. It is indirectly determined by the direction of bending inside the magnetic field. If a track has a charge defined as positive, it is bent towards higher polar angles and vice versa.

3.7. Simulation

The extraction of particle yields from data leads to results systematically below the actual values. This mainly has two reasons. One is that the detector system has a finite efficiency due to detector dead times. Another reason is the geometrical acceptance of the detector system. Both effects can be corrected by correcting the extracted yields for the determined *Acceptance* $\times$ *Efficiency* value. To determine this value, Monte-Carlo simulations are performed and subsequently transported through a *GEANT* representation of the HADES detector setup. The steps are the following:

1. The *UrQMD* transport model [30] of version 3.3p2 simulates full A+A collisions by colliding two nuclei and evaluating each NN and secondary particle interaction until the kinetic freeze-out. Elementary reaction cross-sections serve as input parameters for the calculations performed. Direct and resonant production mechanisms emulate the in-medium effects during the collision phase. Yield predictions and a comparison to other transport models for Ag+Ag collisions at 1.58 A GeV can be found in [110].

2. Especially for particles with low event multiplicities at these energies, like charged Kaons and ϕ-Mesons, statistics have to be enhanced for differential analysis. To achieve this enhancement, the *PLUTO* event generator [60] is used. It is a C++-based simulation

package executed within the ROOT environment. A thermal particle source is created when executing a simulation, which decays into the desired particles and their possible decay channels predefined by the user. Depending on the input temperature of the thermal source, the momentum and kinetic energy distributions of the produced particles are calculated. The resulting distributions are embedded into the UrQMD simulations and stored in separate files specific to the investigated (decay) channel. For the analysis of light nuclei (A $<$ 5), iQMD simulations (see e.g. [79] for a brief summary) are implemented as well, which model the formation of nuclei in contrast to UrQMD.

3. Finally, the produced particles are transported through an HGEANT (**H**ADES **Ge**ometry **An**d **T**racking) simulation. This is a simulation based on the software GEANT 3.21 [67] which emulates the interactions between particles and materials. The HADES setup is modelled within this framework, and the UrQMD/PLUTO particles are traversing it. While the particles traverse the material, physical interactions are modelled, e.g., deflection due to the magnetic field and specific energy loss. Afterwards, the detector hits in GEANT are digitized and written into DST files. Those processes are analogous to the data. As a result, the simulated events can be read out and analyzed in the same way as the data.

After these steps, the number of reconstructed particles from the GEANT simulation is compared to the UrQMD/PLUTO generated ones. This results in a folded Acceptance $\times$ Efficiency value, which can be used to correct the extracted raw yield from the data. Therefore it is crucial to apply the same PID criteria to the GEANT simulation as to the data. Figure 3.16 sums up the whole procedure of the correction - comparing the analysis steps for data and simulation. Comparisons between simulated and data events are discussed in the *Analysis*-chapters of the corresponding particles.

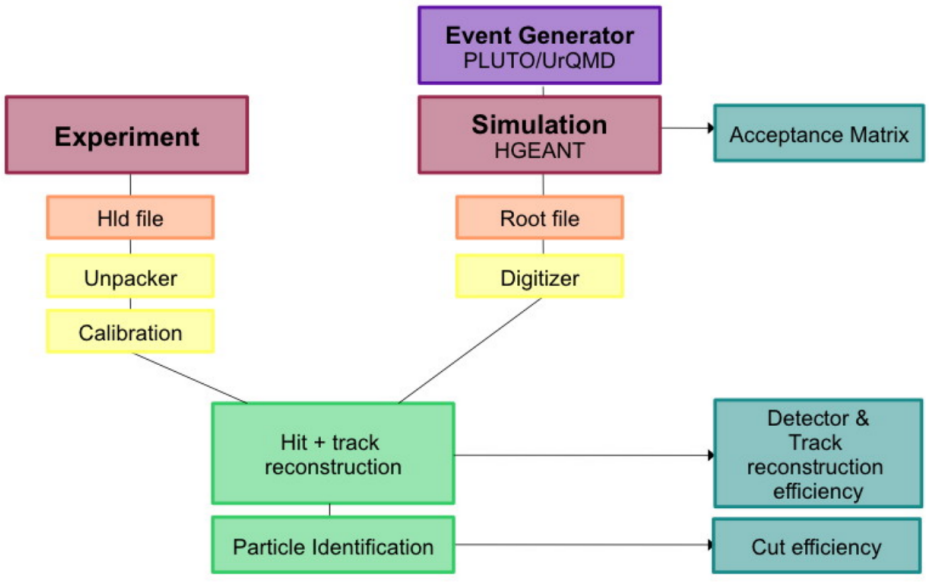

Figure 3.16.: Analysis procedure for data and simulation as taken from [119]. The data is stored in HLD files and calibration parameters for the subdetectors are applied, before the main analysis is performed. The generated events are transported through HGEANT and directly stored in ROOT files. Latter are used for Acceptance $\times$ Efficiency correction of the data. Both, the HGEANT results as well as the data, are treated equally to ensure consistency.

4. Hadron Identification and Analysis

The expected particle abundances of K^- and ϕ lie in the order of 10^{-3} to 10^{-4} particles per event. For the K^+, one can expect a higher yield, however, in the order of 10^{-1} to 10^{-2} per event. Protons and π-mesons have multiplicities which are orders of magnitude higher. This poses challenges for identification and count rate extraction, as the K^+ signal is hidden by the tails of the mass distributions of proton and π^+ signals. The rare K^- signal is overlapped by the tails of the π^- mass distribution.
Moreover, neutrons emerging from the collision create signals in the META detectors, which can overlap with simultaneous signals from charged particles and might lead to systematic shifts in the reconstructed time of flight and the corresponding reconstructed particle mass. The implications and complications for the presented analysis are discussed in section 4.1.7.

Generally, the particle identification is performed via the reconstructed momentum (see section 3.1.4) and mass, as well as the specific energy loss of the particle in the MDCs and TOF. Likewise, these criteria are used for background suppression. The ϕ meson has to be reconstructed via the daughter particles from the investigated decay channel. After successful particle identification and count rate extraction, the resulting yields are corrected as described in section 3.7. The results are then discussed and analysed in chapter 5.
The complete analysis is performed within the $0-30\%$ centrality range as defined within the Glauber Monte-Carlo calculations. The choice for an upper limit of 30% centrality is motivated by an Ag+Ag sample purity of $> 95\%$ until this value. In addition, investigations are ongoing to suppress Ag+C contaminations in more peripheral collision events.

4.1. Analysis of Charged Kaons

The analysis is performed multidifferentially in an $m_t - y$ grid for $0-30\%$ most central events. Additionally, a system size-dependent analysis is done by performing the same analysis on centrality classes in $0-10\%$, $10-20\%$ and $20-30\%$ most central collisions.
Figure 4.1 shows a summary of the charged Kaon analysis procedure performed in this work. It shows the analysis steps performed for measured data and simulation and highlights two major differences. In simulations, it is well-defined which collision system is generated. In measured data, selection criteria have to be applied to exclude other than pure Ag+Ag events. Furthermore, the particle type for each track is known in simulations. Querying the particles' ID consequently results in a pure sample of that particle type originating from Ag+Ag collisions, making any background description unnecessary. In data, the background has to be described and subtracted to obtain the data sample of interest. Nevertheless, the same track quality selection criteria as for data are applied in simulation. This is necessary later to correct the data for track selection efficiency losses. In the following sections, a detailed motivation and explanation of each track selection criterion, as well as comparisons of data and simulation, is given.

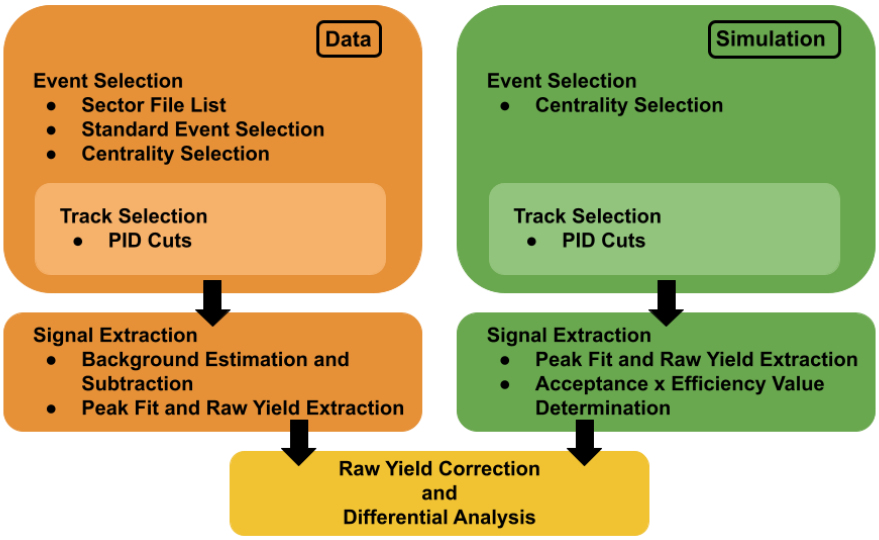

Figure 4.1.: Flow chart for the charged Kaons analysis. See text for details.

4.1.1. Count Rate Extraction

The cubic spline interpolation method of ROOT [113] is used for background estimation below the signal peak. The mathematical formulation for this ansatz is explained in appendix A.2. In this section, the application for the $K^{\pm}$ count rate estimation is presented.
The background estimation is done in an iterative procedure: Initially, the algorithm reads in the mass distribution within a range of $200 < M < 800$ MeV/c^2. Then, the first attempt for a fit of the $K^{\pm}$ peak is performed, setting the initial values for the mean μ_M to the nominal $K^{\pm}$ mass and the width to $\sigma = 15$ MeV/c^2. Finally, if the fit converges, the resulting μ_M and σ are used to define six interpolation points at the values $\mu_M \pm i \cdot \sigma$ with $i = [3.5, 5, 7]$. If the gaussian fit does not converge, the predefined starting values are returned to determine the interpolation points.
Next, for each point, the number of entries of the affiliated bin is stored as the corresponding y-value. The interpolation algorithm does not take the statistical errors of points into account. To compensate for the bin-to-bin fluctuations due to low statistics, an average over the affiliated mass bin and the two neighbouring bins is performed in the case of the K^-. The first and second derivatives are determined for the stored interpolation points in the following called nodes.
A twice continuously differentiable polynomial of third order is applied on each subinterval, yielding a system of six equations with the following boundary conditions:

- for each interpolation, the function has to match the boundary nodes of each interval for the corresponding values
- for each node, the corresponding first and second derivative between the point and the function has to match
- the second derivative of the first and last interpolation point are equal to zero (natural boundary conditions)

Further information on the interpolation algorithm can be found in [68].
Finally, the converged algorithm results in a parameterised polynomial, which is used for the background description, as depicted in figure 4.2(a) where an exemplary mass distribution with its interpolated background (red) is depicted. After background subtraction, the resulting mass

distribution (Figure 4.2(b)) is integrated in a $\pm 2\sigma$ range around the mean value of the peak to obtain the multi-differential $K^{\pm}$ count rate. Finally, the mean value μ_0 is determined by applying a Gauss-fit onto the distribution.

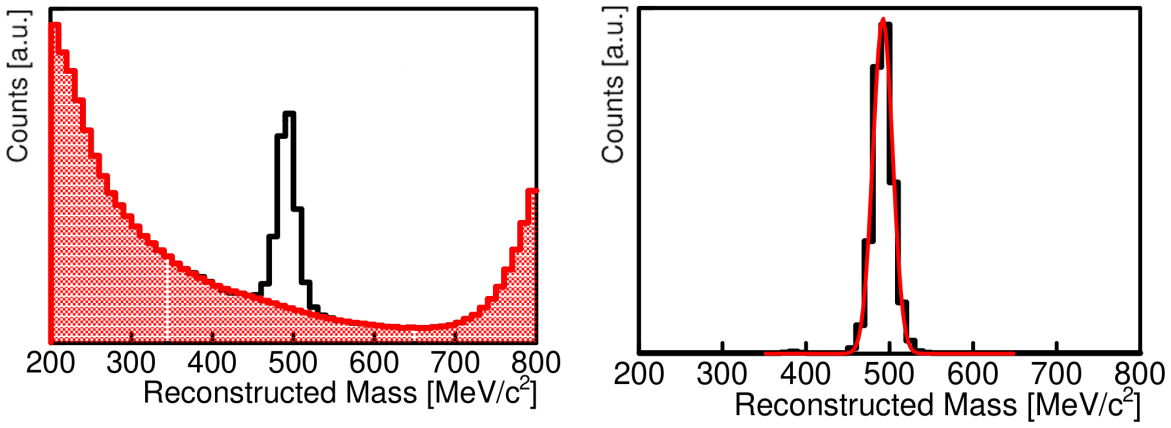

(a) (b)

Figure 4.2.: Example for a K^+ count rate extraction within one multidifferential $m_t - y$ bin. The background estimation (red area) is performed via the interpolation method (a). The corresponding subtracted spectrum is displayed in (b), showing the applied Gaussian fit in red.

4.1.2. Track Quality Parameter Constraints

To optimise the significance of the extracted signal, a systematic comparison of its resulting distribution within the χ^2_{RK}-χ^2_{MM}-plane is used. The latter two represent the track quality criteria used to define the goodness of a track candidate (see sections 3.1.3 and 3.1.4). Stricter constraints, hereby, lead to a higher purity but less statistics.
At the same time, the acceptance $\times$ efficiency correction should not be biased by the selection of the cut criteria. This will be the case if simulation and data show a different response to track quality constraints. Figures 4.3 and 4.4 show a comparison of significance values in the χ^2_{RK}-χ^2_{MM}-plane. All plots were created with a starting sample of for 15×10^6 track candidates at maximum values for $\chi^2_{RK} = 400$ and $\chi^2_{MM} = 3$ for RPC and TOF combined.
For the region $\chi^2_{RK} < 150$ and $\chi^2_{MM} > 1.3$ variations within $\approx 7\%$ are found in case of the K^+. Outside this region, the values only decrease for another 10% along the χ^2_{RK}-axis. The largest impact on the significance comes from the χ^2_{MM} criterion. Along its axis, assuming a constant χ^2_{RK}, the maximum difference in significance reaches $\approx 75\%$.
Judging from this observation, low χ^2_{RK} and high χ^2_{MM} cut-off values are the appropriate choice. Nevertheless, as indicated by the bin-to-bin fluctuations visible in figure 4.4, the count rate extraction can become less reliable by decreasing the available statistics too strongly when applying strict track selection criteria. Due to the better time-resolution of RPC compared to TOF, which results in more narrow signal peaks, also and especially for the neighbouring π^+ and p, the signal extraction proved more stable over the entire χ^2_{RK}-χ^2_{MM}-plane. It can be observed for TOF, that a few bins fluctuate up or down relative to the global trend, which can be attributed to the more challenging signal extraction.

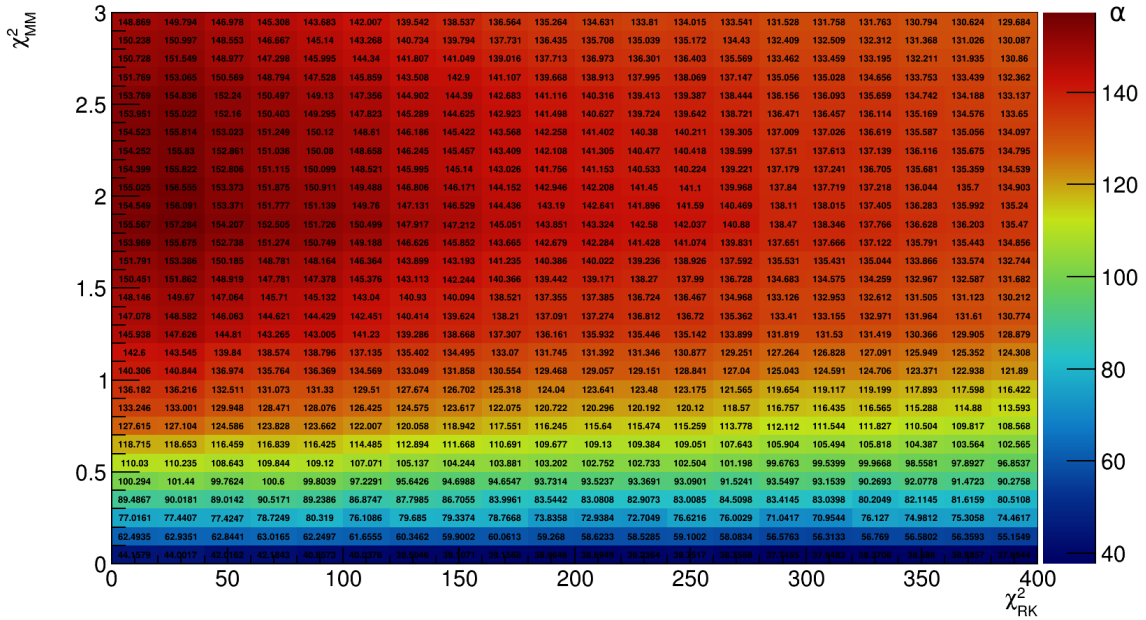

Figure 4.3.: Extracted K^+ significance α in the χ^2_{RK}-χ^2_{MM}-plane in the polar angle region covered by the RPC detector. On the colour-coded z-axis, the significance of reconstructed K^+ signals is depicted. The largest values are achieved for $\chi^2_{RK} < 150$ and $\chi^2_{MM} > 1.3$.

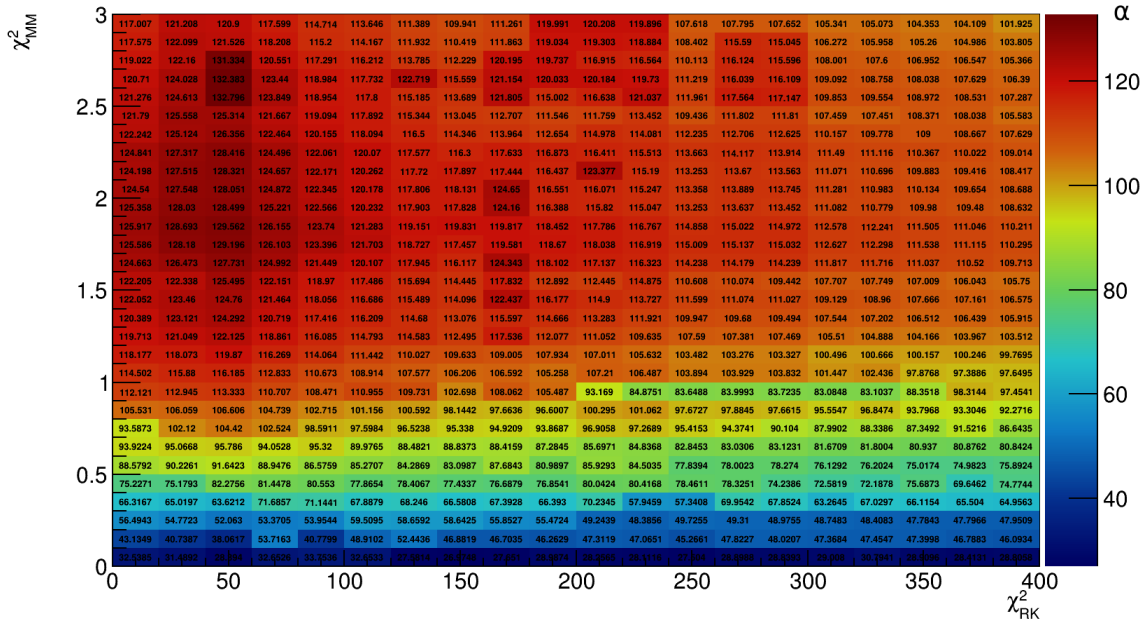

Figure 4.4.: Extracted K^+ significance α in the χ^2_{RK}-χ^2_{MM}-plane in the polar angle region covered by the TOF detector. On the colour-coded z-axis, the significance of reconstructed K^+ signals is depicted. The largest values are achieved for $\chi^2_{RK} < 150$ and $\chi^2_{MM} > 1.3$.

The same analysis is performed for K^- candidate tracks. This is not done for optimisation reasons but to evaluate if the previously estimated cut values are applicable similarly.
The spectra for the TOF polar angle region indicate clearly that the background description for the K^- is a crucial optimisation problem. Specifically, the fluctuations in figure 4.7 underline the challenging signal extraction. Additionally, the TOF mass signal is broadened as the time

resolution of the TOF detector is lower, resulting in a broadened momentum distribution. Besides the statistics being lowered by up to two orders of magnitude, compared to the K^+, the background contribution discussed in section 4.1.7 contributes in the same order of magnitude as the K^- signal peak. This makes the signal extraction in the TOF region particularly difficult. Figure 4.5 shows two examples of integrated K^- spectra after the basic hadron candidate selection criteria for different track quality criteria cut-offs.

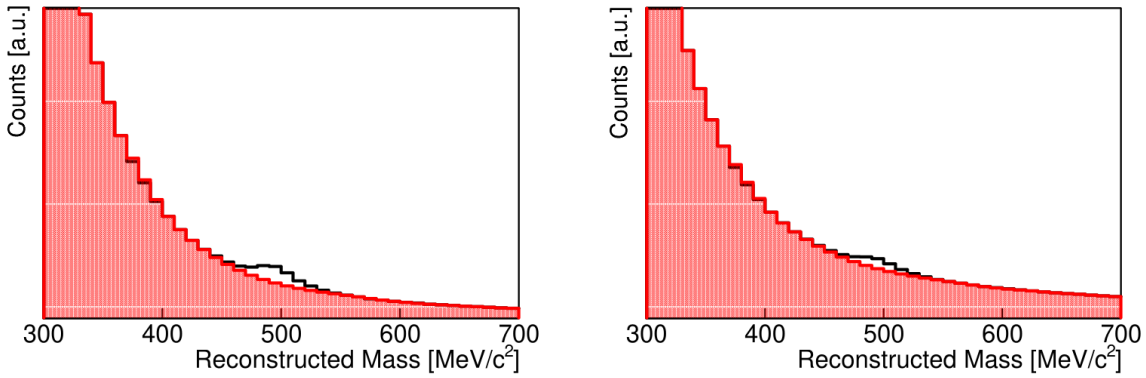

(a) $\chi^2_{RK} < 20$ and $\chi^2_{MM} < 0.2$ (b) $\chi^2_{RK} < 240$ and $\chi^2_{MM} < 1.6$

Figure 4.5.: Examplary mass distributions for the signal extraction of K^- for different cut-settings. Both spectra show integrated mass distributions of the polar angle region covered by the RPC detector.

In contrast, the integrated K^+ signal is more prominent, as it can be seen, e.g., in figure 4.17 where the reconstructed particle masses, multiplied by the sign of the particles' charge, are plotted after each applied selection criterion. Nevertheless, the cut-off criteria trends, estimated using the extracted K^+ signal, are consistent in both cases.

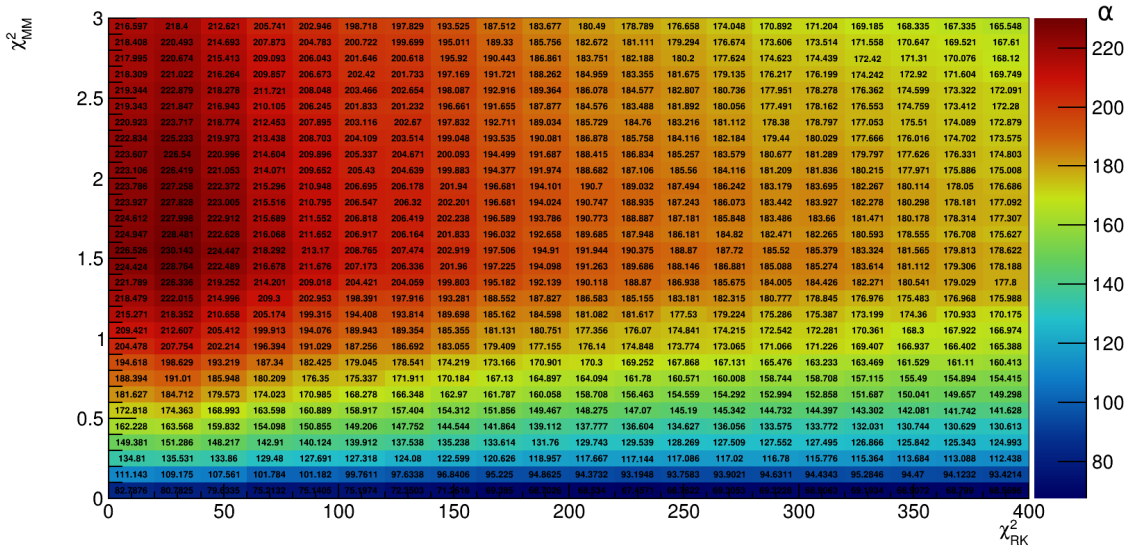

Figure 4.6.: Extracted K^- significance α in the χ^2_{RK}-χ^2_{MM}-plane in the polar angle region covered by the RPC detector. On the colour-coded z-axis, the significance of reconstructed K^- signals is depicted. The largest values are achieved for $\chi^2_{RK} < 150$ and $\chi^2_{MM} > 1.3$.

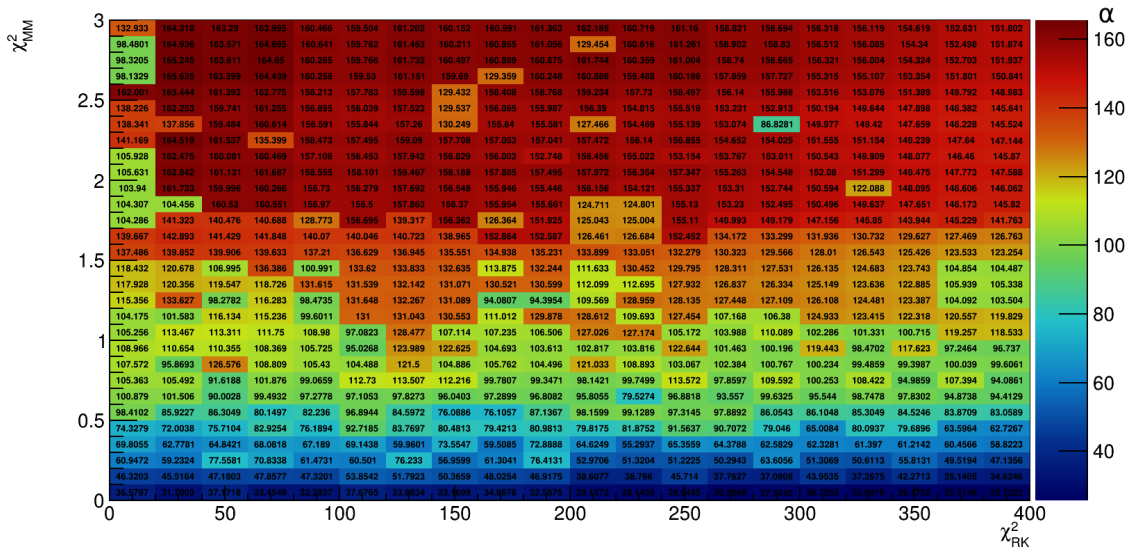

Figure 4.7.: Extracted K^- significance α in the χ^2_{RK}-χ^2_{MM}-plane in the polar angle region covered by the TOF detector. On the colour-coded z-axis, the significance of reconstructed K^- signals is depicted. The largest values are achieved for $\chi^2_{RK} < 150$ and $\chi^2_{MM} > 1.3$.

Comparison with Simulation

A comparison of parameter distributions from data and simulation, transported through the HGeant representation of HADES, is made to ensure that the charged track reconstruction efficiency is accurately modelled for the chosen cut parameters. This comparison of the integrated distributions of the χ^2_{RK} and χ^2_{MM} criteria between data and simulation is shown in figure 4.8. These distributions of all reconstructed track candidates in the RPC and TOF polar angle regions are plotted against the corresponding simulated distributions. Each simulated distribution is normalised to the integral of the data distribution. The data distributions prove to be wider in relation to the simulated ones. As the width of the track quality parameter distributions differs

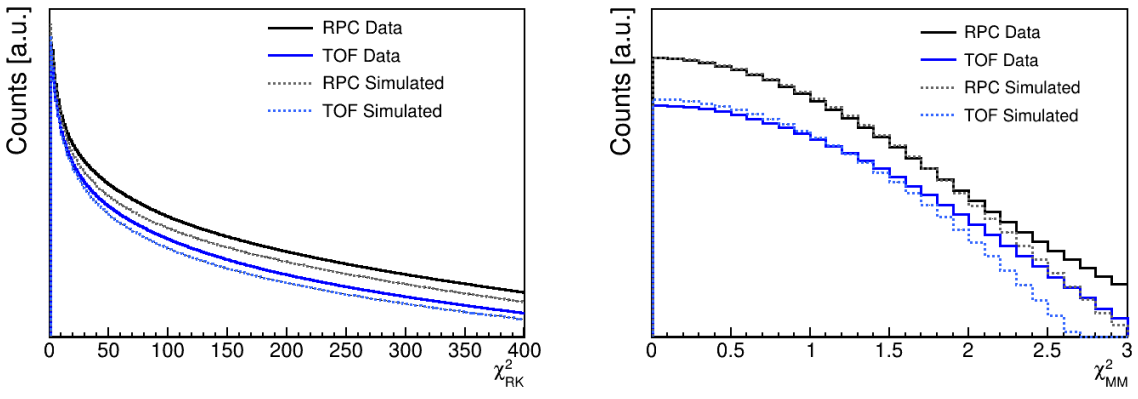

(a) χ^2_{RK} (b) χ^2_{MM}

Figure 4.8.: Integrated χ^2_{RK} and χ^2_{MM} distributions of all single particle tracks obtained for data and simulation.

between data and simulation, strict selection constraints will lead to systematic deviations. To

reduce the impact of the track selection criteria on, e.g., yield corrections, the track quality criteria cut-offs are set to the highest possible values without impairing the quality of the signal reconstruction.
To find a compromise between the quality of accepted track candidates and available statistics, the χ^2_{RK} and χ^2_{MM} deviations between data and simulation are, both for RPC and TOF, systematically compared using ratios. Initially, the simulated distribution is scaled by the ratio of the data distribution integral divided by the simulated distribution's integral. Then, a ratio R(x) is formed according to

$$\mathrm{R}(x) = \frac{\sum_{i=0}^{x} \chi^2_{i,\mathrm{Data}}}{\sum_{i=0}^{x} \chi^2_{i,\mathrm{Sim}}}$$

where x represents the number of the χ^2_{RK} or χ^2_{MM} bin. The results are filled into a new histogram, resulting in an asymptotic curve as displayed in figure 4.9. Here, one can see the

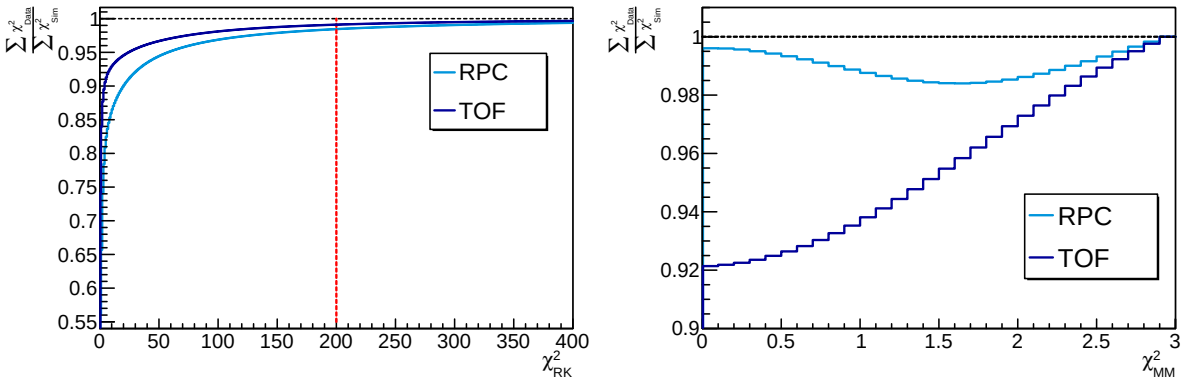

(a) χ^2_{RK} (b) χ^2_{MM}

Figure 4.9.: Saturation curves for the number of reconstructed particles dependent on the track quality parameter cuts.

distribution for the ratios between the integral of the number of tracks from data and simulation in the RPC polar angle region and the TOF polar angle region for each given observable. The horizontal black lines represent a ratio of one, while the red vertical line in figure 4.9(a) indicates the selected cut-off value of $\chi^2_{RK} = 200$.
In both cases visible in figure 4.9(a), RPC and TOF polar angle region, the deviation between data and simulation lies below 2% at $\chi^2_{RK} = 200$. The cut-off value also lies close to the χ^2_{RK} region for the crossover of the curves. In [125], and [99], systematic effects of $\approx$ 2-3% are observed for the corrected count rates of protons and charged pions which agrees with the observations from the presented saturation curves. As discussed in section 5.3.1, this is well below the systematic uncertainties arising from other sources. Consequently, it shows that a χ^2_{RK} cut-off at 200 is a reasonable compromise between significance and systematic bias within the acceptance $\times$ efficiency correction.
The distribution in figure 4.9(b) presents with a minimum for the RPC polar angle region between $1 < \chi^2_{MM} < 2$. Furthermore, the ratio for the TOF polar angle region reaches 98% around a value of $\chi^2_{MM} \approx 2.5$. Taking into account the significance distribution as a function of χ^2_{MM} and χ^2_{RK}, as shown in figures 4.3 and 4.4, a cut-off at a χ^2_{MM} value of 3 is justified to minimise a bias due to track quality selection criteria.

4.1.3. MDC Specific Energy Loss Constraints

The relation between energy loss and momentum of a particle is used as an additional selection criterion, leading to an increase in the signal-to-background ratio and the significance of the $K^{\pm}$ signal when applied. The energy-loss-momentum correlation of particles appears as a band, which can be seen as exemplary in figure 2.14.
Constraints on the specific energy loss can be realised in two ways. One is given by the exclusion criterion, which discards all track candidates in a certain area of the energy-loss-momentum-plane. The other possibility is an inclusion criterion, which only accepts track candidates in a certain area in the energy-loss-momentum-plane. The latter is mainly used for abundant particles, which can be well separated from one another. In figure 2.14, where the MDC specific energy loss of all positively charged particles of mass $200 < M < 800$ MeV/c^2 within the RPC polar angle region is plotted, it can be seen that this is not the case for the $K^{\pm}$. The available statistics and widths of the proton and $\pi^{\pm}$ distributions do not allow for a clear separation of the particles at momenta higher than 600 MeV. As a consequence, the first approach is chosen. The $\pi^{\pm}$ constraint was developed in the scope of [99]. The proton distributions were analysed in the scope of [125].
The MDC-specific energy loss constraints are determined as follows. First, subsamples are created from the available data. To this purpose, all positively charged track candidates within 740 and 1140 MeV/c^2 (proton candidates) are filled into the energy-loss-momentum-plane. Respectively, all track candidates with a mass lower than 500 MeV/c^2 ($\pi^{\pm}$ candidates) are filled into the energy-loss-momentum-plane. Next, momentum slices are defined, in which an integrated projection for the MDC-specific energy loss is stored. The distributions of each slice are then fitted with a logarithmic asymmetric Gaussian fit function as used in [125]:

$$f(x) = C \cdot \exp\left(\frac{(\log(x)-\mu)^2}{2(\Theta_1(\mu-\log(x))\sigma_L + \Theta_0(\log(x)-\mu)\sigma_U)^2}\right) \tag{4.1}$$

Here Θ denotes the Heaviside step-function

$$\Theta(x) \equiv \int_{-\infty}^{x} du\delta(u) = \begin{cases} 1 & \text{, for x>0} \\ 0 & \text{, for x<0} \end{cases}$$

and σ_L and σ_U are the lower and upper values for the standard deviation. Figure 4.10 (a) shows an example of a fit to an energy loss distribution in a momentum slice for the π^-. After applying the fits for all slices over the reconstructable momentum range, a 2-dimensional representation in the energy-loss-momentum-plane can be extracted. Figure 4.10 (b) shows the resulting 2-dimensional MDC specific energy loss cut for the π^- as a black line for an interval of $\pm 1.5\sigma$.
The same procedure is performed for protons, with the result displayed in figure 4.11. The black lines correspond to the $\pm 1\sigma, 2\sigma$ and 3σ intervals around the arithmetic mean μ. Around a specific energy loss value of $\approx 10^5$ MeV cm^2/g horizontal structures are visible in these distributions, which is an artifact of an applied upper limit (100000 MeV cm^2/g) for the calculation of the energy loss from the measured signal. All specific energy loss values higher than that are truncated at this limit. However, comparisons show that this region is mainly relevant for the analysis of light nuclei [125].
As the specific energy loss over momentum regions of protons, $K^{\pm}$ and $\pi^{\pm}$ overlap for most of the momentum range, only track candidates within a 1σ range of both presented fits are excluded. To illustrate the impact of the overlap on the track selection process, figure 4.12 displays the MDC-specific energy loss over momentum distribution for all particle tracks of positive charge with a reconstructed mass between 200 and 800 MeV/c^2 for the RPC polar angle region. The blue lines frame the $\pm 1\sigma$ regions around the arithmetic mean of the distributions of protons

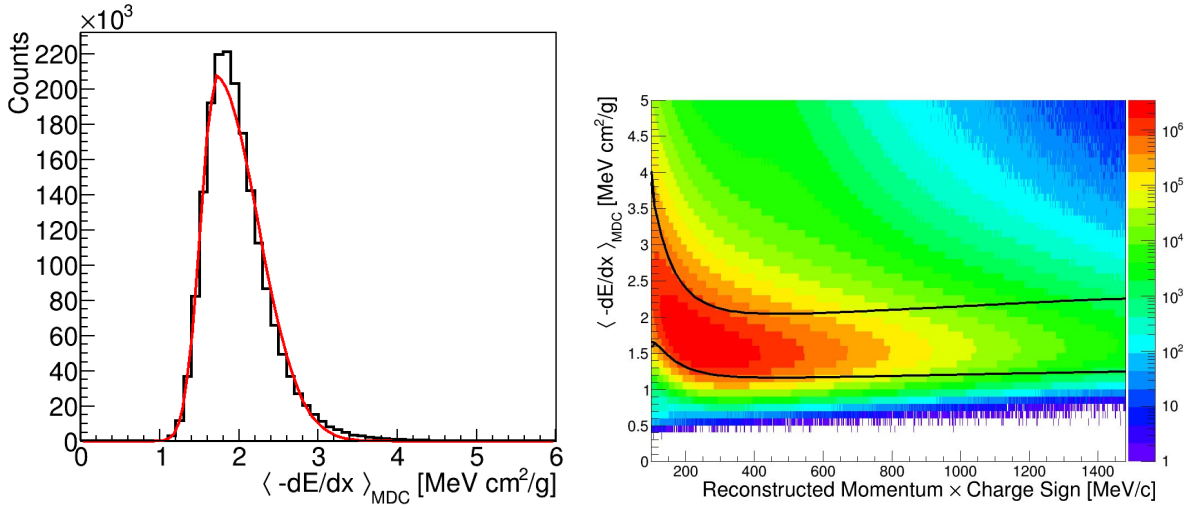

(a) (b)

Figure 4.10.: Exemplary momentum slice ($160 < p < 180$ MeV/c) of the π^- MDC specific energy loss distribution in the TOF polar angle region and the applied asymmetric Gaussian fit function (red) [100] are shown. Finally, (b) shows the resulting 2-dimensional energy loss constraint for a 1.5σ interval [99].

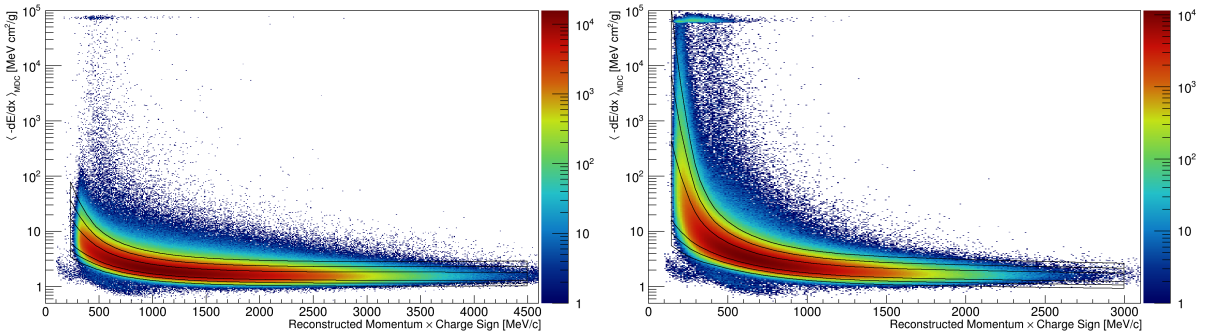

(a) RPC (b) TOF

Figure 4.11.: MDC specific energy loss over momentum distributions for the preselected proton sample in the polar angle region for RPC (a) and TOF(b) with the resulting fit obtained from the momentum slices [125].

and π^+, which are excluded after applying the cut. The black line shows the theoretical Bethe Bloch curve for the K^+.

The benefits of this selection for the stability of the count rate extraction for charged Kaons are presented and discussed in section 4.1.7. Furthermore, section 5.4 discusses the extraction of inverse slope parameters. Without the MDC dE/dx criterion, this extraction proved unreliable. The impact of this cut on the integrated single particle mass spectrum is shown in figure 4.17. The application of the MDC-specific energy loss constraint suppresses the tails of the p and $\pi^\pm$ mass distributions, enhancing the K^+ signal.

The application on simulated data is performed in the same manner as for measured data. By querying the particle species, a pure sample is generated. Correspondingly, the MDC-specific energy loss vs momentum correlation is fitted in the same way it is done for data. The resulting exclusion regions are applied to the simulated data to emulate the loss in the count

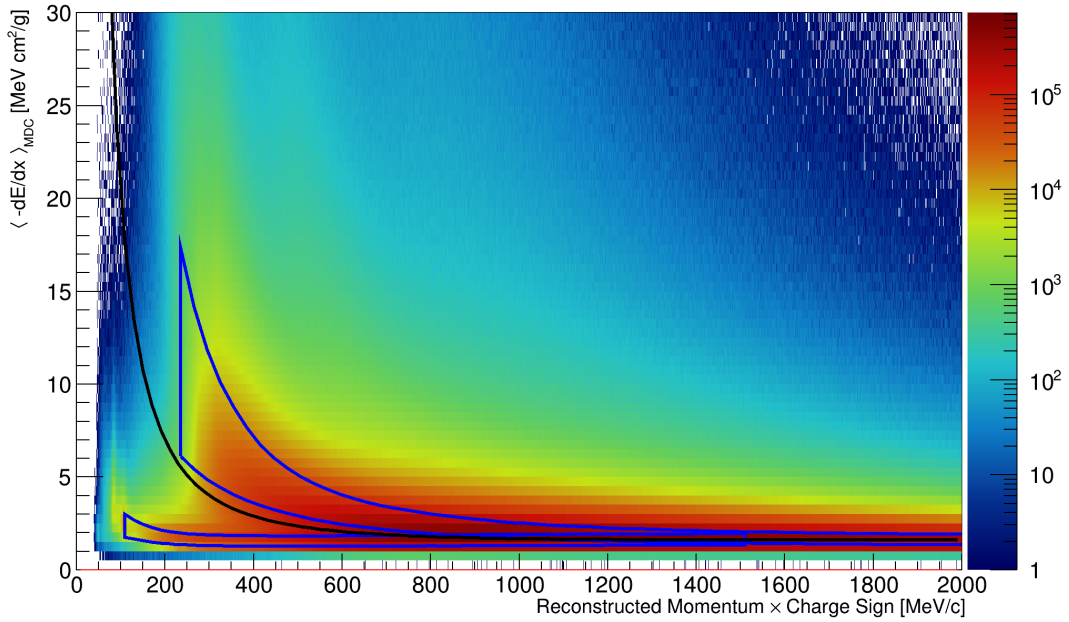

Figure 4.12.: MDC dE/dx over momentum distributions for particle tracks of positive charge with $200 < M < 800$ MeV/c^2. The blue boxes represent the proton and π^+ energy loss exclusion cuts, while the black line denotes the Bethe Bloch curve for the K^+.

rate experienced in measured data due to the applied constraint. This information is used to correct the final particle production yields for corresponding reconstruction efficiency losses.

4.1.4. TOF Specific Energy Loss Constraints

As introduced in section 2.2.5, the TOF detector also measures the specific energy loss of charged particles. Figure 4.13 shows the specific energy-loss-β-plane of all negatively charged particle tracks with a hit in the TOF detector. Within the area framed by the black line, a distribution is visible, which deserves further discussion.
As analogously found in [119], the distribution can be identified as unphysical, as the observed energy loss corresponds roughly to that of a proton. At a centre of mass energy of 2.55 GeV, the production of an antiproton is, however, not expected as the excess energy for the process in individual NN interactions is

$$\sqrt{s_{\mathrm{exc}^{p\bar{p}}}} = \sqrt{s} - \sqrt{s_{\mathrm{thr}^{p\bar{p}}}} = 2.55\ \mathrm{GeV} - 3.75\ \mathrm{GeV} = -1.20\ \mathrm{GeV}$$

with

$$\sqrt{s_{\mathrm{thr}^{p\bar{p}}}} = 4 \cdot m_{\mathrm{Nucleon}} \cdot c^2\ .$$

Here, $p\bar{p}$ has to be produced as a pair to conserve the baryon number. As this excess energy is about four times larger than the excess energy for the production of a K^- or $\phi(1020)$-meson, it should be highly suppressed in comparison, if at all present. However, as it is shown in section 4.1.7, the contribution from this region is in the order of magnitude of the contribution by the K^- to the spectra. Furthermore, as also shown in section 4.1.7, this region quite precisely encapsulates a region which can be associated with a set of reconstructed particle candidates with a wrong time of flight information. Consequently, the area framed by the black line in figure 4.13 is removed from the data sample for negatively and positively charged particles, where the

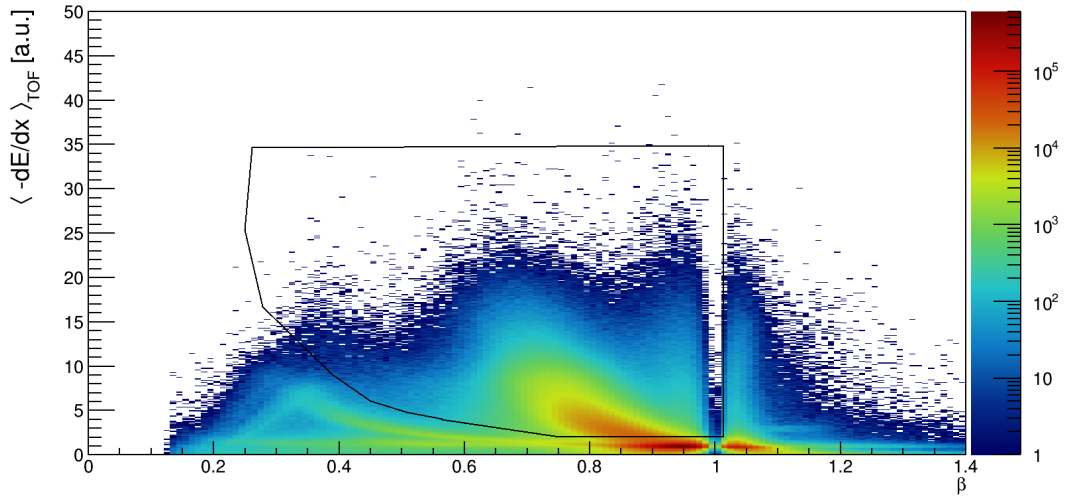

Figure 4.13.: TOF specific dE/dx plotted against particle β for all negatively charged particles.

same effect is observed.

Comparison with Simulation

Figure 4.14 shows the simulated TOF energy loss distribution of negatively charged particles as a function of β. The same graphical cut area is plotted as in the data. One can identify the energy loss band for the minimum ionising K^- and π^-, while no unphysical structure is visible for $0.7 < \beta < 1$. Even though this contribution is not adequately reproduced, the same cut as for data is applied during the selection process to quantify the impact on the $K^{\pm}$ reconstruction efficiency, for which the extracted count rates are corrected.

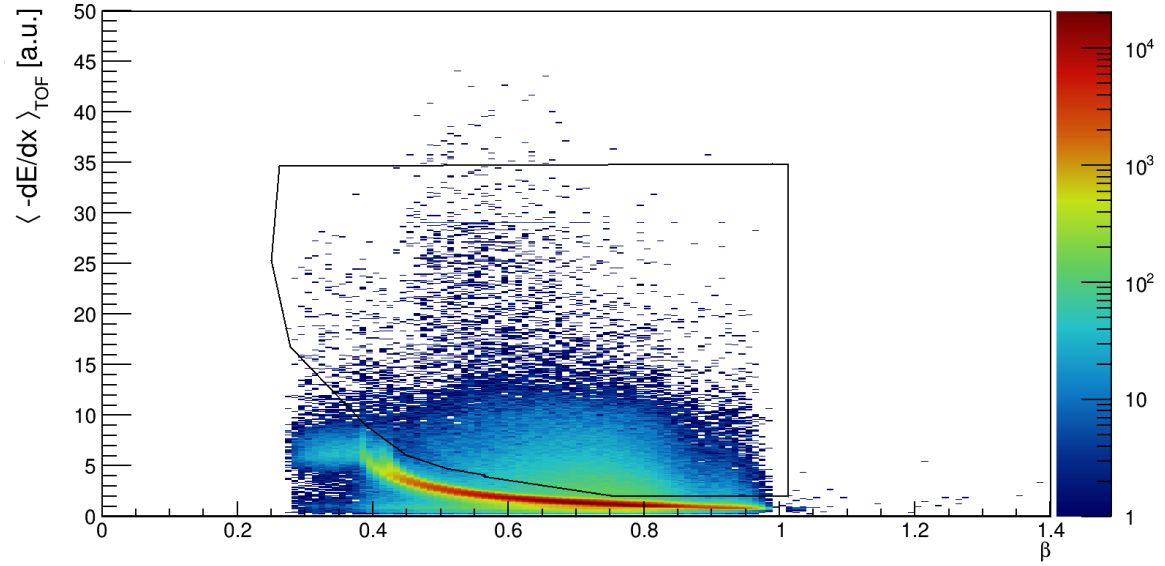

Figure 4.14.: Simulated TOF specific dE/dx plotted against particle β for all negatively charged particles.

4.1.5. Lower Momentum Cut-Off

In figures 4.15 and 4.16, the momentum of all track candidates is plotted over the mass multiplied by the particles' charge sign, each for the RPC and the TOF polar angle regions. At momenta below 200 MeV/c, for masses below 700 MeV/c^2, several horizontal distributions of constant momentum and varying mass can be observed. However, the track candidates contained within these low momenta distributions are at the edge of being reconstructable, which indicates that there is no valuable information to this analysis contained within.

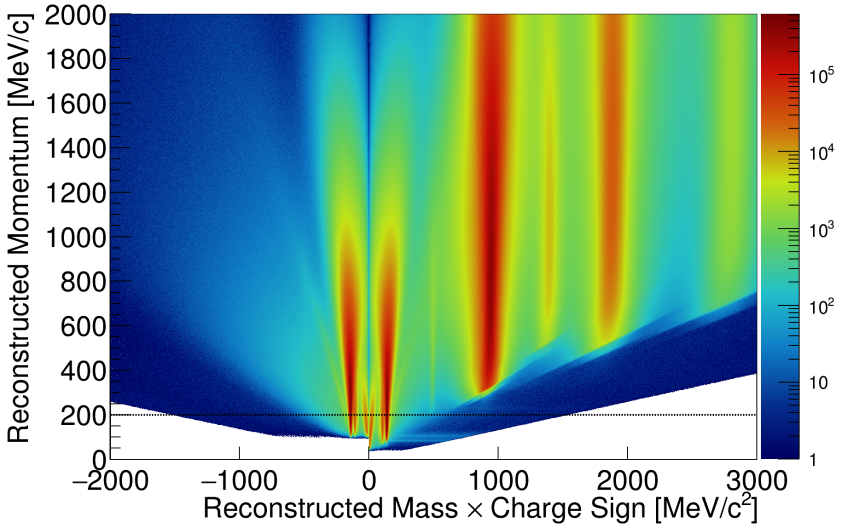

Figure 4.15.: Momentum over mass × charge in the polar angle region of RPC. Particle tracks with a momentum of $p < 200$ MeV/c are rejected as this region is dominated by background.

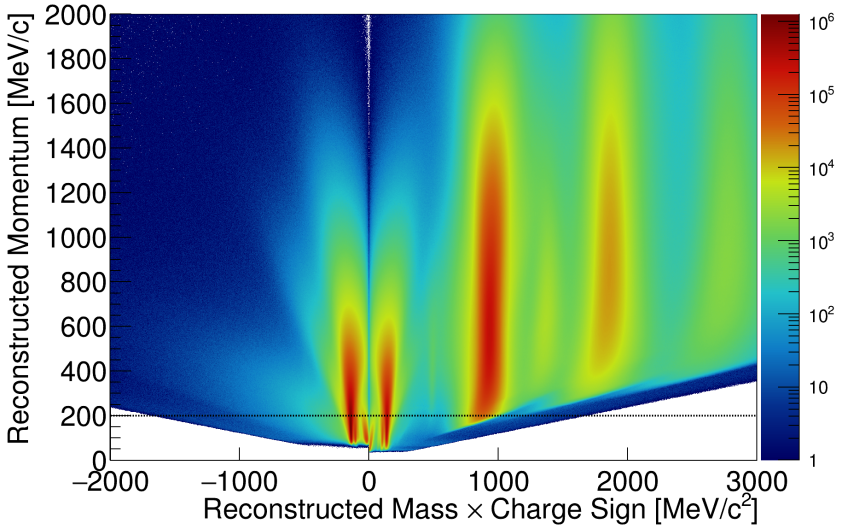

Figure 4.16.: Momentum over mass × charge in the polar angle region of TOF. Particle tracks with a momentum of $p < 200$ MeV/c are rejected as this region is dominated by background.

Consequently, a low momentum cut-off at $p = 200$ MeV/c is applied to suppress those tracks with unphysical mass features. The value of $p = 200$ MeV/c was chosen, as for $p \approx 250$ MeV/c, the $K^{\pm}$ count rates become significant within the integrated mass distribution and to prevent

an influence on the multidifferential phase space reconstruction.

4.1.6. Impact of the Presented Selection Criteria

To visualise the impact of the presented cut criteria on the integrated mass spectrum, figure 4.17 displays the effect of each criterion step by step. This visualisation was created with a subset of 2.45×10^6 events. A summary of all selection criteria can also be found in table 4.2. The χ^2_{RK} and χ^2_{MM} criteria are presented as one combined criterion, as the removal of track candidates with $\chi^2_{MM} > 3$ is already performed in the scope of the preselection introduced in section 3.6.2.

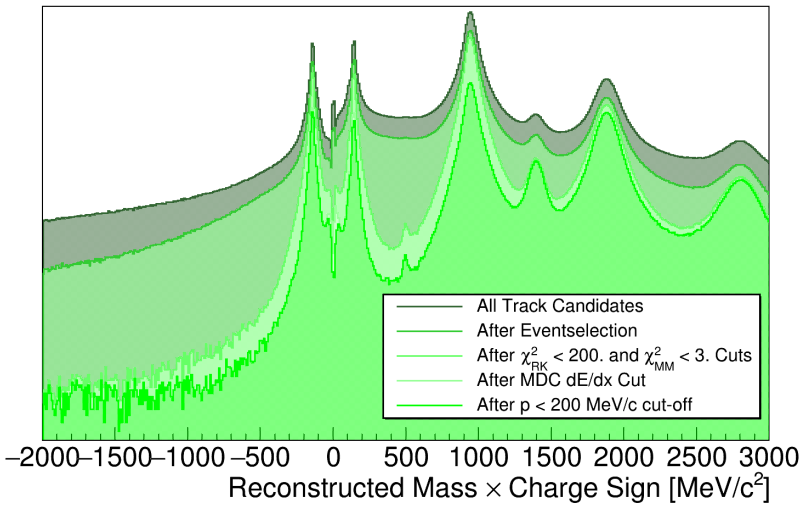

(a) RPC

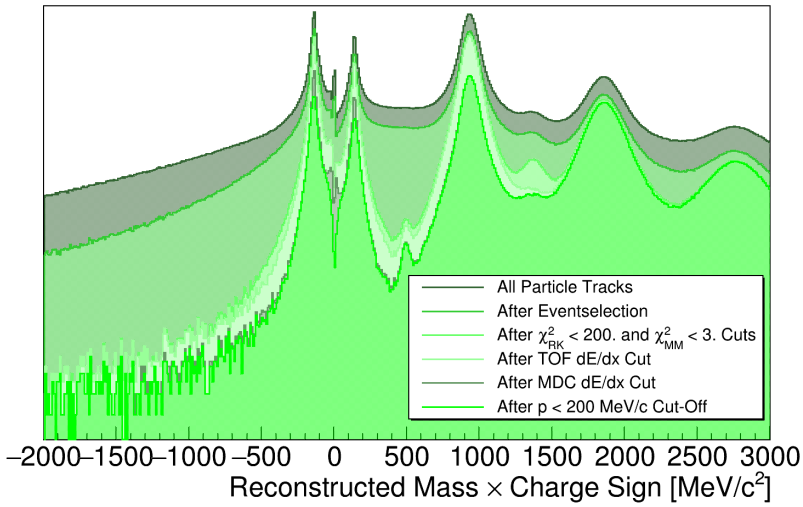

(b) TOF

Figure 4.17.: Impact of the different event and track selection criteria previously presented onto the global data sample of tracks in the polar angle region for RPC (a) and TOF(b).

The K^+ signal around the nominal mass of approximately 494 MeV/c^2 [141] becomes more prominent with each selection step, while an apparent suppression of the background is visible. The K^- peak is not visible in this representation, as the statistics in the corresponding mass ×

charge sign area are too low for the chosen amount of events. In the momentum-mass × charge-sign-plane of figures 4.15 and 4.16, which were created with the entire available statistics, the K^- distribution is visible around the nominal mass for negative charges. In the same figure, a structure with a slight inclination, emerging from the $\pi^{\pm}$ distributions, is prominently visible. This structure is also visible in figure 4.13, which is suppressed by the presented exclusion cut. The possible origin of the contribution is discussed in the following section.

4.1.7. Investigations Concerning a Systematic Time Offset

In the Au+Au data taken in 2012, a structure in the momentum-mass distribution of charged particles [119][122] was observed, which could not be seen in GEANT simulations. The hypothesis was that a wrong matching between a π-META-signal and a p track caused a shift in the reconstructed flight time of the particle. As shown in figures 4.15 and 4.16, the contribution is also observed in the present dataset. This phenomenon directly impacts the multidifferential analysis of the K^- and the ϕ-Meson. Therefore, further investigations are performed.

Using equation 3.8, the direct dependence of the reconstructed mass on the measured time of flight becomes apparent:

$$m = p \cdot \sqrt{\frac{1}{(\frac{s/t}{c})^2} - 1} \tag{4.2}$$

Consequently, the effect can be reproduced in simulation by applying an offset in the time of flight to all charged pion tracks in a preselected subsample. In figure 4.18, a time offset of 2 nanoseconds is chosen for a sample of $\pi^{\pm}$-candidates, selected via a $\mu \pm 2\sigma$ mass-constraint, reproducing this systematic shift qualitatively. A second inclined branch can be seen towards lower masses, which comes from muons which fall into the accepted mass range of the applied cut. The time value to reach accordance between the artificially shifted pions and the ones contained in the data lies around 1.3 ns.

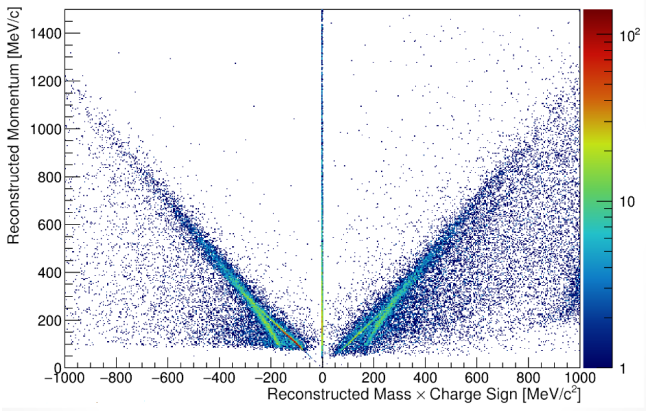

Figure 4.18.: Correlation between momentum and mass × charge for a sample of $\pi^{\pm}$-candidates with a time of flight offset of 2 ns assigned.

To test the idea of an incorrect matching proposed in [119], the assignment of tracks and META hits within the HParticleTrackSorter routine are investigated. As explained in section 3.6.1, a particle candidate contains several track segments and one META hit. Different particle candidates can share the same reconstructed track segments as candidates for the individual META hits. This can lead to two conflicting cases:
Several META hits can be matched to the same track segment, which results in a competition of these hits for the same track segment and a possible incorrect assignment.
Also, several track segments can compete for the same META hit and, within detection accu-

racy, fulfil the selection criteria equally, leading to an incorrect assignment.

Consequently, all particle candidates within one event, sharing the the same META hit, as well as all particle candidates sharing the same track segments for different META signals, are removed. If one (or both) of the possibilities of wrong assignment are causing the structure, it should be suppressed relative to the K^- signal when those particle candidates are removed from the data sample. The momentum range of $500 < p < 600$ MeV/c is chosen for this investigation so that the unphysical structure distribution (left) and the K^- (right) peaks are well separated, as it can be seen in figure 4.19. Here, the red curve represents the interpolated background distribution, while the black line represents the data.

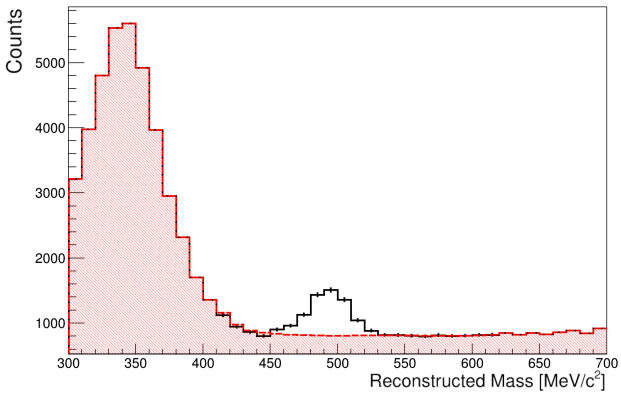

Figure 4.19.: Mass distribution in the RPC polar angle region for negatively charged particle candidates within the momentum range from 500-600 MeV/c. The peak around 350 MeV/c^2 originates from the discussed structure. See text for details.

The results for a comparative count rate extraction of the background source and the signal are presented in table 4.1.

	Structure		K^-	
	S/B	**Significance**	**S/B**	**Significance**
Standard	0.469 ± 0.004	427.9 ± 3.4	0.159 ± 0.003	92.1 ± 1.8
No competing hits	0.649 ± 0.007	$408,4 \pm 4.1$	0.263 ± 0.005	98.2 ± 1.9
No competing tracks	0.451 ± 0.006	244.7 ± 3.2	0.131 ± 0.004	42.9 ± 1.2

Table 4.1.: The Signal-to-Background ratio and Significance for the unphysical structure in comparison to the K^- in the momentum interval of 500 to 600 MeV/c in RPC. All provided uncertainties are statistical.

Any suppression attempt results in a comparable loss between the structure and the K^- signal. This leads to the statement that there is no evidence supporting the hypothesis of a random mismatch between a track and a hit at the META detector.
Taking into account the discussion from section 3.5.2 about a background contribution from inefficiencies in the t_0 reconstruction, one could consider explaining the time offsets by event-wide time of flight offsets due to a wrong starting time. However, as discussed in this same chapter, this effect does not produce a narrow and constant time-offset. Furthermore, should the unphysical structure then be significantly less prominent in later days of the beamtime, which is not observed. Additionally, for events with a particle candidate in the region of the unphysical structure, there exists no correlation with time-offsets for other reconstructed particle candidates. This indicates an effect which only affects individual particle candidates of an event.

The constraint on the specific energy loss measured with the TOF detector, introduced in section 4.1.4, proves to be a criterion of high suppression power for this structure. The background

contribution is primarily included in the exclusion region indicated in figure 4.13. Figure 4.20 shows the momentum over mass distribution for negatively charged particles in the TOF polar angle region around the nominal K^- mass - once without the selection criteria and once with the exclusion criteria applied. For the case of the applied cut, the K^- distribution is visible, while the overlapping background is nearly entirely suppressed.

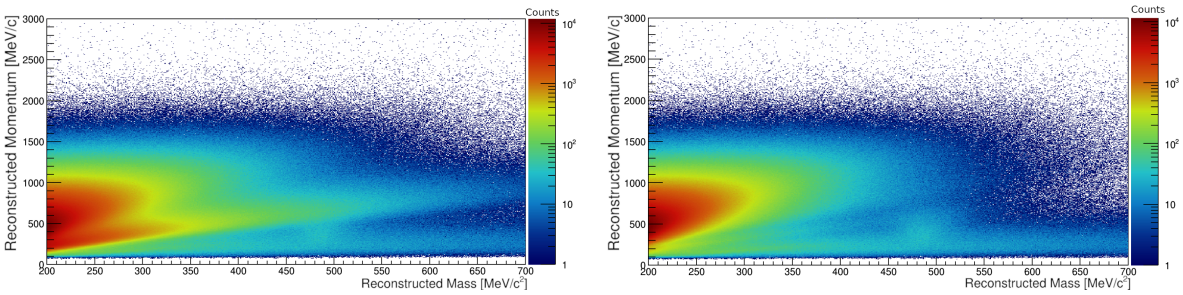

(a) No TOF dE/dx exclusion

(b) With TOF dE/dx exclusion

Figure 4.20.: Distribution of momentum over mass around the nominal K^- mass without (a) and with (b) TOF energy loss exclusion criterion. See text for further details.

The energy loss distribution for this background in figure 4.13 coincides with the values one can find for protons. Furthermore, the distribution is systematically shifted towards higher β, calculated from the reconstructed time of flight of the track and its length. This hints toward a particle track with an approximate proton m/q-ratio and a systematically reduced time of flight, though a random combination of a π^- hit with a proton track has been excluded as a cause. One possible assumption is, therefore, a neutron hit signal overlapping with one from a $\pi^\pm$ track intersecting the same META cell.
Previous studies show a possible detection rate of 10^{-3} to 10^{-2} neutrons per event for the META detector [82]. Though this does not allow for an estimation of the coincidence rate necessary to produce this effect, it coincides well with the observed relative counting rate of the structure compared to the K^-. Consequently, the following working hypothesis is formulated:
Initially, a traversing charged pion excites the scintillation material along the track, which results in the emission of a light pulse. While this light pulse travels to the attached PMTs on both ends of the rod, a neutron reacts with the material close to the current location of light propagation. This causes another signal which overlaps with the pion light-pulse. As the neutron signal has a reduced rise time in the PMT compared to the pion signal, on one side, only the neutron signal is registered, while on the opposing side, the original charged pion signal is detected.

The delay arising from the time a signal pulse needs to surpass the detection threshold indicated on the intensity pulse sketch on the right side of figure 4.21 is called the *timewalk effect*

$$\Delta t_{\text{timewalk}} \propto \frac{\text{const.}}{\sqrt{\frac{\text{dE}}{\text{dx}}_{\text{particle}}}} \tag{4.3}$$

with the constant having a value between 2.5 and 3 ns [131]. This is corrected in the detector calibration procedure to remove the delay in the signal detection and, consequently, a prolongation of the measured time of flight. The sum of the total registered charges at the PMTs on both sides of the rod is used to calculate the particle candidates' energy loss $\frac{dE}{dx}$. Due to the pulse overlap on one side, a systematically higher energy loss than the true $\pi^\pm$ energy loss is calculated, which leads to an under-correction of the rise time and an overestimation of the $\pi^\pm$

time of flight. In figure 4.21, the formulated working hypothesis is depicted for the case of a TOF scintillator rod.

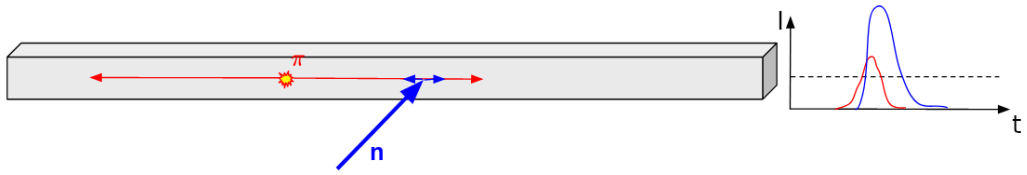

Figure 4.21.: The overlap of a pion signal by a neutron signal in the same TOF rod causes a too high reconstructed specific energy loss and thusly an under-correction of the time walk effect. For more details, see the text.

As the length of a TOF rod varies between 1 m and 2 m, [77], there should be a maximum coincidence time window of about 0-3 to 0-6 ns for the light propagation in the most inner rods and 0-6 up to 0-12 ns for the most outer rods for the neutron to arrive after the pion reacted with the detector. As a typical proton time of flight is about four ns longer than an average pion time of flight [131], it is reasonable to expect a similar time of flight for a neutron. Both time windows are, therefore, well in agreement.

To obtain an estimate whether this hypothesis can explain the observed multiplicities of the structure, a simplified first-order estimation can be made. For the $0-10\%$ most central Ag(1.58 A GeV)+Ag collision events the average number of participating nucleons per collision is $\langle A_{\text{part}} \rangle|_{0-10\%} \approx 161$, which translates into 71 protons and 90 neutrons. Assuming, that protons and neutrons form light nuclei in the same rate of $\approx 30\%$, this leaves 63 free neutrons emerging from the collision zone. Assuming the geometrical acceptance of protons ($60-85\%$ [125]) and taking into account the average neutron detection efficiencies of $\approx 2\%$ for TOF and $\approx 1\%$ for RPC [82], one can conservatively estimate a hit detection probability for a produced neutron of $\approx 0.8\%$.
The probability for a proton hitting the same TOF rod as a π^+ within the required coincidence interval can be estimated from simulations. Even though GEANT simulations do not directly reproduce the observed effects, as the time walk effect is not included, it is possible to emulate the effect with a coincidence requirement. A coincidence between a proton and a pion hit in the same TOF rod within the given time interval is queried manually for a simulated track candidate to be classified as resulting in such a contribution. The ratio is formed between all pions fulfilling the coincidence conditions and those overall reconstructed as a function of event multiplicity.
Similarly, in data, the number of particles within the contamination region highlighted in figure 4.13 is divided by the number of charged pions and plotted against the event multiplicity in META. Figure 4.22 shows the ratio distributions for data (a) and simulation (b). It can be observed that the overall shape of the distributions is in good agreement. However, a difference of a factor of ≈ 2 can be identified for the obtained ratios.
Correspondingly, the probability for a proton hitting the same TOF rod as a π^+ within the required coincidence interval is $\approx 0.4\%$ for the $0-10\%$ most central collisions. Using the fact that the number of protons and neutrons is nearly identical, assuming a comparable coincidence rate and multiplying this value with the 0.8% detection probability for a neutron leads to a final $n-\pi$ coincidence probability of 0.0032% or $3.2 \cdot 10^{-5}$. From this, multiplied with 63 free

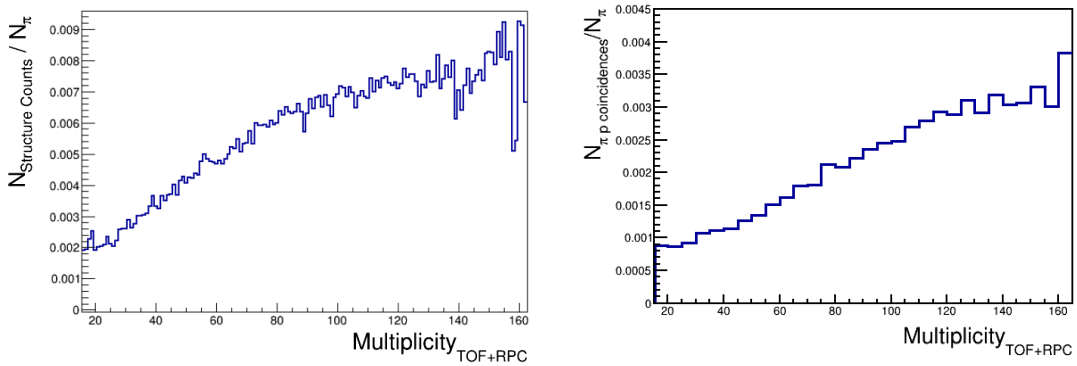

(a) Data (b) Simulation

Figure 4.22.: Relative abundance of the unphysical structure in relation to the charged pion abundance as a function of event multiplicity [131]. Case (a) is extracted from measured data via the TOF energy loss constraint. For simulations (b), this effect was emulated by using pion signals which coincided with a proton in the same TOF rod.

neutrons per event, one would estimate this effect to result in $\approx 2 \cdot 10^{-3}$ structure contributions per event. The amount of reconstructed K^- for the $0-10\%$ most central collisions, without corrections, is found to be $\approx 5.3 \cdot 10^{-5}$ per event. If one interpolates the background under the structure peak as visible in figure 4.19, and the K^- signal and, for both, sums over the bins within a range $\mu \pm 2\sigma$ around the arithmetic mean, a difference in count rate of more than one order of magnitude is observed. Taking into account, that the detection rate of this structure is only roughly estimated and neutron detection efficiencies vary as a function of momentum, this hypothesis can be assumed as a realistic possibility. Furthermore, the estimation for the structure does not take into account, that not every signal can be reconstructed in data due to the background from and the overlap with the $\pi^{\pm}$ mass distributions towards low reconstructed momenta in the laboratory frame of reference. Also, not every potentially coinciding pion track passes the selection criteria and not every K^- signal within acceptance can be reconstructed, due to the significant background. It is, however, difficult to quantify these individual contributions.
In $10-20\%$ most central collisions, ≈ 45 free neutrons are produced per event. With the same geometrical acceptance as above, as well as the detection efficiencies and a coincidence probability of 0.3%, an expectation value of about $1 \cdot 10^{-3}$ structure entries per event is obtained. The amount of reconstructed K^- in this collision centrality interval, without corrections, is about $\approx 3 \cdot 10^{-5}$.
Going to $20-30\%$ most central collisions, ≈ 32 free neutrons are produced per event. Taking into account the same geometrical acceptance as above, as well as the detection efficiencies and a coincidence probability of 0.2%, an expectation value of about $5 \cdot 10^{-4}$ structure entries per event is obtained. From the K^- data $\approx 2 \cdot 10^{-5}$ can be reconstructed per event without applying any corrections.

Hence, as both show a similar scaling behaviour, a similar dependency of the structure count rate compared to one of the charged Kaons as a function of collision centrality in data would support the hypothesis of an effect caused by multiple consecutive hits. For this comparison, the same momentum range as in figure 4.19 is used and the interpolation is performed under the structure as well as the K^- peak. Afterwards, the interpolated background is subtracted and the resulting peaks are fitted with a Gaussian function in order to determine the width σ

and mean μ of each distribution. For both peaks the sum over the bins within a range $\mu \pm 2\sigma$ is formed. This is done for each interval in collision centrality.
When comparing the count rates of the structure and the K^- as a function of collision centrality, one observes the following behaviour: Between the intervals of 0-10% and 10-20% most central events, a count rate decrease of $\approx (25 \pm 2)\%$ is observed for both. Going to 20-30% most central events, another drop of $\approx (19 \pm 1)\%$ can be seen for both distributions. Consequently, the trend of the extracted count rates as function of collision centrality confirms the previously formulated hypothesis. However, it has to be emphasised that a definite conclusion on neutrons as a source of this effect can only be reached by directly identifying individual pion-neutron coincidences in events with this signature. HADES is not equipped for such measurement at this stage.

To demonstrate the influence of the currently applied time walk correction on the data, the energy loss of all negatively charged particles in the TOF region is plotted over the ratio between the applied time walk correction with the reconstructed specific energy loss ($t_{\text{twc, dE/dx reconstructed}}$) and the time walk correction determined for a charged particle with $\pi^\pm$ mass to charge ratio ($t_{\text{twc, dE/dx } \pi^\pm}$). As the negatively charged tracks are predominantly π^-, the ratio distribution is expected to have a mean at or close to one for a successful correction. Figure 4.23 depicts the distribution obtained from 10 million data events. The red curve represents the fit on the time walk correction ratio.

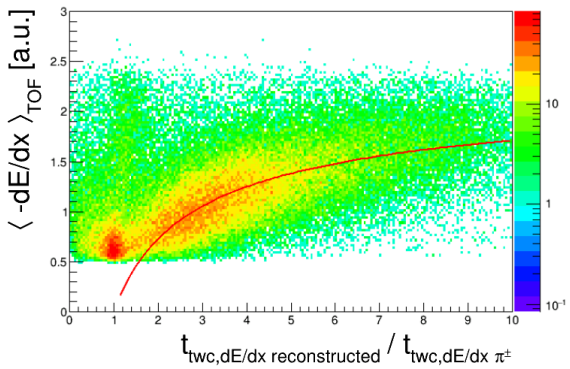

Figure 4.23.: TOF specific energy loss over the ratio between the applied time walk correction and the time walk correction of a charged pion [131]. The strong deviation from 1 shows that many tracks are corrected inaccurately.

The distribution with a time offset is a significant contribution, deviating strongly from the expectation value. Furthermore, the reconstructed energy loss lies higher than the π^- energy loss. This shows, that there exists a set of negatively charged particle tracks which obtain a too small timewalk correction, which ultimately also supports the $n-\pi^\pm$-coincidence hypothesis.

For the differential analysis in the following sections, the unphysical structure is the limiting factor for the K^- count rate extraction beyond 600 MeV/c momenta in the laboratory frame of reference, as a reliable count rate extraction becomes impossible in most cases. The overlap of the signal and the introduced background contribution biases the extracted count rates. Figure 4.19 depicts an example for a K^- signal which is not extractable due to the described problem.

To summarise the presented investigations regarding the $\pi^\pm$-tracks with a systematic time of flight offset, the final conclusion regarding the origin remains not conclusively answered. While the $n - \pi^\pm$-coincidence hypothesis appears to be confirmed by many observations, still several questions remain open at this point in time. On one side, the difference of one order of magnitude between the calculated background contribution and the extracted one is not fully accounted for, even though many possible explanations exist. Simulations containing a timewalk effect emulation could result in more realistic estimations as it would allow for a direct comparison between simulation and data and would directly show if this reproduces the observed effect in

the simulated single particle spectra.
Secondly, the factor two between figure 4.22(a) and figure 4.22(b) is not understood. While the selection from data naturally contains additional background in addition to the structure, it certainly does not account for the entire difference. While the slope shows the same scaling behaviour as a function of with RPC and TOF detected event multiplicity for both cases, this will have to be investigated in further analyses.
Another point for discussion are further contributions to the effect due to knock-out reactions in a crossbrace in front of TOF-module four. It has been observed, that the count rate of the structure extracted from data is enhanced in module four and GEANT simulations for the production of secondary particles within the detector material show a significant activity for this crossbrace. This way, also knocked-out protons could create a META hit. However, detailed investigations in this direction are still to be performed.

All investigations shown above are performed with the help of the TOF detector. However, there is no observable available for the RPC detector with a comparable separation power. Thus it can only be assumed that an analogous process is also happening in the RPC detector. A final conclusion might be possible in future planned Au+Au beamtimes at lower energies, where ECAL enables for full coverage in the RPC polar angle region and could possibly confirm coincidences between the structure and neutron hits.

4.1.8. Multidifferential Analysis

The multidifferential charged Kaon production rate per event is extracted in a 2-dimensional $(m_t - m_0) - y$ grid. Alternatively, using p_t in the transverse direction is also possible. Due to the limited phase space coverage of the $K^{\pm}$ and the low statistics compared to most other charged particle species (e.g. $\pi^{\pm}$,p), $(m_t - m_0)$ proved to be the most stable observable for the later fitting procedures. For further information on the kinematic observables see section 1.2.2. The grid interval widths in rapidity and transverse mass are chosen differently for K^+ and K^-, as the covered phase space and the available statistics differ. The final choices for the interval widths are presented in table 4.2.
For each grid interval, a mass histogram for RPC and TOF polar angle region is filled separately. It contains all charged Kaon candidates accepted after the applied criteria summarised in table 4.2. The separation into TOF and RPC region is due to the different time resolution of both detectors resulting in wider mass distributions for TOF compared to RPC. Consequently, the resulting mass spectra for both detectors have to be treated with different parameterisations for the interpolation algorithm. Furthermore it allows for a more differential quality assurance for the signal extraction procedure.
For each K^+ mass spectrum a range between 200 and 800 MeV/c^2 is considered. For the K^- only a mass range between 300 and 700 MeV/c^2 has to be used. This is done, as the K^--statistics is much lower, which results in a smaller mass range necessary to guarantee stable background estimations.
The background of each mass spectrum is individually estimated by the interpolation method introduced in section 4.1.1. Figure 4.24 shows an exemplary case for the rapidity range $0.57 < y < 0.67$ in the RPC polar angle region and the corresponding $m_t - m_0$ intervals for the K^+ in the centrality range from $0 - 30\%$ most central events. In the TOF polar angle region, the TOF energy loss cut suppresses the pions with a wrong reconstructed time of flight. Consequently, the exemplary comparisons are performed in the RPC polar angle region.
Subtracting the interpolated background from the data results in a mass distribution consisting ideally only of the true signal. Figure 4.25 shows the resulting K^+ mass peaks after the background subtraction for the same interval as shown in figure 4.24.

In the mass spectra presented in figure 4.24, the background contribution introduced in section 4.1.7 can be identified as a second peak, whose arithmetic mean shifts from the direction of the nominal π^+ mass towards the nominal p mass with increasing $m_t - m_0$. However, with the applied selection criteria, this has no significant impact on the precision of the background description for the K^+.
In the case of the K^-, as shown in figure 4.26, the unphysical background contribution introduced in section 4.1.7 has a larger count rate than the actual signal. This reduces the phase space in which the K^- count rate can be extracted due to larger inaccuracies in the background estimation close to the kinematic overlap region between the K^- signal and the contamination. In figure 4.26, the structures' peak in the presented mass spectra can be seen with the arithmetic mean shifting towards and, finally, overlapping the K^- mass distribution towards higher transverse masses. Consequently, it is essential to quantify the goodness of the background description to remove spectra from the sample where the criteria for a reliably extracted mass signal are not met.

A Gaussian function of the form [37]

$$f(m;\mu,\sigma) = \frac{1}{\sqrt{2\pi}\sigma} e^{-\frac{(m-\mu)^2}{2\sigma^2}} \tag{4.4}$$

is fitted onto the subtracted distributions, which is a function of the mass m, symmetric around a value μ. This gives information about the width σ and the mean value μ for an extracted $K^\pm$ signal. The count rate is determined via the sum over all signal bin entries within a $\mu \pm 2\sigma$ region. Furthermore, figures 4.25 and 4.27 also contain the determined significance α.

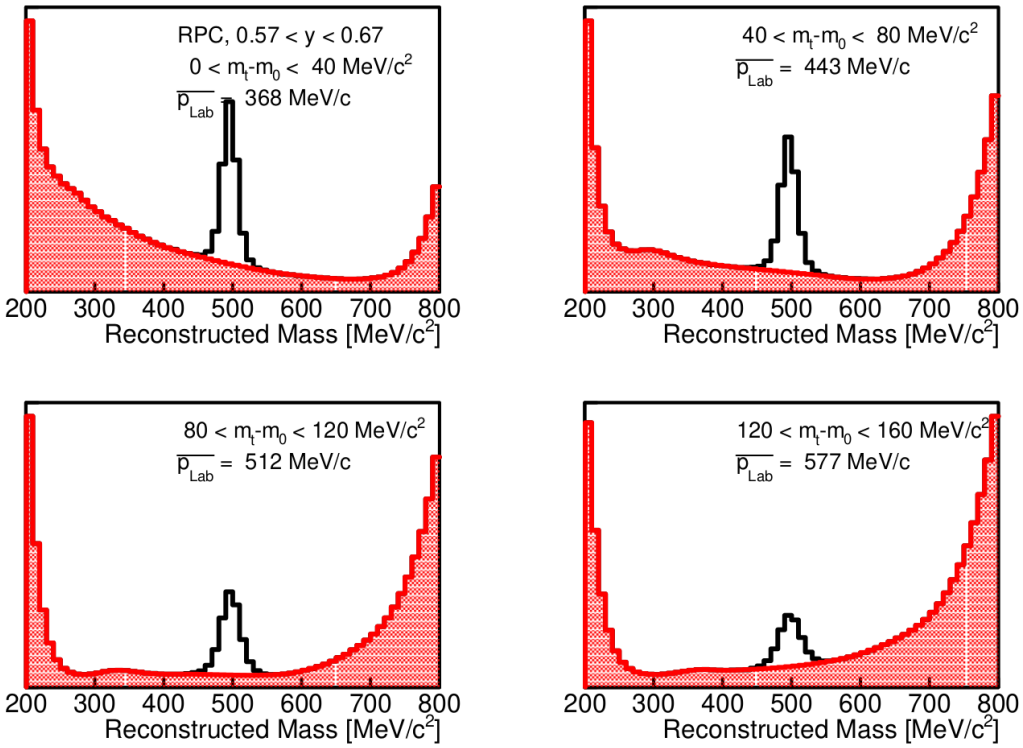

Figure 4.24.: Multidifferential K^+ mass region spectra for $0.57 < y < 0.67$ in $0-30\%$ centrality with the interpolated background (red) within the RPC coverage.

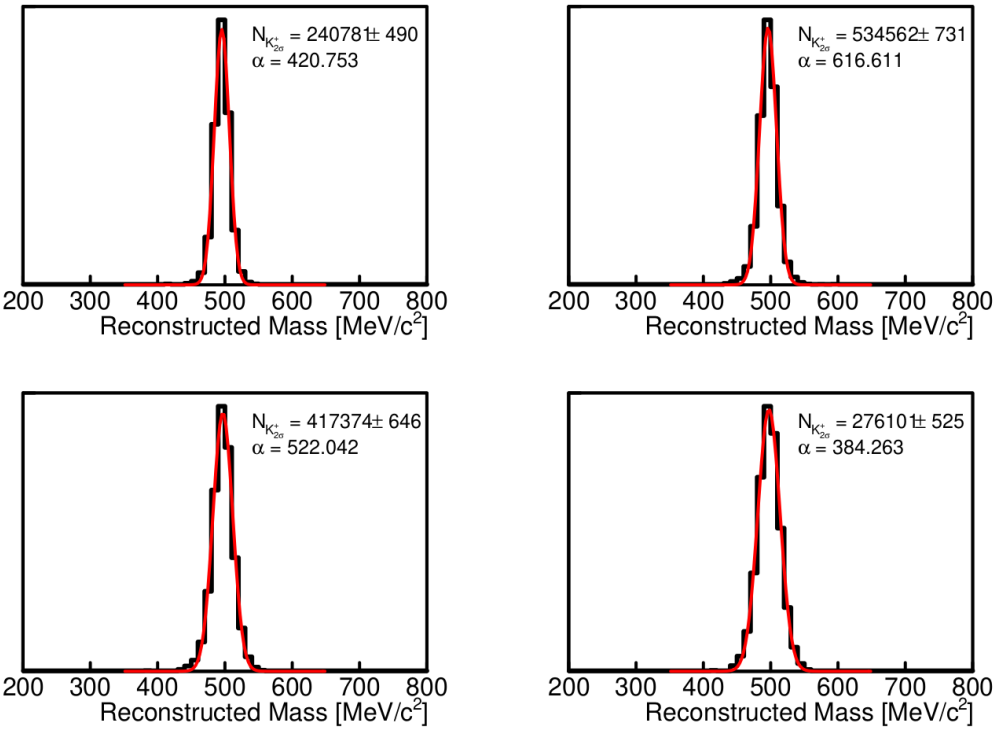

Figure 4.25.: Subtracted multidifferential K^+ mass spectra for $0.57 < y < 0.67$ in $0-30\%$ centrality within the RPC coverage.

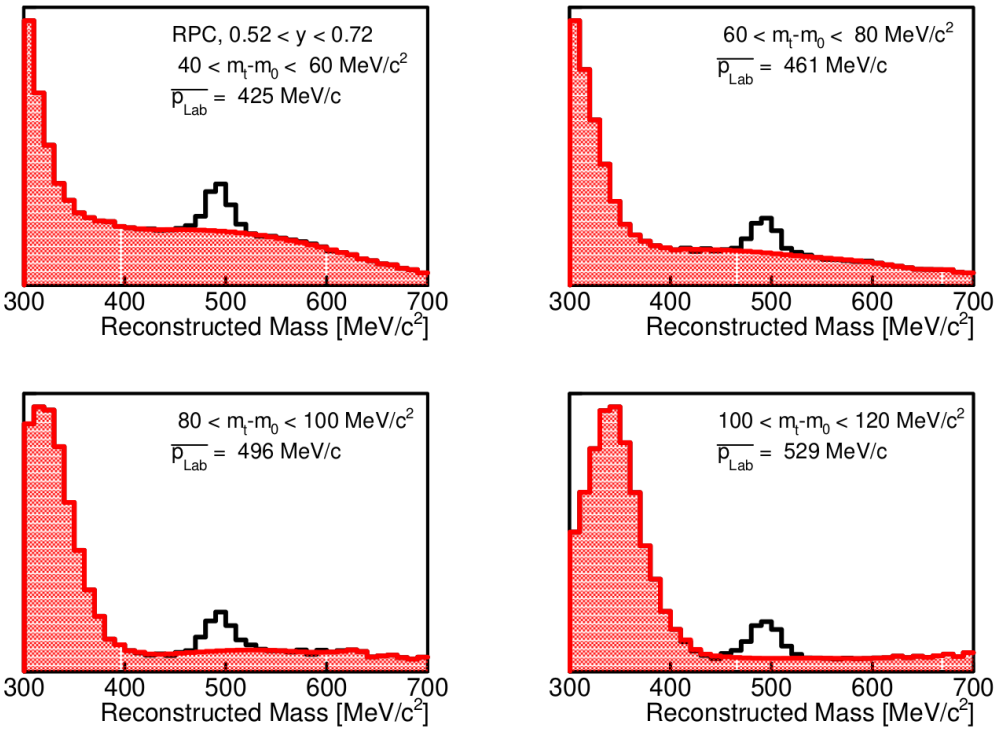

Figure 4.26.: Multidifferential K^- mass region spectra for $0.52 < y < 0.72$ in $0-30\%$ centrality with the interpolated background (red) within the RPC coverage.

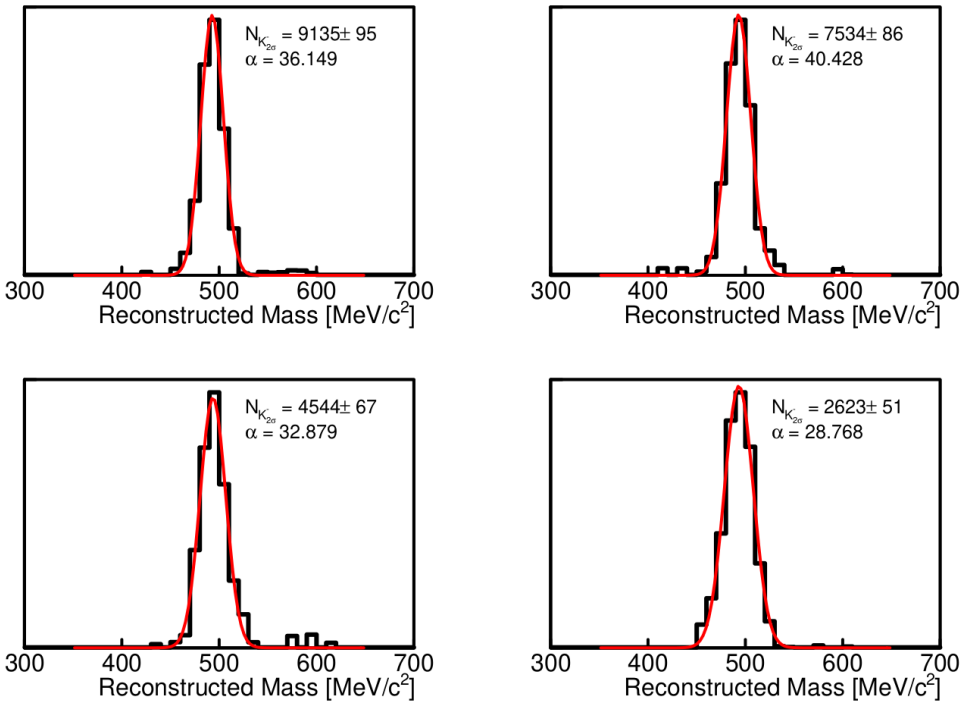

Figure 4.27.: Subtracted multidifferential K^- mass spectra for $0.52 < y < 0.72$ in $0 - 30\%$ centrality within the RPC coverage.

The significance α (see equation A.2) for the K^- is one order of magnitude smaller than for the K^+. Furthermore, the background description for the K^- becomes inaccurate at an $m_t - m_0$ value of about 140 MeV/c^2 due to the structure discussed in section 4.1.7. For the K^+, a reliable signal can be extracted until an $(m_t - m_0)$ value of about 280 MeV/c^2. This also motivates the smaller $(m_t - m_0)$ intervals chosen for the K^-. The presented method of estimating and subtracting the background and fitting the resulting mass spectrum with a Gaussian is applied to all phase space grids for both META detectors' polar angle regions.
To obtain a quantitative measure to judge whether a signal should be accepted, the first and second moments of each phase space bin distribution are compared with the obtained values from simulations in the same phase space bin, as displayed in figures 4.28 and 4.29. This serves as a quality assurance, as incorrectly estimated backgrounds below the peak and failed fits display as discontinuities within the distributions. The direct comparison between data and simulation enables an additional quality assurance, as the simulated mass distributions give an estimate on the values for the first and second moment of the true signal.
Assuming an accurate kinematic description of the reconstructed phase space within the PLUTO-generated events as well as an accurate GEANT emulation of the HADES detector, the extracted $K^\pm$ signal is expected to have comparable values for σ and μ and follow the same global trend as a function of transverse mass. The spectrum is cut off whenever data and simulation results for both observables diverge. This is especially important for estimating the influence of the structure containing pions with incorrect times of flight on the extraction of $K^\pm$ signals. Also, the influence of individual selection criteria can be quantified this way. The resulting first and second moments as a function of transverse mass for each interval of rapidity is shown in figures 4.28 and 4.29 for all the accepted data bins. The global trend agrees well between the accepted signals in data and simulation. For the K^-, an analogous selection procedure is performed. In addition, the spectra are cut off as soon as the background description of a phase space bin is visibly impaired by the structure.

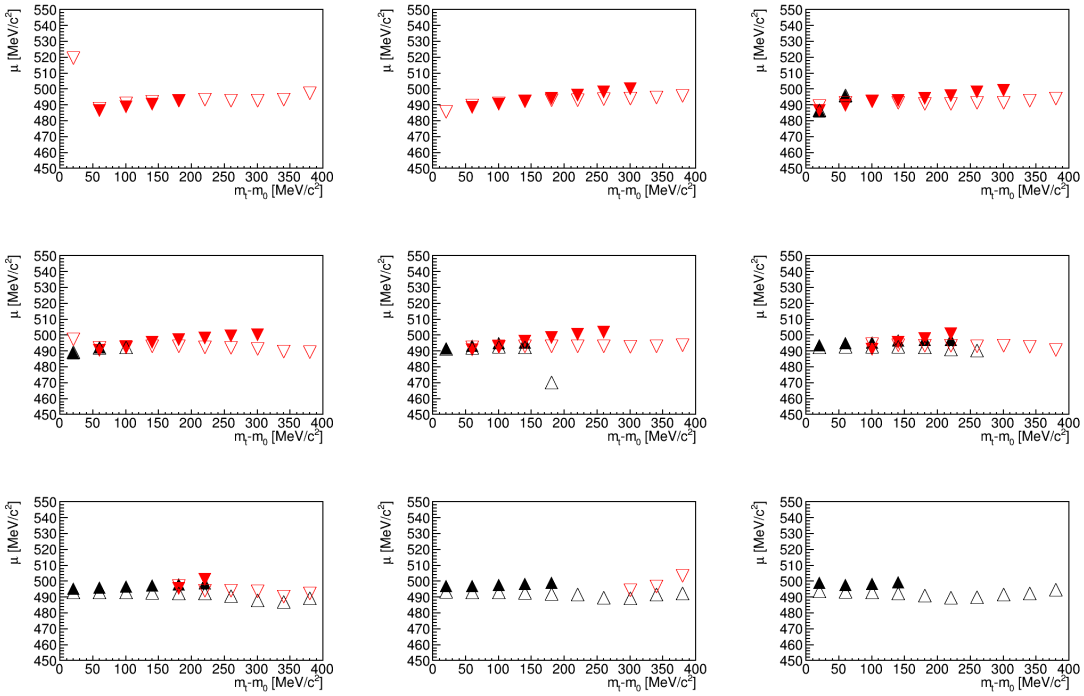

Figure 4.28.: Comparison of the μ values for the K^+ signals in different phase space bins. The filled triangles represent data, and the open triangles represent simulation results. Red colour stands for the TOF polar angle region, and black for the RPC polar angle region.

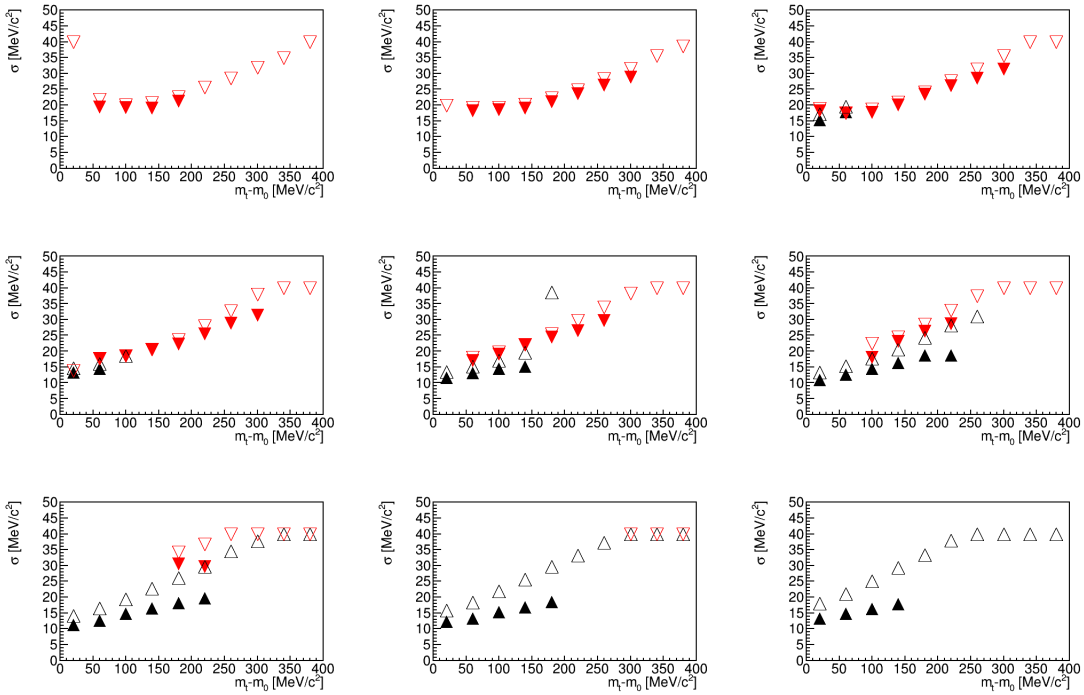

Figure 4.29.: Comparison of the σ values for the K^+ signals in different phase space bins. The filled triangles represent data, and the open triangles represent simulation results. Red colour stands for the TOF polar angle region, and black for the RPC polar angle region.

The resulting integrated count rate distributions in the $(m_t - m_0)$-y-grid can be seen for both particles in figures 4.30 and 4.31. Here the transverse mass $(m_t - m_0)$ is plotted on the y-axis and the rapidity y on the x-axis. The colour coding represents the amount of reconstructed $K^{\pm}$ in the corresponding bin.

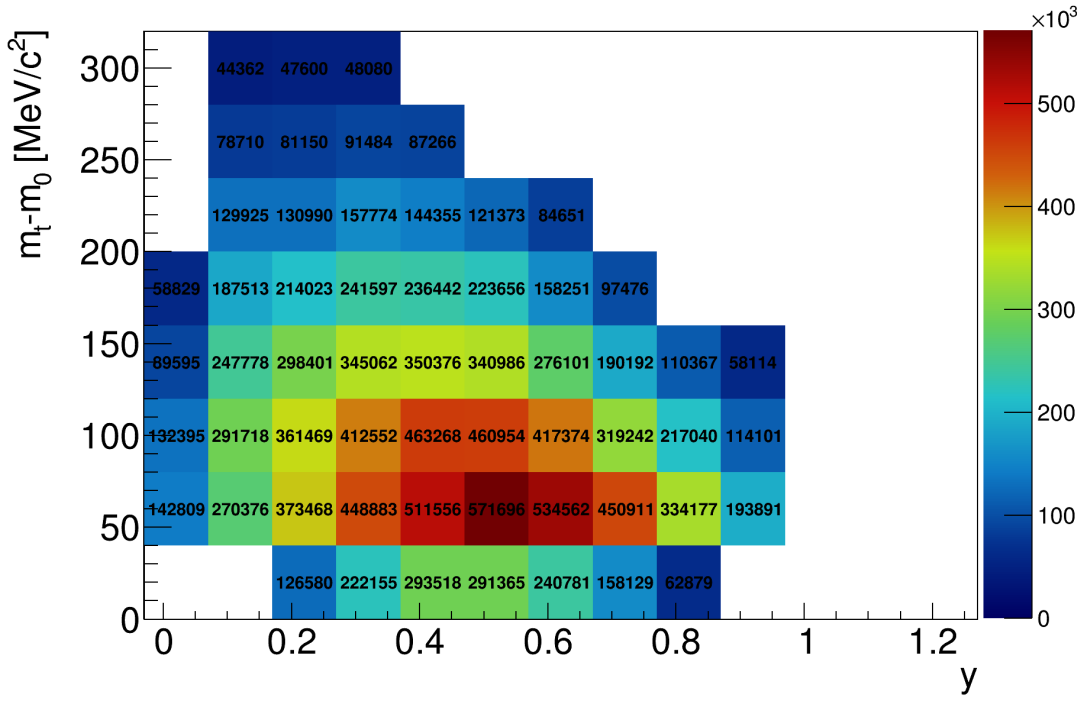

Figure 4.30.: Reconstructed phase space for K^+ and the corresponding extracted count rates.

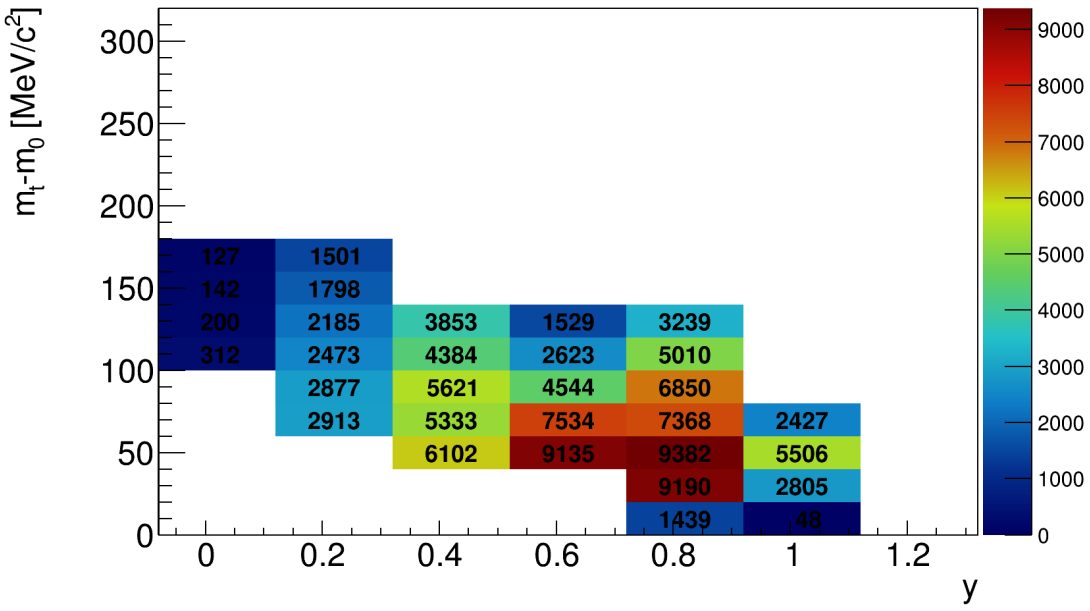

Figure 4.31.: Reconstructed phase space for K^- and the corresponding extracted count rates.

4.1.9. Acceptance × Efficiency Correction

Extracted count rates are corrected for influences from the HADES specific geometrical detector acceptance and inefficiencies due to the track selection procedure. The measured and extracted count rate is, due to these influences, always smaller than the true multiplicity.
Transport models are therefore used to simulate collision events whose emitted particle spectra are then transported through a GEANT emulation of the HADES detector. To enhance the available statistics, $K^{\pm}$ generated with PLUTO are embedded into the UrQMD simulations. The entire procedure is described in section 3.7. The same track selection criteria applied to measured data are also used for the simulated data. Furthermore, the phase space distribution is subdivided into the same intervals within the $(m_t - m_0)$-y plane. To obtain the individual correction factors, the count rates extracted from the GEANT simulation are divided by the ones initially generated, which results in an Acceptance × Efficiency correction matrix, displayed for the K^+ in figure 4.32 and the K^- in figure 4.33.
Though, as presented in previous sections, the usage of selection criteria is performed under the premise of the least possible discrepancy between simulated and measured data to avoid systematic biases, while simultaneously aiming for the highest possible purity, there still exist finite systematic uncertainties due to small discrepancies. To take this into account, multidifferentially extracted particle production rates for different combinations of applied selection criteria are compared in section 5.3.1 and their relative differences taken into account as systematic uncertainties for the final results.
The correction is performed by dividing the count rates of each phase space interval from measured data by the corresponding Acceptance × Efficiency correction matrix element. For the correction, a lower limit value of 1 % is chosen, below which the spectra are cut off. This way, phase space intervals with large statistical uncertainties are excluded by default.

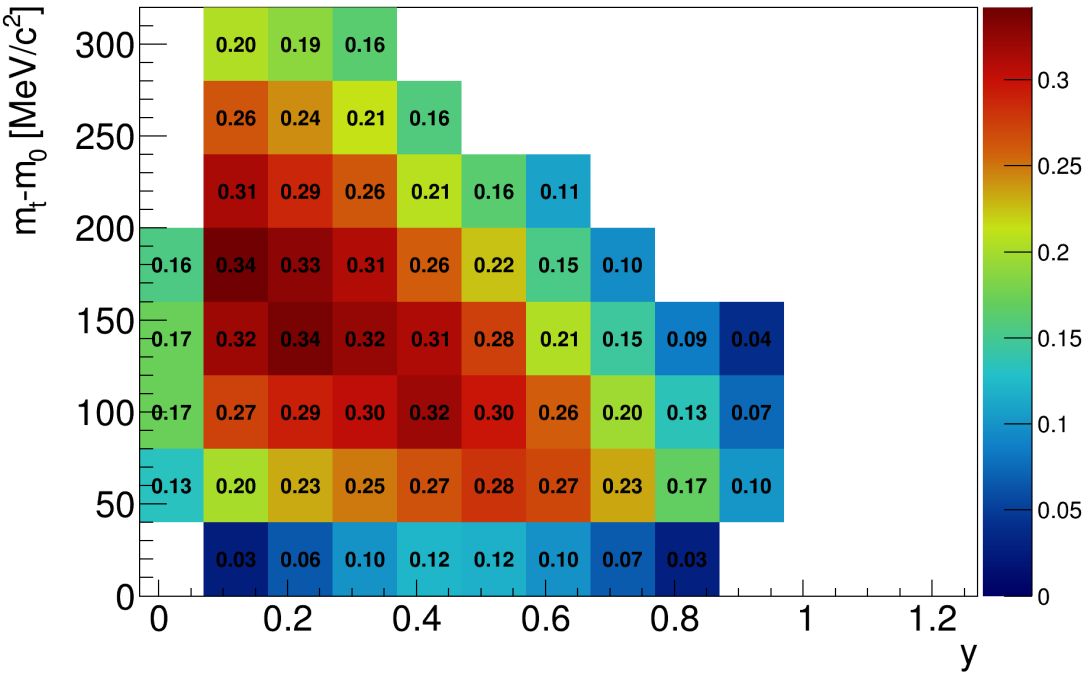

Figure 4.32.: Acceptance × Efficiency matrix of the K^+-meson. The z-axis represents the relative amount of, after the full analysis chain, reconstructed K^+ per phase space bin in relation to the initially generated ones.

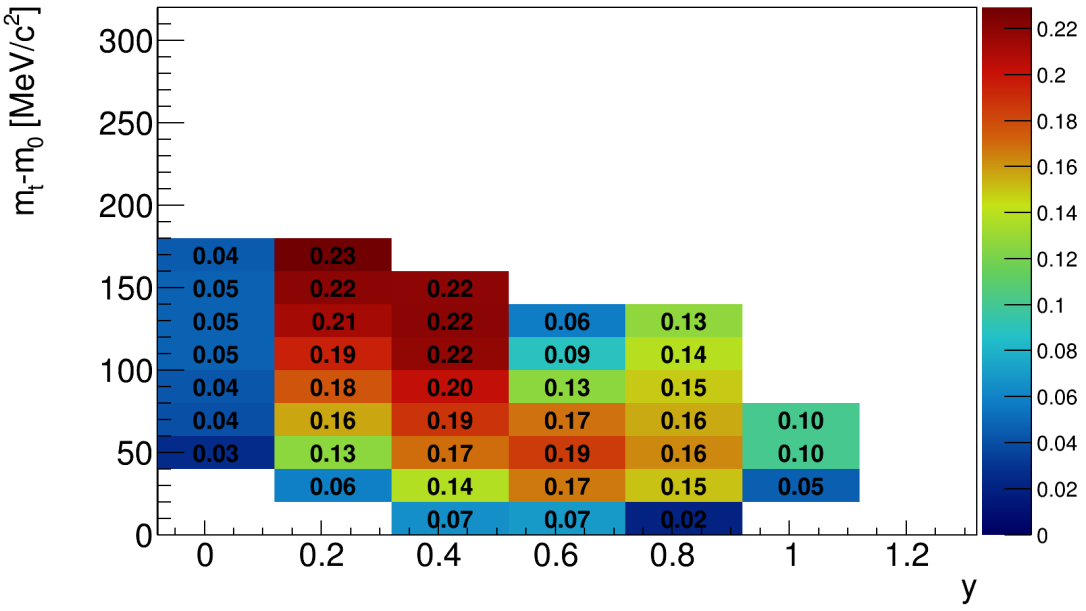

Figure 4.33.: Acceptance × Efficiency matrix of the K^--meson. The z-axis represents the relative amount of, after the full analysis chain, reconstructed K^- per phase space bin in relation to the initially generated ones.

4.1.10. Sector Dependence

In the case of negatively charged pions, a discrepancy between sectors 5 and 6 and the remaining four sectors in the slope of the $(m_t - m_0)$ spectra is observed. As this slope significantly influences the extracted particle production rate and effective temperature, this effect is expected to significantly affect the K^- signal extraction with its comparably low statistics.

To investigate the necessity of exclusion of these sectors from the K^- analysis, one can compare the particle production rates as a function of rapidity (more details in section 5.4) between the sectors, which is done in figure 4.34.

Figure 4.34.: K^- dN/dy spectra obtained for different sectors in $0-30\%$ centrality. Results from sectors 5 and 6 (red) are drawn against results from sectors 1 and 2 (black).

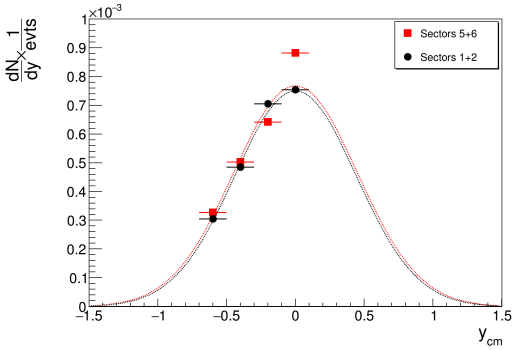

The resulting increase in the slope towards midrapidity is inconsistent with corresponding extrapolations within sectors 1-4. This ultimately leads to systematically higher integrated yields and shifted inverse slope parameters extracted from the transverse mass spectra (see section 5.4). Those sectors are, consequently, excluded from the K^- multidifferential analysis.

Final Selection Criteria

All previously introduced selection criteria are equally applied for the $K^{\pm}$ analysis. The only exception is the exclusion of sectors 5 and 6, which is exclusively done for the K^{-} (see section 4.1.10). Table 4.2 summarises the introduced and applied selection criteria and the chosen phase space intervals for the multidifferential analysis.

Criterion	K^{+}	K^{-}
χ^2_{MM}	< 3	
χ^2_{RK}	< 200	
TOF dE/dx	yes	
MDC dE/dx	yes (π^{+} and p exclusion)	yes (π^{-} exclusion)
Acceptance $\times$ Efficiency Cut-Off	1%	
Maximum $m_t - m_0$ [MeV/c^2]	800	
m_t Bin Width [MeV/c^2]	40	20
Y Range	-0.03 - 1.97	-0.08 - 1.92
Y Bin-Width	0.1	0.2
Lower Momentum Cut [MeV/c]	200	
Sectors	1-6	1-4

Table 4.2.: Summary of the applied charged Kaon candidate selection criteria. See the text for details.

4.2. Reconstruction of the short-lived $\phi(1020)$

Due to the short lifetime of $c\tau \approx 4.63 \times 10^{-14}$ m [47], the ϕ-meson reconstruction is done via identifying the decay products, commonly called *daughter particles*. This work analyses the decay of $\phi \to K^{+}K^{-}$.

4.2.1. Selection of $K^{\pm}$ Daughter Candidates

The preselection of $K^{\pm}$ candidates is performed by accepting track candidates within a specific reconstructed mass window, applying track quality cuts. However, as demonstrated in section 4.1, the charged Kaon tracks cannot be extracted from the data sample without significant background contributions by protons and $\pi^{\pm}$. Hence, in addition to an expectedly small contribution from $K^{\pm}$ combinatorial background, background from misidentification of protons and $\pi^{\pm}$ tracks as $K^{\pm}$ is an issue. Table 4.3 summarises the applied criteria.
As the ϕ-meson is produced rarely, the set of chosen cut criteria should affect the available $K^{\pm}$ candidate statistics as little as possible. The MDC dE/dx criterion reduces the amount of reconstructed ϕ-mesons by nearly 50%, which is why the criterion is not applied in contrast to the single-particle analyses of $K^{\pm}$.
The upper momentum cut-offs for the selection of $K^{\pm}$ candidates are motivated by the observed broadening of the $\pi^{\pm}$ and p mass distributions at higher momenta, leading to an increased overlap with the $K^{\pm}$ mass region. This can be explained by the decrease of precision in time of flight reconstruction towards higher momenta. As visible in figure 4.20, no significant charged Kaon contributions can be found beyond the indicated momentum cut values.

To select only $K^{\pm}$ pair candidates originating from the same source, the topological constraints introduced in section 4.2.2 are applied. In addition, to aid this selection, the opening angle (α)

Criterion	K^+	K^-
Charge	$+1$	-1
Mass Window [MeV/c^2]	$430 < M < 540$	
Lower Momentum Cut [MeV/c]	150	
RPC Region Upper Momentum Cut [MeV/c]	800	
TOF Region Upper Momentum Cut [MeV/c]	1000	800
Sectors	1-6	
χ^2_{MM}	< 3	
χ^2_{RK}	< 200	
TOF dE/dx	yes	
MDC dE/dx	no	

Table 4.3.: Summary of the selection criteria applied onto the $K^\pm$ daughter particle candidates.

distributions of the $K^\pm$ pair candidates are compared between data and simulation. Figure 4.35 shows this comparison with the simulated distribution normalised such that, to guide the eye, the maximum coincides with the data points. Using this comparison, opening angle α between the daughter pairs is expected to be distributed within the range $5° < \alpha < 85°$.

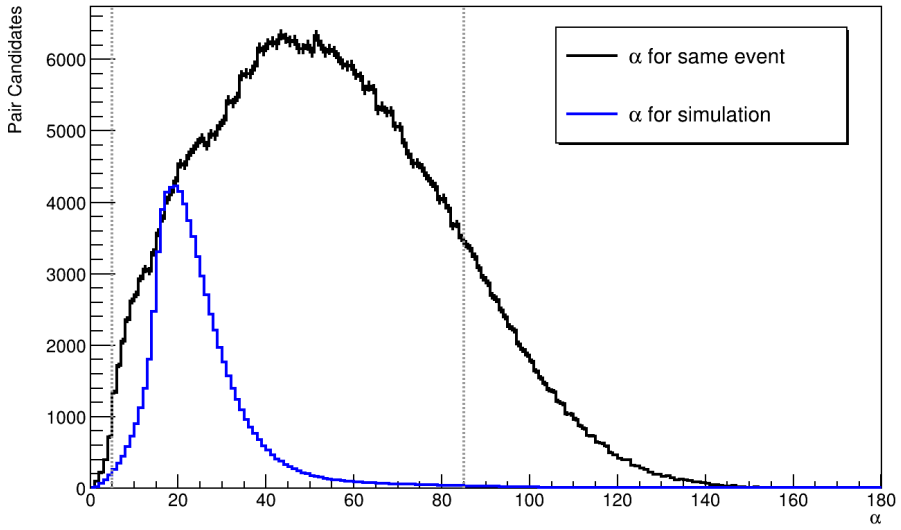

Figure 4.35.: Distribution of opening angles α between the daughter particle candidates for experimental data (black) and simulated ϕ-meson candidates (blue). The grey lines mark the cut-range $5° < \alpha < 85°$.

The choice of this opening angle region for the selection of ϕ-meson candidates is supported when comparing the extracted signals from the invariant mass spectra for different upper opening angle cuts. Figure 4.36 shows a comparison between the extracted $\phi(1020)$ signal without (a) and with (b) an upper opening angle cut of 85°.
There is no statistically significant change in the extracted raw counts, while background is suppressed in the higher invariant mass region, which increases the overall purity of the sample. To demonstrate that, the ratio between the K^+K^- invariant mass spectra for the case of no upper opening angle cut and an upper opening angle cut of 85° is shown in figure 4.37.
Consequently, a constraint for this angle range is chosen. Furthermore, the lower value is chosen such that two daughter particles do not share the same MDC cells, which significantly suppresses

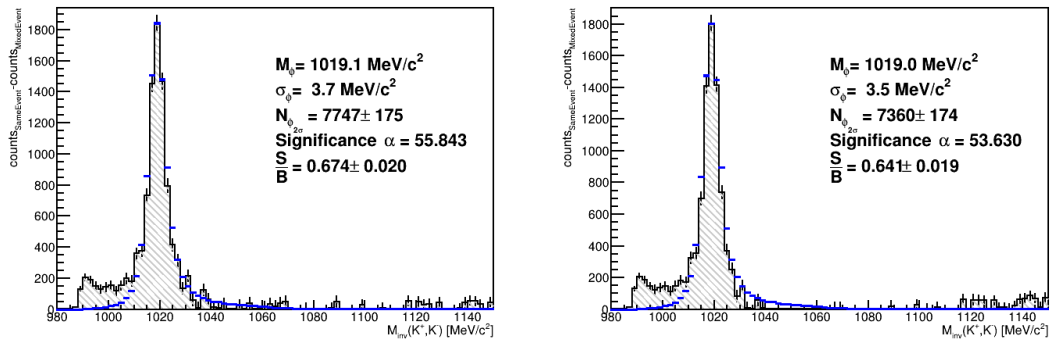

(a) $\alpha > 5°$ (b) $5° < \alpha < 85°$

Figure 4.36.: ϕ-meson invariant mass signal extracted from data as for the cases of no upper opening angle cut for the decay into K^+K^- (a), as well as with an upper opening angle cut of 85° (b).

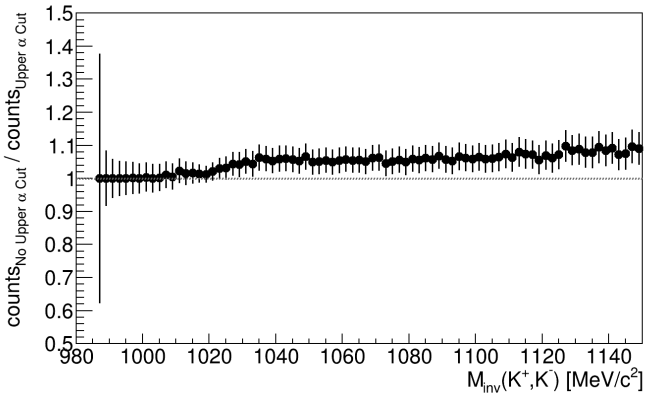

Figure 4.37.: Ratio between the K^+K^- invariant mass spectra for the case of no upper opening angle cut and an upper opening angle cut of 85°.

the background.

Furthermore, contaminations within the $K^\pm$ mass spectra are observed for low momenta, as it can be seen when plotting the momentum over mass × charge distribution of all track candidates. Figures 4.15 and 4.16 depict these contaminations in the low momentum region, close to the nominal $\pi^\pm$ and $K^\pm$ masses. This effect is most prominent within the $0-10\%$ centrality range and can be traced back to charged pions wrongly identified as charged Kaons. When plotting the invariant mass (equation 4.5) of the $K^\pm$ pair candidates, as they are assigned the nominal charged Kaon mass, the contribution manifests at low invariant masses, which is depicted in figure 4.38(a). This happens, as the respective reconstructed mass from data is mostly lower or equal to the nominal Kaon mass. As a result, the energy-component of the four-momentum is recalculated to fit the three-momentum of the particle with the newly assigned mass, leading to a calculated invariant mass mostly smaller or equal to the invariant mass of a true $K^\pm$-pair emerging from a ϕ-meson decay. In these plots, the invariant mass distribution is shown once for the case of no lower momentum cut applied (left) and once for the case of an applied lower momentum cut at 250 MeV/c. The red area represents the mixed event background estimation (see section 4.3.1).

This contamination at low invariant masses is strongly suppressed when applying a lower momentum cut-off at 250 MeV/c for the daughter particle candidates, as visible when comparing figures 4.38(a) and 4.38(b), and yields a better agreement between data and the estimated background with a loss of statistics of around 7%. The relative shift between estimated background

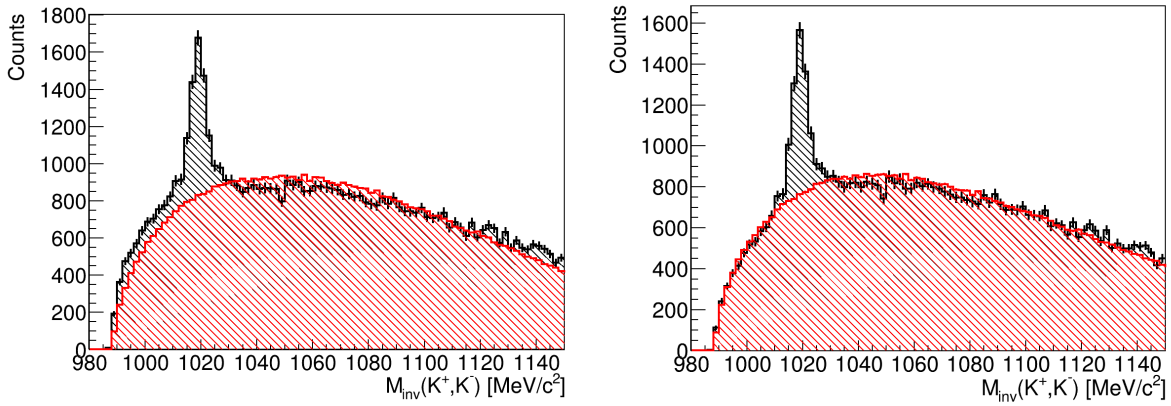

(a) No Momentum Cut

(b) Momentum Cut at 250 MeV/c

Figure 4.38.: Invariant mass distribution for all accepted $\phi \to K^+K^-$ candidates in $0-10\%$ most central events without a lower momentum cut for the $K^\pm$ (a) and with a lower momentum cut-off at 250 MeV/c (b).

and data background also indicates, that the currently used event mixing technique does not sufficiently describe the correlated background of wrongly identified π^- from the $\Lambda \to p\pi^-$ channel which is coupled to the K^+ via the common direct production channel $NN \to N\Lambda K^+$. However, this effect proves unsignificant for the multidifferential analysis as a function of transverse mass and rapidity, as the affected low transverse mass regions generally do not contain a clean signal peak and suffer from a large background. Consequently, as the low momentum cut-off also excludes most of these contributions, no further optimisation of the mixing algorithm is necessary.
Momentum constraints might lead to a potential bias in the reconstructed phase space distribution of the ϕ-meson. However, the multidifferential analysis showed no statistically significant fluctuations in the case of a momentum cut-off at 150 MeV/c. Consequently, this value was chosen to suppress the misidentification background at the low invariant masses.

4.2.2. Selection of ϕ(1020) Candidates

The mother particle mass is reconstructed from the daughter particle candidates by using the daughter particles' measured kinematical properties. The determined *invariant mass* of the mother particle is defined as [29]

$$M^2 = \left(\sum_{i=1}^{k} E_i\right)^2 - \left(\sum_{i=1}^{k} \overrightarrow{p}_i\right)^2 \tag{4.5}$$

Applied to the $\phi \to K^+K^-$ decay channel, the invariant mass of the ϕ-meson defines as [119]

$$M_{\text{inv}} = \sqrt{\left(m_{K^+}^2 + m_{K^-}^2\right) + 2\left(\sqrt{m_{K^+}^2 + \overrightarrow{p}_{K^+}^2}\sqrt{m_{K^-}^2 + \overrightarrow{p}_{K^-}^2} - |\overrightarrow{p}_{K^+}||\overrightarrow{p}_{K^-}|\cos\theta\right)}$$

where $m_{K^\pm}$ denotes the daughter particle mass, $\overrightarrow{p}_{K^\pm}$ the corresponding three-momentum and θ the opening angle between two daughter particles. As the reconstructed masses of the $K^\pm$, daughter particles are not corresponding to a fixed value but rather follow a Gaussian-like dis-

tribution due to the uncertainties in the time of flight measurement, the nominal PDG-value [141] for the $K^{\pm}$ mass is assigned to all selected daughter particle candidates.

In addition to the selection of daughter particle candidates, decay topology parameters, as used in [125], are utilised to mainly select pair candidates originating from the event vertex. Figure 4.39 shows a not-to-scale depiction of the vertices used for applying geometrical constraints. As the ϕ-meson lifetime is $c\tau \approx 46$ fm [47], its decay vertex is indistinguishable from the reconstructed event vertex.

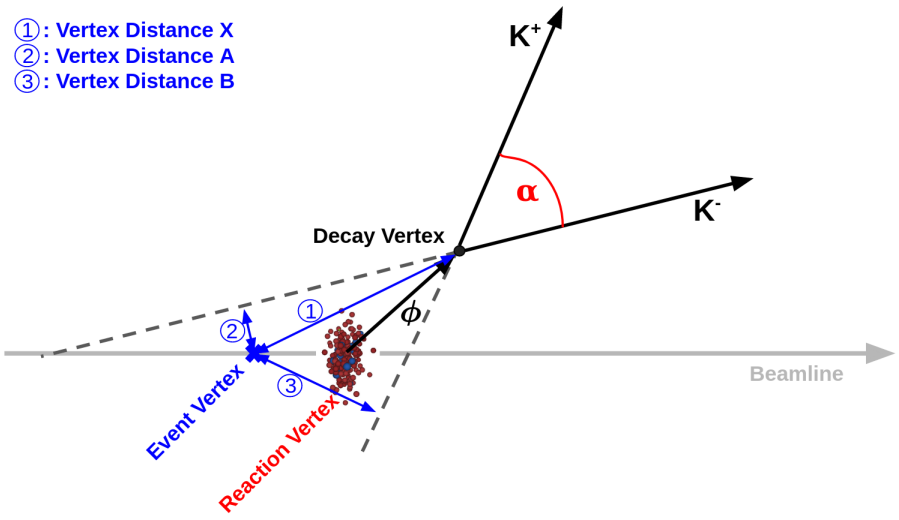

Figure 4.39.: Not to scale representation of the different vertices used as geometrical constraints for the reconstruction of the ϕ-meson candidates. The difference between event and decay vertex is indistinguishable for current detectors. More information in the text.

As the event vertex resolution lies in the mm-scale, the following criteria and values are used:

- Vertex Distance X < 10 mm
- Vertex Distance A/B < 10 mm

Vertex Distances A and B represent the *Distance of Closest Approach* (DCA) of the backwards extrapolated $K^{\pm}$ trajectory towards the reconstructed event vertex. Vertex Distance X represents the distance of the ϕ decay-vertex to the event vertex. It is essential to point out the differentiation between the reconstructed event vertex and the actual reaction vertex. As the vertex resolution is in the millimetre scale, the used value of the event vertex does not necessarily represent the true reaction vertex. Figure 4.40(a) shows the two-dimensional distribution for K^+K^--pair-candidates after full selection (without geometrical vertex cuts) in the Vertex-Distance-A-Vertex-Distance-B-plane.
For Vertex Distances A and B there exists a distinct maximum at around 1.5 mm , while for Vertex Distance X this lies at around 3 mm. For both cases, these distributions fall off steep, resembling a Landau distribution. To demonstrate the importance of this criterion for the identification and extraction of ϕ-meson candidates, figure 4.41 displays the effect of these cuts. While the invariant mass signal remains mainly unaffected, this criterion suppresses a large proportion of the low invariant mass background distribution.

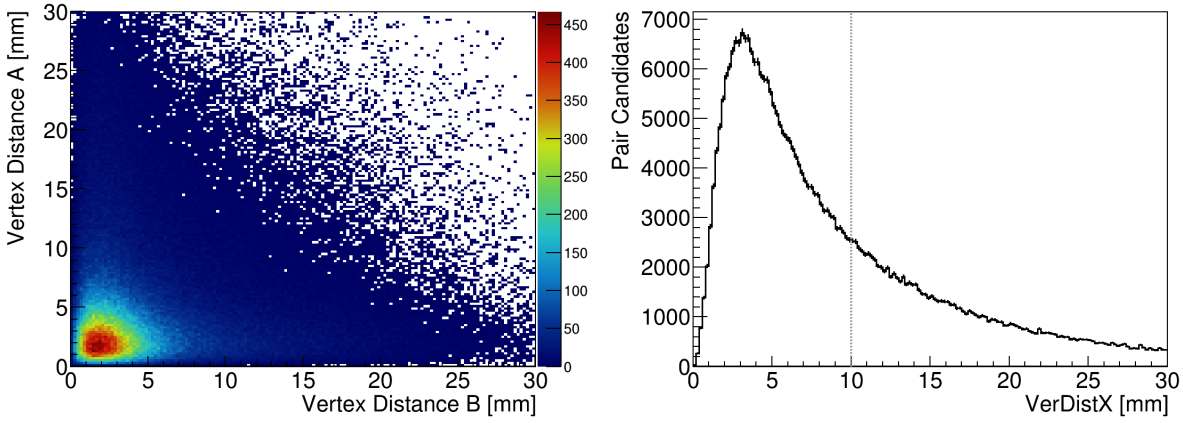

(a) (b)

Figure 4.40.: Distribution of selected K^+K^--pair-candidates in the Vertex-Distance-A-Vertex-Distance-B-plane (a) and as a function of Vertex Distance X (b).

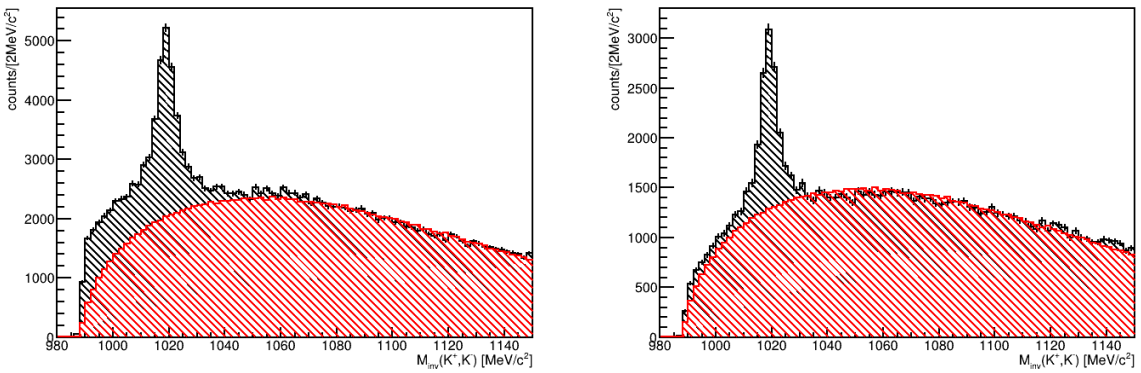

(a) (b)

Figure 4.41.: Invariant mass distribution for all accepted $\phi \to K^+K^-$ candidates in $0-30\%$ centrality without (a) and with geometrical Vertex Distance cuts (b).

4.3. The $\phi(1020)$ Signal Extraction

All K^+K^- pair candidates originating from a common collision event and passing the selection criteria are used to reconstruct ϕ-meson candidates. This results in an invariant mass distribution, as displayed in figure 4.42. The ϕ signal around the nominal mass of 1019.46 MeV/c^2 [141] is located on top of a wide distribution of background. The background can be separated into two sources: The *combinatorial background* consists of $K^\pm$, which do not originate from the same ϕ-meson decay. The *misidentification background* consists of $\pi^\pm$ and p tracks misidentified as $K^\pm$ tracks. Those are assigned the nominal $K^\pm$ mass, possessing four-momentum which does not match that of an actual $K^\pm$ pair originating from a ϕ-meson-decay. The resulting invariant masses form a wide distribution around the nominal $\phi(1020)$ mass signal.
The shape of the background distribution presents wide and continuous, as the initial selection of charged Kaon candidates for the pair matching algorithm is performed with only rough mass- and momentum-constraints. The mass distributions of protons and charged pions, strongly overlapping with the orders of magnitude smaller true charged Kaon signals, result in a wide

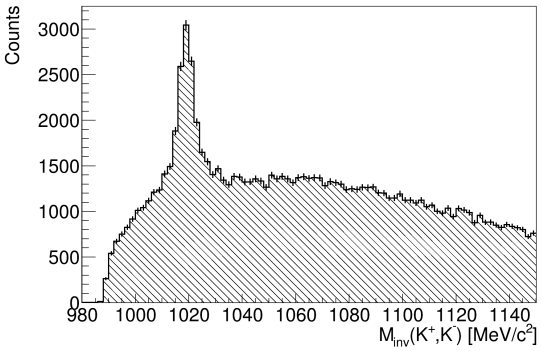

Figure 4.42.: Invariant mass distribution for accepted K^+K^- pair candidates. Besides the signal peak, a wide distribution of background is visible.

kinematic distribution for the uncorrelated particles incorrectly identified and paired as charged Kaons. Consequently, the resulting invariant mass distribution for those incorrect matches also presents as a wide distribution. For the true $K^{\pm}$ pairs from ϕ-meson decays, however, their correlation and the assignment of the nominal rest mass results in a narrow peak around the nominal ϕ-meson mass. As previously mentioned, a certain additional correlated contribution is expected from π^- from Λ-decays, wrongly identified as K^-. These additionally modify the line shape at low invariant masses.
To perform further differential analyses on the ϕ-meson, a crucial task is the description and subtraction of this background. Though the interpolation method introduced for the charged Kaons offers a valid method for background estimation, it does not offer a physical motivation for the background. Furthermore, as described in section 3.5.2, the ϕ-meson is sensitive to various background sources, which must be removed from the sample to reach the highest possible purity. For this purpose, the background description is performed via the so-called *mixed event technique*.

4.3.1. Calculation of the Mixed Event Background

This method aims to emulate the uncorrelated background below the ϕ-meson-peak to extract the signal from the spectrum. The selection of $K^{\pm}$ pair candidates for this procedure is performed the same way as before, this time only pairing daughter track candidates from different events. Furthermore, the tracks are only mixed if they originate from events with a similar multiplicity ($\Delta\text{Mult}_{\text{event}} < 10$) and a similar vertex position along the beam axis ($\Delta(\text{Event Vertex}_Z) < 5$ mm). Figure 4.43 shows the mixed event invariant mass distribution of $K^{\pm}$ pair-candidates. As

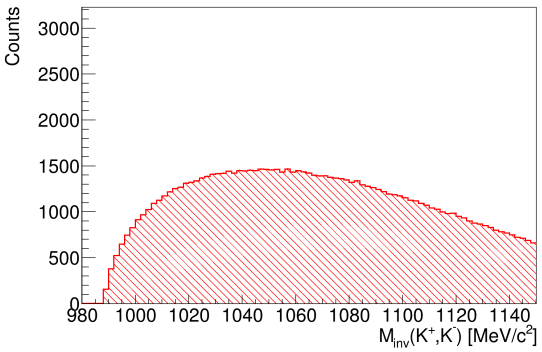

Figure 4.43.: Normalised invariant mass distribution resulting from the mixed event technique.

tracks from different events are paired, this method allows the generation of higher statistics than the same event data and, hence, must be normalised to data. For the normalisation, the focus is set on a reliable background estimation below the peak, using the regions left ($980 < M < 1005$ MeV/c^2) and right ($1030 < M < 1055$ MeV/c^2) of the signal simultaneously for normalisation.

4.3.2. Signal Extraction

The data and the normalised mixed event distributions are plotted against each other and subtracted to obtain the ϕ-meson signal. The result for the integrated spectra is depicted in figure 4.44.

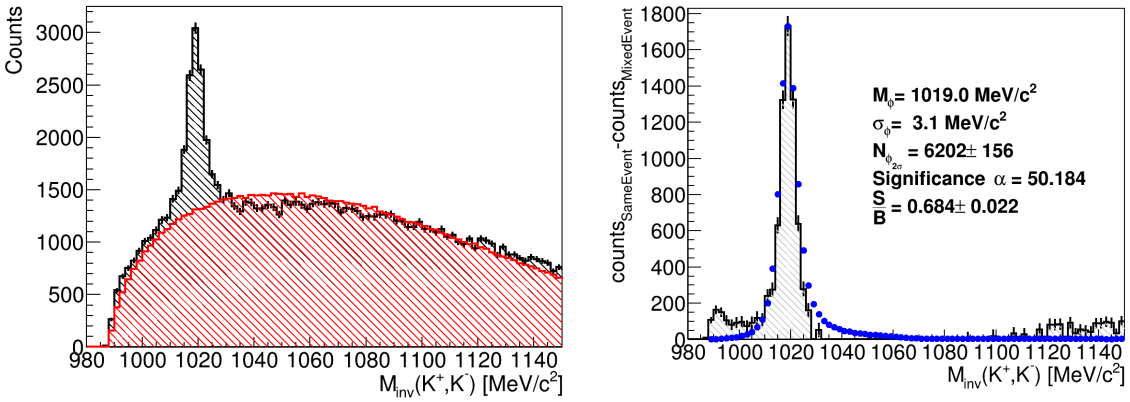

(a) Data and Mixed Event

(b) Data - Mixed Event

Figure 4.44.: Invariant mass distribution for all accepted $\phi \to K^+K^-$ candidates for $0-30\%$ most central events plotted against the corresponding normalised mixed event distribution (a) as well as the final subtracted spectrum (b). The blue distribution in (b) corresponds to the signal obtained from the simulation.

In figure 4.44(b), the y-axis contains the index-labelling *same event*, which indicates that the $K^{\pm}$ daughter candidates were accepted only coming from the same event. The shape of the distributions is visibly deviating, which becomes apparent when looking at the lower invariant masses in figure 4.44(b). These deviations originate from a correlated background source of π^- from Λ-decays wrongly identified as K^-, which is not accurately reproduced by the mixed-event technique.

4.3.3. Multidifferential Analysis

In analogy to the charged Kaons, the phase space of the ϕ-meson is subdivided into intervals within the $(m_t - m_0)$-y-plane. Table 4.4 summarises the parameters for this division.

Parameter	**Value**
$m_t - m_0$ Maximum [MeV/c^2]	800
m_t Bin-Width [MeV/c^2]	20
y-Range	$-0.08 < y < 1.92$
y Bin-Width	0.2

Table 4.4.: Summary of the phase space parameters for the differential $\phi(1020)$ analysis.

For each phase space bin, the invariant mass spectra for data and the mixed event are plotted against each other and then subtracted to obtain the signal from which the count rate can be extracted. For example, figure 4.45 shows the invariant mass distributions for the different phase space intervals within the rapidity range of $0.52 < y < 0.72$ as compared to the mixed event distributions.

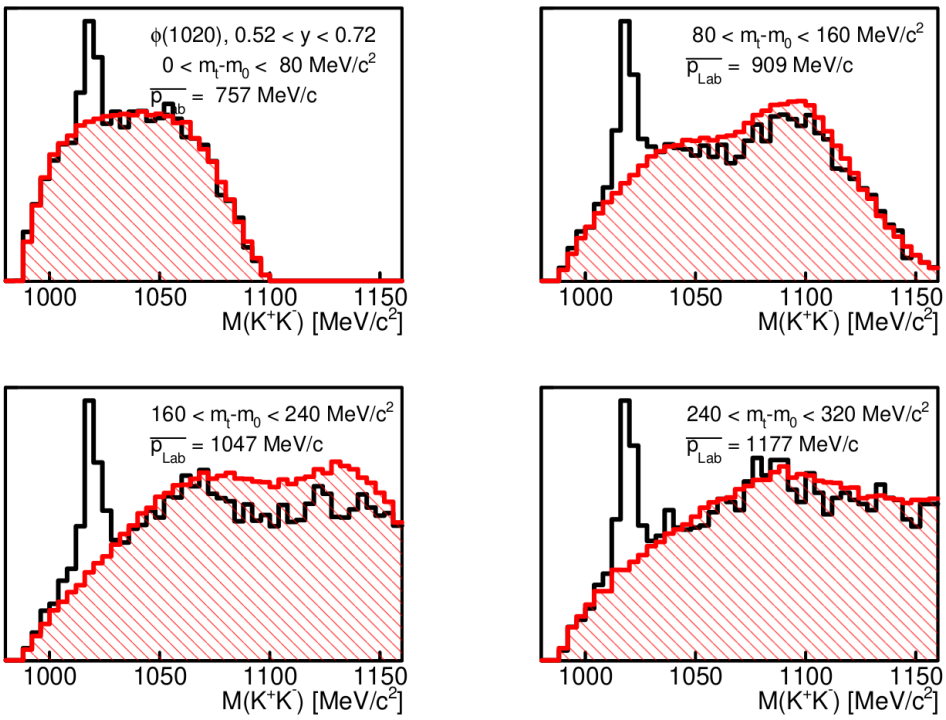

Figure 4.45.: Exemplary invariant mass (data and mixed event) spectra for the different m_t phase space bins within the rapidity interval $0.52 < y < 0.72$.

The mixed event technique describes the background under the peak reliably over all phase space intervals. Potential deviations between the data and mixed-event invariant mass distributions towards higher invariant masses are not important to the differential count rate extraction. The normalisation regions described in section 4.3.1 are optimised for the background description below the signal.

The introduction of additional constraints, by applying the MDC-specific energy loss criterion on the reconstructed daughter particles or by rejecting track candidates with a momentum of $p > 600$ MeV/c (overlap region between charged Kaons and the structure discussed in section 4.1.7), does not visibly improve the quality of the background description. Though both selection criteria improve the purity of the obtained sample, both also reduce the number of reconstructed ϕ-meson candidates by a factor of ≈ 2. As a result, no MDC-specific energy loss criterion is applied in the following analysis.

Though the method used for describing the background via the mixed event technique is robust, as the underlying combinatorics are well understood, a systematic effect can be caused by the normalisation procedure. Figure 4.45 illustrates this effect within the first (upper left) invariant mass distribution. Due to statistical fluctuations in the data, the mixed event background normalisation factor can vary depending on the normalisation range and the fluctuations between bins.

This leads to an over- or underestimation of the background and a bias in the count rate, which simulations can not correct for. Furthermore, due to the low statistics of the ϕ-meson, compared to even rare probes like the K^-, minor systematic effects in the order of a few counts in the count rate extraction lead to a bias of several per cent.

After background subtraction, the resulting invariant mass peaks are fitted with a Gaussian function and integrated over within a $\mu \pm 2\sigma$ range, which is shown in figure 4.46.

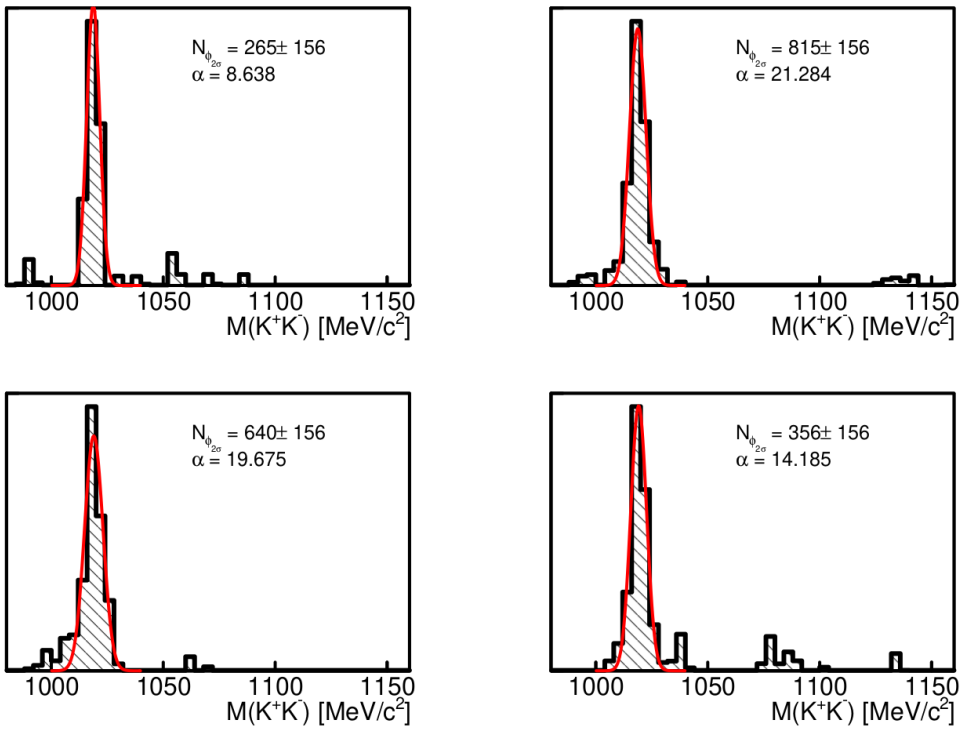

Figure 4.46.: Exemplary subtracted invariant mass spectra for the different m_t phase space bins within the rapidity interval $0.52 < y < 0.72$.

Writing the extracted raw count rates of each phase space interval into the corresponding grids within the $(m_t - m_0)$-y-plane results in a distribution as shown in figure 4.47.
Bins with a count rate of less than 20 ϕ-mesons are marked and ignored for the final differential results.

4.3.4. Acceptance × Efficiency Correction

This distribution is then corrected by an Acceptance × Efficiency matrix which contains the folded values for the geometrical detection and the reconstruction efficiency for each phase space bin. The procedure is analogous to what is presented in section 4.1.9. The PLUTO framework is used to generate ϕ-mesons according to a thermal distribution, which then decay into $K^{\pm}$ pairs. Those pairs are embedded into the UrQMD-generated events to enhance the available statistics for the $\phi(1020)$.
In contrast to the charged Kaons, the acceptance × efficiency values here lie within a few per cent. It comes due to the necessity of simultaneous measurement of both daughters ($K^{\pm}$) and the introduction of different selection criteria. Figure 4.48 depicts this correction matrix for the raw yields.
After applying the correction matrix to the data, the resulting phase space distribution for the ϕ-meson is obtained and used for further analysis steps.
These results will be analysed and discussed in chapter 5.

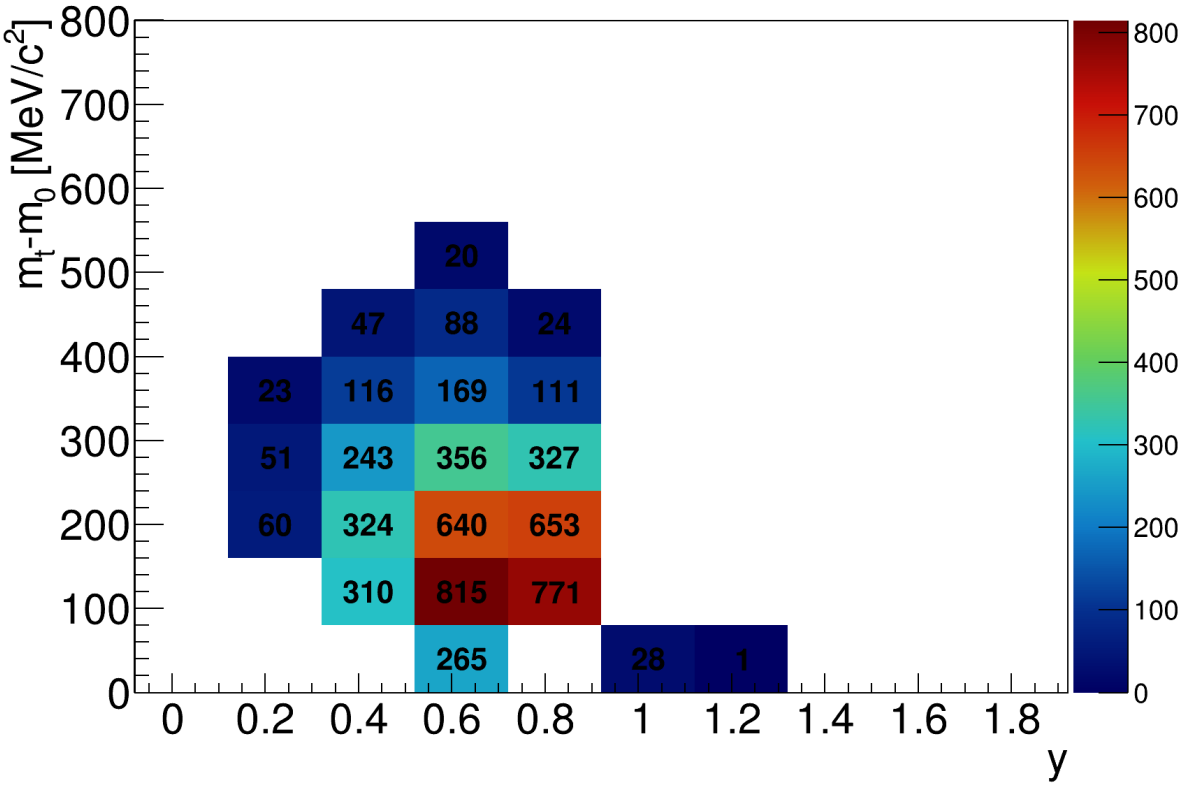

Figure 4.47.: Raw yields of reconstructed ϕ-mesons within the $(m_t - m_0)$-y-plane.

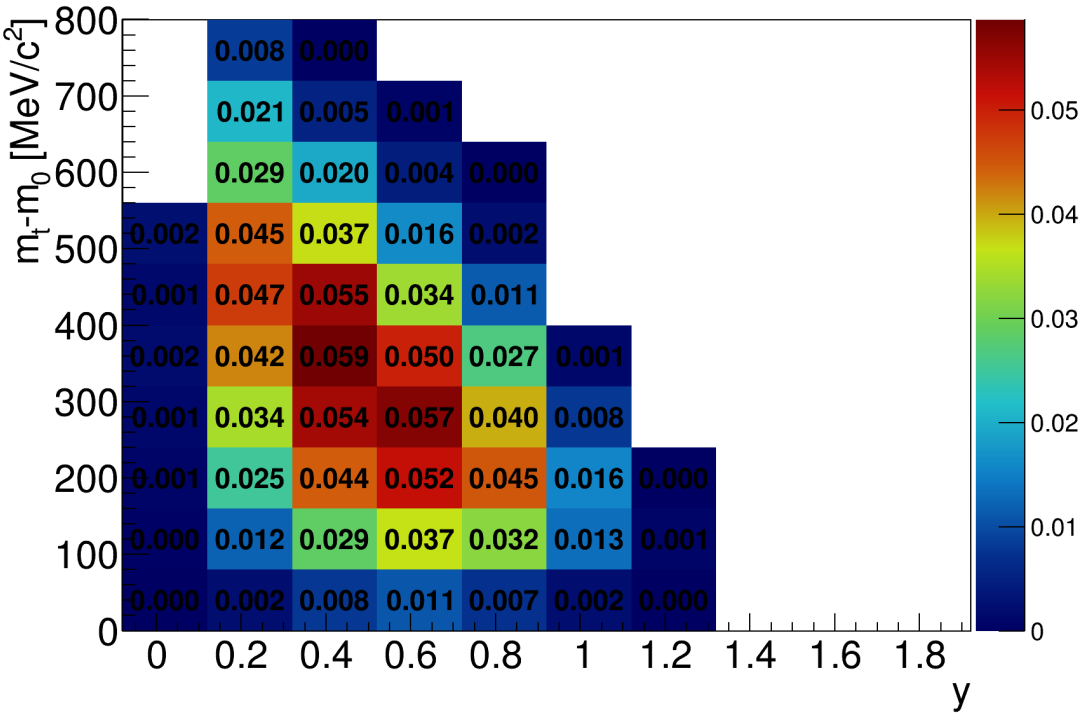

Figure 4.48.: Acceptance $\times$ Efficiency correction matrix for ϕ-mesons within the $(m_t - m_0)$-y-plane.

5. Results

In the previous chapter, the analysis methods are presented, exemplary for the $0-30\%$ most central events. This chapter presents the resulting multidifferential spectra, focussing on the different intervals in collision centrality. Furthermore, their extrapolation in transverse mass and rapidity direction is discussed.

5.1. Transverse Mass Spectra

5.1.1. K^+

The corrected K^+ count rates are investigated multi-differentially as a function of transverse mass m_t, shifted by the rest mass m_0, and rapidity y as defined in section 1.2.2. Consequently, for each rapidity interval, the projections along the $(m_t - m_0)$-direction are plotted and scaled by the number of events as well as $1/m_t^2$ to obtain the Boltzmann representation. Figure 6.5 displays the invariant transverse mass spectrum of the K^+ for $0-30\%$ as well as $0-10\%$, $10-20\%$ and $20-30\%$ most central events. Each $(m_t - m_0)$ spectrum is scaled by a factor $\times 10^i$, with i representing the rapidity bin number, for better visibility.
In the m_t-direction, the spectra show little visible deviations from the global trends in all centrality classes. The transverse mass spectra reach close to values of m_0, while spanning up to ≈ 300 MeV/c^2. In the rapidity direction, the coverage lies between -0.03 and 0.87 in the laboratory reference frame, where 0.82 represents midrapidity.
Here, the limiting factors for the phase space coverage are acceptance limitations as well as the effects discussed in sections 4.1.3 and 4.1.7. Acceptance hereby means the geometrical coverage of the detector, which lies between 18° and 85° in polar direction of the laboratory frame of reference, while it covers $\approx 360°$ in azimuthal direction with frames and support structures being the only notable exceptions. As the MDC energy loss distributions as a function of particle momentum strongly overlap beyond $p_{\mathrm{Lab}} \approx 600$ MeV/c for K^+, π^+ and p, the applied exclusion criterion also results in an exclusion of the majority of K^+ candidates beyond this point. However, if not applied, the contamination due to the structure with a systematic time of flight offset overlaps with the signal peak from that value on, modifying the extracted count rate and leading to a systematic bias. Furthermore, for lower laboratory momenta and without any MDC energy loss constraints, the structure modifies the background around the signal peak, so that the background estimation and signal extraction is less stable. Systematic effects, like the systematic uncertainties due to incomplete knowledge of the true background, displayed by the error boxes in figure 6.5, are discussed in section 5.3.1. The relative statistical uncertainties of the extracted count rate in each transverse mass bin lie around values of 1%.

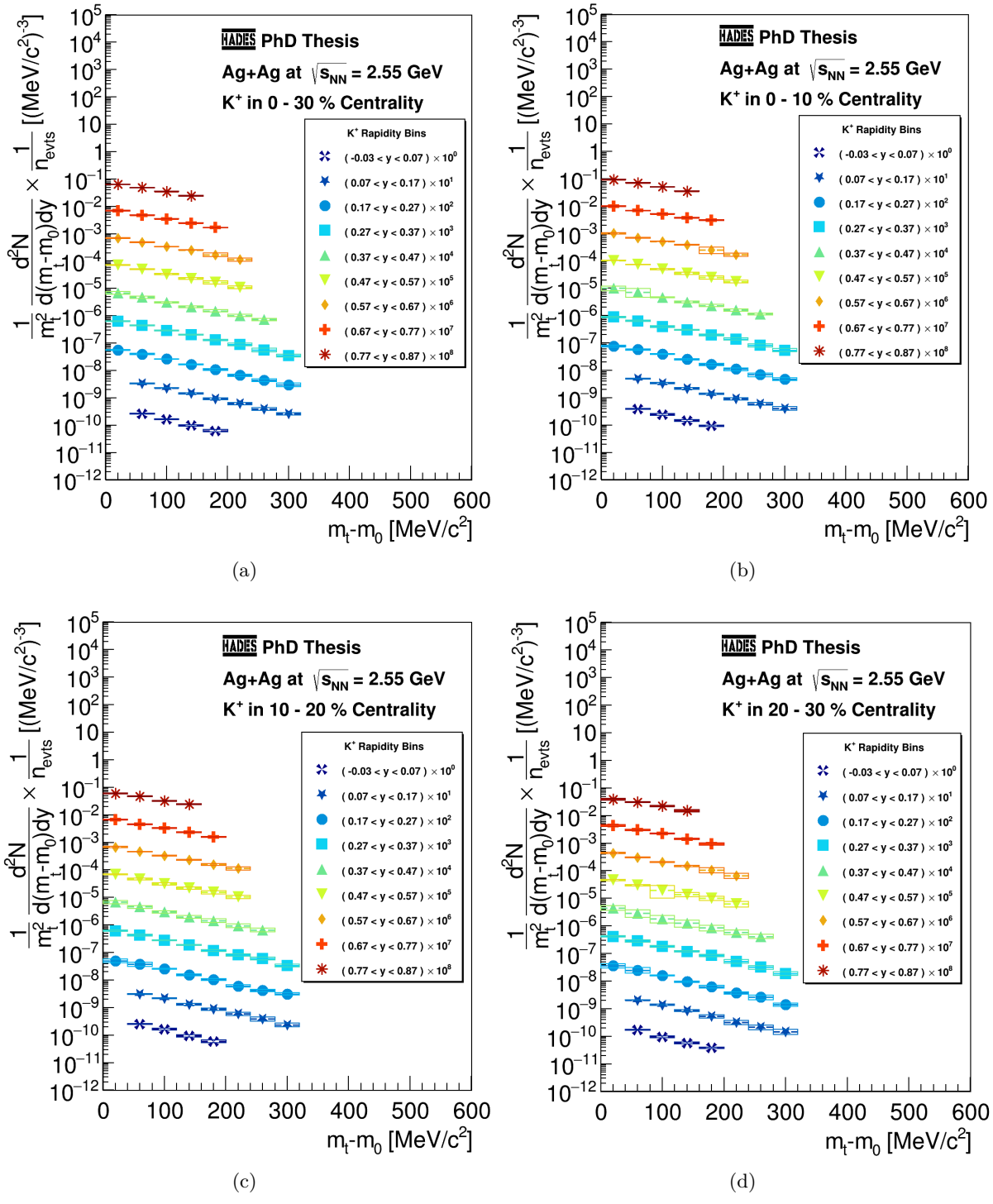

Figure 5.1.: K^+ invariant transverse mass spectra in the HADES acceptance for different collision centrality intervals. Details can be found in the text.

5.1.2. K^-

Figure 5.2 depicts the K^- count rates in the HADES acceptance as a function of transverse mass for the same centrality intervals as for the K^+. The $(m_t - m_0)$ spectra of each rapidity bin are scaled by the number of events as well as $1/m_t^2$ to obtain the Boltzmann representation.

The error boxes represent the systematic count rate extraction effect discussed in section 5.3.1.

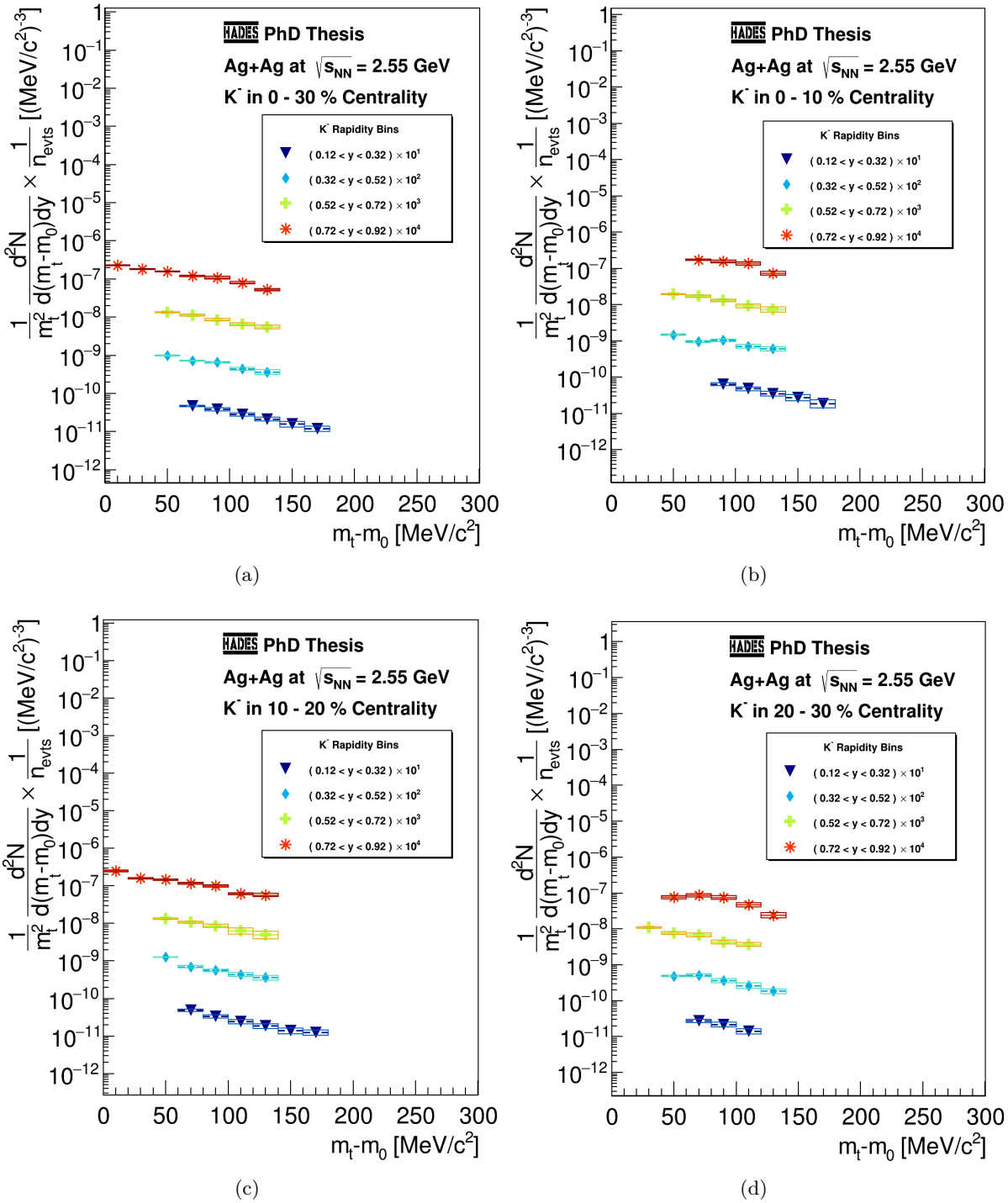

Figure 5.2.: K^- invariant transverse mass spectra in the HADES acceptance for different collision centrality intervals. Details can be found in the text.

The reconstructed rapidity range for the K^- lies between 0.12 and 0.92 in the laboratory reference frame. In the transverse mass direction, the coverage reaches down to values close to m_0, spanning up to ≈ 200 MeV/c^2.
The structure introduced in section 4.1.7 modifies the shape of the background around the K^-

mass signal significantly the closer the laboratory momentum value is to the overlap region at ≈ 600 MeV/c, as figure 4.26 illustrates. This introduces modifications of the background close to the signal peak with the slope of the background distributions varying between different applied track selection criteria. Due to a one order of magnitude smaller significance of the multidifferential K^- signals compared to K^+ and the significantly more difficult background estimation, a precise determination of the resulting systematic uncertainties proves difficult. In $20-30\%$ most central events, for the midrapidity transverse mass spectrum, the observed apparent deviation of the slope from the Boltzmann exponential shape is most likely explained by systematics from the signal extraction process, which the sideband analysis, introduced in section 5.3.1, does not sufficiently account for. This behaviour is not observed in other intervals of centrality, nor does it appear as a result of each subset of selection criteria.
Additionally, due to the structure's significantly larger count rate than the K^-, the K^- signal is completely suppressed in the overlap region. This poses limitations to the count rate extraction and the reconstructed phase space compared to the K^+, as for it, the impact of the structure is significantly less prominent. To compensate for this, the $(m_t - m_0)$ interval step-sizes are reduced to 20 MeV/c^2, half the size used for the K^+. It increases the granularity aiding the later extrapolation into the uncovered invariant transverse mass region. In return, it reduces the available statistics per interval of invariant transverse mass and rapidity, which results in more significant bin-to-bin fluctuations for the smaller centrality steps (figures 5.2(b), 5.2(c) and 5.2(d)).
In the polar angle overlap region between RPC and TOF, which corresponds to the rapidity region $0.32 < y < 0.52$, the additionally introduced TOF energy loss cut leads to a systematic count rate bias for $0 < (m_t - m_0) < 40$ MeV/c^2. Consequently, the final count rates do not match the trend of the remaining bins within the spectrum. Therefore, they are excluded from the sample; otherwise, the invariant transverse mass distribution slope and the subsequent extrapolation are inaccurate.
The accepted invariant transverse mass bins typically possess significances of the mass signal between 30 to 40. This translates into comparably minor statistical uncertainties in the range of a few per cent.

5.1.3. ϕ(1020)

Figure 5.3 shows the acceptance $\times$ efficiency corrected count rates for the ϕ meson in the previously discussed centrality intervals. They are plotted as a function of invariant transverse mass and rapidity, scaled by the number of events and $1/m_t^2$ to obtain the Boltzmann representation. As for the charged Kaons, the spectra are also scaled by 10^i, with i being the rapidity bin number. In contrast to K^+ and K^-, the error emerging from the background description below the peak is not plotted, as the corresponding errors are significantly smaller than 1% and would impair the visibility of the data.
In the rapidity direction, the coverage for the $0-30\%$ most central events is the same as for K^-, from 0.12 to 0.92 in the laboratory reference frame. For the invariant transverse mass direction, the minimum values reach close to 0 MeV/c^2 while the maximum values can be found at 560 MeV/c^2 for the $0-30\%$ most central events and 400 MeV/c^2 for the centrality sub-intervals.
Typical values for significance lie in the area of 5 to 15. This coincides with statistical uncertainties in the range of around 20% on average. Due to the biases from the background description in the underlying invariant mass spectra, discussed in section 4.3.3, several invariant transverse mass bins are expected to lie notably further from the global trend than the 1σ deviations of purely statistical fluctuations. This effect is to be investigated and is discussed in section 5.3.2.

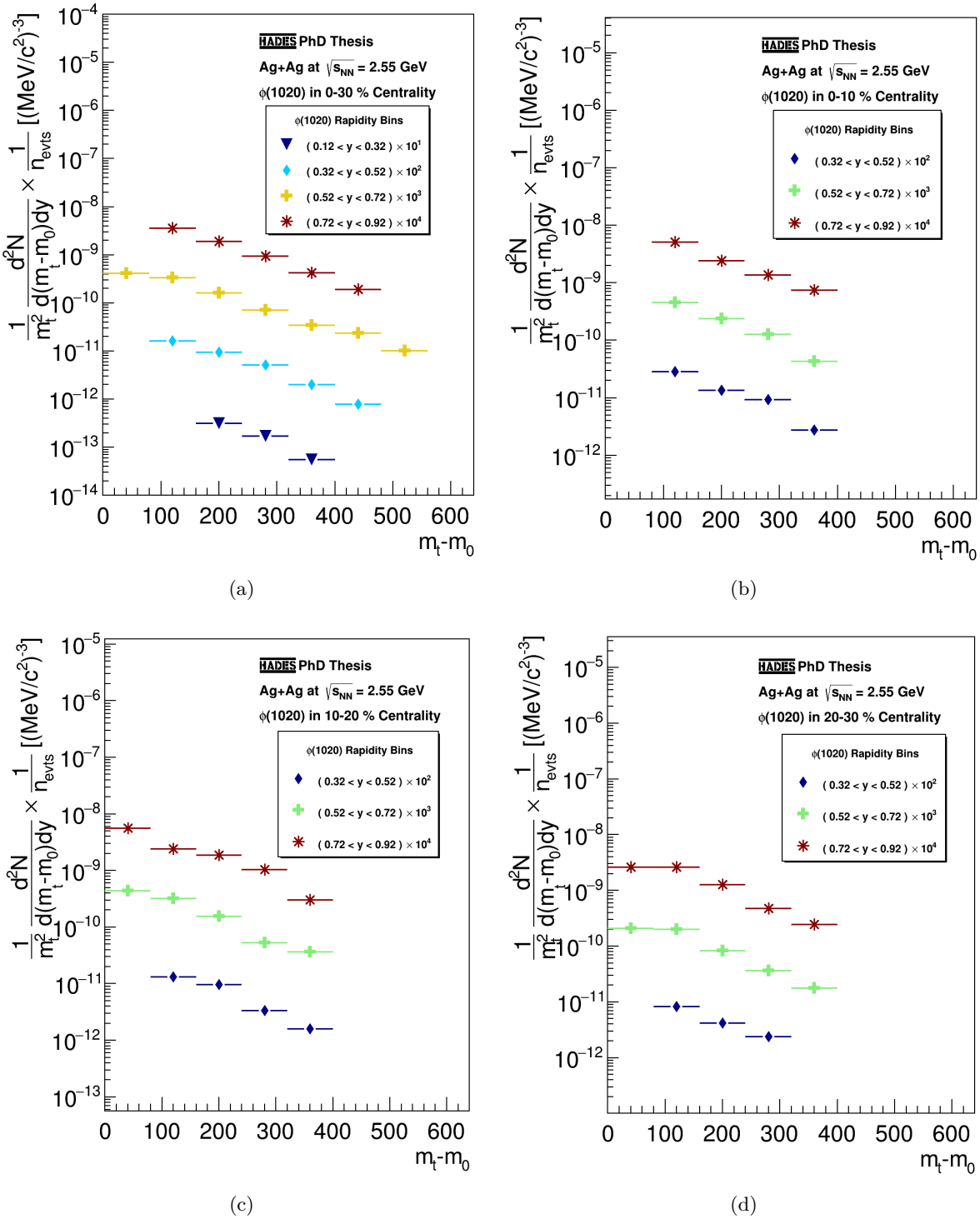

Figure 5.3.: ϕ-meson invariant transverse mass spectra in the HADES acceptance for different collision centrality intervals. Details can be found in the text.

5.2. Extrapolation in Transverse Direction

The previously introduced invariant transverse mass spectra cover a limited range in which $K^{\pm}$ and ϕ-mesons are emitted. Therefore, the data is extrapolated into the transverse mass direction

to obtain the total yield as a function of rapidity by fitting a thermal distribution to the data, which is integrated in the uncovered phase space. For all fits applied for this purpose, an initial value determination is done by performing a 2-dimensional fit to the complete reconstructed and corrected $(m_t - m_0)$-y-plane. The resulting fit parameters are then used as starting values for each invariant transverse mass spectrum to enhance fit stability - particularly for K^- and ϕ-meson. The applied Boltzmann functions are introduced below, followed by a description of their application to the data.

5.2.1. Thermal Model

The slopes of the transverse mass spectra of charged Kaons and ϕ-mesons, as shown in the previous section, indicate thermal particle distributions in the final state. Therefore, to describe the $(m_t - m_0)$ spectra of these particles as a function of rapidity, a fit function representing a spherically symmetric source $\left(\frac{d^2N}{dm_t dy}\right)_{\mathrm{IS}}(m_t - m_0, y)$ is used. This is motivated by the fact, that rapidity y and transverse mass m_t are Lorentz-invariant variables.
The radially symmetric source emitting particles isotropically, in the following called *isotropic staistical* (IS) source, is consequently described by a Boltzmann distribution according to [92]:

$$\left(\frac{d^3N}{d^3p}\right)_{\mathrm{IS}} = C \cdot \exp\left(-\frac{E}{T_{\mathrm{Eff}}}\right) \tag{5.1}$$

with C representing a normalization factor and T_{Eff} the temperature of the system.
The derivative term on the left-hand side of equation 5.1 can be rewritten in terms of invariant transverse mass m_t and azimuthal angle ϕ to

$$\frac{d^3N}{dp_x dp_y dp_z} = \frac{1}{m_t}\frac{1}{E}\frac{d^3N}{dm_t d\phi dy}$$

using relation (8.3) in [92]. Due to the assumption of spherical symmetry and the analysis of particle spectra independent of their orientation relative to the event plane, integration over $d\phi$ from 0 to 2π yields:

$$\left(\frac{d^2N}{dm_t dy}\right)_{\mathrm{IS}} = 2\pi \cdot m_t \cdot E \cdot C \cdot \exp\left(-\frac{E}{T_{\mathrm{Eff}}}\right)$$

Introducing the relation $E = m_t \cosh(y)$ [57], and including the constant factor 2π within C, we obtain the correlation between the experimentally measured number of particles per m_t-y interval and the corresponding model

$$\left(\frac{d^2N}{dm_t dy}\right)_{\mathrm{IS}} = C \cdot m_t^2 \cdot \cosh(y) \cdot \exp\left(-\frac{m_t \cdot \cosh(y)}{T_{\mathrm{Eff}}}\right) \tag{5.2}$$

The experimental data are scaled by $1/m_t^2$ and $1/n_{\mathrm{Events}}$. Furthermore, as it makes direct comparisons between particles easier, the rest mass is subtracted from m_t. Consequently, m_t has to be replaced by $(m_t - m_0)$ in equation 5.2.1. Defining T_B as

$$T_B = \frac{T_{\mathrm{Eff}}}{\cosh(y)} \tag{5.3}$$

we can identify T_{Eff} as the system's temperature under the assumption of a purely thermal source. Equation 5.3 is used to fit the T_{Eff} over y distributions and extract the resulting average Boltzmann temperature of the corresponding particle source at freeze-out.

The analytic integration of equation is performed over the transverse mass

$$\left(\frac{dN}{dy}\right)_{\mathrm{IS}} = \int_{m_0}^{\infty} C \cdot m_t^2 \cdot \cosh(y) \cdot \exp\left(-\frac{m_t \cdot \cosh(y)}{T_{\mathrm{Eff}}}\right) dm_t$$

as the resulting distribution

$$\left(\frac{dN}{dy}\right)_{\mathrm{IS}} = C \cdot T_{\mathrm{Eff}} \cdot \exp\left(-\frac{m_0 \cosh(y)}{T_{\mathrm{Eff}}}\right) \cdot \left(m_0^2 + 2m_0 \frac{T_{\mathrm{Eff}}}{\cosh(y)} + 2\frac{T_{\mathrm{Eff}}^2}{\cosh^2(y)}\right) \tag{5.4}$$

can be approximated as a Gaussian distribution. This is done by performing a second order Taylor expansion of $\cosh(y) \approx 1 + \frac{y^2}{2} + ...$ around 0 and assuming the rightmost bracketed term of equation 5.4 to be constant. The latter can be done, as by introducing the average Boltzmann temperature, only constant factors remain within the expression so that it can be included in the scaling factor C.
Ultimately, one arrives at

$$\left(\frac{dN}{dy}\right)_{\mathrm{IS}} \approx C \cdot \exp\left(-\frac{y^2}{2\sigma^2}\right) \tag{5.5}$$

defining σ as $\sigma = \sqrt{\frac{T}{m_0}}$.
Figure 5.4 shows exemplary distributions obtained from the model for a particle with the nominal $K^{\pm}$ particle mass with an effective freeze-out temperature of 120 MeV. In figure 5.4(b), the resulting Gaussian shape for the dN/dy distribution becomes visible.

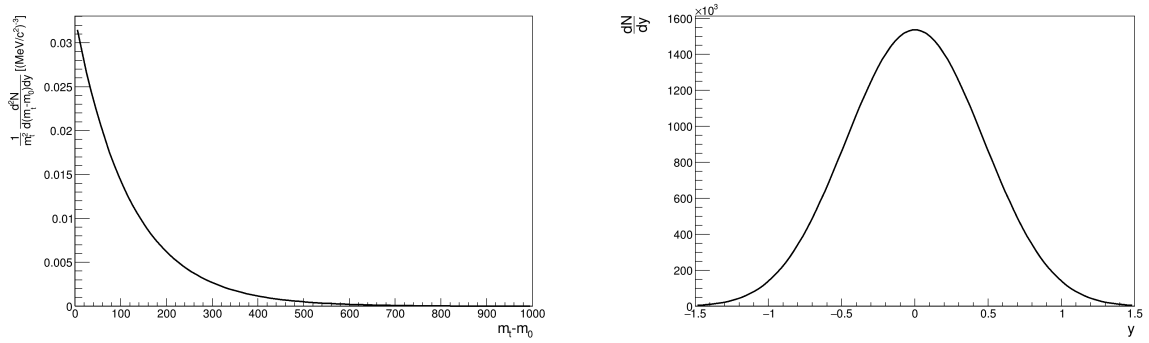

(a) $m_t - m_0$ (b) dN/dy

Figure 5.4.: Resulting distribution shapes from the thermal model for a particle of $K^{\pm}$ mass, emerging from a system with a freeze-out temperature of 120 MeV. The scaling parameter C is set to 1. For the $m_t - m_0$ spectrum, midrapidity ($y = 0$) was chosen.

5.2.2. K^+

By applying equation 5.2.1 as a fit function for the invariant transverse mass spectra, using the resulting fit parameters from the 2-dimensional fit as starting values for the minimisation, we obtain the results presented in figures 5.5 to 5.8. They show the invariant transverse mass spectra of the K^+ in the same representation as in figure 6.5.
Each figure furthermore depicts the ratio between data points and the applied fit function on the right side. As the applied Boltzmann function has a direct physical interpretation, so do the corresponding fit parameters.

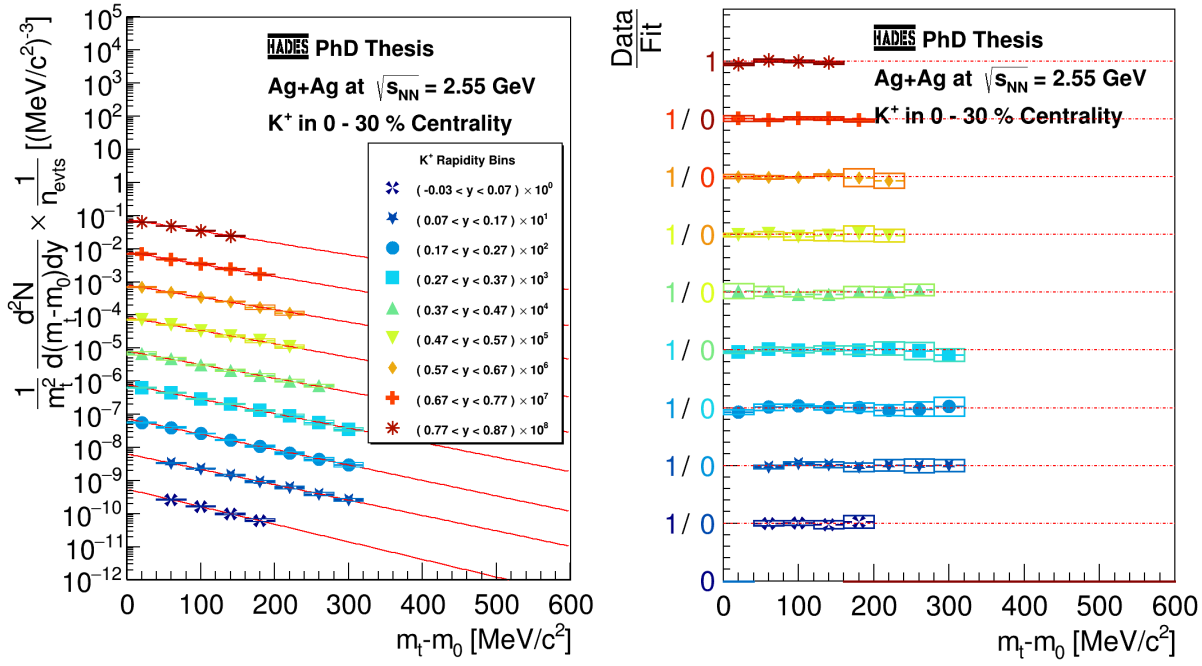

(a) (b)

Figure 5.5.: Fitted K^+ invariant transverse mass spectra for $0-30\%$ most central events (a) and the ratio between data and the applied Boltzmann fit (b). Details can be found in the text.

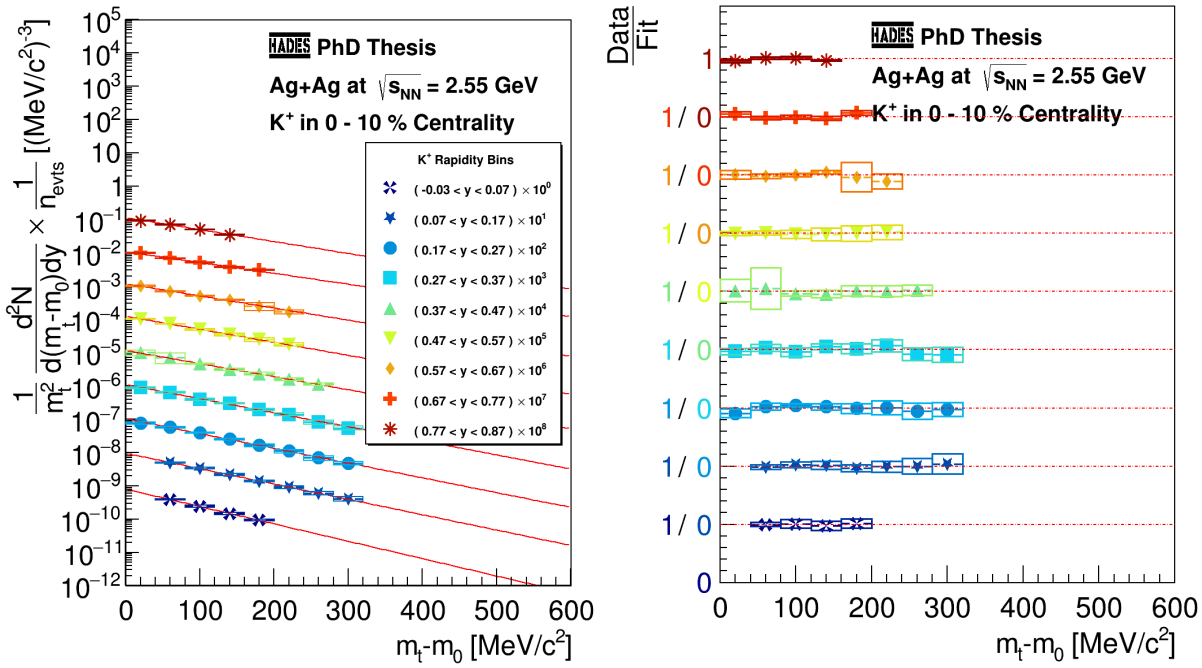

(a) (b)

Figure 5.6.: Fitted K^+ invariant transverse mass spectra for $0-10\%$ most central events (a) and the ratio between data and the applied Boltzmann fit (b). Details can be found in the text.

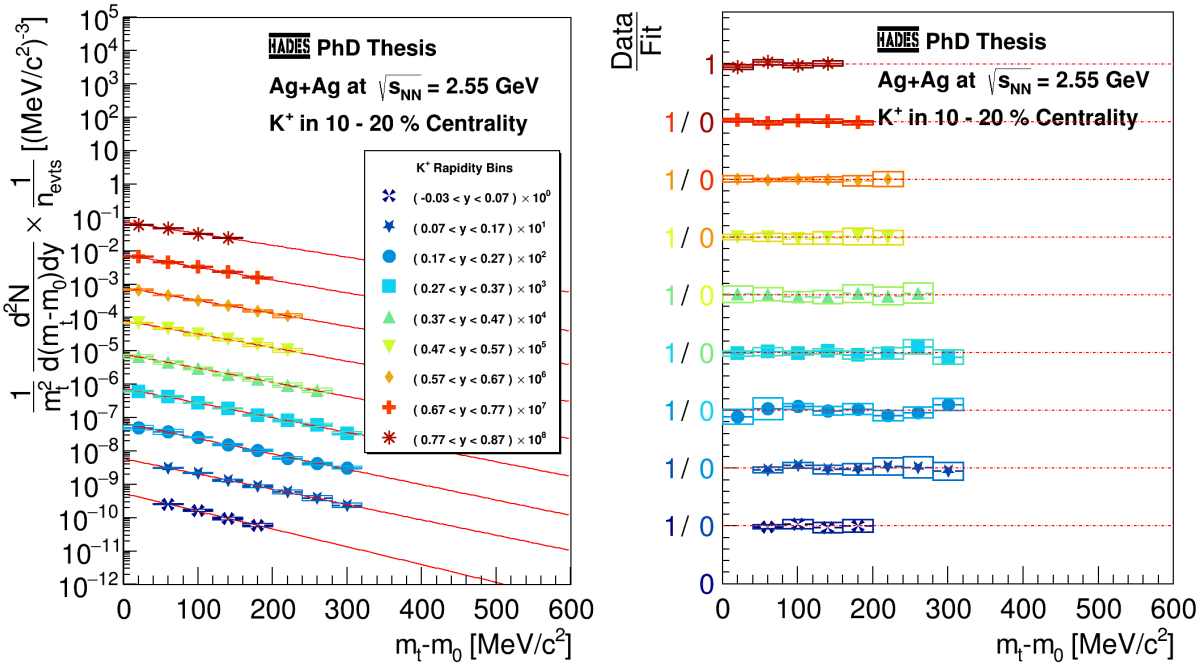

(a) (b)

Figure 5.7.: Fitted K^+ invariant transverse mass spectra for $10-20\%$ most central events (a) and the ratio between data and the applied Boltzmann fit (b). Details can be found in the text.

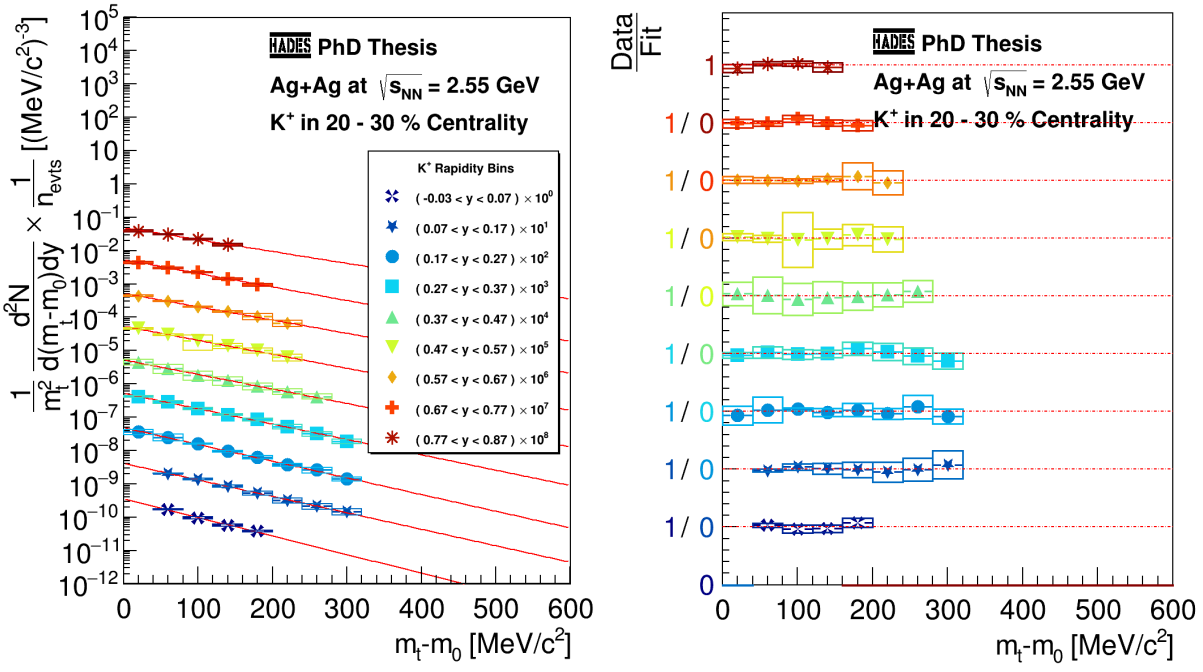

(a) (b)

Figure 5.8.: Fitted K^+ invariant transverse mass spectra for $20-30\%$ most central events (a) and the ratio between data and the applied Boltzmann fit (b). Details can be found in the text.

The first parameter is the K^+ rest mass. The second parameter represents the scaling parameter C and is set individually to the content of the first reconstructed m_t bin of each spectrum. Finally, the third parameter represents the exponent in the $1/m_t^2$ scaling.
As illustrated in figures 5.5(b) to 5.8(b), the model fit describes the data well, and there is no significant deviation of the data from the Boltzmann shape. For each rapidity interval, summing over the data in transverse mass direction and integrating the fit function for extrapolation, the particle production rate per interval of rapidity (dN/dy) is obtained. The fitting procedure takes into account only statistical uncertainties. Projecting the extracted count rate per event as a function of rapidity gives the final dN/dy distribution for the entire reconstructed phase space, as depicted in figures 5.9 and 5.10 to 5.12 for different intervals in collision centrality. Empty circles represent mirrored data points around midrapidity to visualise the degree of symmetry. A shift of rapidity values by 0.82 (midrapidity) is performed to transform the spectra from the laboratory reference frame into the centre of mass frame.

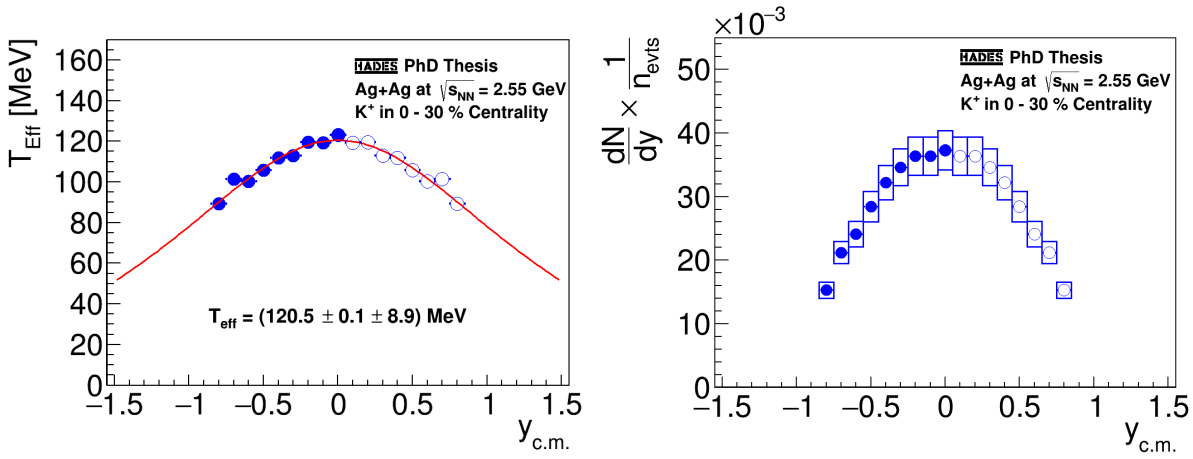

(a) (b)

Figure 5.9.: Resulting K^+ T_{Eff} and dN/dy spectra for the $0-30\%$ most central events.

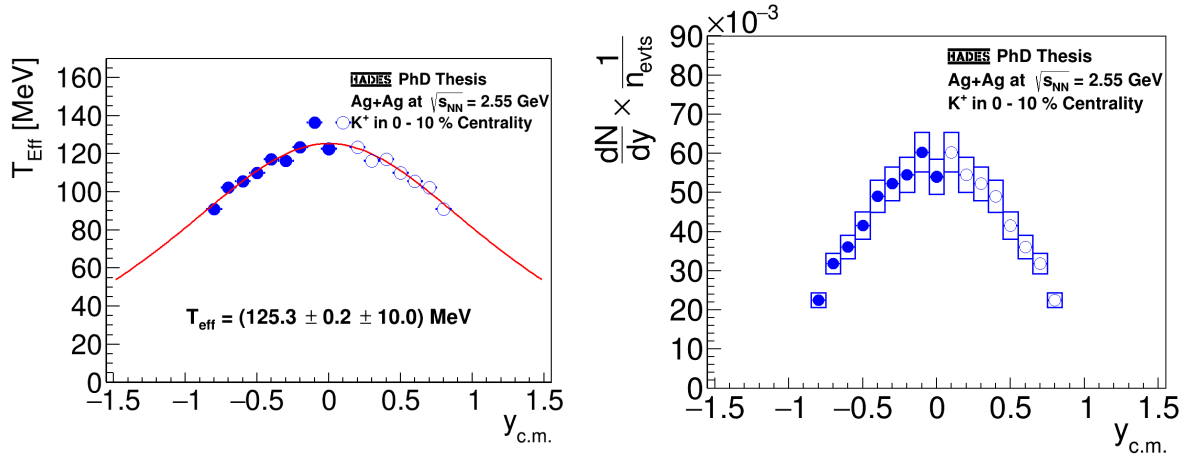

(a) (b)

Figure 5.10.: Resulting K^+ T_{Eff} and dN/dy spectra for the $0-10\%$ most central events.

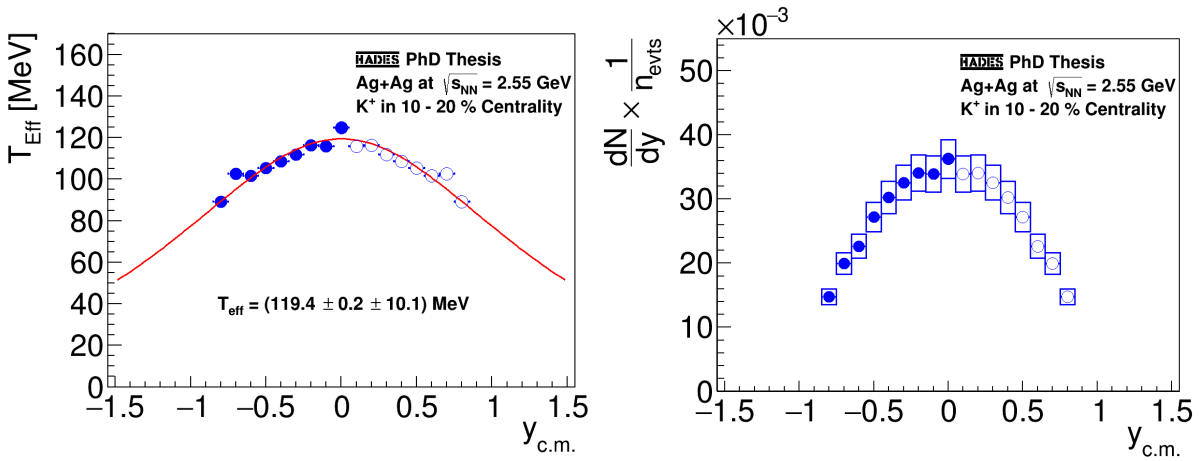

(a) (b)

Figure 5.11.: Resulting K^+ T_{Eff} and dN/dy spectra for the $10-20\%$ most central events.

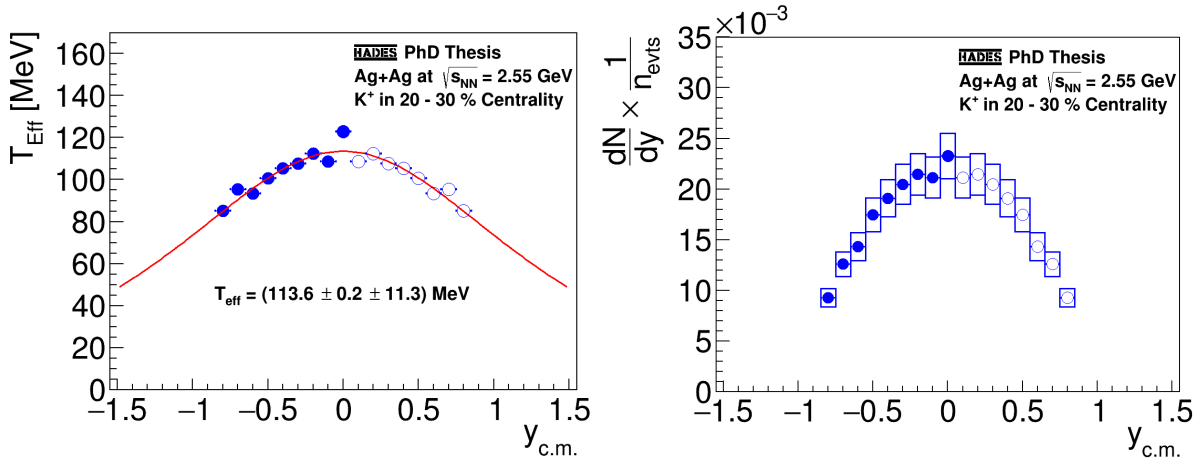

(a) (b)

Figure 5.12.: Resulting K^+ T_{Eff} and dN/dy spectra for the $20-30\%$ most central events.

A discussion of the resulting systematic effects is done in section 5.3.1. For K^+, those lie around 8%. The previously introduced distribution of the inverse slope parameter as a function of rapidity is fitted with equation 5.3. As the phase space coverage in transverse mass direction is reduced towards midrapidity, systematic uncertainties increase towards the area crucial for the extraction of T_{Eff}. This fitting procedure is performed to compensate for this in parts, and the effective temperature is extracted from it at $y = 0$. This is shown in figures 5.9(a) to 5.12(a). It yields $T_{\mathrm{Eff}} = (120.2 \pm 0.1(\mathrm{stat.}) \pm 9.1(\mathrm{syst.}))$ MeV in $0-30\%$ most central events.

5.2.3. K^-

Figures 5.13 to 5.16 show the result of the fitting procedure for the K^- invariant transverse mass spectra previously shown in figure 5.2.

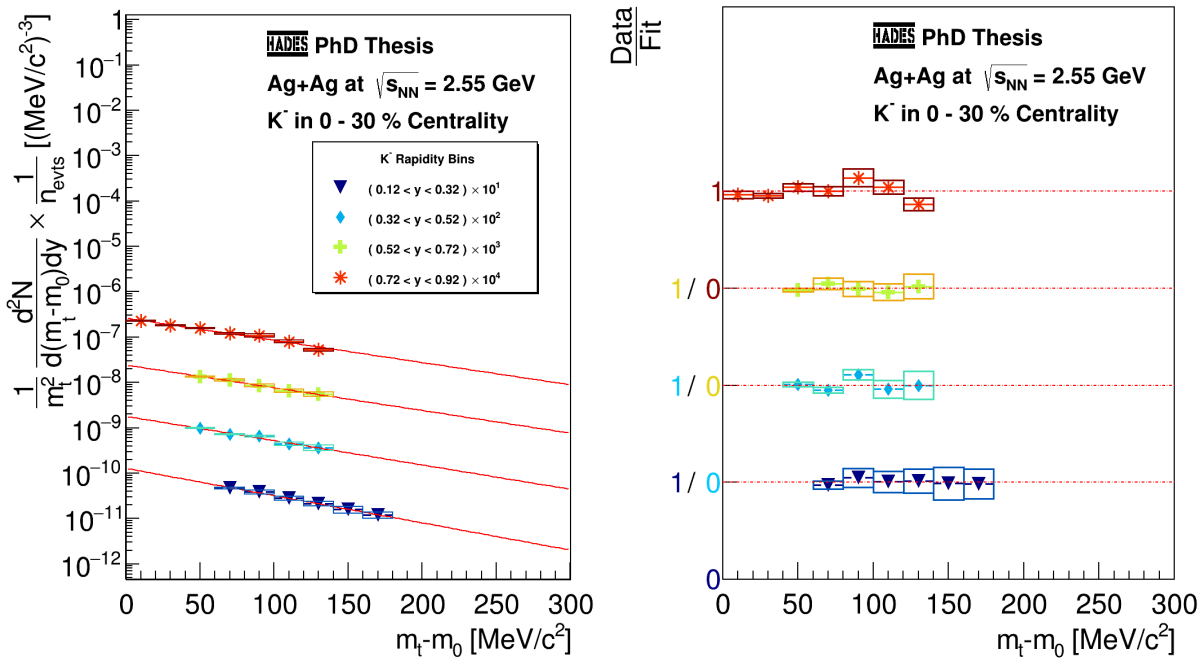

(a) (b)

Figure 5.13.: Fitted K^- invariant transverse mass spectra for $0-30\%$ most central events (a) and the ratio between data and the applied Boltzmann fit (b). Details can be found in the text.

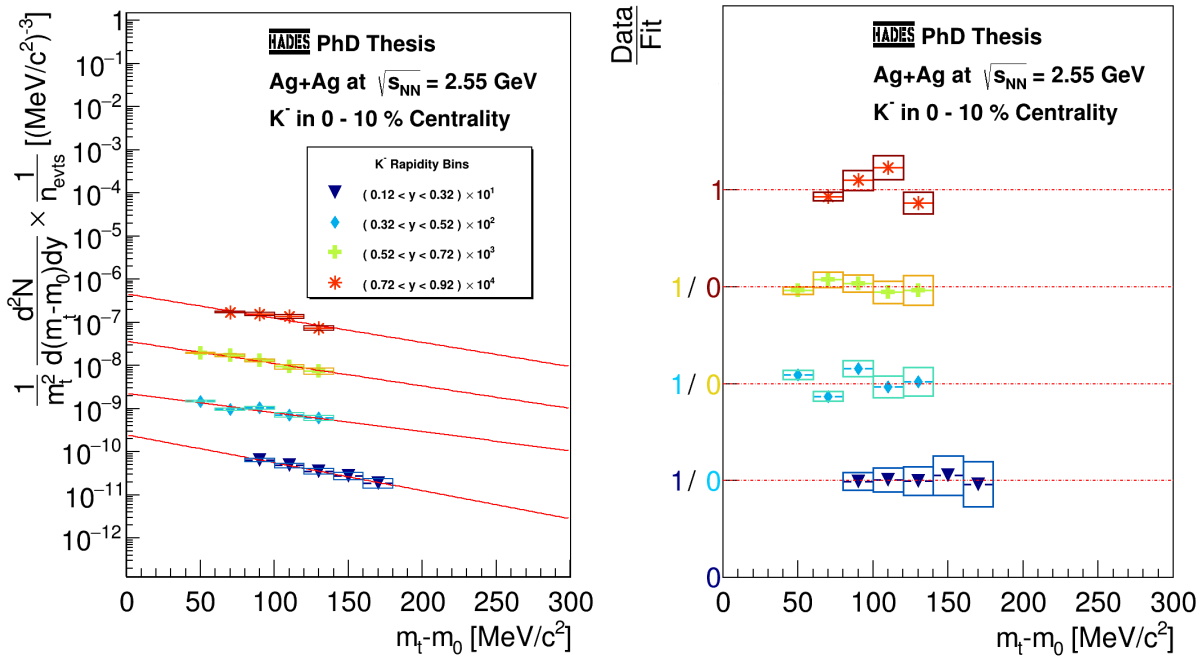

(a) (b)

Figure 5.14.: Fitted K^- invariant transverse mass spectra for $0-10\%$ most central events (a) and the ratio between data and the applied Boltzmann fit (b). Details can be found in the text.

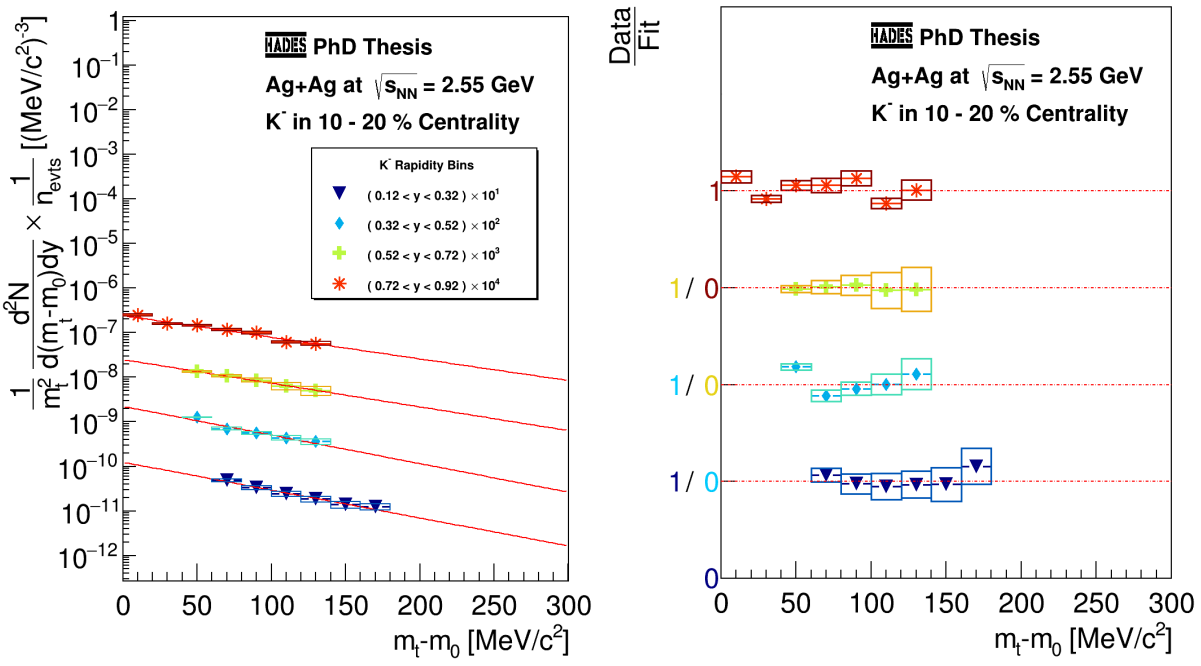

(a) (b)

Figure 5.15.: Fitted K^- invariant transverse mass spectra for $10-20\%$ most central events (a) and the ratio between data and the applied Boltzmann fit (b). Details are in the text.

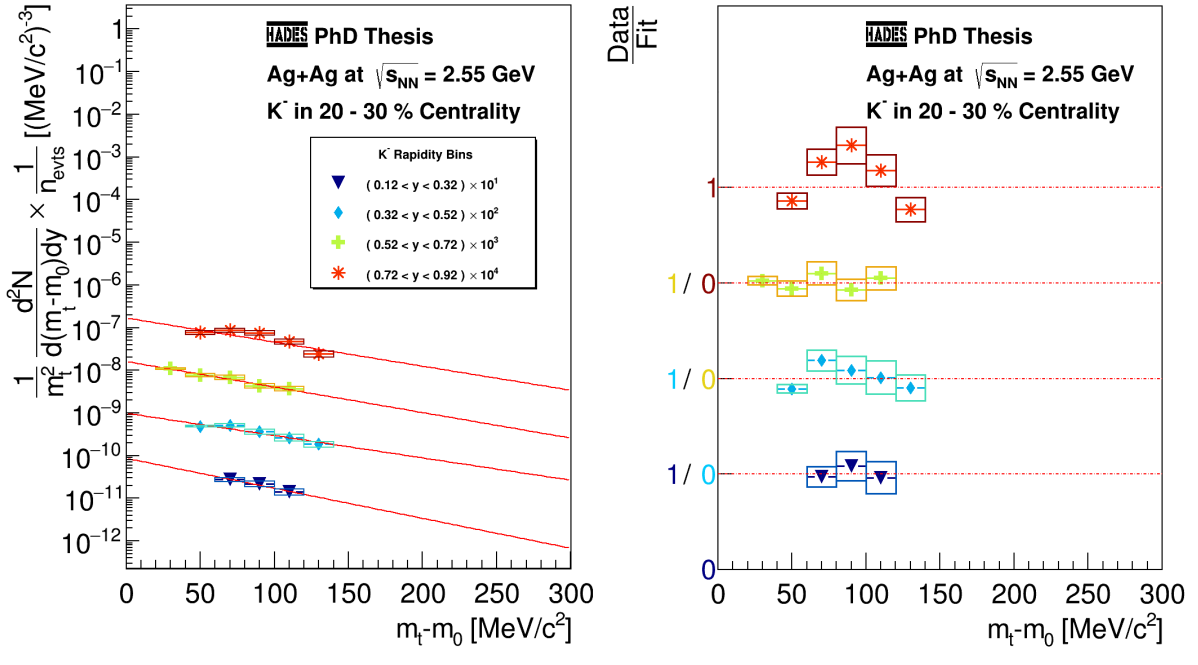

(a) (b)

Figure 5.16.: Fitted K^- invariant transverse mass spectra for $20-30\%$ most central events (a) and the ratio between data and the applied Boltzmann fit (b). Details are in the text.

For each figure, the right side shows the accordance between the applied model fit function and the data. The slope in the rapidity interval $0.32 < y < 0.52$ is consistent with the global trend for $0-30\%$ most central events, which justifies the exclusion of the overlap region discussed in section 5.1.2 as a necessary step. Nevertheless, the behaviour of the slope of the distribution varies between different intervals of collision centrality, leading to significant variations from the inverse slope parameter trends extracted for this bin.
The general problem of systematic effects influencing the slope is demonstrated by the distributions of the inverse slope parameters as a function of rapidity in figures 5.17 and 5.18 to 5.20. The substantial modifications of the background around and below the K^- mass peak need further investigation to reduce the visibly large systematic effects. In figure **??**, the T_{Eff} distribution in $0-30\%$ most central events is shown with the corresponding $\cosh(y)$ fit function applied.

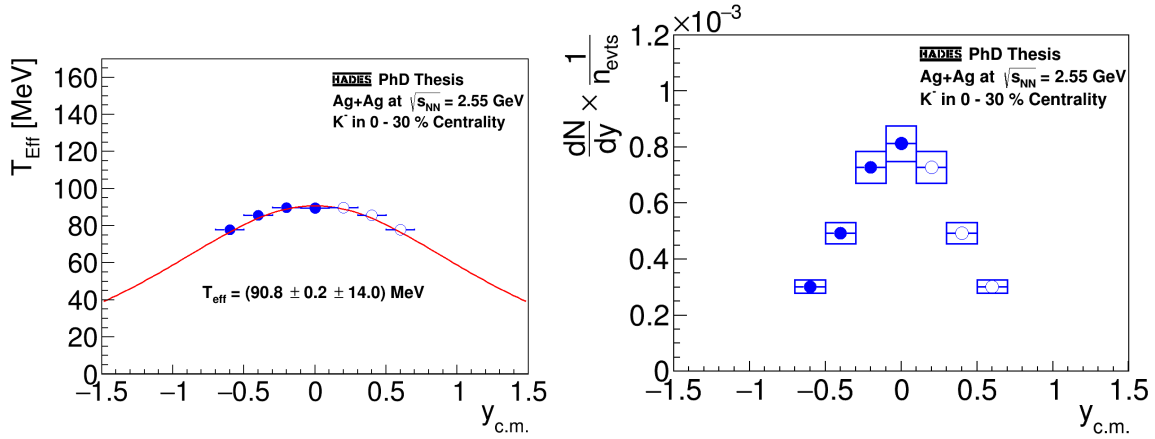

(a) (b)

Figure 5.17.: Resulting K^- T_{Eff} and dN/dy spectra for the $0-30\%$ most central events.

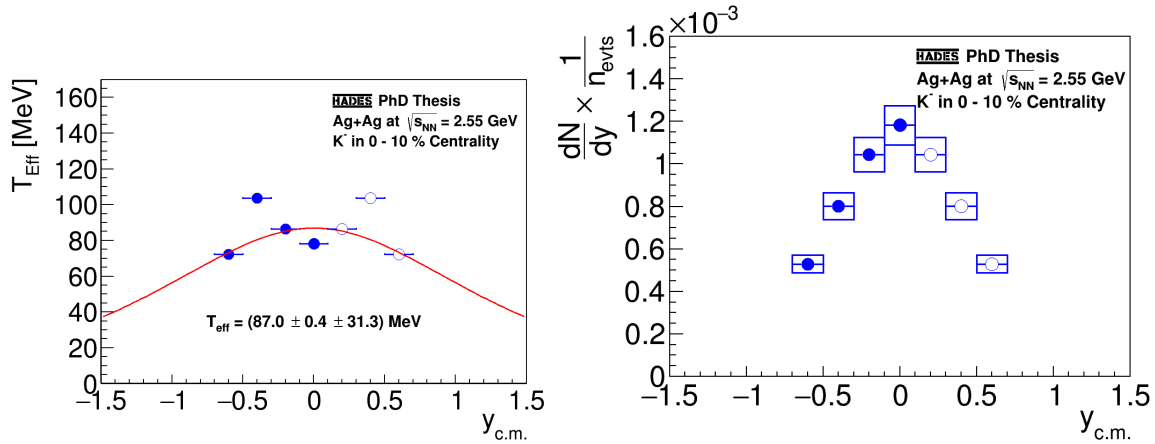

(a) (b)

Figure 5.18.: Resulting K^- T_{Eff} and dN/dy spectra for the $0-10\%$ most central events.

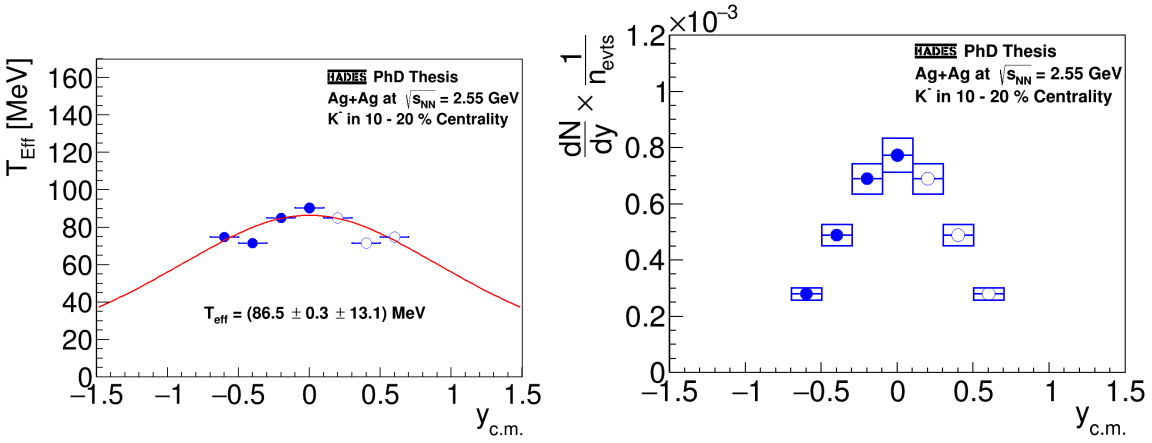

(a) (b)

Figure 5.19.: Resulting K^- T_{Eff} and dN/dy spectra for the $10-20\%$ most central events.

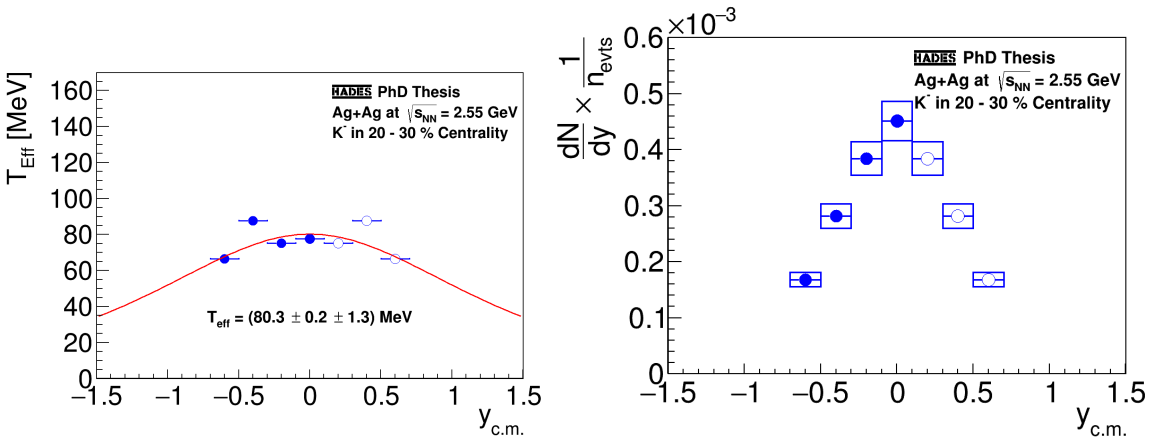

(a) (b)

Figure 5.20.: Resulting K^- T_{Eff} and dN/dy spectra for the $20-30\%$ most central events.

A good accordance of data and fit function, with fluctuations typically in the range of less than 5%, underlines the reliability of the signal extraction as well as the acceptance $\times$ efficiency correction methods. A larger available phase space would allow for significantly reduced systematic effects.
Figures 5.17 and 5.18 to 5.20 indicate a significant deviation of the T_{Eff} parameter in comparison to the K^+. For the K^-, a value of ≈ 91 MeV is obtained. Including the systematic errors of T_{Eff} from K^+ and K^-, both values consistently deviate by a value of $\approx 3\sigma$. Thusly, the difference can not be explained by any systematic effect in the extraction procedure. The implications are discussed in section 6.4.1.

5.2.4. $\phi(1020)$

For the fitting procedure with equation 5.2.1, the same representation is chosen as for the K^+ and K^-. This is displayed in figures 5.21 to 5.24.

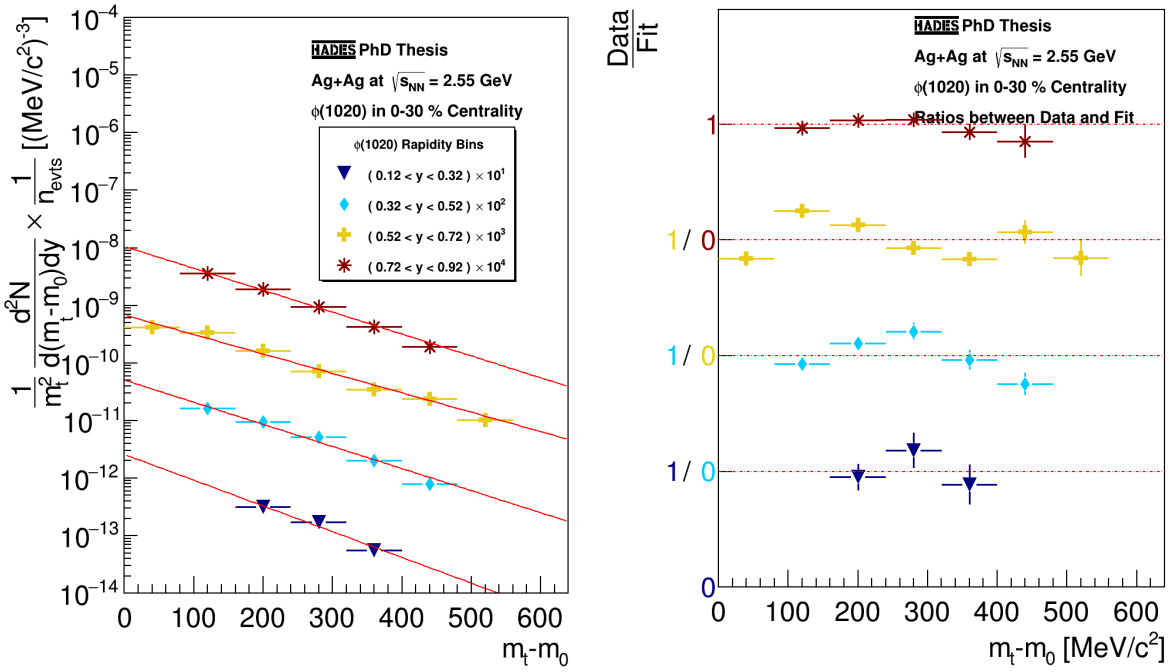

(a) (b)

Figure 5.21.: Fitted ϕ-meson invariant transverse mass spectra for $0-30\%$ most central events (a) and the ratio between data and the applied Boltzmann fit (b). Details in the text.

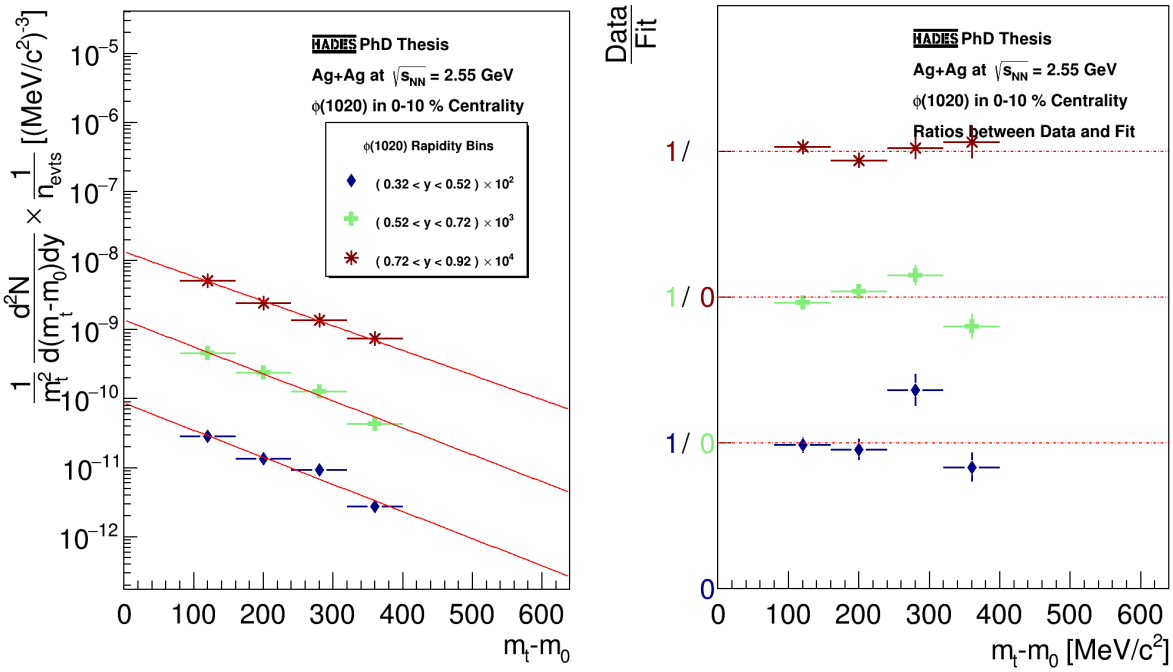

(a) (b)

Figure 5.22.: Fitted ϕ-meson invariant transverse mass spectra for $0-10\%$ most central events (a) and the ratio between data and the applied Boltzmann fit (b). Details in the text.

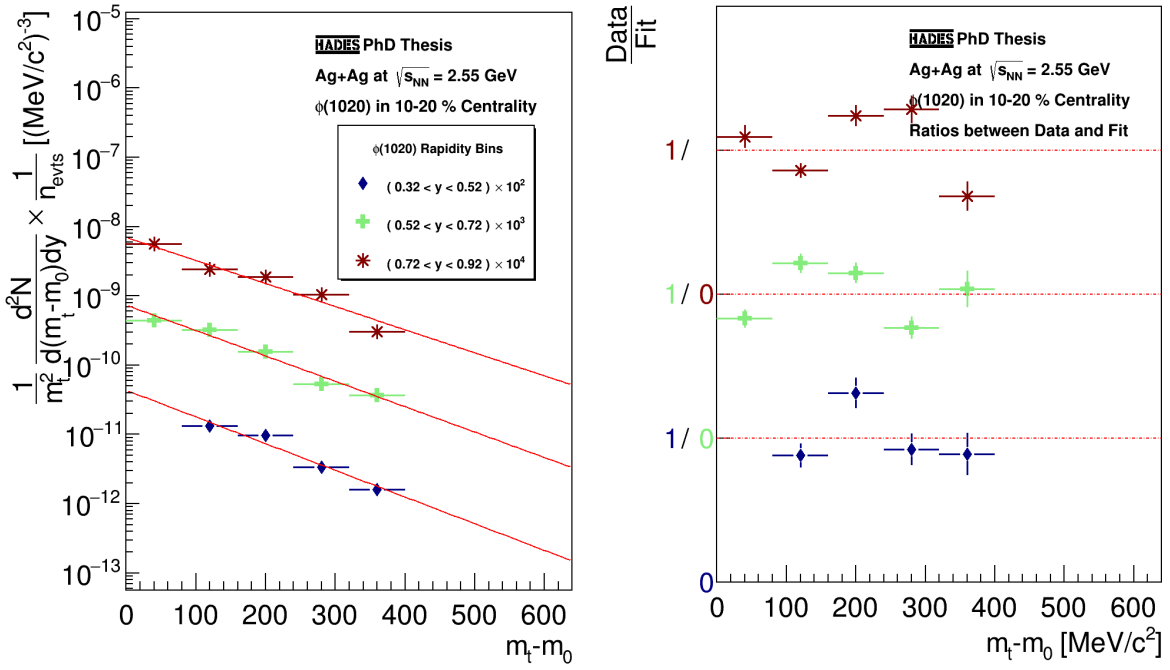

(a) (b)

Figure 5.23.: Fitted ϕ-meson invariant transverse mass spectra for $10 - 20\%$ most central events (a) and the ratio between data and the applied Boltzmann fit (b). Details in the text.

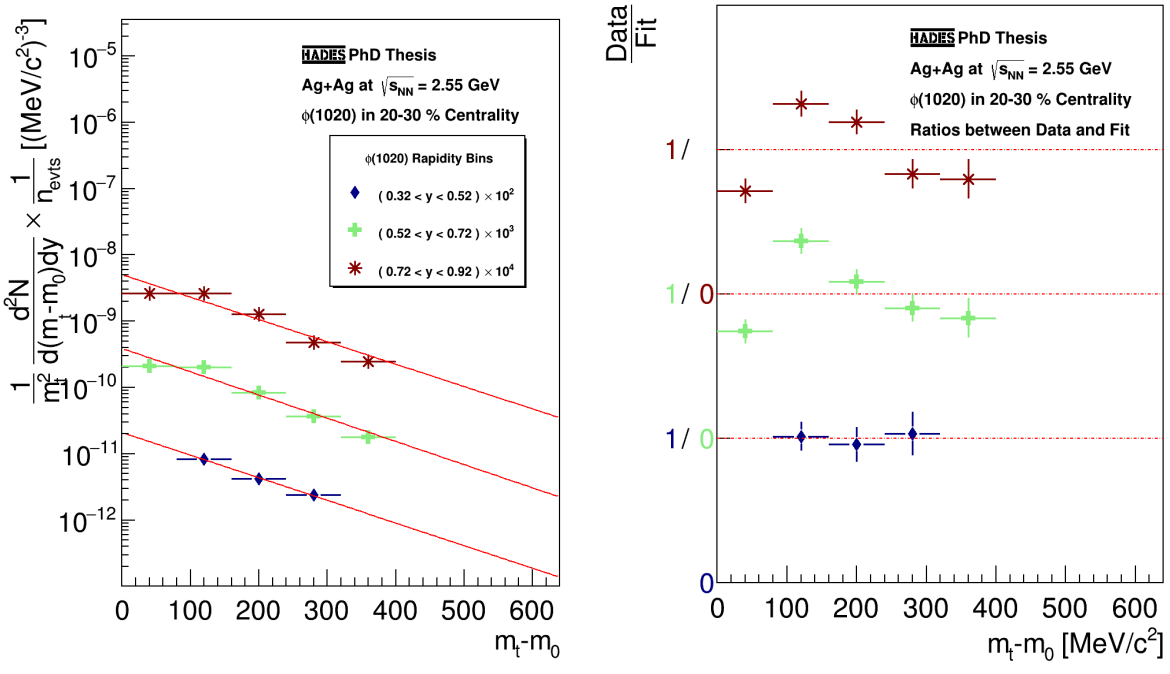

(a) (b)

Figure 5.24.: Fitted ϕ-meson invariant transverse mass spectra for $20 - 30\%$ most central events (a) and the ratio between data and the applied Boltzmann fit (b). Details in the text.

As it can be seen in the ratio plots, the $(m_t - m_0)$ spectra of the rapidity intervals $0.32 < y < 0.52$ and $0.52 < y < 0.72$ (in $20 - 30\%$ centrality $0.52 < y < 0.72$ and $0.72 < y < 0.92$) deviate significantly from the global trend at low invariant transverse mass bins. This is due to the effect discussed in section 5.1.3 that a merely detectable overestimation of the subtracted background leads to a significantly undercorrected counting rate. The resulting systematic effect and how it is taken into account is discussed in section 5.3.1. In general, the fluctuations in invariant transverse mass direction can be accounted for by the uncertainty in the precision of the normalisation procedure between the mixed event background and the invariant mass distributions obtained from data.
The results obtained from the fitted invariant transverse mass distributions are summarised in figures 5.25 and 5.26 to 5.28 with the distributions of the inverse slope parameters and the extracted ϕ count rates per event, both as a function of rapidity.

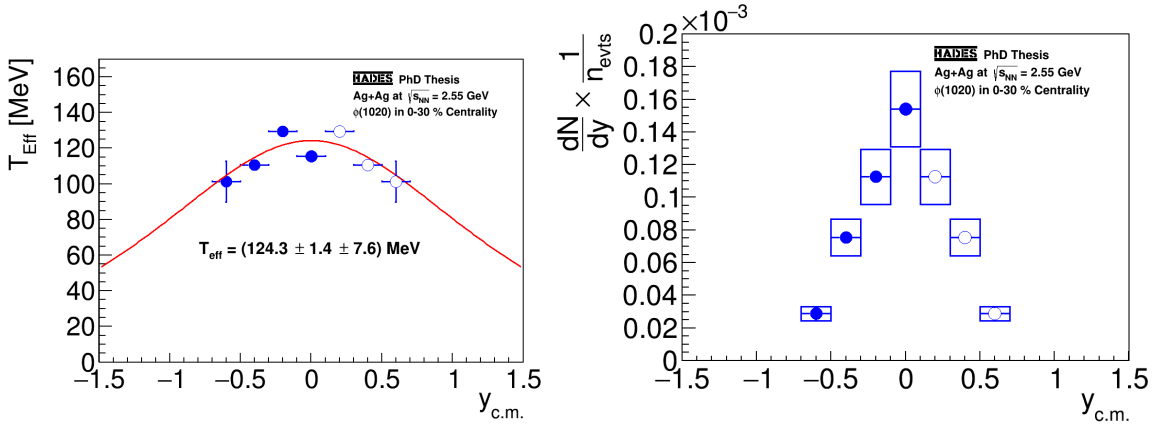

(a) (b)

Figure 5.25.: Resulting ϕ-meson T_{Eff} and dN/dy spectra for the $0 - 30\%$ most central events.

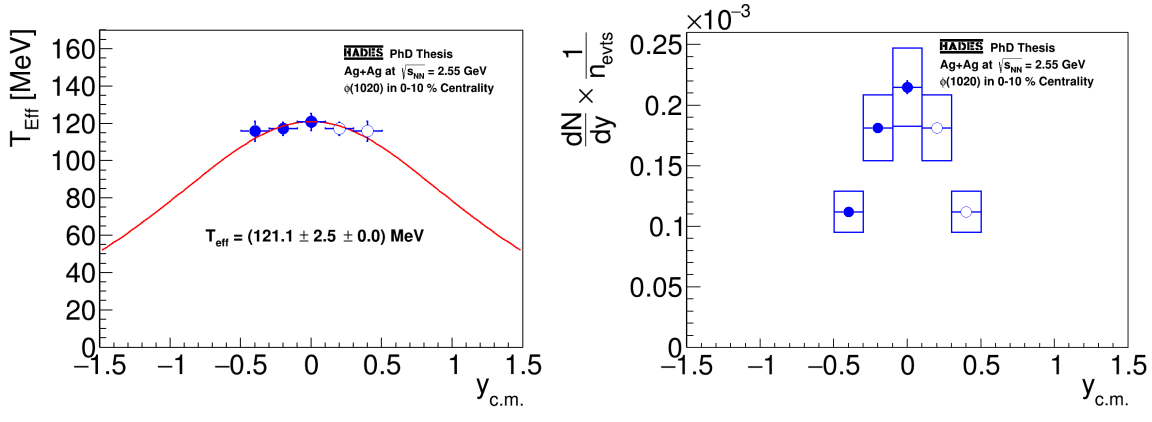

(a) (b)

Figure 5.26.: Resulting ϕ-meson T_{Eff} and dN/dy spectra for the $0 - 10\%$ most central events.

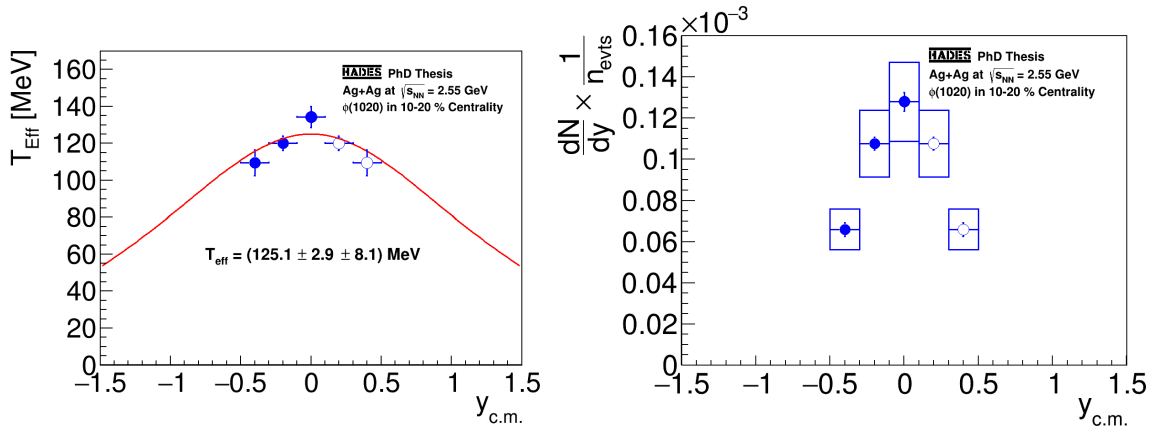

(a) (b)

Figure 5.27.: Resulting ϕ-meson T_{Eff} and dN/dy spectra for the $10-20\%$ most central events.

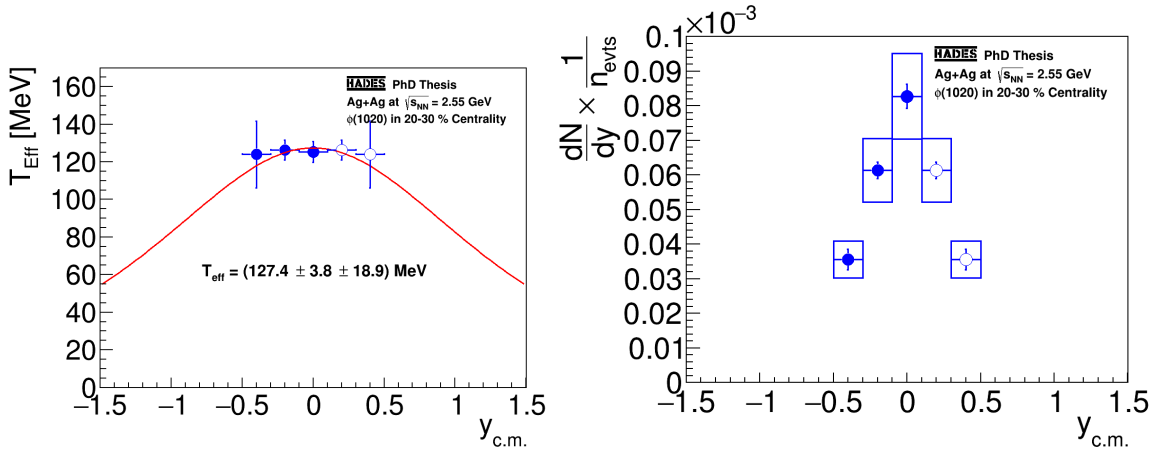

(a) (b)

Figure 5.28.: Resulting ϕ-meson T_{Eff} and dN/dy spectra for the $20-30\%$ most central events.

As in the previous cases, the inverse slope parameter is extracted by applying equation 5.3 to the T_{Eff} spectrum as depicted in figure 5.25(a). The obtained value is entirely consistent, within errors, with the approximately 120 MeV for the K^+, also consistently deviating from the K^- result with more than 3σ. Even though the systematic effects are expected to be significant, it is apparent that the obtained values for the ϕ-meson and the K^+ are in accordance, while the value of ≈ 90 MeV obtained for the K^- lies well outside any systematic effect.

5.3. Systematic Error Evaluation

5.3.1. Systematic Error Evaluation for $K^{\pm}$

Besides the statistical uncertainties arising from the amount of statistics available, several other sources of uncertainty must be considered. There are at least three sources of systematic uncertainties present in the data previously presented:

- A possible bias in the background description affects the signal extraction accuracy.

- An inaccurate Acceptance × Efficiency correction due to deviations in the response between GEANT simulation and experimental data to the application of track selection criteria.
- A potential bias due to the applied fitting and extrapolation method for differential spectra.

The first uncertainty is not quantifiable in a simple manner. As the background below the $K^{\pm}$ mass signal peak is generally dominated by non-gaussian tails of the p and $\pi^{\pm}$ mass distributions, which are difficult to model with sufficient accuracy, there is no direct measure for the goodness of the description. Furthermore, the slopes of the $K^{\pm}$ mass distribution tails are generally not well known due to the variable background shape, which additionally affects the background description. Nevertheless, in the first order, the error of the background description below the peak can be assumed to be similar to the error of the background descriptions in the sidebands of the mass distribution. Consequently, the relative deviation of the signal and the background counts in the interpolation regions

$$\Delta_{\text{interpol}} = \frac{\left|\left(\sum_{\mu-7\sigma}^{\mu-4\sigma} y_{i,\text{Data}} + \sum_{\mu+4\sigma}^{\mu+7\sigma} y_{i,\text{Data}}\right) - \left(\sum_{\mu-7\sigma}^{\mu-4\sigma} y_{i,\text{Back}} + \sum_{\mu+4\sigma}^{\mu+7\sigma} y_{i,\text{Back}}\right)\right|}{\sum_{\mu-7\sigma}^{\mu-4\sigma} y_{i,\text{Data}} + \sum_{\mu+4\sigma}^{\mu+7\sigma} y_{i,\text{Data}}} \tag{5.6}$$

is used to estimate the relative deviation of the background description by the interpolator concerning the true background. Here y_i stands for the bin content of bin i, either for data or for the interpolated background. For both cases, the sum over the sideband bin entries in the range $\mu \pm 4\sigma$ to $\mu \pm 7\sigma$ is formed and subtracted from each other. The resulting deviation is divided by the total number of data entries in these areas. This results in a relative deviation of the interpolator background description from the true background in the data. Figure 5.29 depicts an exemplary mass distribution with the interpolated background in red and the interpolation sideband regions marked by the arrows.

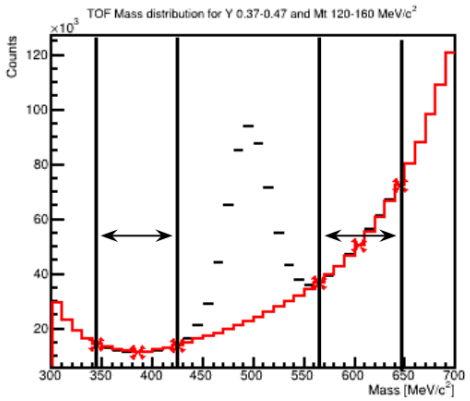

Figure 5.29.: Example of a K^{+} mass spectrum with the applied interpolated background description. The vertical lines indicate the sideband areas in which data and interpolation are compared.

This is performed on all mass spectra within the $(m_t - m_0)$-y plane. Finally, via Gaussian error propagation, the relative error resulting from the background description is derived for each rapidity interval individually.

The second source for uncertainties, an inaccurate acceptance × efficiency correction, can be estimated by the variation of track selection criteria. As mentioned in section 3.6.2, there exists an upper limit for the χ^2_{RK} and χ^2_{MM} values accepted for track candidates. As shown in section 4.1.2, data and simulation converge around these values to reach the same relative statistics loss due to the applied criteria. Consequently, the full analysis chain is performed several times, always varying one selection parameter. As $\chi^2_{MM} = 3$ coincides with the initial hadron selection criterion, this parameter is not varied. χ^2_{RK} is set to 200 for all analyses in this work. There is no

significant gain in significance for lower χ^2_{RK}-values and the number of reconstructed particles, relative to the case of no applied criterion, differs increasingly between data and simulation, the lower the value is chosen (see section 4.1.2). Therefore, to prevent large biases in the correction, χ^2_{RK} is set to 200.
To estimate the systematic uncertainty arising from the correction due to this parameter, the resulting production rate in each rapidity interval is compared between the spectra for $\chi^2_{RK} = 200$ and $\chi^2_{RK} = 400$. The relative deviation globally lies around 3% and is therefore considered. Likewise, the same comparison is performed with and without additional constraints due to the MDC-specific energy loss cut. As this criterion is partly momentum dependent, each rapidity interval is assigned an individual uncertainty.
As introduced in section 4.1.10, for negatively charged pions, sectors 5 and 6 behave differently from sectors 1-4, which the K^- data confirm. This is accounted for by comparing the resulting dN/dy spectra for the K^+ obtained from only sectors 1 and 2 to those obtained from sectors 5 and 6. For the K^-, these sectors are excluded from the analysis, as the resulting dN/dy spectra otherwise show large fluctuations around midrapidity, which is not well understood at this point. Therefore, by exclusion of these sectors, the inclusion of this undefined behaviour in the analysis is avoided. For the extracted 4π-yield this proves to result in no difference within the systematic uncertainties.
For each comparison, it is checked if the obtained yield difference per interval of rapidity is consistent with 1σ of the statistical uncertainty of the analysed data sample. If this is the case, the individual systematic effect is regarded as not distinguishable from a statistical fluctuation and set to zero.

Ultimately, a potential description and extrapolation bias for the invariant transverse mass spectra has to be considered. This is done by comparing the extracted particle production rate per rapidity interval between the ones extracted from transverse mass and transverse momentum. The absolute difference between both results, divided by the count rate extracted from the invariant transverse mass spectra, yields the relative systematic uncertainty contribution. Figure A.17 shows the corresponding transverse momentum spectra for the K^+ in $0-30\%$ centrality. Suppose the resulting deviation does not coincide within the 1σ deviation of the statistical uncertainty. In that case, it is used as a systematic deviation in the extrapolation procedure into the uncovered invariant transverse mass regions.

The final relative systematic uncertainty for one dN/dy interval consists of the square root of the quadratic sum of the different sources of systematic effects, which are inconsistent with a statistical fluctuation. For the K^+, the final error per bin of rapidity is defined as the square root of the quadratic sum of all relative deviations:

$$\Delta^{K^+}_{\text{sys},y_i} = \sqrt{\Delta^2_{\text{interpolation},y_i} + \Delta^2_{\chi^2_{RK},y_i} + \Delta^2_{\text{Sectors},y_i} + \Delta^2_{\text{MDC dE/dx},y_i} + \Delta^2_{m_t\text{-extrapolation},y_i}} \,. \quad (5.7)$$

Correspondingly, for the K^- the equivalent equation is:

$$\Delta^{K^-}_{\text{sys},y_i} = \sqrt{\Delta^2_{\text{interpolation},y_i} + \Delta^2_{\chi^2_{RK},y_i} + \Delta^2_{\text{MDC dE/dx},y_i} + \Delta^2_{m_t\text{-extrapolation},y_i}} \,. \quad (5.8)$$

The individually determined sources of systematic effects and their relative magnitude for the case of the K^+ and K^- are displayed in figure 5.30. The y-axis represents the relative systematic uncertainty arising from the criterion, while the x-axis shows the corresponding rapidity interval in the centre of mass frame.

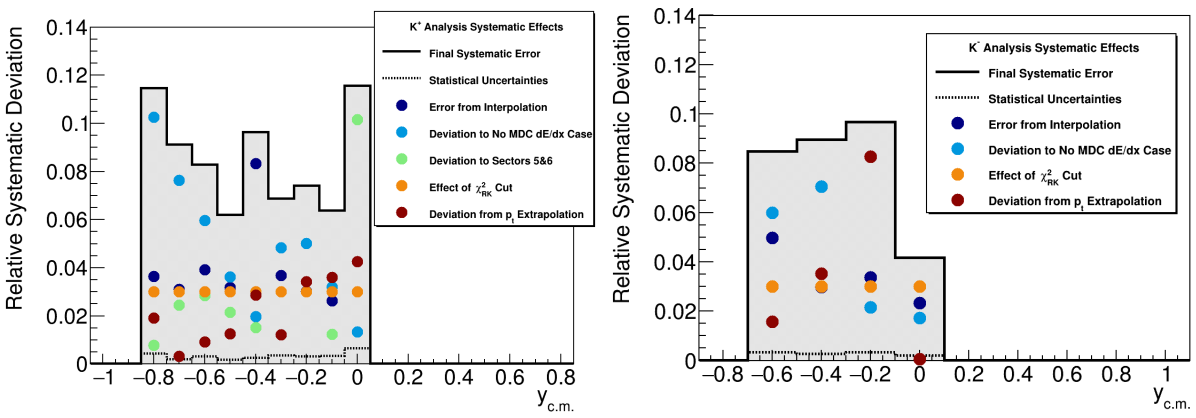

(a) (b)

Figure 5.30.: Relative systematic effects for the K^+ (a) and K^- (b) in $0-30\%$ most central collisions, differentiated by their origins.

The K^- phase space granularity and coverage are very limited. To avoid over-weighting statistical outliers during the determination of systematic effects, the systematic errors of all dN/dy intervals within the same distribution are averaged over and used as the systematic error of each data point. This procedure is also used for the K^+ to remain consistent between the analyses. The resulting average systematic error for the K^+ and K^- each are $\approx 8\%$. Those values are used for all centrality classes.

As the extrapolation of the dN/dy distribution into the uncovered rapidity region of the phase space introduces a potential additional systematic effect, two resulting 4π-yields are compared. The first yield is taken from the data points extrapolated with a model which superimposes two thermal sources of the form defined in equation 5.4, where one is located at $\mu - \eta$ and the other at $\mu + \eta$. A more detailed discussion is found in section 5.4. The other yield is extracted using the dN/dy-distribution obtained from SMASH [135] simulations, which are normalised to data. The utilised distributions from SMASH simulations of Ag+Ag collisions at 1.58A GeV are not obtained via the complete analysis chain but directly by filling the corresponding spectra of observables. This avoids any biases due to acceptance or efficiency effects.
To obtain the final systematic uncertainty for the 4π-yield, the particle production rates for both cases are directly compared, and their relative deviations are added to the quadratic sum previously introduced in equation 5.7:

$$\Delta_{\text{systematic}} = \sqrt{\sum_i \Delta^2_{\text{sys},y_i} + \Delta^2_{dN/dy\text{-extrapolation}}} \,. \tag{5.9}$$

For the T_{Eff} parameter, the systematic uncertainty is derived from the difference between the results from invariant transverse mass and transverse momentum spectra fits, as the effective temperature as a fit parameter directly depends on the correct description and interpolation of existing data. This makes transverse momentum (p_t) fits the most direct approach to testing the systematic effects emerging from the description. Consequently, the systematic error given for the effective temperature is the deviation between the two extracted T_{Eff} parameters from the $1/\cosh(y)$ fits at midrapidity. In figure 5.31, this direct comparison can be seen for the K^+. It can be argued that the direct comparison of midrapidity data point deviations is expected to measure the systematic effects better. This line of argumentation is valid for particles with count

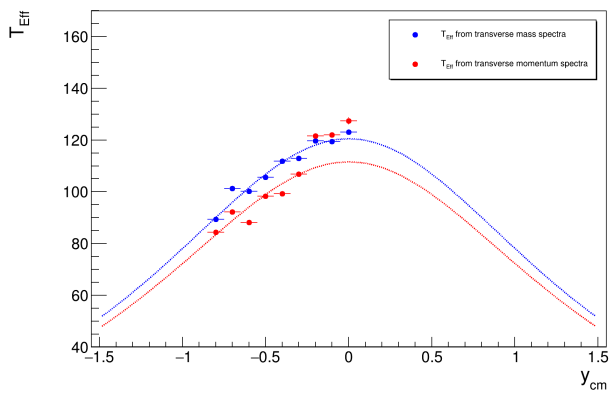

Figure 5.31.: Comparison of K^+ T_{Eff} distributions from transverse mass and transverse momentum spectra for systematic effect estimation in $0-30\%$ most central events.

rates of at least one particle produced per event. In contrast, the $K^{\pm}$ suffer from comparably low count rates and a significantly reduced phase space coverage, leading to significant uncertainties in determining the inverse slope parameter. Using the result from the fit for extracting the parameter globally reduces the chance of an incidental over- or underestimation of systematic effects. This holds for other observables as well, why the relative deviations were chosen to be compared in the form of integrated spectra.

5.3.2. Systematic Error Evaluation for the ϕ-Meson

For the ϕ-meson, the determination of systematic effects is based on the same principles as for the charged Kaons. Minor differences are that the sideband analysis is performed on the mixed event background and not on the interpolation. Furthermore, the range of comparison is limited to the normalisation region between mixed events and data. The calculation of the deviation is otherwise performed in the same manner as in equation 5.6.
Another critical difference is the determination of the systematic uncertainty in the determination of the inverse slope parameter. There is substantial pion contamination visible in the invariant mass spectra in the low invariant transverse mass regions. On the other hand, the available statistics decrease strongly beyond a invariant transverse mass of 400 MeV/c^2. Those factors contribute to a less stable background description and normalisation. Consequently, two fits are performed independently on the invariant transverse mass spectra. One iteration is made to describe the entire range of the spectra, while a second fit is limited to the invariant transverse mass range $80 < (m_t - m_0) < 400$ MeV/c^2. The resulting slopes are compared, and their difference is taken into account as a systematic uncertainty for the determination of the T_{Eff}-parameter.
An overview of the systematic effects considered for the ϕ-meson and their relative contribution as a function of the interval of rapidity is shown in figure 5.32.
Due to the significant statistical uncertainties, a clear separation between systematic effects and statistical fluctuations is not always straightforward. For the midrapidity bin, for example, all systematic effects are indistinguishable from a statistical fluctuation, which would result in a total error of zero. Consequently, as there exists no straightforward determination of the systematic errors, the calculated resulting average of a relative systematic error of $\approx 14.5\%$ is rounded to a global average of 15%, which is used thereafter.

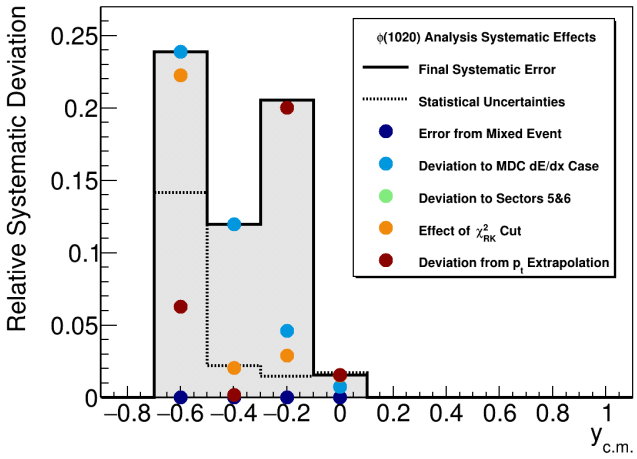

Figure 5.32.: Relative systematic effects for the multidifferential ϕ-meson analysis in $0-30\%$ most central collisions, differentiated by their origins.

5.4. Extrapolation in Rapidity Direction

5.4.1. K^+

To extrapolate into the uncovered rapidity region, a superposition of two thermal distributions in the style of equation 5.5 is fitted onto the data. The means of these distributions are shifted relative to the mean μ of the dN/dy-distribution for the centre of mass frame located at $y_{c.m.} = 0$, by a factor of $\pm\eta$. T is set to the extracted T_{Eff}-parameter, while C and η remain free fit-parameters. A significant deviation of η from 0 indicates a particle emission pattern that a single, radially symmetric and isotropic source function cannot explain solely. The 4π-yield is obtained by integrating the data and extrapolation region and adding up both results. Figure 5.33 shows the dN/dy-distributions for the K^+ in the different intervals of collision centrality, with the blue curve representing the superimposed thermal distributions and the green curve showing the result of a SMASH simulation. Empty circles represent data points reflected around midrapidity.
The final 4π production rate is extracted to $\approx 53\%$ from extrapolation by superpositioning two thermal distributions. As most of the particle production rate is estimated via extrapolation, a significant systematic effect can emerge from the chosen description. For an estimation of the extrapolation uncertainty, the SMASH simulation is normalised to data by integrating both to their integrated particle production rates in the rapidity range where data is available (see section 5.3.1). The extrapolation error is displayed separately in figure 5.33, so that the last two displayed errors represent the terms $\sum_i \Delta_{\text{sys},y_i}$ and $\Delta_{dN/dy\text{-extrapolation}}$ in equation 5.9.
A significant deviation of the η-parameter from 0 is observed for all centrality intervals. Furthermore, η increases with decreasing collision centrality. Consequently, the resulting width deviates from a single purely thermal source and the result obtained from SMASH simulations. Also, the resulting 4π-yields deviate significantly between the extrapolated data and the normalised SMASH simulation.
Table 5.1 contains the extracted 4π yields and T_{Eff}-parameters for the K^+ in the different intervals of centrality. Here the given systematic errors are calculated according to equation 5.9.

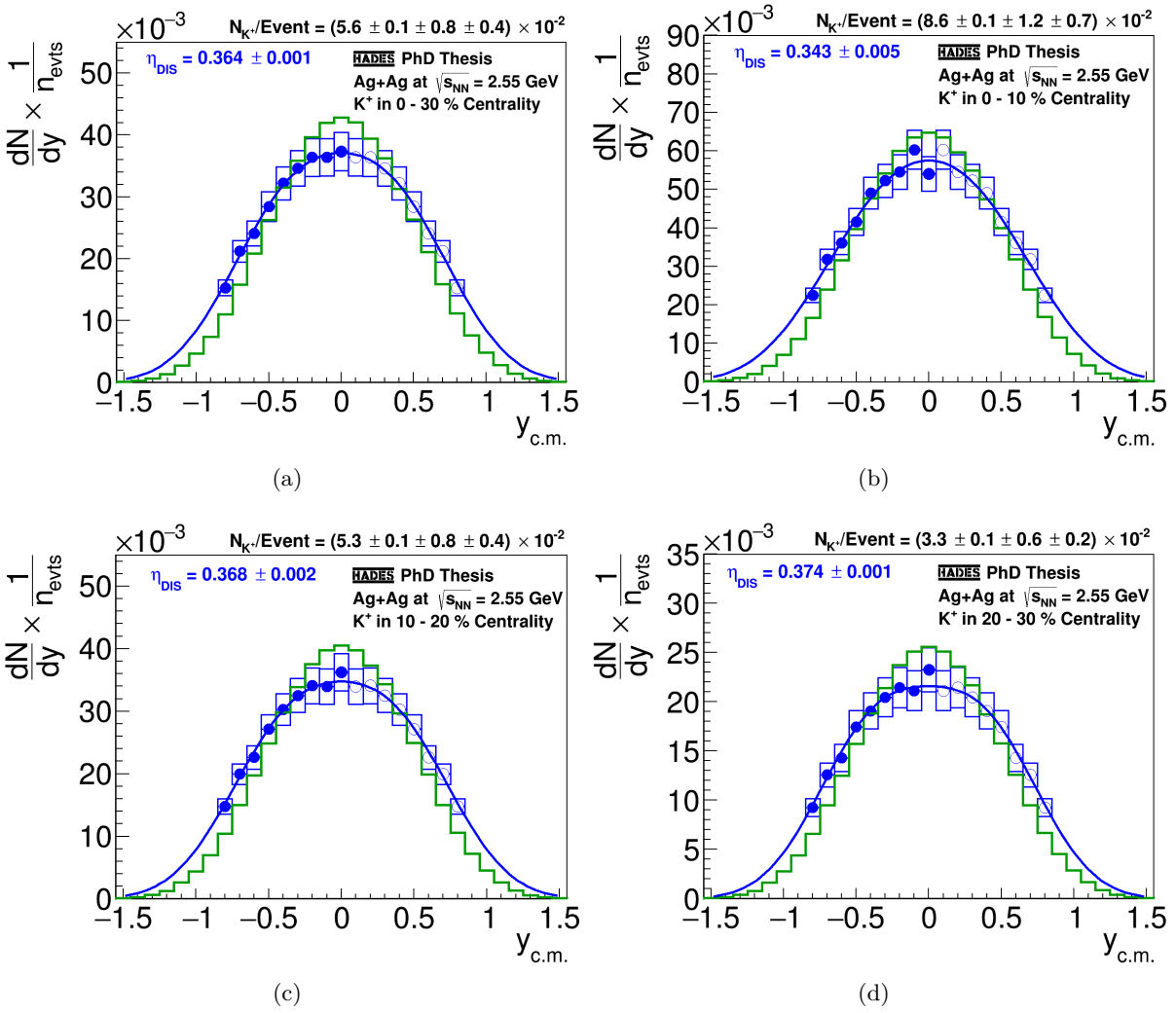

Figure 5.33.: Fitted K^+ dN/dy spectra for the different centrality classes. The displayed errors are the statistical uncertainty, the systematic error for the transverse direction and the extrapolation error in the rapidity direction.

Centrality	$(N_{K^+}/\text{Event}) \times 10^{-2}$	T_{Eff} [MeV]	η
$0-30\%$	$5.6 \pm 0.1(\text{stat.}) \pm 0.9(\text{syst.})$	$(120.5 \pm 0.1(\text{stat.}) \pm 8.9(\text{syst.}))$	0.364 ± 0.001
$0-10\%$	$8.6 \pm 0.1(\text{stat.}) \pm 1.4(\text{syst.})$	$(125.3 \pm 0.2(\text{stat.}) \pm 10.0(\text{syst.}))$	0.343 ± 0.005
$10-20\%$	$5.3 \pm 0.1(\text{stat.}) \pm 0.9(\text{syst.})$	$(119.4 \pm 0.2(\text{stat.}) \pm 10.1(\text{syst.}))$	0.368 ± 0.002
$20-30\%$	$3.3 \pm 0.1(\text{stat.}) \pm 0.6(\text{syst.})$	$(113.6 \pm 0.2(\text{stat.}) \pm 11.3(\text{syst.}))$	0.374 ± 0.001

Table 5.1.: Summary of the K^+ results.

5.4.2. K^-

Like for the K^+, the K^- 4π particle production rate is extracted from the dN/dy-distribution by extrapolating into the uncovered rapidity region with two superimposed thermal distributions (blue curve) located at $\mu \pm \eta$ and summing over the integrated values for data and extrapolation region afterwards. To obtain a measure for the extrapolation uncertainty, the dN/dy distribution obtained from SMASH (green distribution) is normalised to data and integrated over.

Furthermore, the extrapolation error is displayed here separately from the term $\sum_i \Delta_{\mathrm{sys},y_i}$ in equation 5.9. Figure 5.34 displays the distributions for the K^- in different intervals of centrality.

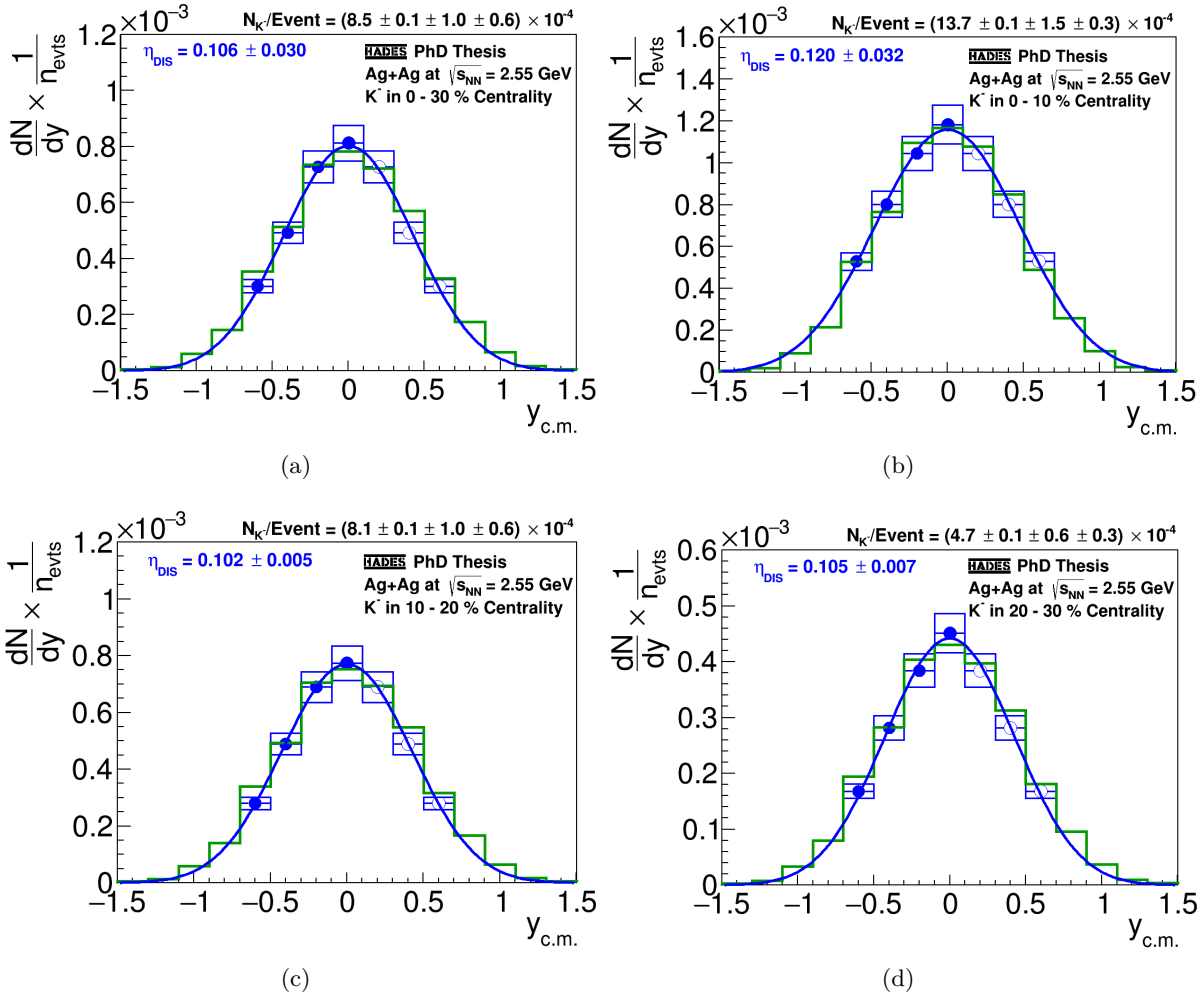

Figure 5.34.: Fitted K^- dN/dy spectra for the different centrality classes. The displayed errors are the statistical uncertainty, the systematic error for the transverse direction and the extrapolation error in the rapidity direction.

As expected, the final production rate of $(8.4 \pm 0.1 \pm 1.5) \times 10^{-4}$ K^- per event in the $0-30\%$ most central events lies rwoughly two orders of magnitude below the corresponding K^+ production rate per event. Another observation is the good accordance between the results obtained from SMASH and the extrapolated data. The extracted η-parameter is not equal to zero. Nevertheless, the value is, within the systematic uncertainty $dy = 0.2$ of the rapidity bin-width and the statistical errors of the parameters, consistent with lying within the midrapdity bin. Consequently, the distribution follows the description by a single thermal source, which contrasts the observations concerning the K^+.
Table 5.2 shows an overview of the extracted 4π-yields and T_{Eff}-parameters for the K^- in different intervals of centrality. Here the systematic error is calculated according to equation 5.9.

Centrality	$(N_{K^-}/\text{Event}) \times 10^{-4}$	T_{Eff} [MeV]	η
$0-30\%$	$8.5 \pm 0.1(\text{stat.}) \pm 1.2(\text{syst.})$	$(90.8 \pm 0.2(\text{stat.}) \pm 14.0(\text{syst.}))$	0.106 ± 0.030
$0-10\%$	$13.7 \pm 0.1(\text{stat.}) \pm 1.5(\text{syst.})$	$(87.0 \pm 0.4(\text{stat.}) \pm 31.3(\text{syst.}))$	0.120 ± 0.032
$10-20\%$	$8.1 \pm 0.1(\text{stat.}) \pm 1.2(\text{syst.})$	$(86.5 \pm 0.3(\text{stat.}) \pm 13.1(\text{syst.}))$	0.102 ± 0.005
$20-30\%$	$4.7 \pm 0.1(\text{stat.}) \pm 0.7(\text{syst.})$	$(80.3 \pm 0.2(\text{stat.}) \pm 1.3(\text{syst.}))$	0.105 ± 0.007

Table 5.2.: Summary of the K^- results.

5.4.3. ϕ(1020)

The extrapolation of the ϕ-meson dN/dy spectra into the uncovered region, as well as the 4π-yield extraction and extrapolation error estimation, are done in the same way as previously discussed for K^+ and K^-. Correspondingly, figure 5.35 shows the ϕ-meson dN/dy spectra for the different centrality intervals with the systematic error of the extrapolation displayed separately. The systematic error determination for the ϕ-meson is discussed in section 5.3.2.

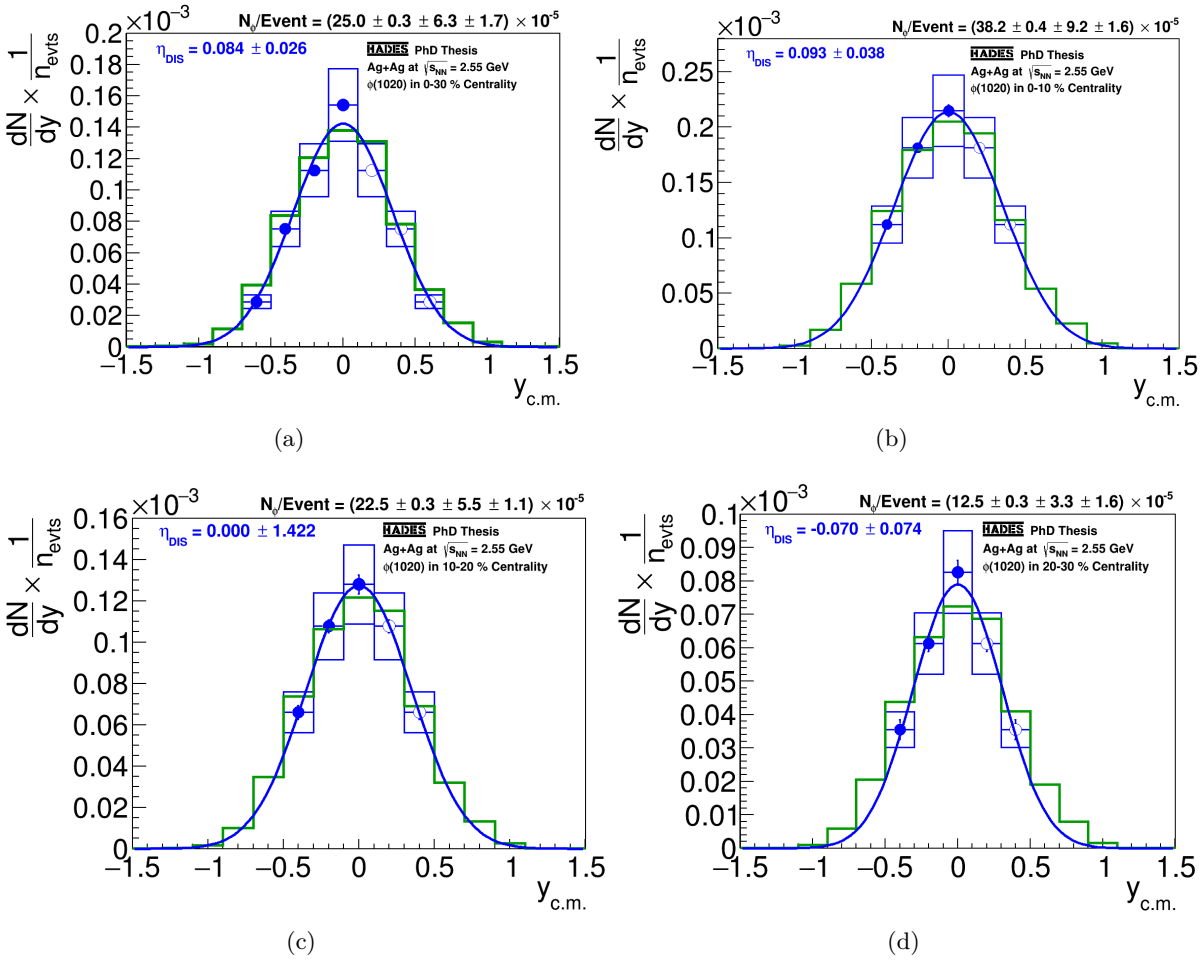

Figure 5.35.: Fitted ϕ-meson dN/dy spectra for the different centrality classes. The displayed errors are the statistical uncertainty, the systematic error for the transverse direction and the extrapolation error in the rapidity direction.

The extracted 4π ϕ-meson production yield per event of $(2.5 \pm 0.1 \pm 0.7) \times 10^{-4}$ lies within the same order of magnitude as the one obtained for K^-. As the branching ratio for the decay

$\phi \rightarrow K^+K^-$ is approximately 50%, it follows that about 15% of all K^- are originating from a decay of a ϕ-meson. This is expected to modify the slope of the invariant transverse mass distributions. A detailed discussion of this matter is performed in section 6.4.1.
Furthermore, the obtained values for η are consistent with a description of the distribution by a single thermal source. As for the K^-, this coincides with a comparably small relative systematic extrapolation effect compared to the K^+. The relative systematic extrapolation effect is smaller by a factor of ≈ 2.
In table 5.3, the results for the 4π-yields and the T_{Eff}-parameters for the ϕ-meson in different intervals of centrality are listed. The systematic error is calculated according to equation 5.9.

Centrality	$(\mathrm{N}_\phi/\mathrm{Event}) \times 10^{-5}$	T_{Eff} [MeV]
$0-30\%$	$25.0 \pm 0.3(\mathrm{stat.}) \pm 6.5(\mathrm{syst.})$	$(124.4 \pm 1.7(\mathrm{stat.}) \pm 8.6(\mathrm{syst.}))$
$0-10\%$	$38.2 \pm 0.4(\mathrm{stat.}) \pm 9.3(\mathrm{syst.})$	$(116.9 \pm 3.1(\mathrm{stat.}) \pm 4.8(\mathrm{syst.}))$
$10-20\%$	$22.5 \pm 0.3(\mathrm{stat.}) \pm 5.6(\mathrm{syst.})$	$(124.2 \pm 3.4(\mathrm{stat.}) \pm 8.5(\mathrm{syst.}))$
$20-30\%$	$12.5 \pm 0.3(\mathrm{stat.}) \pm 3.7(\mathrm{syst.})$	$(128.0 \pm 4.4(\mathrm{stat.}) \pm 19.4(\mathrm{syst.}))$

Table 5.3.: Summary of the ϕ results.

6. Discussion and Conclusions

This chapter uses the results previously obtained and discusses them in a global context. To this purpose, results of previous analyses introduced in section 1.5 are used for comparative analysis. Furthermore, results from [125] are used to complement the data of strange hadrons produced in Ag(1.58 A GeV)+Ag collisions for comparisons with theoretical models.

6.1. Strangeness Balance

One fundamental test for the results is a check for strangeness conservation, called *strangeness balance*. As strangeness is conserved in the strong interaction, the final state particles are expected to possess a balance between s and $\bar{s}$ content. The main contributors are the single-strange Λ and Σ hyperons and the single-anti-strange K^+ and K^0 mesons with a particle production rate of $\approx 10^{-2}$ per event. The Ξ, Ω and K^- have production rates two orders of magnitudes smaller, so they can be neglected. Furthermore, assuming approximate CP symmetry, K^0_S and K^0_L are in the same abundance. This way, the K^0_S results from [125] are multiplied by two to obtain the number of produced K^0. Using the Σ production rates calculated from reconstructed Λ 4π production rates as well as the reconstructed K^0_S 4π production rates [125], table 6.1 shows the results for different intervals of centrality.

Centrality	$N_{\Lambda+\Sigma} \times 10^{-2}$	$N_{K^++K^0} \times 10^{-2}$
$0-10\%$	17.28 ± 0.08	17.60 ± 1.41
$10-20\%$	10.45 ± 0.05	10.74 ± 0.91
$20-30\%$	6.41 ± 0.04	8.04 ± 0.61

Table 6.1.: Comparison of hadrons with single s and single $\bar{s}$ content for a strangeness balance check.

The balance is given within errors for $0-10\%$ and $10-20\%$ most central events. A discrepancy can be seen for $20-30\%$ most central events, which can not conclusively be attributed to any previously considered effect. E.g., the fraction of extrapolation for the determination of the K^+ 4π production rates is given with $\approx 53\%$ in all three centralities, which makes an extrapolation effect unlikely. When comparing the K^+ and K^0 production rates as a function of centrality, the obtained values of $2 \times N_{K^0_S}$ and N_{K^+} are consistent within errors throughout all ranges, which makes a systematic effect in one of the analyses an unlikely cause.
As the natural silver target contains an approximate distribution of 50% of ^{107}Ag and 50% of ^{109}Ag, the collision system possesses an average of about 168 down-quarks and 156 up-quarks for head-on collisions. This results in a ratio of $N_u/N_d \approx 0.929$ and can be used as a measure for the isospin asymmetry, as the main difference between a proton and a neutron is an up or down quark to the existing ud-pair. However, the systematic errors of the K^+ lie at $\approx 8\%$, which does not allow for a differentiation between systematic effects and isospin asymmetry effect. Furthermore, the isospin asymmetry can not explain the 25% difference in the strangeness balance comparison.
A possible reason for this observation is the effect described in [125], that a rise of Σ^0 to Λ is observed for $20-30\%$ most central events. Inside the medium, there are two reaction channels

for neutral Σ^0 to transform into Λ hyperons ($\Sigma^0 n \to \Lambda n$ and $\Sigma^0 p \to \Lambda p$) and, due to charge conservation, only one for charged Σ^+ ($\Sigma^+ n \to \Lambda p$) and Σ^- ($\Sigma^- p \to \Lambda n$). Therefore, the probability for a charged $\Sigma^\pm$ conversion into Λ decreases stronger as a function of centrality compared to Σ^0. The calculated production rates of the Σ^0 do not consider these medium interactions. However, for the used Λ hyperon production yields, the Σ^0 contribution is subtracted. This puts a bias on the cleaned-up Λ production rate and leads to a stronger decrease of the $N_{\Lambda+\Sigma}$ value compared to the $N_{K^++K^0}$ one. To conclusively test the strangeness balance, an experimental reconstruction of the Σ^0 production rate is necessary.

6.2. K^-/K^+ Ratio

The ratio of charged Kaons from Ag(1.58 A GeV)+Ag collisions is, using data from $0-30\%$ most central events,

$$\frac{K^-}{K^+} = (1.52 \pm 0.17) \times 10^{-2} \ .$$

As discussed in section 1.5.2, previously measured data presents with a linear increase of the K^-/K^+-ratio as a function of $\sqrt{s_{\mathrm{NN}}}$ in the depicted energy regime. Therefore, to check whether the data obtained from this work fits this global trend, figure 6.1 shows the ratios obtained from different experiments as a function of $\sqrt{s_{\mathrm{NN}}}$.

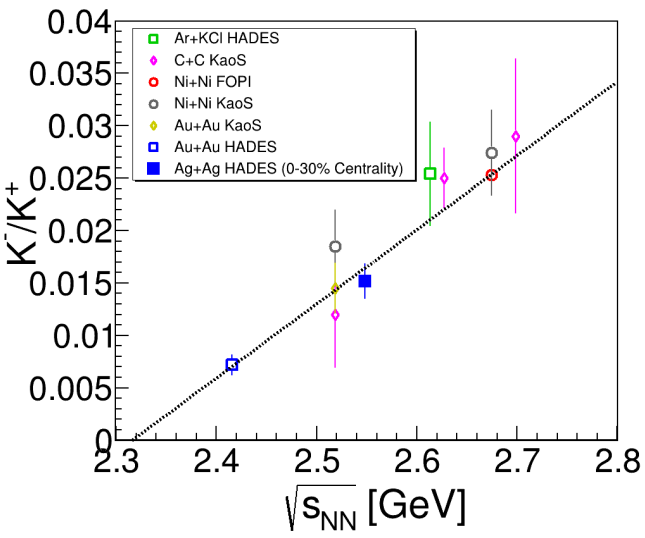

Figure 6.1.: K^-/K^+ ratio for different collision energies and systems, other data points taken from [15][58][120]. The HADES Ag+Ag at $\sqrt{s_{\mathrm{NN}}} = 2.55$ GeV data are taken from $0-30\%$ most central events.

Qualitatively the K^-/K^+ ratio from Ag(1.58 A GeV)+Ag collisions confirms the global trend. Applying a linear fit function of the form $f(\sqrt{s_{\mathrm{NN}}}) = a \cdot \sqrt{s_{\mathrm{NN}}} + b$ as shown in figure 6.1 results in a slope of $a = (0.071 \pm 0.004)$ GeV. None of the 10 data points deviates from the fitted line significantly more than $\pm 1\sigma$, which reconfirms the possibility of a phenomenologically motivated linear parameterisation of the K^-/K^+-ratio as a function of $\sqrt{s_{\mathrm{NN}}}$ in the few GeV energy regime. However, this description does not hold for higher energies, as the ratio asymptotically approaches 1 for RHIC and LHC energies due to the production of K^+ and K^- in equal parts. In [119], it is found that all data points can be described by a slope of $a = (0.089 \pm 0.024)$, which is consistent with the slope after including the point obtained from this work.
To draw quantitative conclusions about the production mechanisms, the global scaling behaviour of strange hadrons as a function of the system size is investigated, the latter being proportional to $\langle A_{\mathrm{part}} \rangle$. This is discussed in section 6.5.

6.3. ϕ/Ξ^- Ratio

The Ξ^--baryon ($|dss\rangle$) with a mass of $m = 1321.71$ MeV/c^2 [141] is a rare probe in the few GeV energy regime. In [125] the reconstruction from Ag(1.58 A GeV)+Ag collisions via the $\Xi^- \rightarrow \Lambda\pi^-$ decay channel is performed and discussed. As it contains two strange quarks, it is additionally suppressed compared to charged Kaons and the ϕ-meson at a few GeV collision energy. As two $s\bar{s}$-pairs need to be produced in a collision, this makes it a sensitive probe to medium effects. In section 1.5.2, previous results are introduced and compared to a THERMUS fit on particle production yields obtained from Au+Au collisions at $\sqrt{s_{\mathrm{NN}}} = 3$ GeV measured with STAR [3]. Adding the

$$\frac{\phi}{\Xi^-} = 6.94 \pm 2.36$$

ratio obtained from Ag(1.58 A GeV)+Ag collisions, the picture presents itself as in figure 6.2.

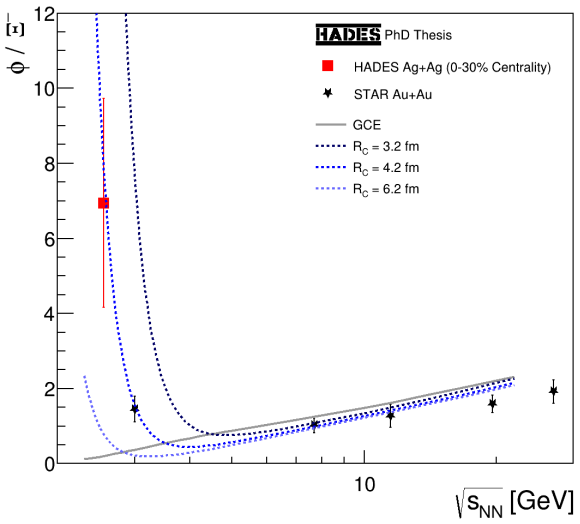

Figure 6.2.: ϕ/Ξ^- ratio for different collision energies and systems [3][4]. The HADES Ag+Ag at $\sqrt{s_{\mathrm{NN}}} = 2.55$ GeV data are taken from $0 - 30\%$ most central events (ϕ-meson) and from $0 - 25\%$ most central events (Ξ^--baryon).

The SHM curves resulting from this specific parameterisation of T and μ_B, as well as a strangeness correlation radius of $R_C = 4.2$ fm, are in good agreement with the STAR Au+Au and HADES Ag+Ag data below 10 GeV.
The SHM description can be tested further by using the same parameterisations for the strangeness correlation radius and comparing the results for the ϕ/K^--ratio with data. This is presented in the following section.

6.4. ϕ/K^- Ratio

In [15], and [119], a steep rise of the ϕ/K^--ratio towards the few GeV regime is observed, which indicates that a substantial amount of K^- is produced via the decay of a ϕ-meson. For the case of Au(1.23 A GeV)+Au collisions this process creates $\approx 1/4$ of all reconstructed K^-. This, combined with the observations described in section 6.4.1, contradicts the previous assumption of strangeness exchange reactions being the single dominant process of K^- production in this energy regime [86]. The previous analyses introduced in section 1.5.2 confirm the observation of a steep rise but suffer from large uncertainties compared to higher energies. Including the ratio

of

$$\frac{\phi}{K^-} = 0.29 \pm 0.05$$

from Ag(1.58 A GeV)+Ag collisions reconfirms this trend with increased precision, as shown in figure 6.3.

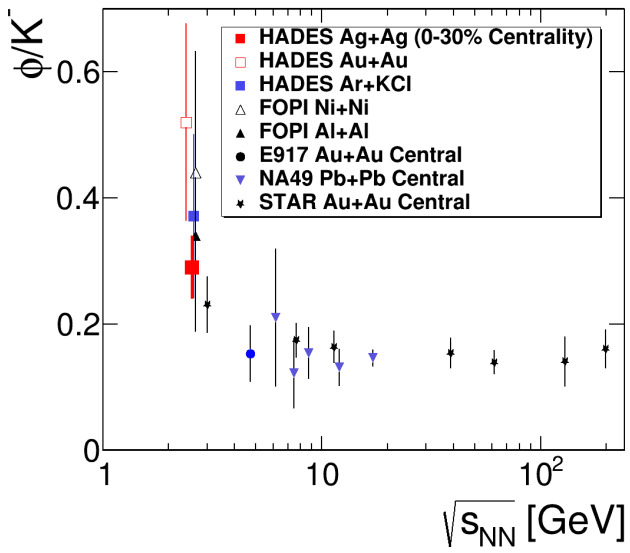

Figure 6.3.: ϕ/K^- ratio for different collision energies and systems [3][9][13][15][66][81][105][119]. The HADES Ag+Ag at $\sqrt{s_{\mathrm{NN}}} = 2.55$ GeV data are taken from $0 - 30\%$ most central events.

The present data reconfirms the steep rise towards low energies. This rise, combined with the decrease of the K^-/K^+ ratio towards lower energies, indicates an increased reabsorption of K^- within the medium.
This way, it is possible to test the descriptive power of the SHM parameterisation introduced in section 6.3 for different values of R_C. The curves resulting from the same T and μ_B parameterisations as shown in figure 6.2 for the case of ϕ/Ξ^- are drawn in figure 6.4 for the ϕ/K^--ratio.

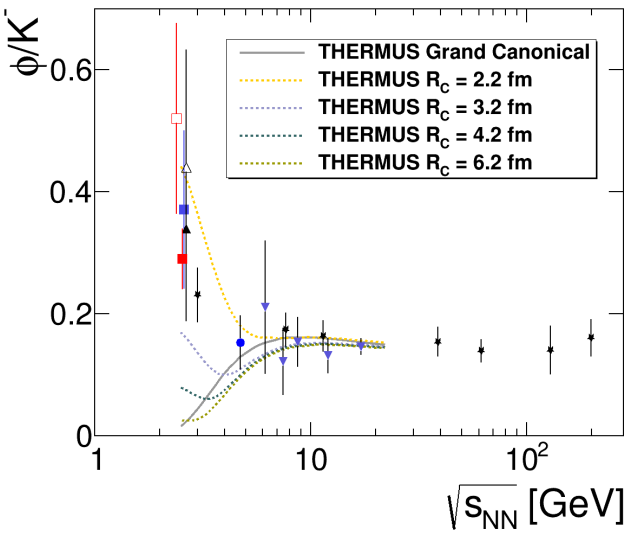

Figure 6.4.: ϕ/K^- ratio for different collision energies and systems with the SHM parameterisation curves applied [3][9][13][15][66][81][105][119].

The choice of $R_C = 4.2$ fm fails to describe the observed ratio entirely, also for the collision system it was determined for [3]. To obtain an accurate data description, the corresponding R_C has to lie between 2.2 and 3.2 fm. Hence, the THERMUS fit does not describe the ϕ/K^- and ϕ/Ξ^- ratios simultaneously. Furthermore, for the $R_C = 2.2$ fm curve, a flattening towards

the Au+Au data point at $\sqrt{s_{\mathrm{NN}}} = 2.4$ GeV can be observed. This way, the ratio observed in data is overestimated in THERMUS for the $\sqrt{s_{\mathrm{NN}}} = 3$ GeV area and underestimated around $\sqrt{s_{\mathrm{NN}}} = 2.4$ GeV using a single T and μ_B parameterisation for the Au+Au collision system at different energies. These observations indicate that introducing a single strangeness canonical radius is insufficient to accurately model the strangeness production mechanisms in the few GeV regime. The canonical description, however, is favourable over the grand canonical one as it qualitatively describes the observed rise towards the few GeV area. Also, it has to be taken into account that this singular parameterisation of thermodynamical fireball properties does not necessarily describe the properties of (other) collision systems at different energies.
From the obtained ratio, an $\approx 15\%$ contribution from the $\phi \to K^+K^-$ decay channel to the kinematic K^- spectra can be extracted. This significantly influences the transverse spectra's slope, as discussed in the following section.

6.4.1. ϕ-Meson Feed-Down

For a long time, it has been hypothesised that the strangeness exchange reaction $\pi Y \to Y^\star \to \bar{K}N$ is the single primary production mechanism for K^- in the few GeV regime [62]. However, recent findings in [119] contradict this standpoint. As shown in the previous section, $\approx 15\%$ of all K^- are produced in a resonant way. Additionally, results by the ANKE collaboration [95] from *pp* collisions slightly above the energetic K^- free NN interaction production threshold show a ratio between resonant and non-resonant production of ≈ 1. Both channels explain at least $\approx 30\%$ of the produced K^-.
Using the data from this work, it is investigated whether the lower inverse slope parameter of the K^- originates from the significant contributions by the decay $\phi \to K^+K^-$ in later stages of the collision superimposed with a purely thermal K^- production in the fireball. PLUTO simulations are performed in which thermally produced K^- and ϕ-mesons decaying into the K^+K^- decay channel are produced by a purely thermal fireball with two parameters set - $E_{\mathrm{beam}} = 1.58$ A GeV and $T_{\mathrm{Eff}} \approx 120$ MeV as obtained from K^+ and ϕ-mesons. The resulting transverse mass and dN/dy-distributions of both contributions are then scaled. The K^--spectra from the $\phi \to K^+K^-$-channel are scaled according to the $(\phi \to K^+K^-)/K^-$-ratio of ≈ 0.14 (branching ratio $(\Gamma_i/\Gamma) \approx 49\%$ [141]), while the thermal contributions are scaled by 1 minus the ratio. Both contributions are added to obtain the shape expected from such a superimposed source. The resulting transverse mass spectrum at midrapidity with both cocktail contributions is shown in figure 6.5(a). The red curve represents a Boltzmann fit onto the distribution to obtain the inverse slope parameter analogously to the measured data.
The resulting T_{eff}-parameter turns out to be $T_{\mathrm{eff}} = 95.2 \pm 0.6$ MeV. In data, 90.8 ± 14 MeV are obtained, while the error given contains statistical uncertainties and the systematic deviation between results from transverse mass and transverse momentum fits. The obtained results are, therefore, fully consistent. Hence, at least $\approx 80\%$ of the difference in slope between K^+ and K^- can be explained by the sources introduced into the cocktail.
However, evaluating systematic effects influencing the slope parameter extraction proves difficult with the available K^- phase space. Therefore, the difference between the values could suggest further relevant contributions, e.g., by strangeness exchange reactions in the final state.
Also, the shapes of the dN/dy-distributions are compared between cocktail and data, as shown in figure 6.6.
The cocktail curve is normalised to the integral over data in the same rapidity region $-0.7 < y < 0.1$. The width of both distributions differs by $\approx 5\%$, while their corresponding Gaussian fits, applied to retrieve the width, possess uncertainties of $\approx 0.5\%$. This is also shown by the ratio plot on the lower part of figure 6.6, where the first two rapidity bins, starting at most backward rapidity, are overestimated in particle production yield. The two bins around

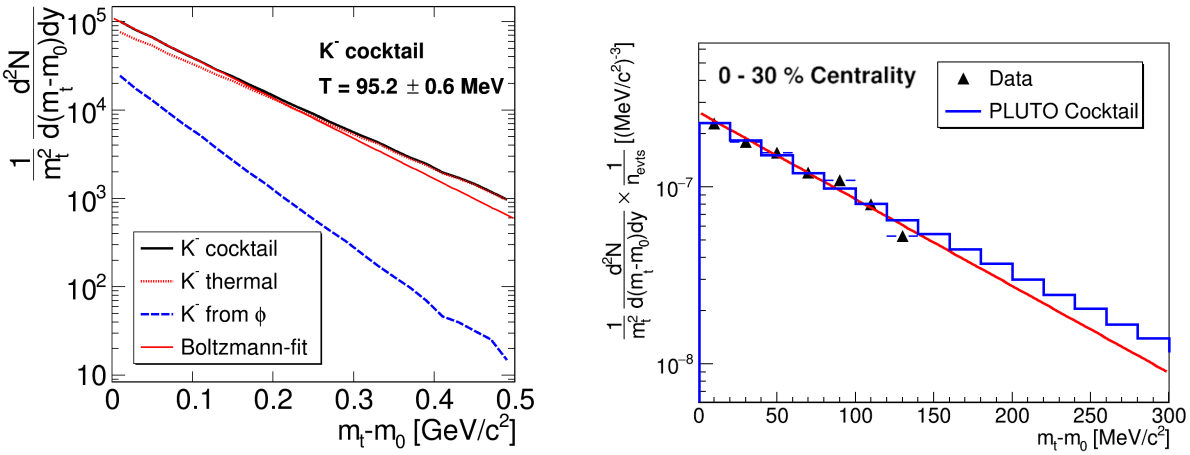

(a) (b)

Figure 6.5.: K^- invariant transverse mass spectrum for the PLUTO generated cocktail with its components (a) compared to the measured midrapidity spectrum for $0-30\%$ most central events (b). The red line in (a) is a Boltzmann-Fit on the cocktail, while in (b), it is the fit on data.

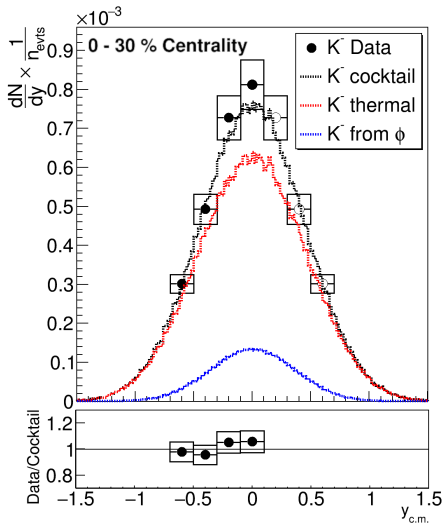

Figure 6.6.: K^- dN/dy-distribution compared to the shape of the PLUTO simulated one. Due to statistical reasons, the data are taken from $0-30\%$ most central events.

midrapidity, in contrast, are underestimated. The deviating widths indicate an incompleteness of this purely thermal picture for Ag(1.58 A GeV)+Ag collisions, though it can mostly explain the observed T_{eff}-parameter and dN/dy-shape. Further clarification in this context could be reached by resolving the background issue discussed in section 4.1.7, allowing for a more extensive phase space coverage and expectedly lower systematic errors on the final results.

6.5. Universal $\langle A_{\mathrm{part}} \rangle$-Scaling for Hadrons Containing Strangeness

In [119] and [140] HADES and STAR separately, at different energies, confirmed the possibility of describing the production yields of hadrons containing strangeness as a function of $\langle A_{\mathrm{part}} \rangle$ with a single slope parameter. The same is done in figure 6.7 for the resulting yields obtained from Ag(1.58 A GeV)+Ag collisions with full black lines representing the global fit and dashed

coloured lines the individual ones.

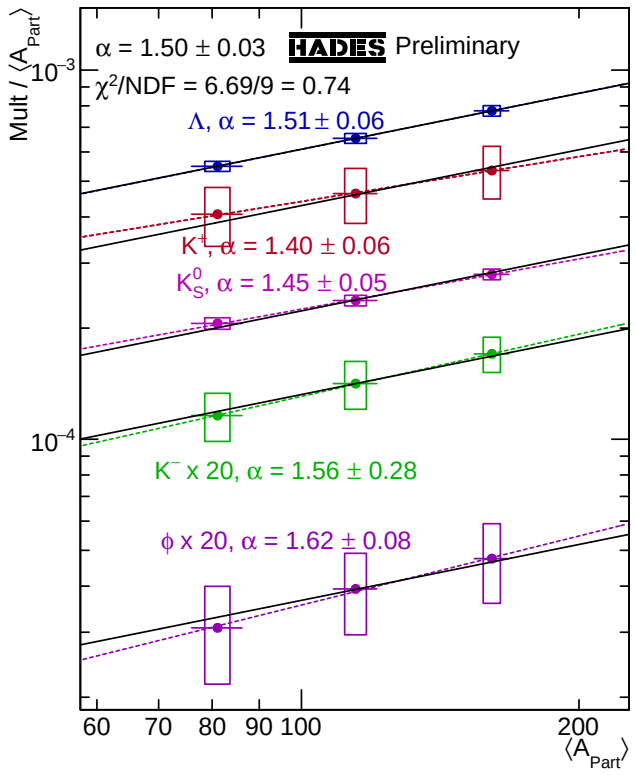

Figure 6.7.: Strange hadron event multiplicities as a function of $\langle A_{\text{part}} \rangle$ - so the number of nucleons participating in the initial Ag+Ag reaction - for Ag(1.58 A GeV)+Ag collisions. Λ and K^0_S data are taken from [125].

As discussed in section 1.2.1, these hadrons possess different threshold energies for their production in binary NN collisions. Therefore one would expect a stronger scaling of K^- and ϕ-meson multiplicities as a function of $\langle A_{\text{part}} \rangle$ compared to K^+,K^0 and Λ which are coupled via their common production channel. In the context of the lower T_{eff}-parameter of the K^-, coupling it to the same channel via the final state strangeness exchange reaction $\pi^-\Lambda \rightarrow K^- n$ ($|\bar{u}d\rangle + |uds\rangle \rightarrow |\bar{u}s\rangle|udd\rangle$) is one ansatz to explain the observation. Due to the large cross-section of 40-70 mb of the $NK^- \rightarrow \pi Y$ channel, it is expected to play the major part in the production of K^- below the binary NN production energy threshold, according to theoretical estimations [49]. Strangeness production is expected to lie in the area of μbarn in the few GeV energy regime. Additionally, reactions of the type $NY \leftrightarrows NNK^-$ are discussed to contribute up to 10% to the K^- production yield [86].
However, as shown in section 6.4.1, this is not the only way to explain the obtained yields - especially when considering that $\geq 80\%$ are explainable by thermal production as well as feed-down by ϕ-mesons. Furthermore, these explanations do not motivate the description of the ϕ-meson yield as a function of $\langle A_{\text{part}} \rangle$ with the same slope parameter as hadrons with net-strangeness. While in [119] a slope-parameter of $\alpha = 1.45 \pm 0.06$ is found, [140] confirms this with an extracted slope of $\alpha = 1.42 \pm 0.04$. The value obtained for Ag(1.58 A GeV)+Ag collisions is $\alpha = 1.50 \pm 0.03$, which is fully consistent with [119] and lies in the same area of [140]. Though individual slopes differ slightly, as the individual fits of figure 6.7 indicate, there are no significant deviations from the global slope. This would not be straightforward expected from a model with the single major contribution of strangeness exchange reactions and suggests that strange quarks are mainly produced as $s\bar{s}$-pairs undergoing subsequent percolation processes until the system freezes out chemically. Phenomenologically, this means that the strange quark is transported through meson clouds of the compressed nucleons, which overlap at densities $\rho \geq 1.8\rho_0$ (*soft deconfinement*), until it freezes out inside a nearby hadron [63]. Figure 6.8 schematically depicts

this process, with the red line representing the path of the quark along the purple meson clouds.

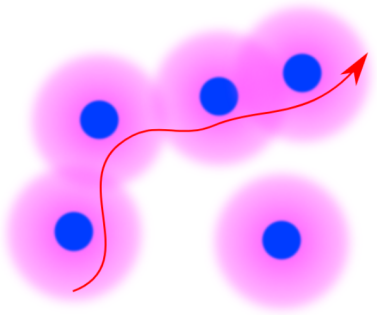

Figure 6.8.: Classical representation of the quark percolation process along the overlapping meson clouds in dense nuclear matter [63].

To underline the degree of consistency, figure 6.9 shows the ratios of K^-/K^+ and ϕ/K^- as a function of $\langle A_{\text{part}} \rangle$.

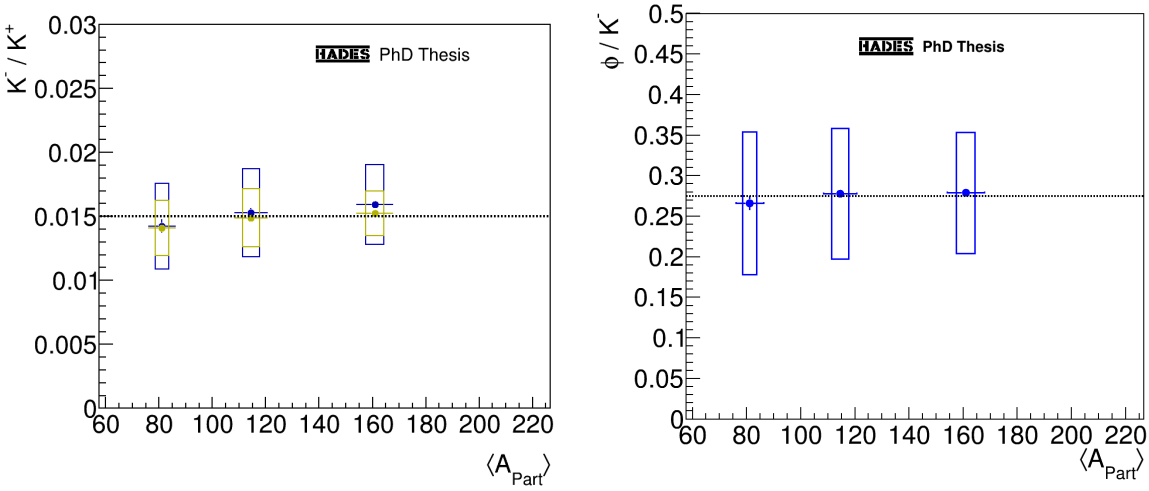

(a) (b)

Figure 6.9.: K^-/K^+- (blue) and K^-/K^0 ratios (a) and ϕ/K^--ratios (b) as functions of $\langle A_{\text{part}} \rangle$. Details can be found in the text.

Besides the K^-/K^+-ratios, the K^-/K^0-ratios are displayed in figure 6.9(a), as one would expect comparable count rates for K^+ and K^0 and, due to the shared production channel, a similar slope. Moreover, this offers an excellent way to check the obtained yields for consistency, as the K^0 signal extraction is done differently via the mixed event method (see [125]). All three ratios are, within errors, constant as a function of $\langle A_{\text{part}} \rangle$. This strongly supports the idea of a production of $s\bar{s}$-pairs and subsequent percolation as the primary process for hadrons containing strangeness.

6.6. Comparisons with Predictions by Transport Models

Several transport models, presented in [110], were used to make predictions for Ag+Ag collisions at 1.58 A GeV, which can be tested. The most fundamental prediction is the resulting production yield of particles as shown in figure 1.10. In figure 6.10, these predictions are directly compared with measured particle production yields in $0 - 10\%$ most central collisions presented in this work and [99][125] by dividing the predicted production yield by the measured one.

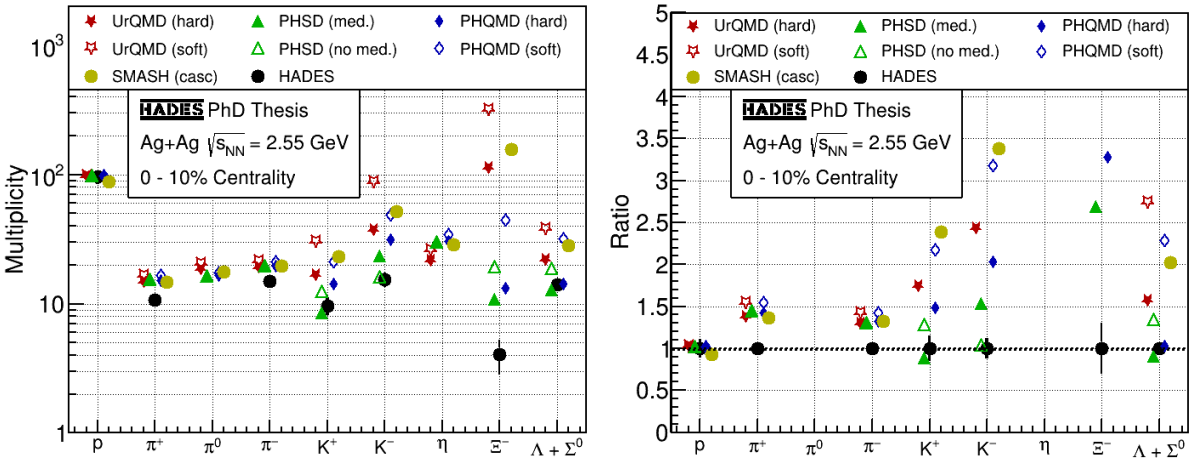

(a) Absolute Yields

(b) Ratios

Figure 6.10.: Comparison of obtained free proton [125] as well as $\pi^{\pm}$ [99], K^+, K^-, Ξ^- [125] and Λ [125] particle production yields from $0-10\%$ most central Ag(1.58 A GeV)+Ag collisions compared to predictions by transport models from [110].

Most transport model predictions overestimate the ones reconstructed from data by several factors. PHSD predictions presented in [110] appear to describe the total obtained particle production yield with the highest precision. However, all transport models predict the $\pi^{\pm}$ production yields to be higher than the ones reconstructed in [99]. This influences the amount of πB interactions inside the medium. In the transport picture, the more pions are present, the higher the chance for forming a resonance which leads to the production of a strange hadron ($\pi B \rightarrow YK^+$ or $\pi B \rightarrow BK^+K^-$). The Ξ^- is affected even more, as it contains two strange quarks. The investigation concerning the origin of the discrepancy is still ongoing and will have to be answered in future analyses.
However, comparing ratios of hadrons containing strangeness is not strongly affected by those differences as long as nucleon-to-pion ratios and the isospin asymmetry are comparable between models and data. Assuming the physical processes are modelled accurately, the corresponding ratios should display a high degree of consistency between both.

Figure 6.11 shows the ϕ/K^- ratio as function of $\sqrt{s_{\mathrm{NN}}}$ with prediction curves from the SMASH [3] and UrQMD [119] transport models.
In the region between $2 < \sqrt{s_{\mathrm{NN}}} < 3$ GeV a good qualitative agreement between UrQMD (version 3.3p2) predictions for Au+Au collisions and data is observed. The ratio is underestimated by a factor of two for higher energy Au+Au collisions, as indicated by the deviation from the data measured by STAR. The predictions made by SMASH (version 2.0) overestimate the ratio for $\sqrt{s_{\mathrm{NN}}} > 2.5$ GeV. This disagreement between a good qualitative description below and an underestimation beyond $\sqrt{s_{\mathrm{NN}}} = 3$ GeV indicates a change in the created medium. Further measurements in this region would help in understanding this transition.
Another question arises from the drop of the ratio predicted by UrQMD slightly above $\sqrt{s_{\mathrm{NN}}} = 2$ GeV. Further measurements in this energy region could enhance the understanding of the medium effects by testing the validity of the drop.
Another observation is made when comparing the shapes of the dN/dy distributions between SMASH simulations and measured data. This is discussed, as an outlook for future analyses, in the following section.

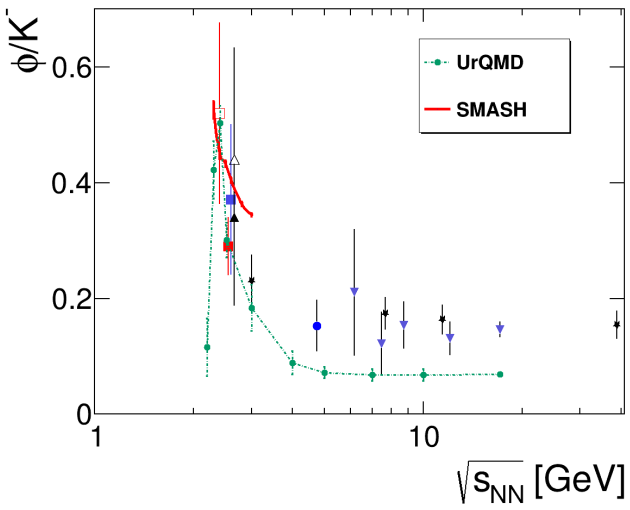

Figure 6.11.: ϕ/K^- ratio for different collision energies and systems [3][9][13][15][66][81][105][119] with SMASH [3] and UrQMD [119] transport model curves applied. The HADES Ag+Ag at $\sqrt{s_{\mathrm{NN}}} = 2.55$ GeV data are taken from $0-30\%$ most central events. See figure 6.3 for an explanation of the symbols.

6.7. Statistical Hadronisation Model Fit

As introduced in section 1.3.2, one of the most surprising findings is that the multiplicities of particles emitted from a heavy-ion collision can be described very accurately by simple considerations based on statistical physics.
In the context of statistical hadronisation models the description of strange hadron yields remains a matter of discussion. As it was demonstrated in sections 6.3 and 6.4, one general ansatz is the definition of a strangeness canonical volume in which strangeness must be strictly conserved and which is smaller than the volume of the fireball. Without the corresponding radius R_C, which suppresses the production of strangeness, the production rates are overestimated by orders of magnitude, which indicates a non-equilibration of strange hadrons in the medium.
Generally, in the framework of an SHM, the final particle production rates can be estimated in two ways: firstly, by taking the produced light nuclei into account via an upscaling of the measured proton yields by the number of protons bound in light nuclei. Secondly, by including light nuclei in the fit. Both cases are presented below. For both cases, the Thermal-FIST [134] framework, version 1.4.2, is utilised, using the list of particles including excited nuclei from the PDG database in 2020. All fits were performed using an ideal Hadron Resonance Gas with the energy-dependent Breit-Wigner distribution for emulating the resonance widths, assuming a constant branching ratio for decays. The $\Delta(1232)$-resonance has a significant non-resonant πN-contribution near the production threshold, which would influence the estimated $\Delta(1232)$ production rate due to the finite width of the resonance. As there is currently no solution for this issue, a reference test case is created by forcing the width to be zero. For the system Ag+Ag, Q/B is fixed to 0.440.

Figure 6.12 displays the results of the fits on the reconstructed particle production yields from Ag(1.58 A GeV)+Ag-collisions. The p, K^0_S, Λ, Ξ^-, Hypertriton and Hyperhydrogen-4 yields are taken from [125], while the charged pion and light nuclei yields are taken from [99][100]. The π^0 and η yields can be found in [103]. From [36], the Σ^0-yield is taken.
For the case of figure 6.12(a) the fit included N_{part}, p, π^0, $\pi^\pm$, $\phi(1020)$, Λ, K^+, K^-, K^0_S, Ξ^-, Σ^0 and η, resulting in a χ^2/NDF-value of 2.028. The extracted temperature of the fireball is found to be $T = 66.384 \pm 1.299$ MeV, while the radius $R = 9.662 \pm 0.567$ fm results in a fireball volume of $V \approx 3777 \pm 665$ fm^3. For the baryochemical potential, a value of $\mu_B = 773.391 \pm 8.820$ MeV is obtained. Looking at the strangeness production, one obtains a strangeness canonical radius of $R_C = 3.209 \pm 0.289$ fm. For the most part, as also indicated by the χ^2/NDF-value,

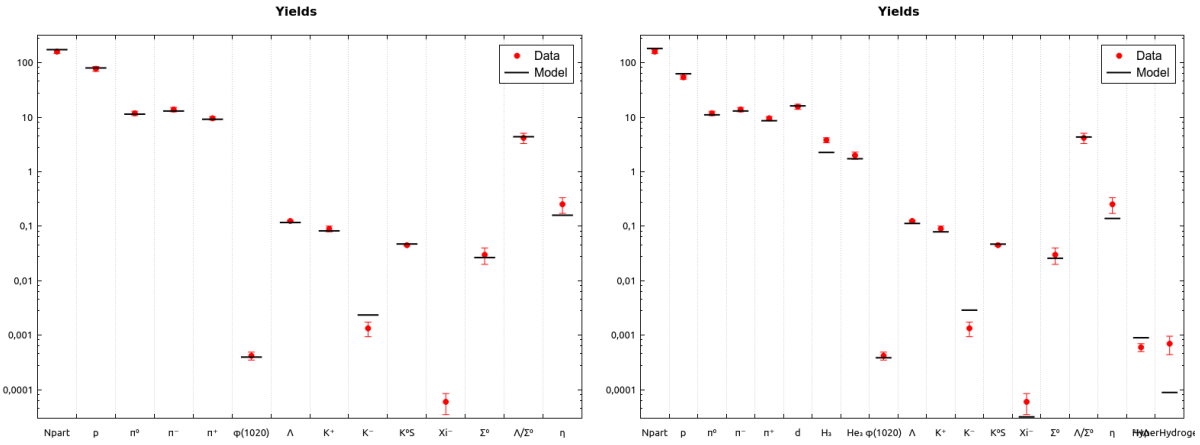

(a) No light nuclei (b) With light nuclei

Figure 6.12.: Thermal-FIST fit to Ag(1.58 A GeV)+Ag data with upscaled protons instead of light nuclei (a) and including light nuclei (b).

this describes the yields obtained from data with high accuracy. However, as the ratio displayed in figure 6.13 shows, some discrepancies can be observed.

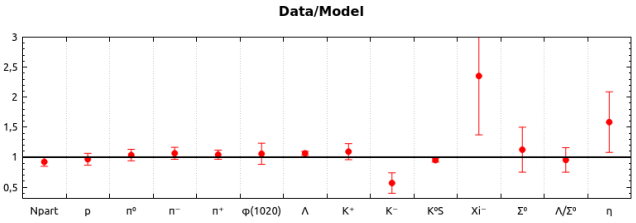

Figure 6.13.: Ratio of data to a Thermal-FIST fit to Ag(1.58 A GeV)+Ag data with upscaled protons instead of light nuclei.

In particular, the model value for the K^- yield lies off by $\approx 40\%$ and the cascade Ξ^- yield by a factor of ≈ 2.5. However, the statistical and systematic uncertainty of the Ξ^- yield is in the order of 30-40 %, which does not allow for a conclusion whether the description is truely inaccurate. Considerable underestimations for the Ξ^--yield at low energy heavy-ion collisions have previously been observed with thermal model fits. In [16] this issue was resolved including higher excited Ξ, Λ and Σ states. Such states are included within the used particle list. A potential discrepancy could be explained either due to the experimentally not well-constrained widths and branching ratios of these higher states, or could hint towards the necessity of including higher $N^\star$-resonances as also discussed in [16]. However, this microscopic transport model-based approach so far lacks experimental evidence for decays into Ξ hyperons.

For the case of figure 6.12(b) the fit included N_{part}, p_{free}, π^0, $\pi^\pm$, d, ^{3}H, ^{3}He, $\phi(1020)$, Λ, K^+, K^-, K^0_S, Ξ^-, Σ^0 and η, resulting in a χ^2/NDF-value of 5.047. The extracted temperature of the fireball is found to be $T = 65.909 \pm 0.863$ MeV, while the radius $R = 9.846 \pm 0.263$ fm results in a fireball volume of $V \approx 3998 \pm 321$ fm^3. For the baryochemical potential, a value of $\mu_B = 753.701 \pm 2.299$ MeV is obtained. Looking at the strangeness production, one obtains a strangeness canonical radius of $R_C = 3.608 \pm 0.187$ fm. All those values are close to the ones obtained in the previous case. Also, in both cases, the inclusion of a finite width $\Delta(1232)$-resonance does not vary the resulting T and μ_B parameterisation by more than a few per cent. Also, as in the previous case, the model yield of the Ξ^- hyperon and the K^- are off by approximately the same amount, as figure 6.14 shows.

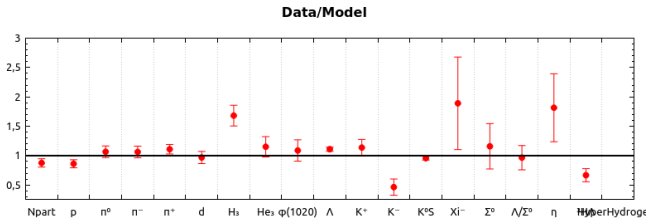

Figure 6.14.: Ratio of data to a Thermal-FIST fit to Ag(1.58 A GeV)+Ag data with light nuclei.

Additionally, the ^{3}H yield is $\approx 80\%$ too high, which explains the overestimation of the hypertriton yield. Hyperhydrogen-4 is underestimated by one order of magnitude. However, in the global parameterisations, there is no significant discrepancy between the obtained results. Table 6.2 summarises the results of the performed fits. The cases presented there are the following: Case 1 is for no nuclei and upscaled proton yield with finite Δ-width (117 MeV), case 2 is for no nuclei and upscaled proton yield with zero Δ-width, case 3 is for included nuclei with finite Δ-width (117 MeV) and case 4 is for included nuclei with zero Δ-width.

	Case 1	**Case 2**	**Case 3**	**Case 4**
T [MeV]	66.384 ± 1.299	67.867 ± 1.703	65.847 ± 0.825	65.909 ± 0.862
μ_B [MeV]	773.391 ± 8.820	786.774 ± 14.236	752.942 ± 2.289	753.701 ± 2.299
R [fm]	9.662 ± 0.566	8.709 ± 0.794	10.021 ± 0.257	9.845 ± 0.263
V [fm^3]	3777.87 ± 665.06	2767.82 ± 757.14	4215.56 ± 325.49	3998.14 ± 320.93
R_C [fm]	3.209 ± 0.289	2.945 ± 0.332	3.578 ± 0.180	3.607 ± 0.187
V_C [fm^3]	138.376 ± 37.377	106.999 ± 36.279	191.969 ± 29.108	196.729 ± 30.666
χ^2/NDF	2.028	1.664	5.046	4.88014

Table 6.2.: Summary of the SHM fit results for Ag(1.58 A GeV)+Ag collisions measured with HADES. Details in the text above.

6.8. Outlook

6.8.1. Identification of Observables Concerning the Systematic Time Offset

In section 4.1.7, a background contribution is discussed, which strongly affects the coverage of the final reconstructed phase space. It is planned to emulate the effect in simulations to understand the underlying issue's precise nature. Suppose it is possible to isolate observables which separate a particle candidate creating this effect from an actual particle candidate. In that case, the knowledge will be applied to data to test if the effect can be removed without further biasing it. This study will, if successful, improve the phase space coverage for charged Kaons, reduce the background below the ϕ-meson signal and reduce the systematic effects on the final results.

6.8.2. A Relative Widening of the K^+ dN/dy-Spectra in Data

When comparing the particle production rates as a function of rapidity between data and transport model simulations, figures 5.33 and 6.15 display a deviation in the width of the distributions. In figure 5.33, an increase in the width of the distribution is observed with decreasing centrality. Including more peripheral centrality intervals in future analyses will help to solidify this observation.
As the simulations are performed without the inclusion of a long-range Coulomb-potential, due to the significantly prolonged runtime of the simulation when included, and due to the previous

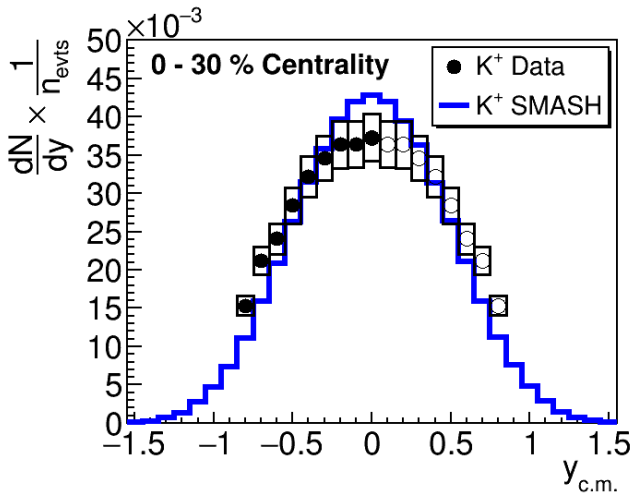

Figure 6.15.: Comparison of shapes between dN/dy-distributions from data and SMASH simulations scaled to data. The HADES Ag+Ag at $\sqrt{s_{\mathrm{NN}}} = 2.55$ GeV data are taken from $0-30\%$ most central events.

observation of such an effect for the for π^+ [8][99], this widening is assumed to be caused by the Coulomb potential. In these two references, a shift of the transverse momentum distributions' maximum towards higher p_t is observed as a result of the repulsive long-range Coulomb interaction.
The underlying assumption is a spherically symmetric and isotropic source, kinematically described by a Boltzmann distribution, containing an additional V_{eff} parameter [8]

$$\frac{d^2N}{dp_t dy} = A \cdot p_t \cdot m_t \cdot e^{-(E \pm V_{\mathrm{eff}})/T} \cdot J \cdot J_{\mathrm{eff}} \tag{6.1}$$

The effective potential V_{eff} contains the Coulomb potential and an energy and mass-dependent term. $J \cdot J_{\mathrm{eff}}$ denotes the full Jacobian of the transformation from the initial to the final kinematical variables. More details can be found in [8]. However, as this is a spherically symmetric and isotropic source function, it can only be purposefully applied in the midrapidity region of the $0-10\%$ most central collision events, as there is no significant amount of spectators modifying the potential.
To test the hypothesis, the midrapidity transverse momentum spectrum of K^0_s from [125] in $0-10\%$ most central events is fitted with the modified Boltzmann and $V_C = 0$ MeV. The parameters A and T are left as free. For the fit, the K^0_S transverse momentum distribution is scaled by a factor of two, to emulate the distribution for the K^0. The K^0 is chosen for reference as the K^- phase space coverage currently does not allow for a precise transverse fit, as the region $m_t - m_0 > 200$ MeV/c^2, which is necessary for the identification of the effect, is not sufficiently covered. The resulting T-parameter from this fit is taken and fixed for a subsequent fit of equation 6.1 to the K^+ transverse momentum spectrum. For this fit, only A is left as a free parameter, assuming that the shape of the K^+ transverse momentum distribution differs from the K^0 one mainly due to the positive charges and the repulsive long-range Coulomb interaction. A second fit is performed, also leaving only A as a free parameter but fixing the value V_C to 8 MeV, as obtained from the charged pion analysis in [99]. For both cases the χ^2/NDF between fit and K^+ midrapidity transverse momentum spectrum are calculated and compared, as displayed in figure 6.16.
A slight shift of the maximum can be observed, as it would indicate an effect due to the long-range Coulomb interaction. However, the observed χ^2/NDF-values as well as the fluctuations of the transverse momentum bins lead to the conclusion, that no significant effect can be verified from the data. However, when including also other rapidity intervals, the question can be posed, whether the inclusion of a long-range Coulomb interaction can significantly alter the shape of

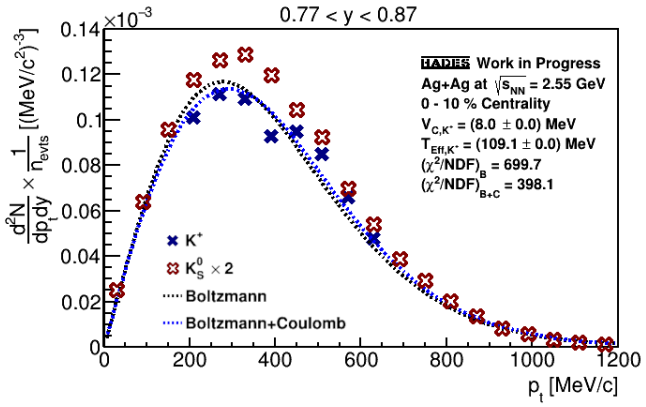

Figure 6.16.: Fit on the K^+ midrapidity transverse momentum distribution without and with the Coulomb-potential obtained in [99]. The scaled K^0_S distribution is shown for comparison.

the dN/dy distribution. Consequently, the production rate as a function of the centre of mass rapidity was determined, once for the case of $V_C = 0$ MeV and once for the case of $V_C = 8$ MeV. The result from the $0 - 10\%$ most central events can be seen in figure 6.17.

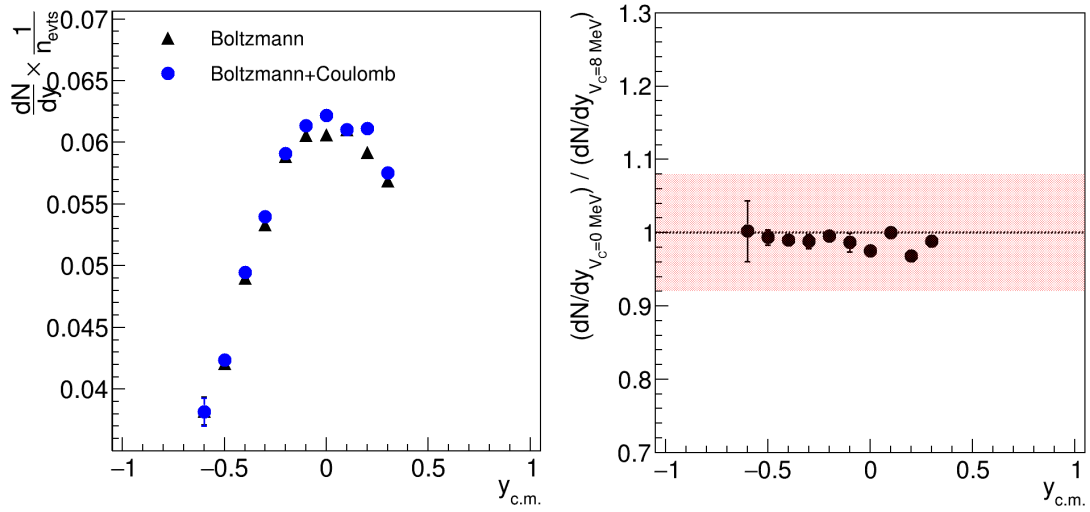

Figure 6.17.: K^+- dN/dy-distribution for the cases $V_C = 0$ MeV and $V_C = 8$ MeV (left) as well as the ratio between both cases with the red box indicating the systematic uncertainty of the multidifferential K^+ analysis of $\approx 8\%$.

As this comparison shows, there is no significant change in the shape of the dN/dy distribution for the inclusion of a long-range Coulomb potential. The change in coverage, with the inclusion of three rapidity bins in the forward direction, was made possible by removing the MDC energy loss constraint. This increases the transverse momentum coverage to stabilise the fitting procedure. However, this reduces the purity of the sample and is not advised for extracting the particle production rate. All obtained values are consistent with previously presented results from chapter 5 within the $\approx 8\%$ systematic uncertainties.

In summary, it can be stated, that the broadening of the K^+ dN/dy-distribution can not be attributed to a long-range Coulomb interaction caused by a spherically symmetric, isotropic source. However, in particular towards more peripheral collisions, this is not expected to be realised. To study this effect further, additional in-depth studies with microscopic transport models have to be performed.

6.8.3. Strangeness Production in Statistical Hadronisation Models

In this work, the focus for describing strange hadron production rates with Statistical Hadronisation Models was put on the strangeness canonical radius R_C. However, as shown in sections 6.3 and 6.4, this poses difficulties when simultaneously trying to describe the ϕ/Ξ^- and ϕ/K^- ratios. Alternatively, one can assume a grand-canonical system with a strangeness suppression factor γ_s, which also offers an alternative way to describe the obtained yields [134].
Another possible ansatz would be the assumption of a grand-canonical system with strangeness contained as an "impurity". For strange hadrons, a factor $N_{s\bar{s}}$ would be determined from measured cross sections, while the non-measured cross sections are interpolated by a model. This ansatz was successfully implemented for hadrons containing charm at LHC energies [23][24][25] and would assume production of $s\bar{s}$-states in the early stages of the collision, while the net-strangeness of the entire grand-canonical system remains zero. However, as the formation time of a strange hadron in Ag(1.58 A GeV)+Ag collisions is ≈ 10 fm/c, while for a charmed hadron at LHC energies, it is ≈ 1 fm/c, it remains to be tested whether this accurately reproduces the measured strange hadron yields.

6.8.4. Ag(1.23 A GeV)+Ag Data

As mentioned in section 2.3, also data on Ag+Ag collisions at $\sqrt{s_{\mathrm{NN}}} = 2.4$ GeV was taken. Despite the lower number of events by a factor of 10, first analyses proved the reconstruction of charged Kaons and the ϕ-meson to be generally possible. Results from this data would enable a direct comparison of two different collision systems at the same energy. Furthermore, it would extend understanding of the system size dependence of strangeness production. This could improve the precision of the universal $\langle A_{\mathrm{part}} \rangle$-scaling for hadrons containing strangeness, investigated in [119].

6.8.5. Beamtime Proposals for Au+Au Collisions Below 1 A GeV

Currently, a proposal for beamtimes with Au+Au collisions below 1 A GeV is being discussed. The corresponding energies would be 0.8, 0.6, 0.4 and 0.2 A GeV. This would be a beam energy scan well below any strange hadron's energetic free NN interaction production threshold. It is expected, at the proposed events rates and beamtime duration, that Λ, K^0_S, K^+ and K^- would be reconstructed at a rate of 10^{-5} to 10^{-3} per event for 0.8 A GeV and 10^{-6} to 10^{-4} per event for 0.6 A GeV. For both cases, the reconstruction of ϕ-mesons is also assumed to be possible. With a successfully reconstructed ϕ-meson, further in-depth studies of medium effects on strangeness production would be possible as in figures 6.3 and 6.7. It would offer exciting analyses, as the excess energy provided by the system would be ≈ 660 MeV (Au(0.8 A GeV)+Au) and ≈ 740 MeV (Au(0.6 A GeV)+Au) for K^- and ϕ-meson. This would provide a strong test for existing models.

7. Zusammenfassung

Diese Arbeit fokussiert sich auf die Analyse der Produktion von Seltsamkeit, speziell von K^+, K^- und ϕ-Mesonen, in Kollisionen von Ag-Kernen bei einer einfallenden Strahlenergie von 1.58 A GeV, gemessen mit HADES. Aufgrund ihrer Produktion unterhalb der energetischen Produktionsschwelle in binären NN-Kollisionen, bieten ihre kinematischen Verteilungen und Produktionsraten einen guten Test für existierende Modelle zur Interaktion von Hadronen in stark wechselwirkenden Medien mit Dichten $\rho > \rho_0$. Zudem haben die Daten aus Schwerionenkollisionen in den letzten Jahren auch Einfluss auf astrophysikalische Studien [6][132].

7.1. Einführung

In diesem Kapitel werden die wichtigsten Grundlagen der Kern- und Teilchenphysik zusammengefasst und der aktuelle Forschungsstand beleuchtet. Die fundamentalsten Bausteinen der Materie sind Quarks. Diese besitzen, neben der elektrischen Ladung, die Farbladungen rot, grün oder blau. Jedes aus Quarks zusammengesetzte System muss farbneutral sein - alle Farben müssen vertreten sein oder Antifarben sie neutralisieren. Zusammengehalten wird das entsprechende Quark-System über die starke Wechselwirkung, welche durch Gluonen übertragen wird, welche ebenfalls Farbladungen tragen (Farbe-Antifarbe). Konsequenterweise können Quarks nicht frei, sondern nur gebunden mit anderen Quarks beobachtet werden, da dies die Farbneutralität verletzen würde - ein Umstand der als *Quark-Einschluss* bekannt ist.
Dies gilt für einzelne Hadronen bei normalen Materiedichten $\rho \leq \rho_0$. Bei der Kollision von Schwerionen hingegen, werden hohe Dichten innerhalb der produzierten Medien erreicht. Im Falle von Kollisionen bei hohen Schwerpunktsenergien passieren die kollidierenden Kerne einander ohne nennenswert abgestoppt zu werden. Es wird ein Medium mit hoher Energiedichte erzeugt - das Quark-Gluon-Plasma (QGP). Dieses Medium besteht aus produzierten $q\bar{q}$-Paaren und Gluonen, welche quasi-frei rekombinieren und neue Hadronen bilden, bis die Dichte des Mediums niedrig genug wird, dass sie in der letztgeformten Konfiguration ausfrieren.
HADES hingegen befindet sich im Bereich niedriger Schwerpunktsenergien mit $\sqrt{s_{\mathrm{NN}}} \approx 2 - 3$ GeV. Im Bereich von wenigen GeV werden die einfallenden Kerne zum großen Teil auf ihrem Weg gestoppt, sobald sie einen anderen Kern treffen. Das hierbei entstehende Medium wird auf das Mehrfache von ρ_0 komprimiert. Innerhalb dieses Mediums werden neue Teilchen produziert - hauptsächlich $\pi^{\pm}$, aber auch solche, die Seltsamkeit enthalten. Seltsamkeit ist kein natürlich existierender Quark-Geschmack und benötigt mindestens ≈ 670 MeV an zusätzlicher Energie durch das einfallende Nukleon, um im energetisch günstigsten Produktionskanal

$$NN \rightarrow NK\Lambda$$

in Hadronenform produziert zu werden. Im Falle von Ag(1.58 A GeV)+Ag Kollisionen liegt die durch den Impuls des einfallenden Kerns bereitgestellte Energie exakt auf dieser Schwelle. Allerdings ist für die übrigen seltsamen Hadronen ungeklärt, wie die Erzeugung von Seltsamkeit abläuft. Eine Möglichkeit ist die Produktion von $s\bar{s}$-Paaren innerhalb der sich überlappenden Pion-Wolken der Nukleonen, wodurch die seltsamen Quarks durch den Prozess der Perkolation entlang dieser überlappenden Wolken wandern, bis das System eine kritische Dichte unterschreitet und das Quark in einem Hadron ausfriert [63]. Eine andere Möglichkeit beschreibt die

Produktion vollständiger Hadronen durch den Zerfall angeregter Nukleon-Resonanzen. Hierbei reagieren zwei Nukleonen, wodurch ein Nukleon energetisch angeregt wird. Wechselwirkt es anschließend mit weiteren Nukleonen und akkumuliert ausreichend Energie für den Zerfall in seltsame Hadronen, zerfällt es mit einer gewissen Wahrscheinlichkeit in diese. Dies wird von Transport-Modellen [30][104] genutzt, um die Produktion von Teilchen in Schwerionenkollisionen bei niedrigen Energien zu modellieren.
Eine rein phänomenologisch motivierte Beschreibung liefert das statistische Hadronisierungsmodell welches den Kollisionsbereich der beiden Kerne rein thermodynamisch betrachtet. Hierbei wird eine ausfrierende Sphäre angenommen, welche thermodynamische Eigenschaften besitzt - auf elementarster Ebene die Temperatur T und das baryochemische Potential μ_B. Gleichungen, die diese Parameter mit der Anzahl produzierter Teilchen korrelieren, werden an die Anzahl der im Experiment rekonstruierter Teilchen angefittet. Auf der Basis der aus dem Fit extrahierten Parameter extrapoliert das Modell die produzierte Anzahl der nicht gemessenen.
Auf der Basis dieses Modells errechnet sich ein Phasendiagramm der QCD Materie mit den Zustandsgrößen T und μ_B. Die in Abbildung 1.12 angedeutete Linie für den Phasenübergang ist hierbei von hohem Interesse und die Natur dieser Übergänge, sowie die Eigenschaften der dadurch entstehenden Materiezustände, ist Gegenstand der aktuellen Forschung. HADES befindet sich hierbei im Bereich niedriger T und hoher μ_B.
In dieser Arbeit werden die kinematischen Eigenschaften und die Teilchenproduktionsraten der seltsamen Mesonen K^+,K^- und ϕ genutzt, um die Eigenschaften dieser Medien zu beleuchten, indem die Daten mit vorangegangenen Messungen, sowie mit theoretischen Modellrechnungen verglichen werden.

7.2. Das HADES-Experiment

Das **H**igh **A**cceptance **DiE**lectron **S**pectrometer (HADES) ist ein Experiment mit fixiertem Kollisionsziel, am SIS18 Synchroton an der GSI in Darmstadt stehend. In azimuthaler Richtung deckt der Detektor nahezu 360° ab, während die Polarwinkel-Abdeckung zwischen 18° und 85° in Vorwärtsrichtung des Laborsystems gegeben ist.

Die Startzeit t_0 jeder Reaktion wird durch den Diamantkristall-Detektor START gemessen. Die produzierten Teilchen passieren danach den Ringabbildenden Cherenkov Detektor (RICH) für die Rekonstruktion von $e^{\pm}$ durch das produzierte Cherenkov-Licht. Dieser Detektor wird für diese Analyse nicht verwendet. Danach passieren die Teilchen die Vieldraht-Driftkammern MDC I-IV, welche auf halbem Weg durch einen Magneten in innere und äußere MDCs unterteilt werden. Die mit Ar/CO_2 Gas gefüllten Detektoren besitzen jeder sechs Fühldrähte, welche zur Spurrekonstruktion und zur Messung des Energieverlustes durch Ladungsdeposition genutzt werden. Aufgrund der rekonstruierten Spur, und der Ablenkung im Magnetfeld zwischen den inneren und äußeren MDCs, kann das Impuls-zu-Ladungs-Verhältnis bestimmt werden. Zur Bestimmung des dazu nötigen Impulses wird die Flugzeitwand der META-Detektoren genutzt. Diese besteht aus dem Resistiven Plattenkammer Detektor RPC und dem Szintillationsdetektor TOF. Letzterer kann somit auch für Energieverlust-Messungen genutzt werden. Zudem fungieren die META-Detektoren ebenfalls als Auslöser über die gemessene Anzahl an registrierten Treffern pro Kollisionsereignis. Das nachfolgende elektromagnetische Kalorimeter (ECal) wird zur Detektion und Identifikation von Leptonen, $\pi^{\pm}$ und Photonen genutzt, erfüllt für diese Analyse aber keine Funktion.
Die Ereignisebene der Kollision wird durch die Vorwärtswand (FW) bestimmt, indem die Spektatoren der Kollision registriert und ihre räumliche Orientierung bestimmt werden.

7.3. Analyse

Die Selektion von möglichst reinen Ag+Ag-Kollisionsereignissen zur Grundlage der Untersuchungen wird durch die Anwendung der in Abschnitt 3.5.1 eingeführten Ereignisselektionskriterien gewährleistet. Zur Feinanpassung dieser Kriterien an die experimentellen Gegebenheiten wird in Abschnitt 3.5.2 beschrieben, wie die vorliegende Analyse dazu genutzt werden kann, einzelne Parameter auf Validität zu testen. Nach Anwendung der Selektionskriterien verbleiben noch etwa 50% der zuvor gemessenen Kollisionsereignisse in der auszuwertenden Datenbank. Die verbleibenden Kollisionsereignisse werden dann durch Selektionskriterien für die produzierten Hadronen gefiltert. Diese umfassen sowohl Energieverlust-Kriterien in MDC und TOF, welche die Beiträge von Protonen und $\pi^{\pm}$ in den Spektren unterdrücken, als auch Gütekriterien für die Qualität der rekonstruierten Spur, vornehmlich χ^2-Tests für die Genauigkeit der Beschreibung der Spurpunkte durch die angewandte Fit-Funktion.
Im Falle der $K^{\pm}$ werden die rekonstruierten Massen der Teilchenspuren, welche die Selektionskriterien in Tabelle 4.2 erfüllen, in Histogramme gefüllt, welche jeweils Intervalle in der Ebene der reduzierten transversalen Masse über der Rapidität $((m_t - m_0) - y)$ repräsentieren. Da das K^+-Signal durch die Flanken der π^+ und p Signale überlagert wird, und das K^- durch die π^- Signalflanke, muss der dadurch entstehende Untergrund noch abgezogen werden. Die Abschätzung dieses Untergrundes wird mithilfe einer Interpolation getätigt. Hierzu wird an der erwarteten Signalposition der geladenen Kaonen ein Gauß-Fit durchgeführt. Danach werden die Interpolationspunkte dreifach links- und dreifach rechtsseitig des Signales in festen σ-Abständen festgelegt. Es folgt ein Minimierungsverfahren eines Polynoms dritten Grades, welches als Randbedingungen die (x, y)-Positionen der vorgegebenen Punkte, sowie deren erste (in allen Punkten) und zweite (in den Randpunkten) Ableitung erfüllen muss. Für alle Einträge außerhalb des Interpolationsbereiches wird als Untergrund der Datenwert angenommen. Nach der Subtraktion der so beschriebenen Untergrundverteilung erhält man die reine $K^{\pm}$-Signal-Verteilung für jeden $((m_t - m_0) - y)$-Bereich, über welche in $\mu \pm 2\sigma$ summiert wird, was in der finalen rekonstruierten Teilchenproduktionsmenge als Funktion von reduzierter transversaler Masse und Rapidität resultiert. In Absolutzahlen sind dies 1.34×10^7 K^+ und 1.21×10^5 K^- innerhalb der gegebenen Akzeptanz und Effizienz. Exakt diese Akzeptanz und Effizienz Effekte werden nun noch heraus korrigiert, indem UrQMD Simulationen von Ag+Ag-Kollisionsereignissen generiert werden, deren produzierte Teilchen durch eine GEANT-Emulation des HADES Detektors transportiert werden. Nun werden auf die durch GEANT rekonstruierten Teilchen die gleichen Bedingungen angewandt wie zuvor auf Daten und die hieraus rekonstruierten $K^{\pm}$-Multiplizitäten als Funktion von $((m_t - m_0) - y)$ durch die Anzahl der generierten geteilt. Dies ergibt den gewünschten Akzeptanz $\times$ Effizienz Korrekturfaktor, mit dem die Daten daraufhin korrigiert werden. Dies ergibt die finalen reduzierten transversalen Massenspektren als Funktion der Rapidität, welche zur finalen Analyse verwendet werden.
Für das ϕ-Meson wird prinzipiell der gleiche Analyseweg gewählt, auch wenn es Variationen in der Selektion und Signalextraktion gibt. Da das ϕ-Meson nach etwa 45 fm/c zerfällt, wird es über die Tochterteilchen im Kanal $\phi \to K^+K^-$ analysiert. Die aus der Impulserhaltung berechnete invariante Masse der akzeptierten Tochterteilchen-Paare des ϕ-Mesons wird dementsprechend als Funktion von $((m_t - m_0) - y)$ des rekonstruierten Mutterteilchens aufgetragen. Konsequenterweise resultiert kein reines ϕ-Signal aus dieser Rekonstruktion, sondern ein Signal welches auf einer breiten Untergrundverteilung sitzt, da einerseits keine reinen $K^{\pm}$ selektiert werden können, andererseits auch K^+-K^--Paare akzeptiert werden können, die nicht von ϕ-Mesonen stammen. Der Anteil wird durch geometrische Einschränkungen (Tabelle 4.3) minimiert, kann jedoch nicht vollständig unterdrückt werden. Die Selektion der $K^{\pm}$ geschieht durch die Einschränkung des akzeptierten Bereiches in der Impuls-Masse-Ebene. Hierzu werden Massen- und Impulsein-

schränkungen formuliert, welche den Bereich einrahmen, aus dem geladene Kaonen zu erwarten sind (siehe Tabelle 4.2). Außerdem wird kein MDC Energieverlust-Kriterium angelegt, da der Statistikverlust der $K^{\pm}$ im hohen Impulsbereich um $\approx 50\%$ jeglichen Vorteilen entgegensteht. In jedem der $((m_t - m_0) - y)$-Intervalle wird der Untergrund unterhalb des Signales durch die Mischung von K^+-K^--Paaren abgeschätzt, was in den meisten Fällen eine sehr genaue Beschreibung des Untergrundes ergibt. Nach Abzug dieses Untergrundes verbleibt das eigentliche ϕ-Meson-Signal, über dessen Histogramm-Einträge ebenfalls in $\mu \pm 2\sigma$ summiert wird. Auf diese Weise werden 5.67×10^3 ϕ-Mesonen für die weitere Analyse rekonsrtuiert. Wie auch für $K^{\pm}$, wird die Akzeptanz $\times$ Effizienz Korrektur durch den Vergleich von durch GEANT rekonstruierten ϕ-Mesonen im Verhältnis zu den generierten durchgeführt. Da ϕ-Mesonen nur selten produziert werden, werden hierbei die Anzahl an ϕ-Mesonen künstlich erhöht, indem PLUTO generierte ϕ-Mesonen mit dem Kanal $\phi \to K^+K^-$ zu den Standardsimulationen hinzugefügt werden.
Ein bisher nicht erwähnter und dennoch zentraler Problemfall bei der vorliegenden Analyse war die Präsenz einer bisher nicht final konklusiv identifizierten Untergrundquelle von geladenen Pionen, die den Phasenraum der geladenen Kaonen stark überlappen und den Rekonstruktionsbereich dessen deutlich einschränken. Dieser Beitrag ist in Abschnitt 4.1.7 diskutiert und stammt höchstwahrscheinlich von überlappenden META-Signalen von $\pi^{\pm}$ und Neutronen und einer daraus resultierenden Unterkorrektur der Zeit die das Signal benötigt, um über die Detektorschwelle zu gelangen. Da die Neutronen allerdings nicht direkt gemessen werden können, ist es schwer, diesen Beitrag aktiv zu belegen. Untersuchungen mithilfe des TOF-Detektors deuten allerdings genau auf diesen Effekt. Es ist geplant, eine Simulationsstudie durchzuführen, um diesen in Simulationen unbeobachteten Effekt zu emulieren und daraus eine potentielle Lösungsstrategie zu entwickeln. Sollte dies erfolgreich sein, könnte sich der rekonstruierte Phasenraum bei geladenen Kaonen in transversaler Richtung im besten Fall nahezu verdoppeln. Dies würde zu einer deutlichen Reduktion systematischer Unsicherheit führen.

Die transversalen Spektren als Funktion der Rapidität werden nun in die nicht durch die Messung abgedeckte Region des Phasenraumes extrapoliert. Hierzu wird eine Boltzmann-Funktion verwendet, welche die Kollisionsregion vereinfacht als einen radialsymmetrischen thermischen Feuerball annimmt. Die transversalen Spektren werden somit durch eine Funktion [125]

$$\frac{d^2N}{d(m_t - m_0)dy} = 2\pi \cdot C \cdot \cosh(y) \cdot e^{-\frac{(m_t - m_0)\cosh(y)}{T_{\text{Eff}}}} \tag{7.1}$$

gefittet. Aus dieser Fit-Funktion kann, in Abhängigkeit von der Rapidität, der Parameter T_{Eff} direkt extrahiert werden. Für die Extraktion der Produktionsrate als Funktion der Rapidität wird über die Daten in transversaler Richtung summiert und im nicht abgedeckten Bereich der Fit integriert. Die Summe aus beiden, multipliziert mit der Gesamtzahl akzeptierter Kollisionsereignisse, ergibt die gesamte Produktionsrate in Abhängigkeit von der Rapidität. Dies wird für alle Teilchen in analoger Form getan. Die Verteilungen von T_{Eff} als Funktion der Rapidität werden durch eine Funktion $T_B = \frac{T_{\text{Eff}}}{\cosh(y)}$ angefittet. Dies dient dem Ausgleich von Fluktuationen welche zum Teil aus der reduzierten Phasenraumabdeckung resultieren. Der extrahierte Wert von T_{Eff} bei $y = 0$ wird somit aus der Fit-Funktion abgeleitet. Hierbei beobachtet man eine interessante Diskrepanz zwischen den T_{Eff}-Parametern von K^+ sowie ϕ-Meson ($T_{\text{Eff}} \approx 120$ MeV) und K^- ($T_{\text{Eff}} \approx 90$ MeV).
Das resultierende Spektrum der Teilchenproduktionsrate als Funktion der Rapidität wird mit einer Superposition der Funktion [125]

$$\frac{dN}{dy} \approx C \cdot \exp\left(-\frac{y^2}{2\sigma^2}\right) \tag{7.2}$$

beschrieben, wobei $\sigma = \sqrt{\frac{T}{m_0}}$. Dies ist motiviert durch die Tatsache, dass eine Verbreiterung des K^+ dN/dy-Spektrums im Verhältnis zum K^- beobachtet wird. Dementsprechend wird für dN/dy ein zwei-Quellen-Modell angewandt, wobei beide thermischen Quellen im Abstand $\pm\eta$ zu $y = 0$ lokalisiert sind. Vergleiche mit SMASH-Berechnungen bestätigen eine tatsächliche Verbreiterung - während die Form der K^- und ϕ-Mesonen durch SMASH nahezu perfekt beschrieben wird, ist die Diskrepanz für K^+ signifikant. Siehe hierzu die Abbildungen 5.33, 5.34 und 5.35.

7.4. Ergebnisse und Diskussion

Auf der rein phänomenologischen Seite konnten die Verläufe der $K^{\pm}$-Anregungsfunktionen durch die erhobenen Daten ergänzt werden. Dies zeigt die Relevanz der Messungen durch HADES, wie in den Abbildungen 1.14 und 1.15 deutlich wird. Bisher existierten hauptsächlich Messungen jenseits der Produktionsschwelle in freien NN-Kollisionen von geladenen Kaonen und ϕ-Mesonen. Auch zeigen die Daten eine Bestätigung der linearen Skalierung des K^-/K^+-Verhältnisses, wie Abbildung 6.1 verdeutlicht. Einen der spannendsten Befunde stellt die Messung des ϕ/Ξ^--Verhältnisses dar, da neuerliche STAR-Daten [3] bei der Schwerpunktsenergie $\sqrt{s_{\mathrm{NN}}} = 3$ GeV einen Anstieg des Verhältnisses zu niedrigen Energien anzeigen. Dies ist nun durch die vorliegenden Daten (Ξ^- aus [125]) bestätigt worden, wie Abbildung 6.2 verdeutlicht. Weiterführend ermöglicht diese Messung einen elaborierten Vergleich der Ergebnisse des Fits eines statistischen Hadronisierungsmodells THERMUS [136] an die STAR [3] Daten unter der Verwendung verschiedener mikrokanonischer Seltsamkeits-Korrelationsradien. Innerhalb dieser Radien muss Seltsamkeit, als Randbedingung, exakt erhalten sein. Es stellt sich heraus, dass unter Verwendung der gleichen Seltsamkeitskorrelationsradien die gleichzeitige Beschreibung der Verhältnisse von ϕ/Ξ^- und ϕ/K^- nicht möglich ist. Siehe Abschnitt 6.4 für ausgiebigere Details.
Weiterhin wird aus den Daten ersichtlich, dass $\approx 15\%$ aller K^- aus dem Zerfall eines ϕ-Mesons stammen. In Anlehnung an Ergebnisse aus [119], wird in Abschnitt 6.4.1 der Effekt dieses hohen Anteils auf den T_{Eff}-Parameter des K^- untersucht, indem rein thermische Spektren von PLUTO generierten K^- und ϕ-Mesonen, welche in K^+K^--Paare zerfallen, simuliert und die kinematischen Verteilungen der dort vorliegenden K^- gemäß dem 15%-Verhältnis mischt. Die resultierenden transversalen Verteilungen und der daraus extrahierte T_{Eff}-Parameter stimmen nahezu mit den gemessenen Werten überein. Auch die Form der dN/dy-Verteilung lässt sich so nahezu exakt reproduzieren. Etwa 80% des beobachteten Unterschiedes zwischen K^- und K^+ sowie ϕ-Meson sind somit durch thermisch produzierte K^- und den Beitrag des ϕ-Meson Zerfalles erklärbar. Dies widerspricht der vorigen Annahme des Seltsamkeitsaustausches $\pi^-\Lambda \rightarrow K^-N$ als alleinig dominantem Prozess zur K^--Produktion.
Eine Betrachtung der Multiplizitäten aller bisher in Ag(1.58 A GeV)+Ag Kollisionen rekonstruierten seltsamen Hadronen als Funktion der mittleren Anzahl der an der Kollision teilnehmenden Nukleonen $\langle A_{\mathrm{part}} \rangle$, gezeigt in Abbildung 6.7, ergibt ein universales Skalierungsverhalten. Dies wurde zuvor bereits in Au+Au-Kollisionen bei 2.4 Gev und 3 GeV Schwerpunktsenergie beobachtet, welche alle eine ähnliche Steigung aufweisen. Durch die Tatsache, dass die K^--Produktion nicht ausschließlich an den K^+, K^0 und Λ Kanal gekoppelt scheint, und, dass das ϕ-Meson als seltsamkeits-neutrales Teilchen keinen kanonischen Beschränkungen unterliegt, unterstützt diese Beobachtung die Idee der Produktion von $s\bar{s}$-Paaren an der Stelle ganzer Hadronen. Diese perkolieren nach der Produktion durch die überlappenden Pion-Wolken der an der im Kollisionszentrum befindlichen Nukleonen, bis das System ausfriert und somit die Formierung neuer Hadronen stattfindet.

A. Appendix

A.1. Definition of Statistical Metrics

In the scope of this thesis several statistical measures are discussed and used. It is important to formally define them once for further reference. This list does not claim to be a complete coverage of every relevant statistical measure.

- The *Signal to Background Ratio* basically can be described by its name, providing a measure for how much signal (S) has been reconstructed in comparison to the overall background (B) under the extracted signal peak. In the case of the analysis presented in this work, signal and background are always separately integrated in a range of $\pm 2\sigma$ around the arithemtic mean of the signal-peak. Formally this means

$$\frac{\mathrm{S}}{\mathrm{B}} = \frac{\int_{\mu-2\sigma}^{\mu+2\sigma} f_{\mathrm{Signal}}(x)dx}{\int_{\mu-2\sigma}^{\mu+2\sigma} f_{\mathrm{Background}}(x)dx} \tag{A.1}$$

  It has to be kept in mind, that in the practical application the histograms are discrete, so that the integral turns into a sum.

- *Significance* is an extension of the Signal to Background Ratio, as it also takes into account the amount of statistics available in a data sample. This is done by dividing the signal by the statistical error approximation $\sqrt{N}$, which represents the standard deviation of a Poission-random-distribution

$$\alpha = \frac{\mathrm{S}}{\sqrt{\mathrm{S}+\mathrm{B}}} \tag{A.2}$$

- Furthermore, when applying models on the data, the χ^2-value is used to quantify the accordance of the model with the given datapoints. Here y_i represents the i-th y-value of the discrete data distribution, $f(x_i)$ the functional value at the same point (with binned histograms it is always the centre of the bin) and σ_i the corresponding gaussian error of the measurement (for binned histograms the statistical error $\sqrt{N}$ of the bin) [37]

$$\chi^2 = \sum_{i+1}^{n} \left(\frac{y_i - f(x_i)}{\sigma_i} \right)^2 \tag{A.3}$$

A.2. The Cubic Spline Interpolation

Cubic spline interpolation plays a crucial role for the HADES tracking and was, in the context of this thesis, also introduced as a tool for the background estimation for single particles. In practical terms the method can be called from the *ROOT::Math::Interpolator* class, which is an implementation from the GNU Scientific Library. The documentation can be found in [59] and correspondingly in the ROOT documentation. This appendix focuses on a more broad understanding of the method, using [69] as a general source.

The basic problem for a cubic spline interpolation is the search for a function, which smoothly connects several points. As in the case of the background estimation under a peak, as demonstrated in section 4.1.1, one subdivides the interval $[a, b]$ into a set of subintervals $\Delta = \{x_i | i = 0, 1, ..., n\}$. Further we define $a = x_0 < x_1 < ... < x_n$, which basically says, that each subsequent point must have a higher value in x. This is also important for the implementation in ROOT. Furthermore we define $Y = \{y_i | i = 0, 1, ..., n\}$ as a set of $n + 1$ real numbers.
The stepsize between two knots x_j and x_{j+1} is then defined via

$$h_{j+1} = x_{j+1} - x_j$$

with $j = 0, 1, ..., n - 1$. Defining the spline-function as $S_\Delta(Y; x)$, we can define its moments

$$M_j = S''_\Delta(Y; x_j) \tag{A.4}$$

with $j = 0, 1, ..., n$, as the second derivative of the spline-function. So the basic idea of this method is to determine the various moments M_j as solutions of a linear system of equations. From these then the spline-function $S_\Delta(Y; x_j)$ can be derived. In case of the algorithm implemented in ROOT, this means, that for each given knot x_j the derivatives are taken into account for the final result. This has an advantage over classical plynomial fitting methods, as these often exclusively use derivatives of the first and the last point in the set.
As $S''_\Delta(Y; x)$ is linear in every interval $[x_j, x_{j+1}]$, it can be described in terms of M_j as

$$S''_\Delta(Y; x) = M_j \frac{x_{j+1} - x}{h_{j+1}} + M_{j+1} \frac{x - x_j}{h_{j+1}}$$

for $x \in [x_j, x_{j+1}]$. Via integration and parameterization one arrives at the expression

$$S_\Delta(Y; x) = \alpha_j + \beta_j(x - x_j) + \gamma_j(x - x_j)^2 + \delta_j(x - x_j)^3 \tag{A.5}$$

a third order polynomial, depending on the derivatives, moments and the stepsize between two neighbouring knots. The corresponding parameters are defined via

$$\alpha_j = y_j$$

$$\beta_j = S'_\Delta(Y; x_j) = \frac{y_{j+1} - y_j}{h_{j+1}} - \frac{2M_j + M_{j+1}}{6} h_{j+1}$$

$$\gamma_j = \frac{S''_\Delta(Y; x_j)}{2} = \frac{M_j}{2}$$

$$\delta_j = \frac{S'''_\Delta(Y; x_j^+)}{6} = \frac{M_{j+1} - M_j}{6h_{j+1}}$$

As now the polynomial is defined as a function of the moments, M_j have to be calculated. Using the continuity of $S_\Delta(Y;x)$ at the knots $x = x_j, j = 1, 2, ..., n-1$, $n-1$ equations are obtained. Further parameterization leads to a compact form of

$$\mu_j M_{j-1} + 2M_j + \lambda_j M_{j+1} = d_j$$

where $j = 1, 2, ..., n-1$ with the following parameters

$$\lambda_j = \frac{h_{j+1}}{h_j + h_{j+1}}$$

$$\mu_j = 1 - \lambda_j = \frac{h_j}{h_j + h_{j+1}}$$

$$d_j = \frac{6}{h_j + h_{j+1}} \left(\frac{y_{j+1} - y_j}{h_{j+1}} - \frac{y_j - y_{j-1}}{h_j} \right)$$

For different additional constraints, further simplifications can be performed. This equation can then be used to determine the moments of the spline-function and ultimately lead to the desired solution. As seen in this chapter, this method does only take absolute values into account. All real measurements contain errors, so the method has certain disadvantages for data with significant fluctuations between subsequent datapoints. In these cases the choice of knots is crucial to guarantee a stable interpolation.

A.3. K^+ Multidifferential Example Spectra

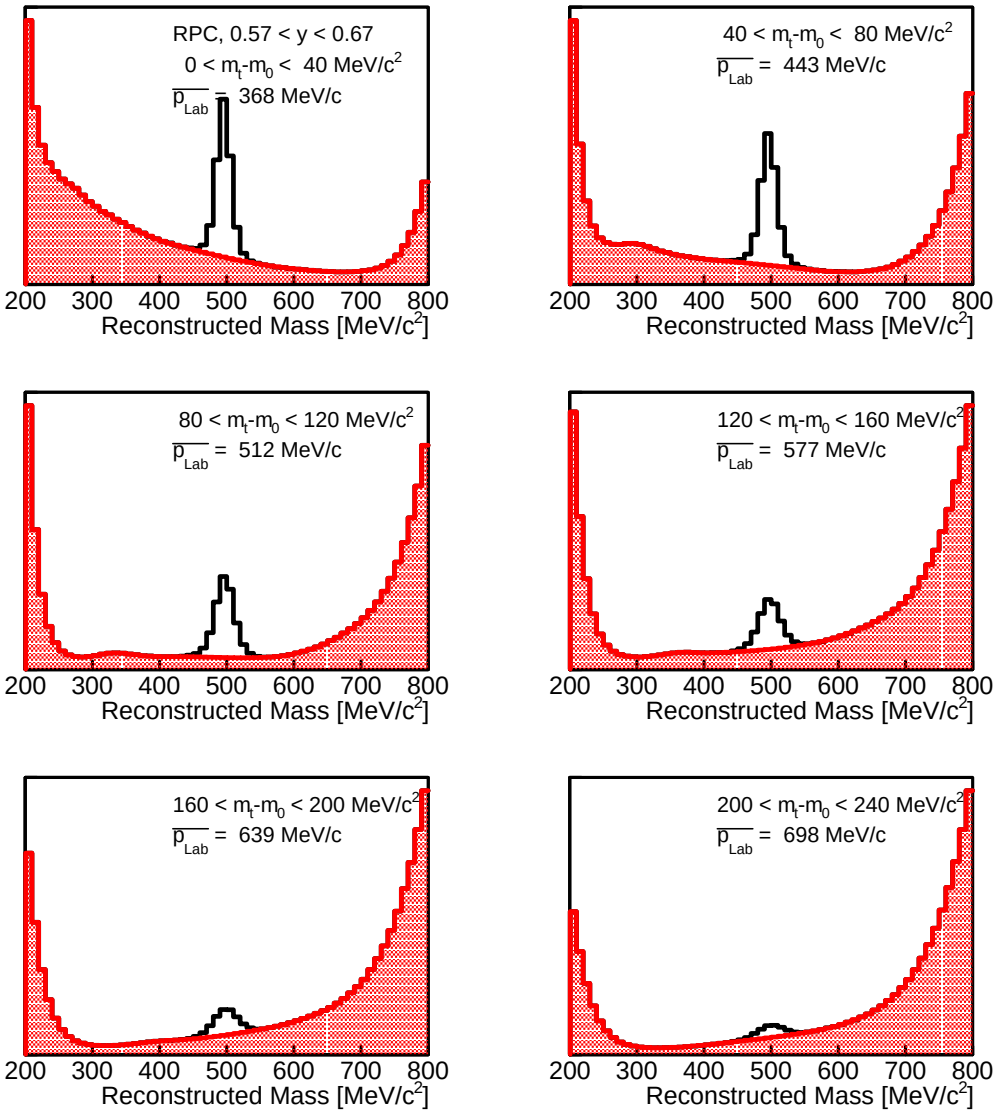

Figure A.1.: Exemplary RPC K^+ mass spectra in the rapidity range $0.57 < y < 0.67$ for the $0 - 30\%$ centrality range.

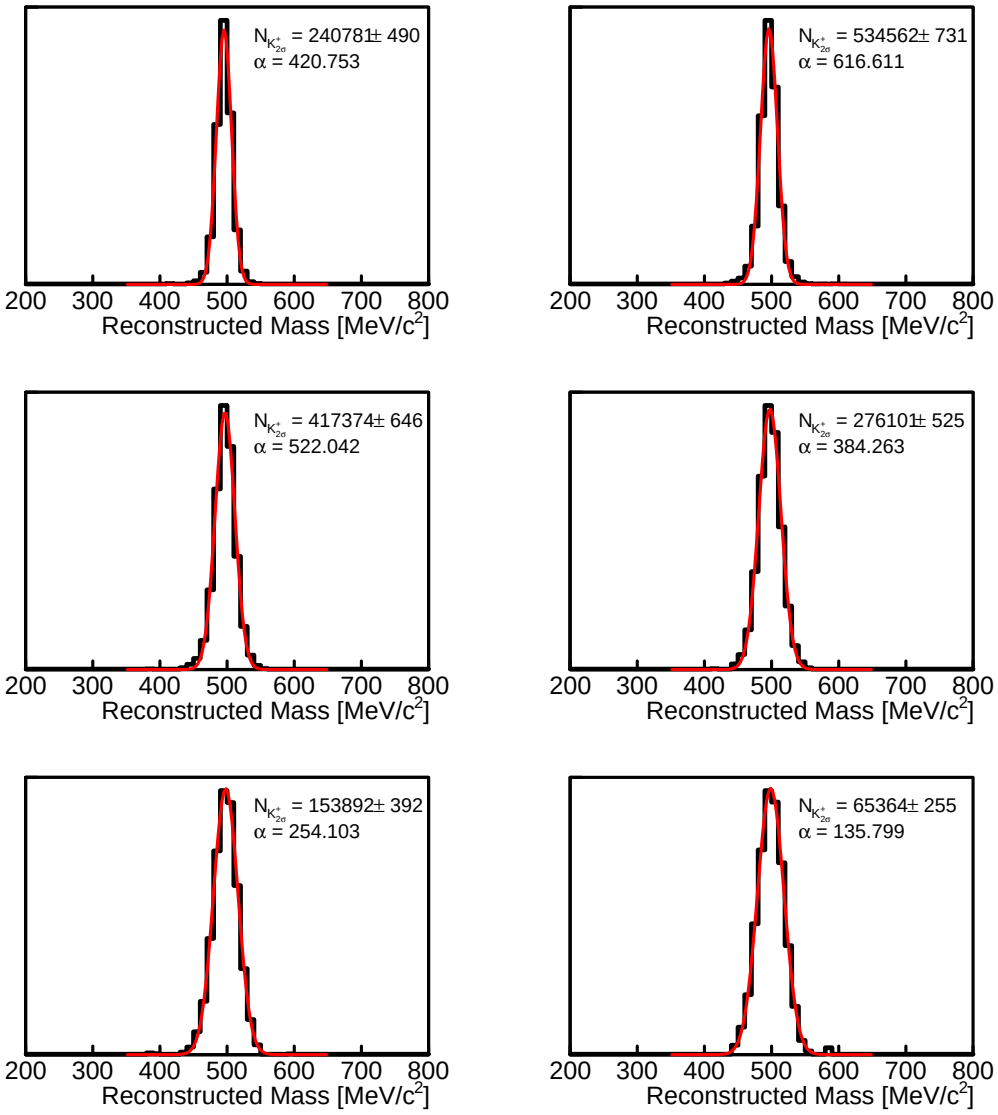

Figure A.2.: Subtracted exemplary RPC K^+ mass spectra in the rapidity range $0.57 < y < 0.67$ for the $0 - 30\%$ centrality range.

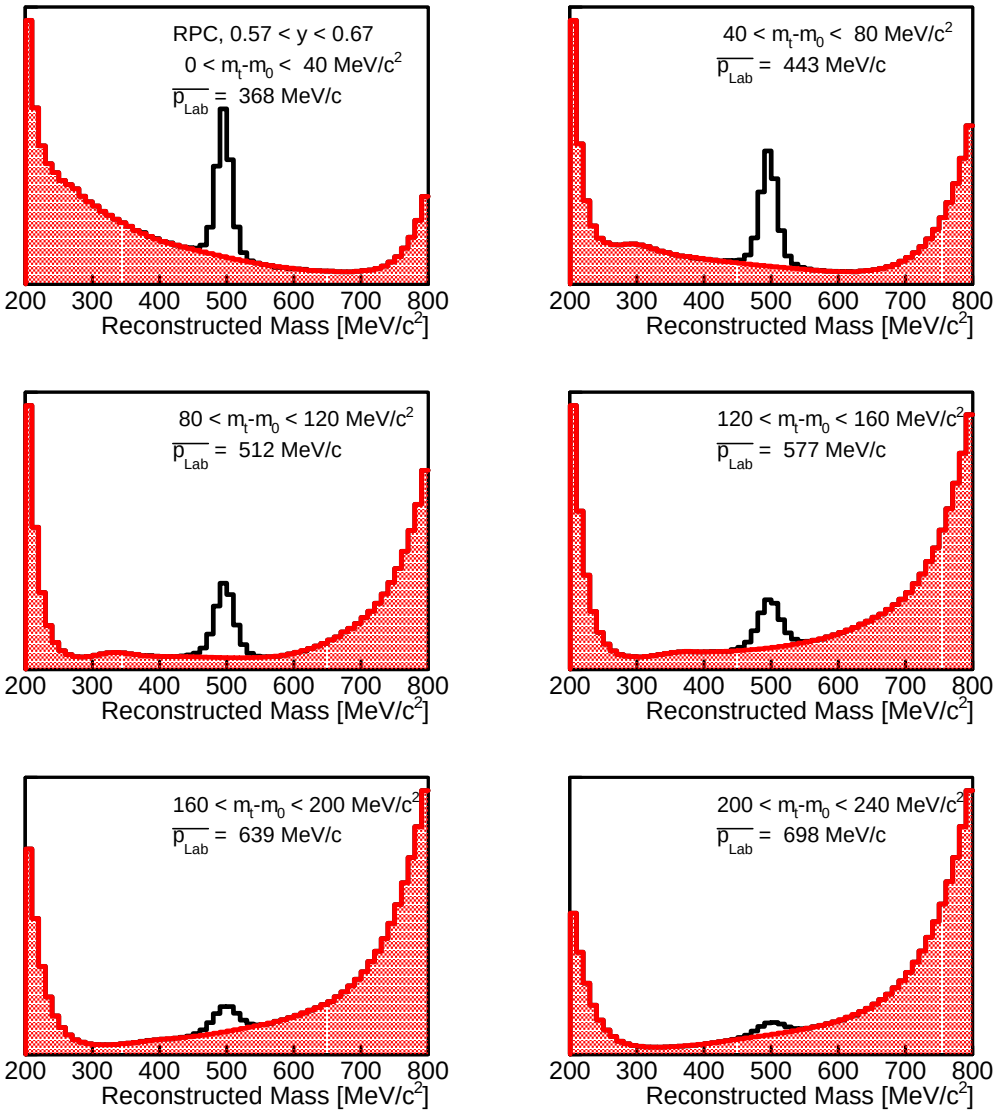

Figure A.3.: Exemplary RPC K^+ mass spectra in the rapidity range $0.57 < y < 0.67$ for the $0 - 10\%$ centrality range.

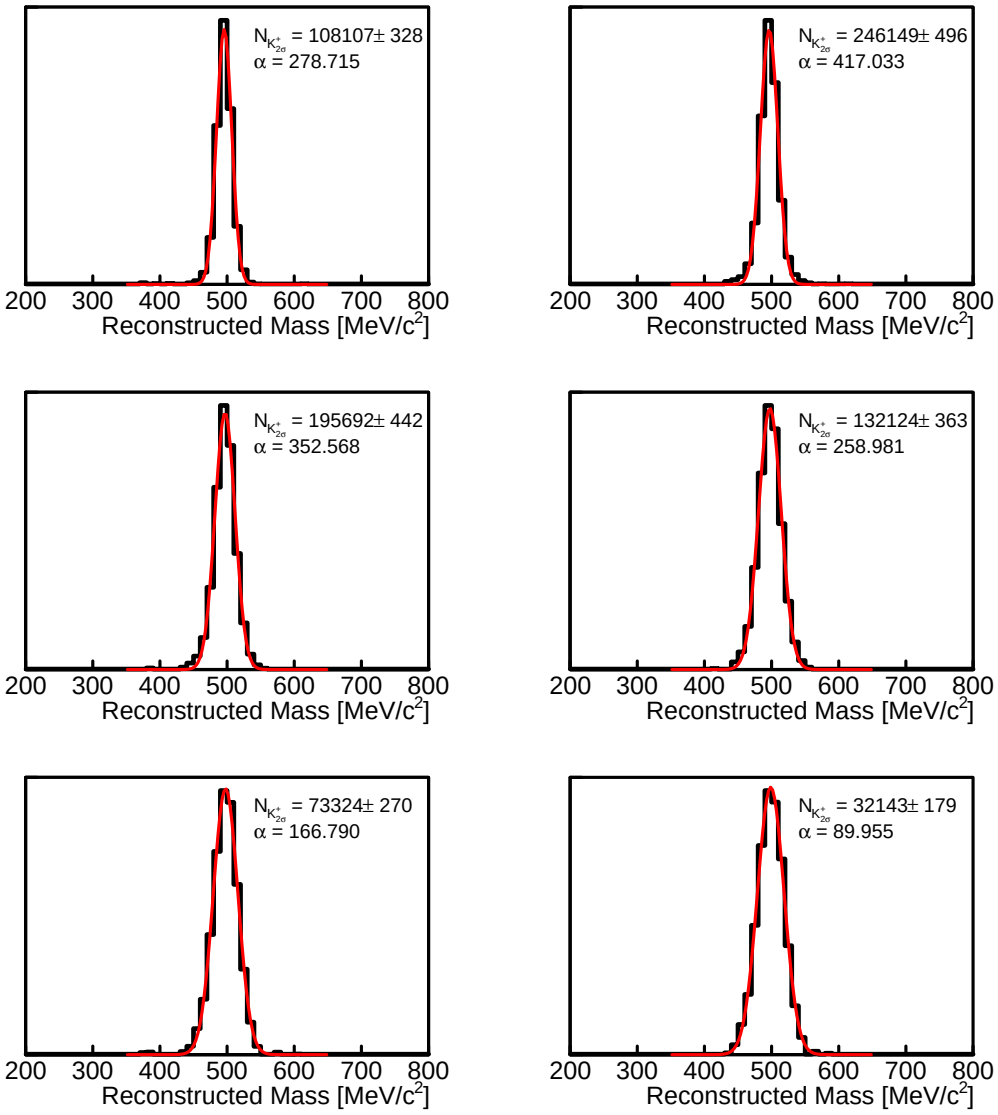

Figure A.4.: Subtracted exemplary RPC K^+ mass spectra in the rapidity range $0.57 < y < 0.67$ for the $0 - 10\%$ centrality range.

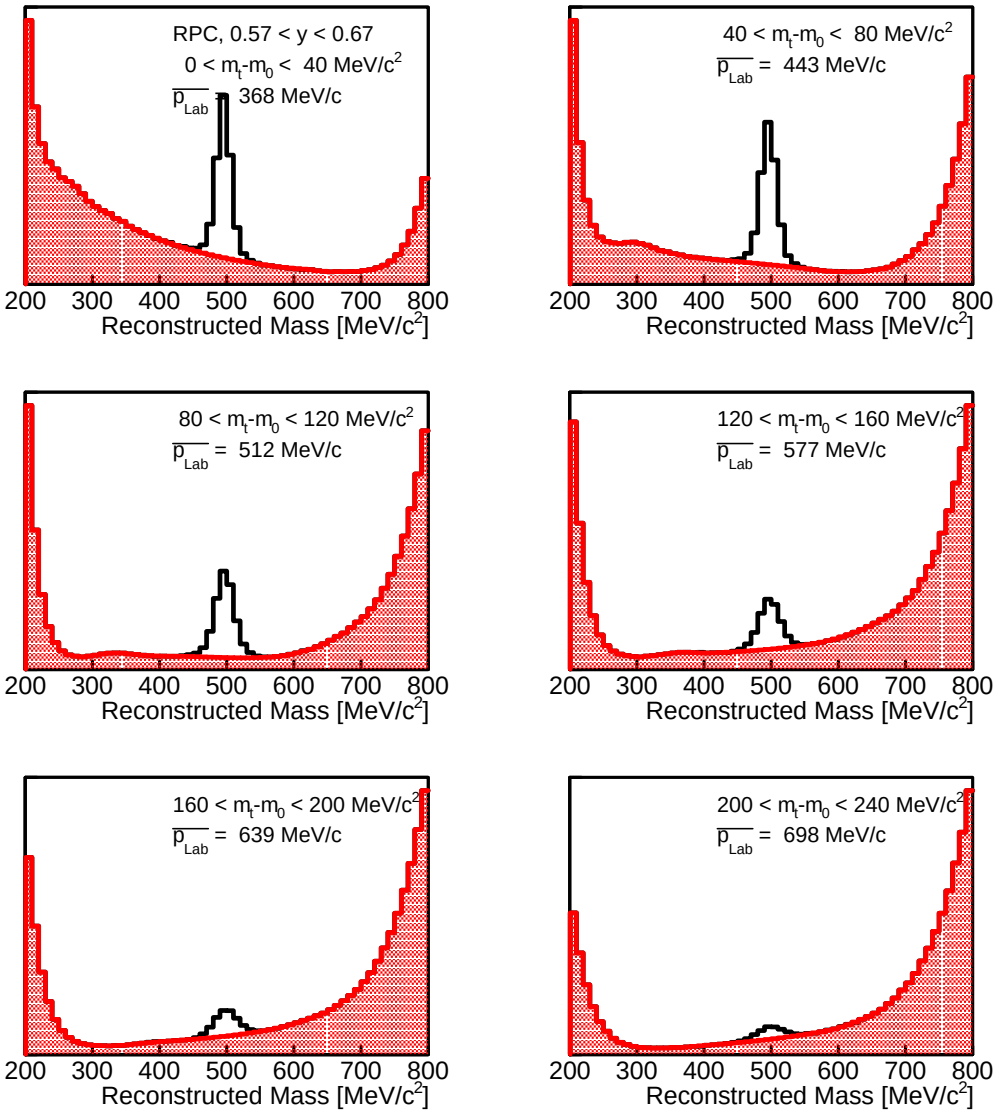

Figure A.5.: Exemplary RPC K^+ mass spectra in the rapidity range $0.57 < y < 0.67$ for the $10 - 20\%$ centrality range.

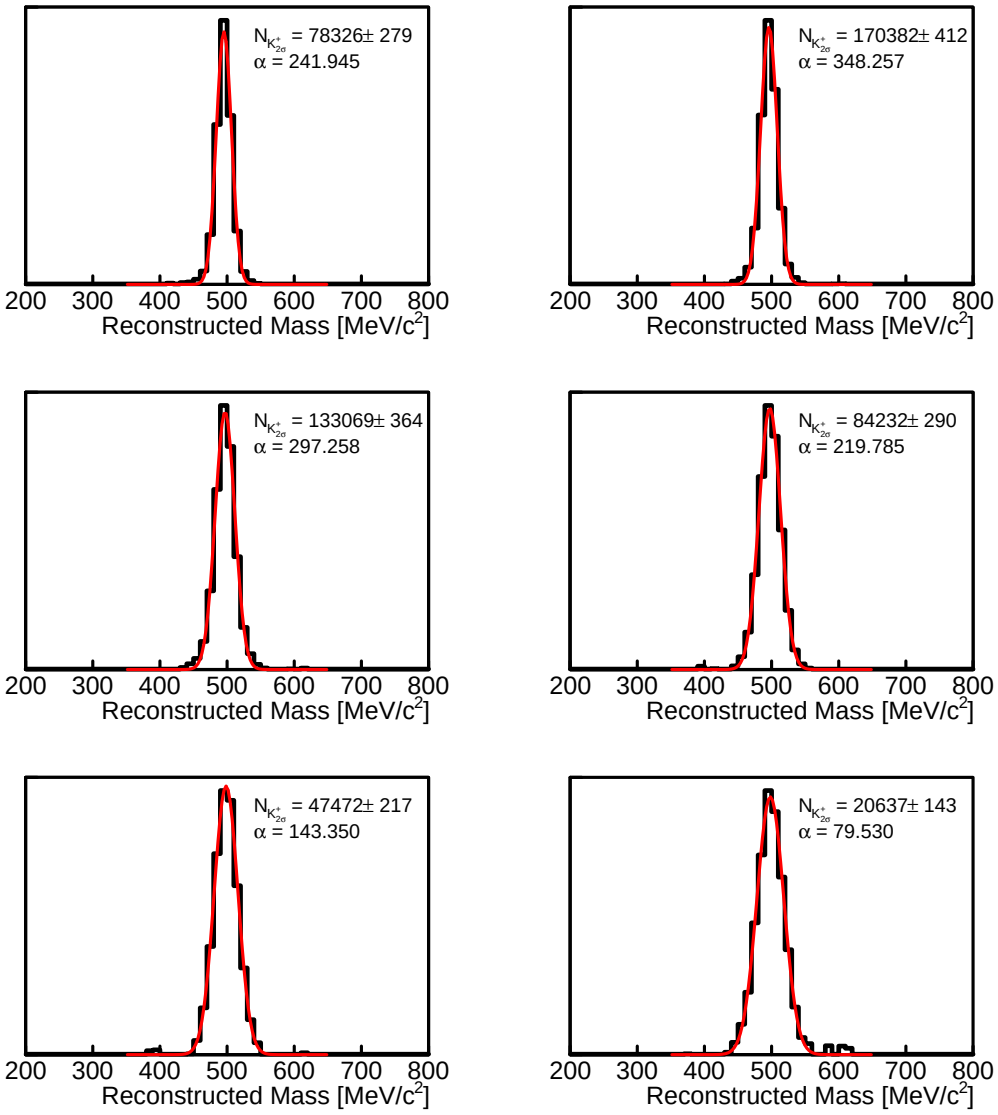

Figure A.6.: Subtracted exemplary RPC K^+ mass spectra in the rapidity range $0.57 < y < 0.67$ for the $10 - 20\%$ centrality range.

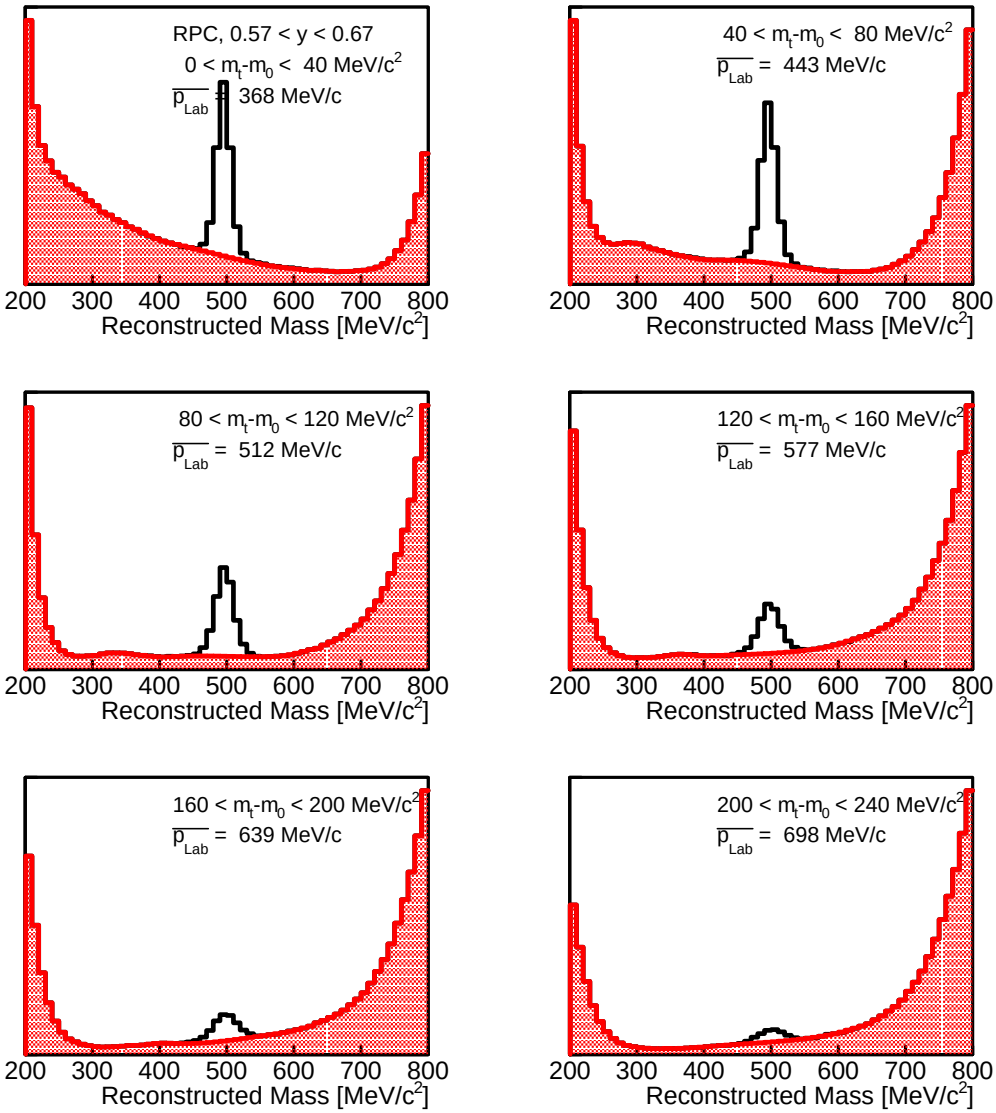

Figure A.7.: Exemplary RPC K^+ mass spectra in the rapidity range $0.57 < y < 0.67$ for the $20 - 30\%$ centrality range.

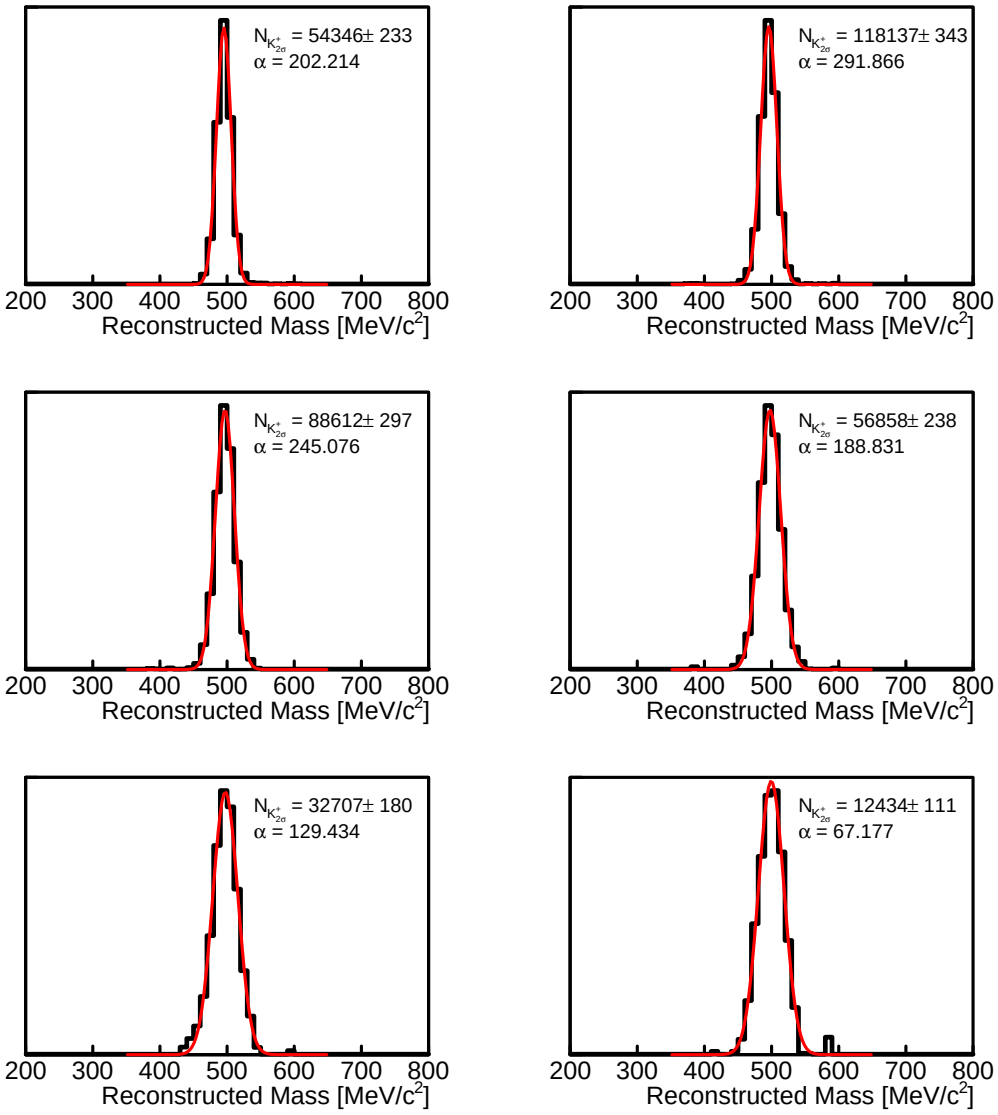

Figure A.8.: Subtracted exemplary RPC K^+ mass spectra in the rapidity range $0.57 < y < 0.67$ for the $20 - 30\%$ centrality range.

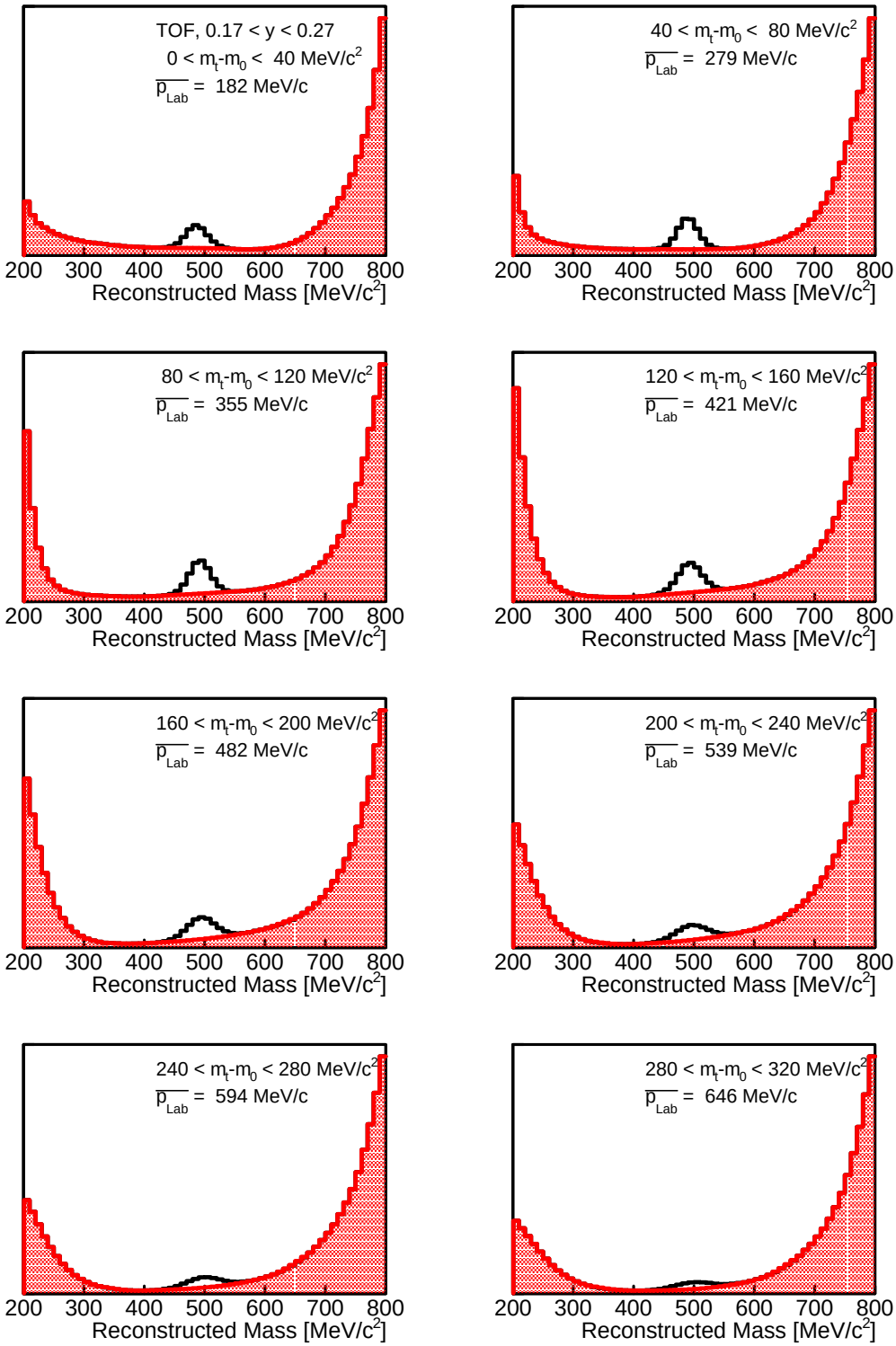

Figure A.9.: Exemplary TOF K^+ mass spectra in the rapidity range $0.17 < y < 0.27$ for the $0 - 30\%$ centrality range.

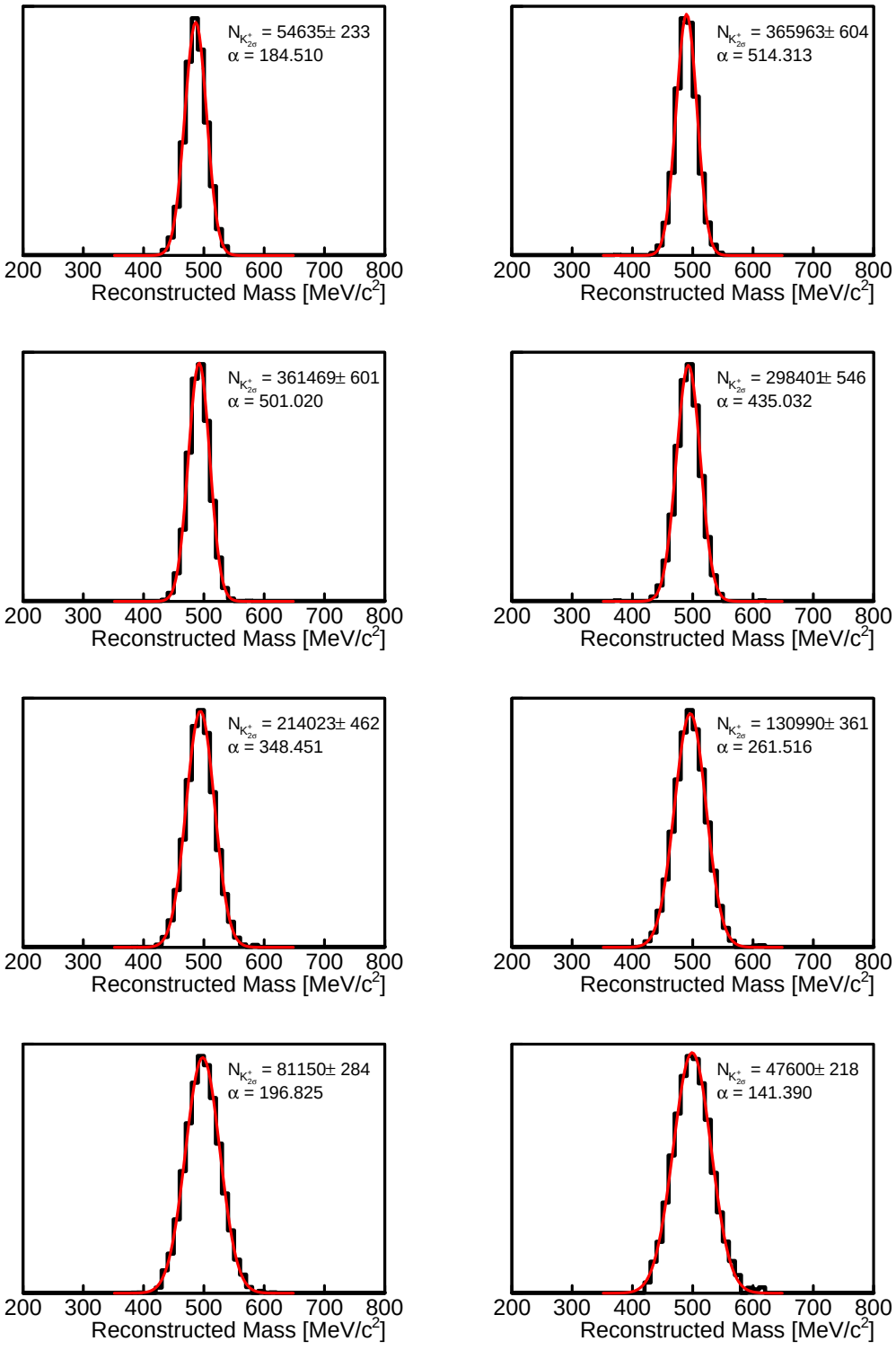

Figure A.10.: Subtracted exemplary TOF K^+ mass spectra in the rapidity range $0.17 < y < 0.27$ for the $0 - 30\%$ centrality range.

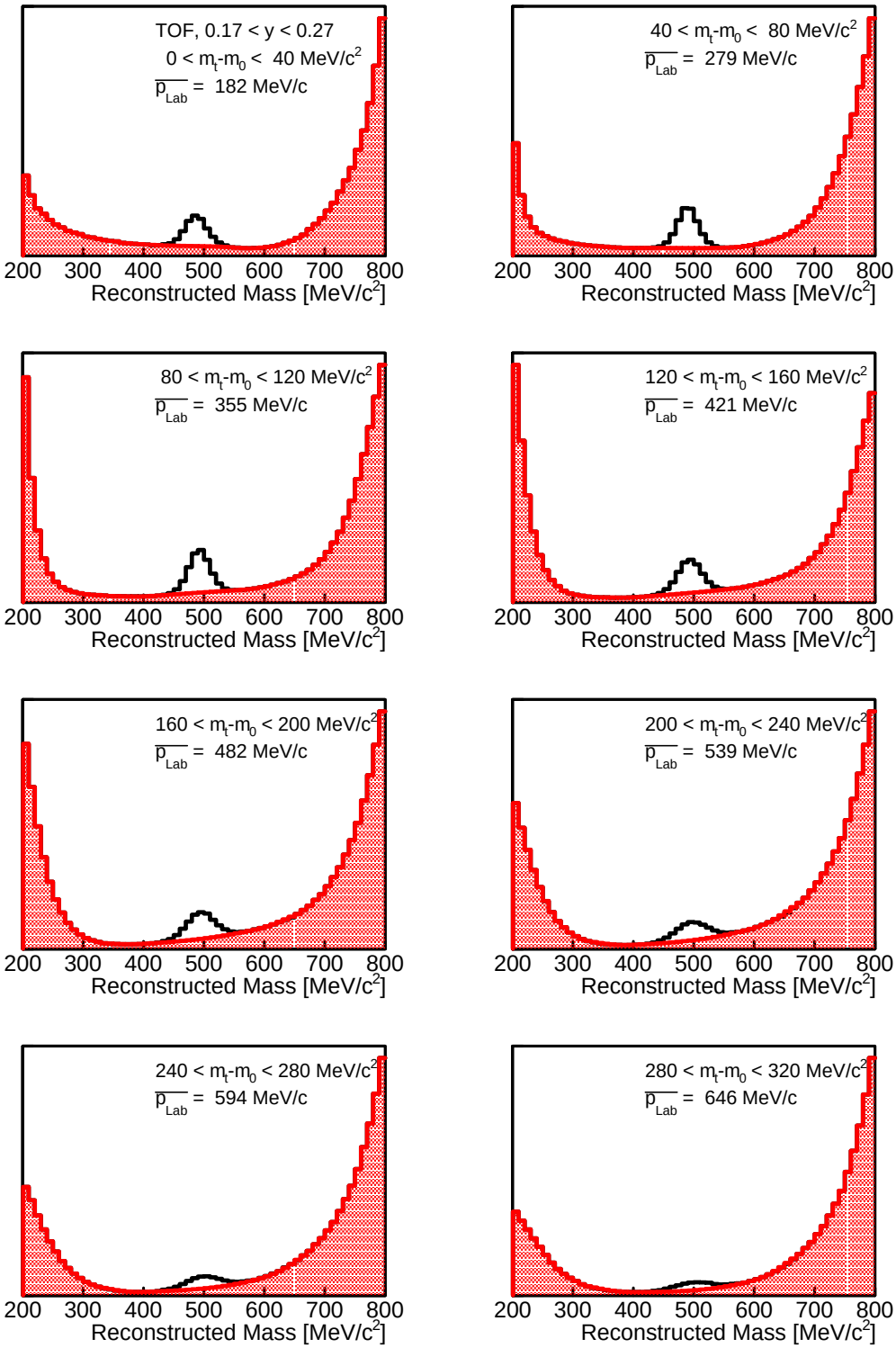

Figure A.11.: Exemplary TOF K^+ mass spectra in the rapidity range $0.17 < y < 0.27$ for the $0 - 10\%$ centrality range.

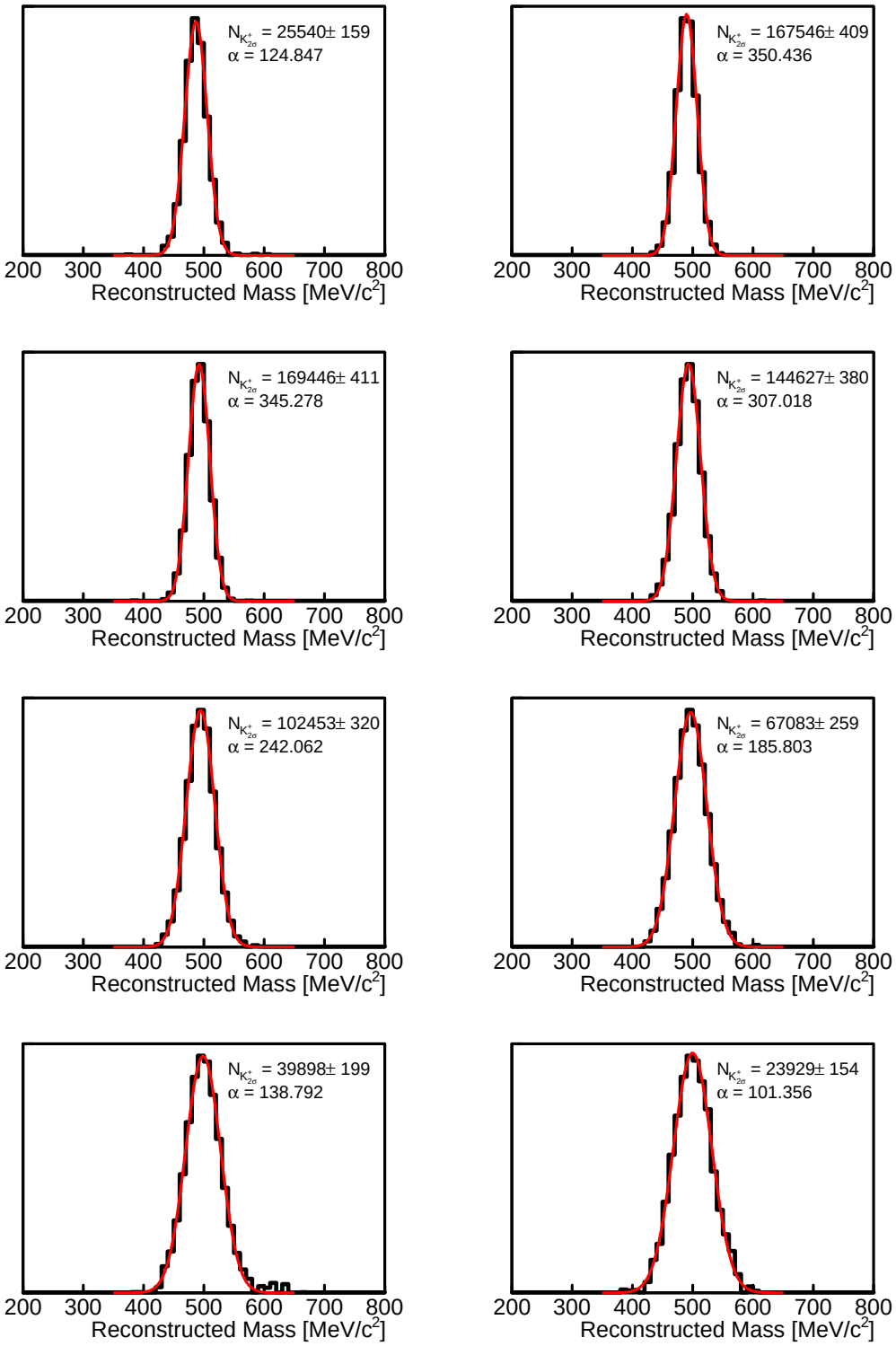

Figure A.12.: Subtracted exemplary TOF K^+ mass spectra in the rapidity range $0.17 < y < 0.27$ for the $0 - 10\%$ centrality range.

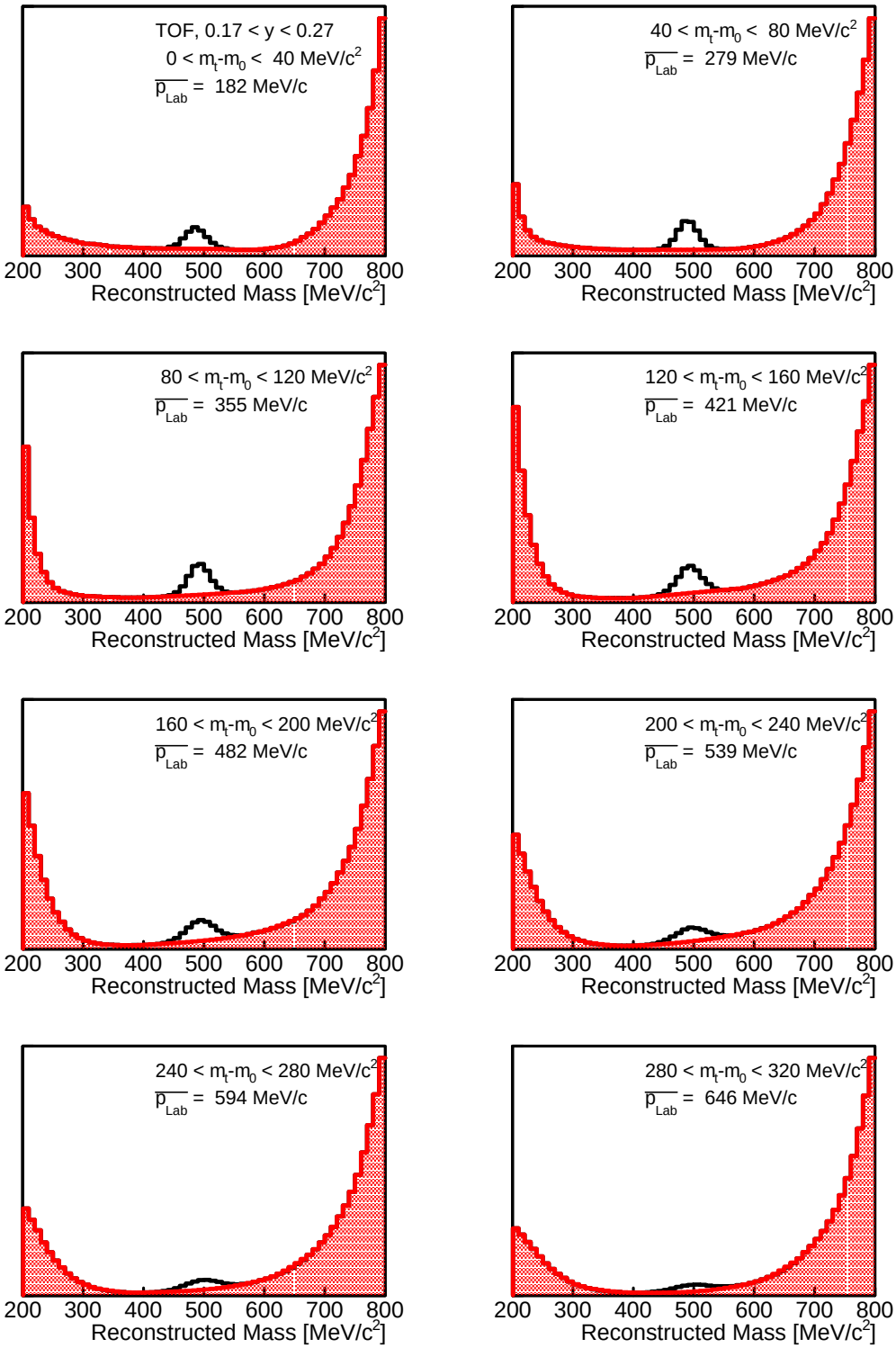

Figure A.13.: Exemplary TOF K^+ mass spectra in the rapidity range $0.17 < y < 0.27$ for the $10 - 20\%$ centrality range.

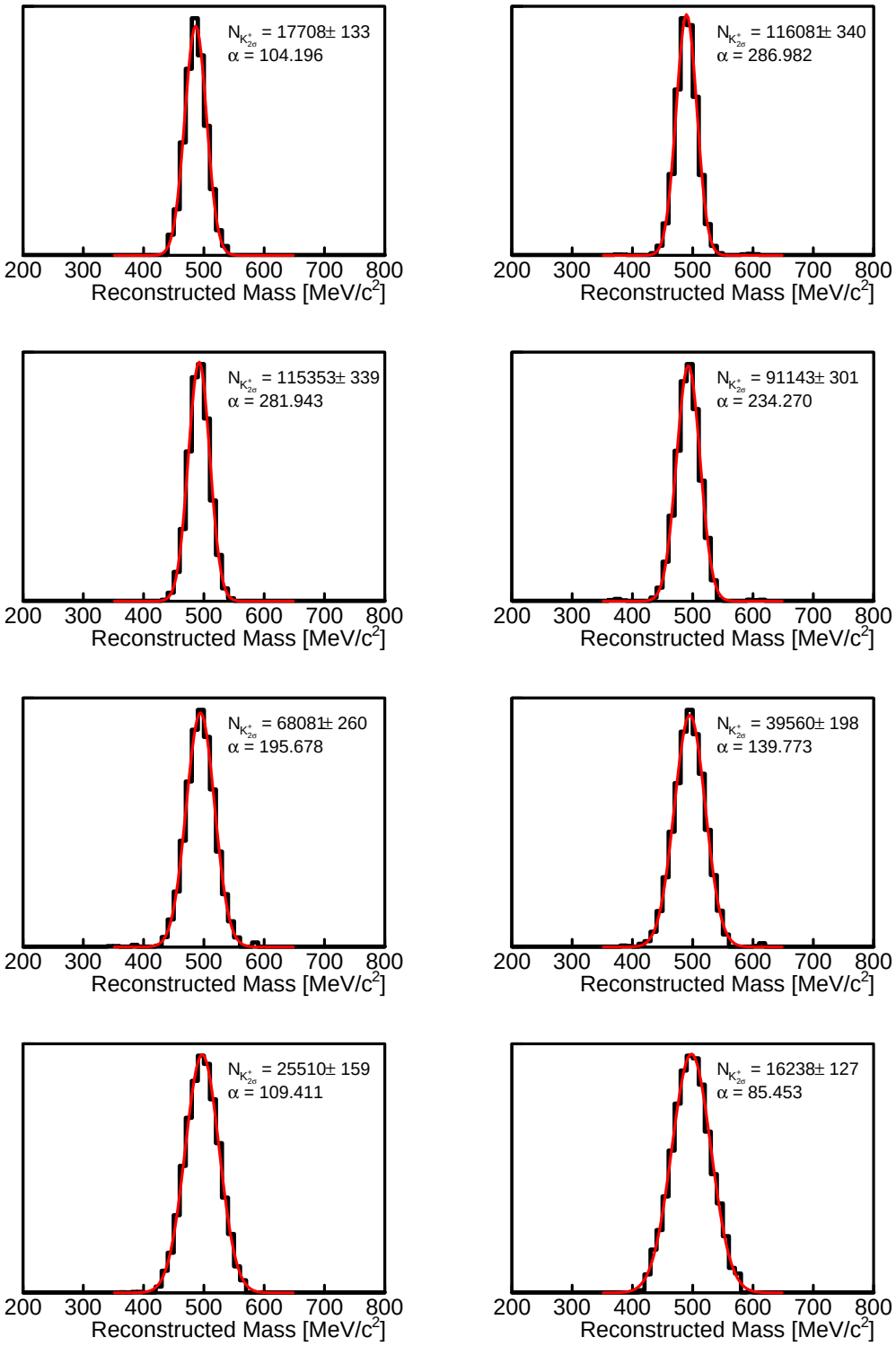

Figure A.14.: Subtracted exemplary TOF K^+ mass spectra in the rapidity range $0.17 < y < 0.27$ for the $10 - 20\%$ centrality range.

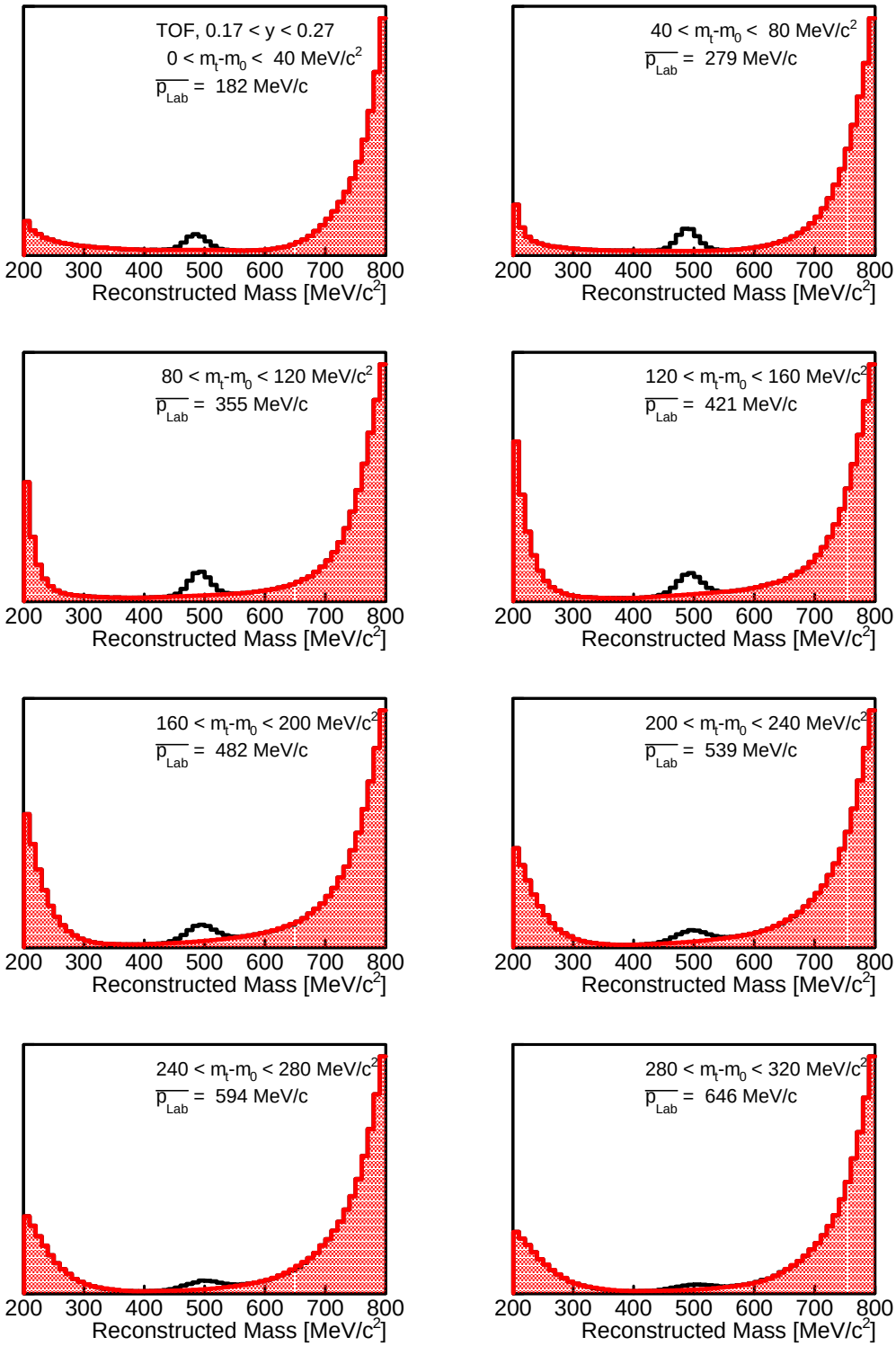

Figure A.15.: Exemplary TOF K^+ mass spectra in the rapidity range $0.17 < y < 0.27$ for the $20 - 30\%$ centrality range.

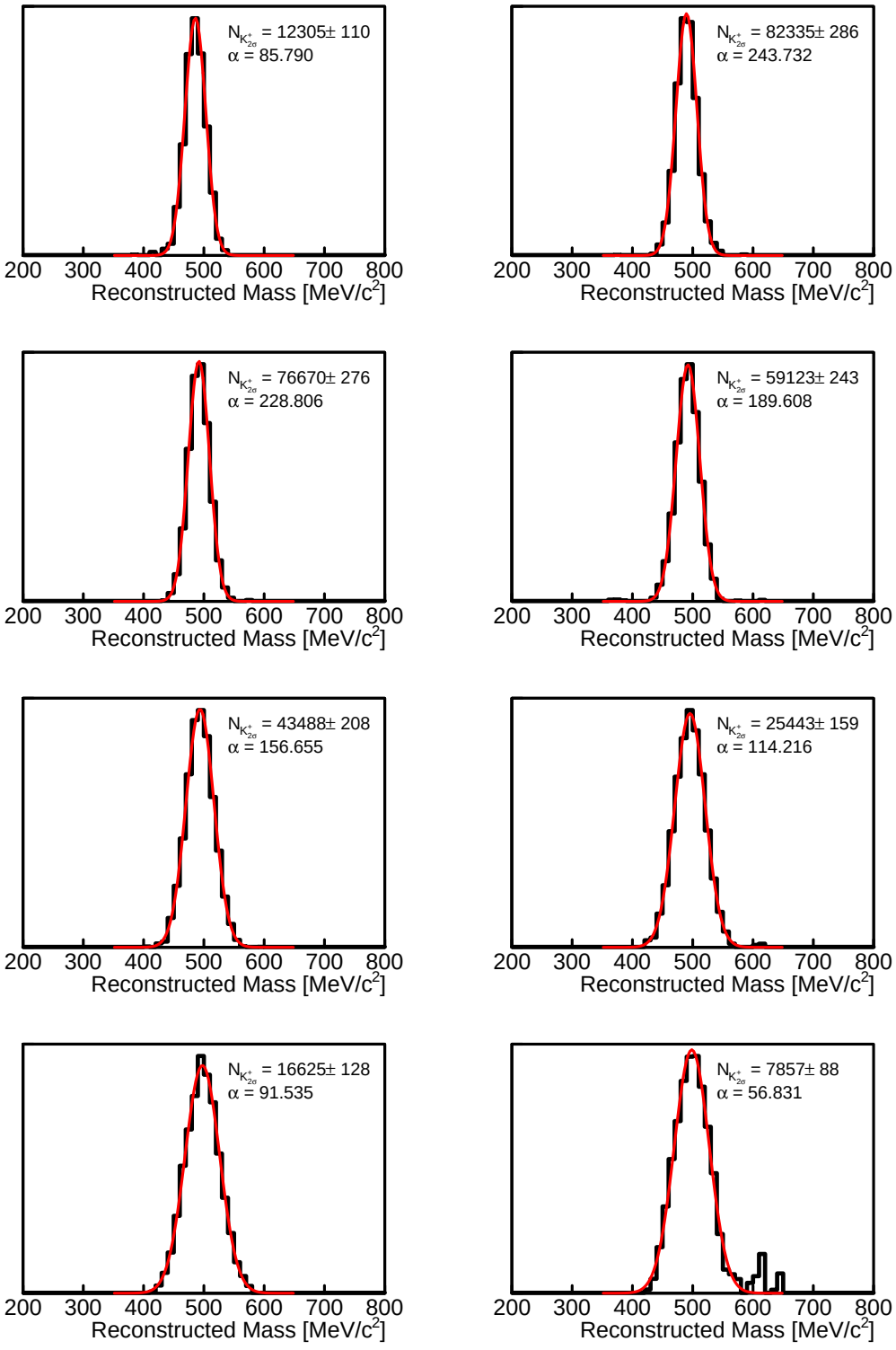

Figure A.16.: Subtracted exemplary TOF K^+ mass spectra in the rapidity range $0.17 < y < 0.27$ for the $20 - 30\%$ centrality range.

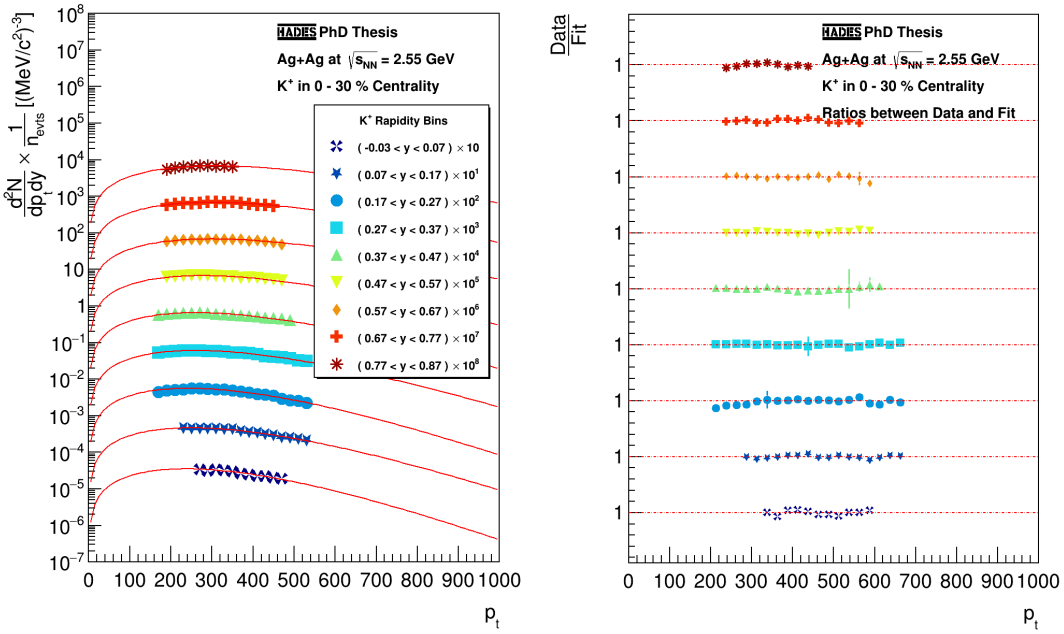

Figure A.17.: Fitted K^+ (p_t) spectra for the $0-30\%$ centrality range.

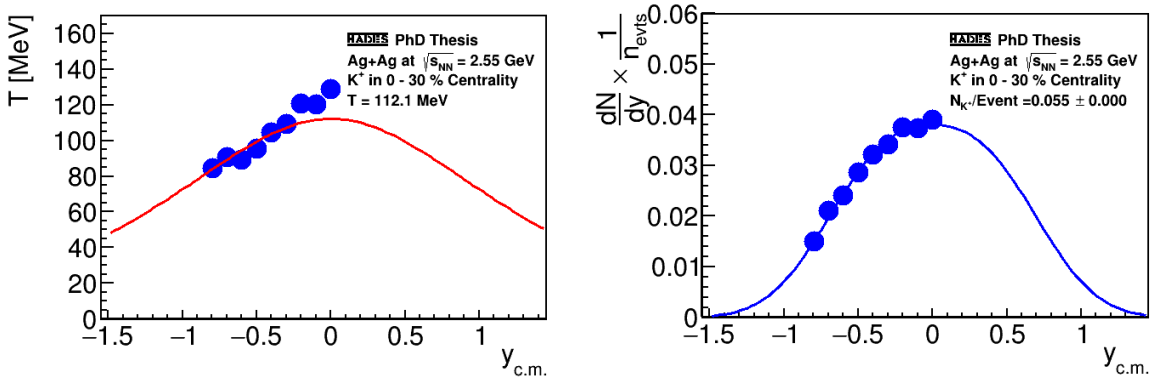

(a) T_{Eff} (b) dN/dy

Figure A.18.: Resulting and fitted K^+ T_{Eff} and dN/dy spectra resulting from the transverse momentum analysis for the $0-30\%$ centrality range.

A.4. K^- Multidifferential Example Spectra

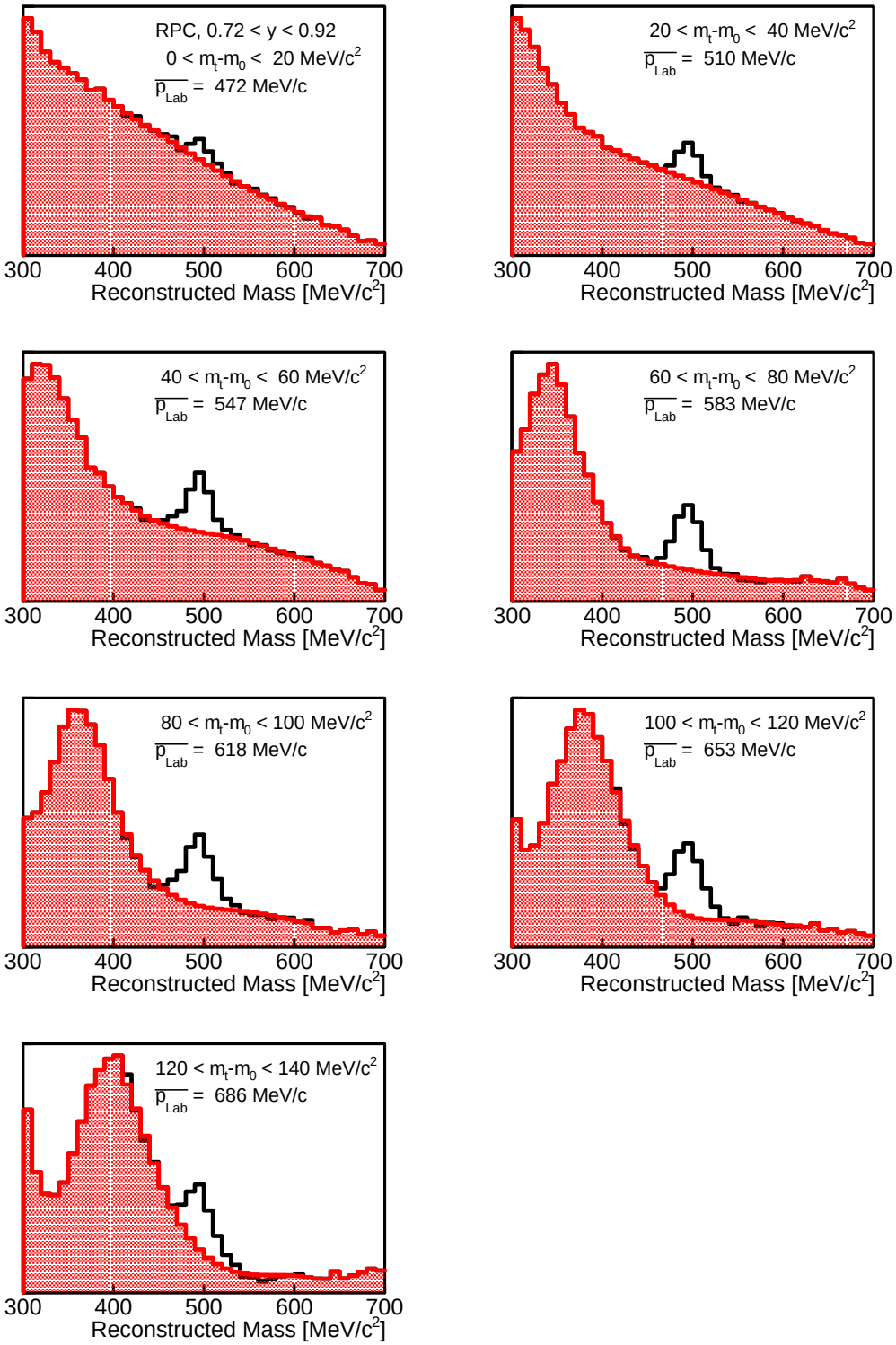

Figure A.19.: Exemplary RPC K^- mass spectra in the rapidity range $0.72 < y < 0.92$ for the $0 - 30\%$ centrality range.

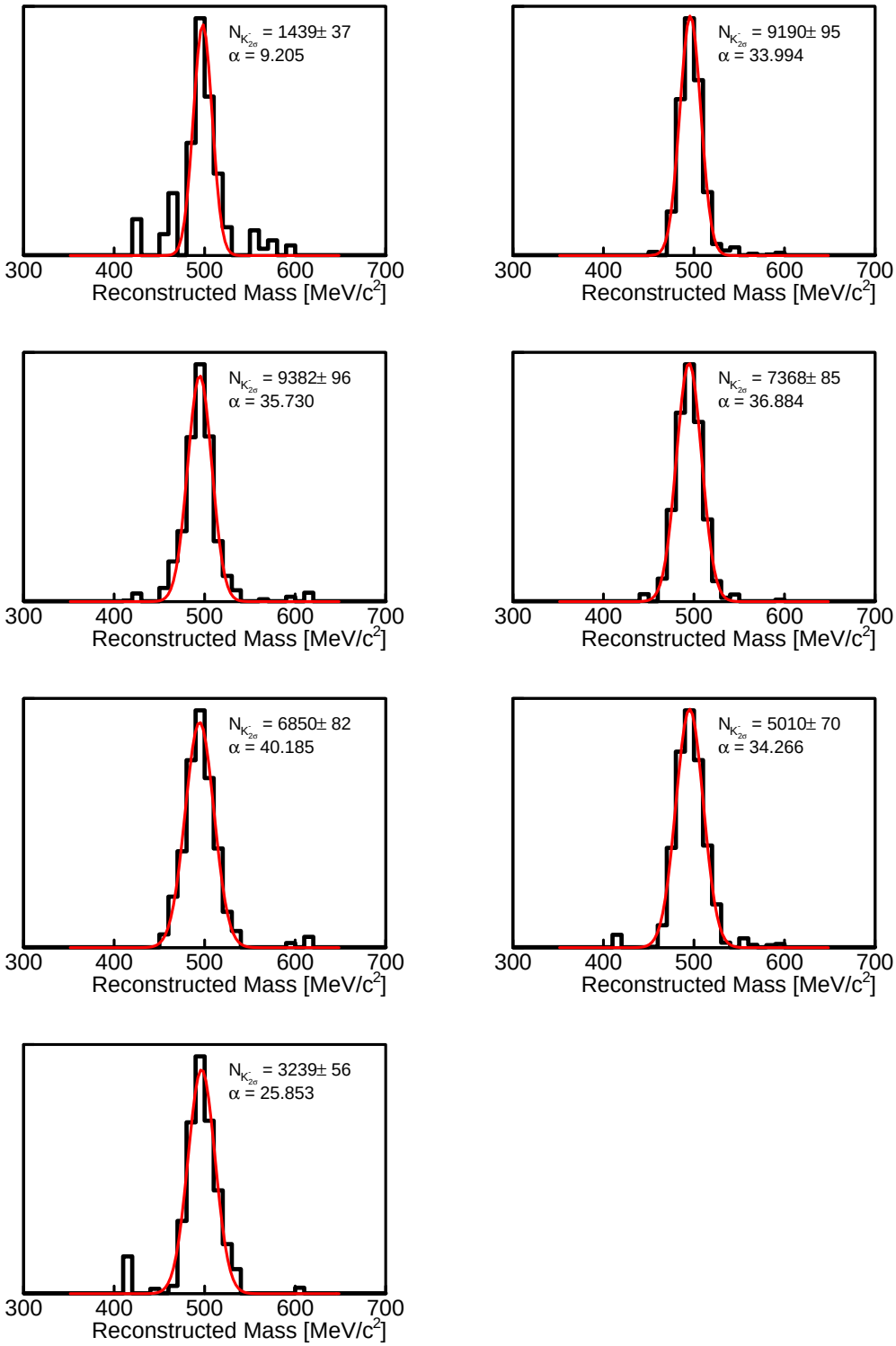

Figure A.20.: Subtracted exemplary RPC K^- mass spectra in the rapidity range $0.72 < y < 0.92$ for the $0 - 30\%$ centrality range.

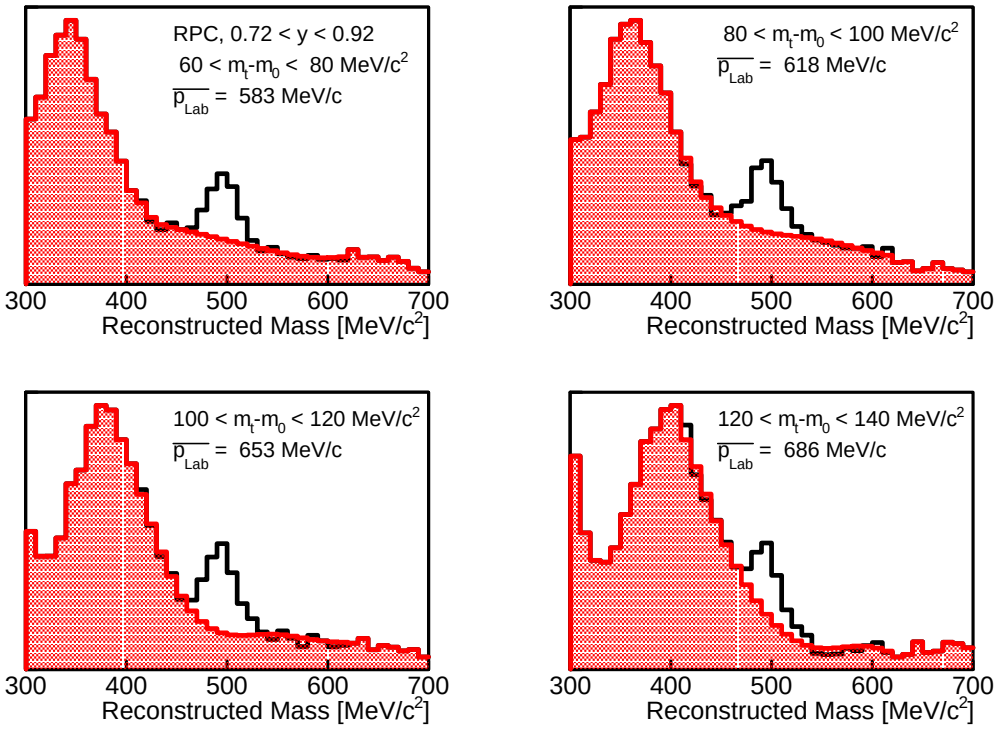

Figure A.21.: Exemplary RPC K^- mass spectra in the rapidity range $0.72 < y < 0.92$ for the $0 - 10\%$ centrality range.

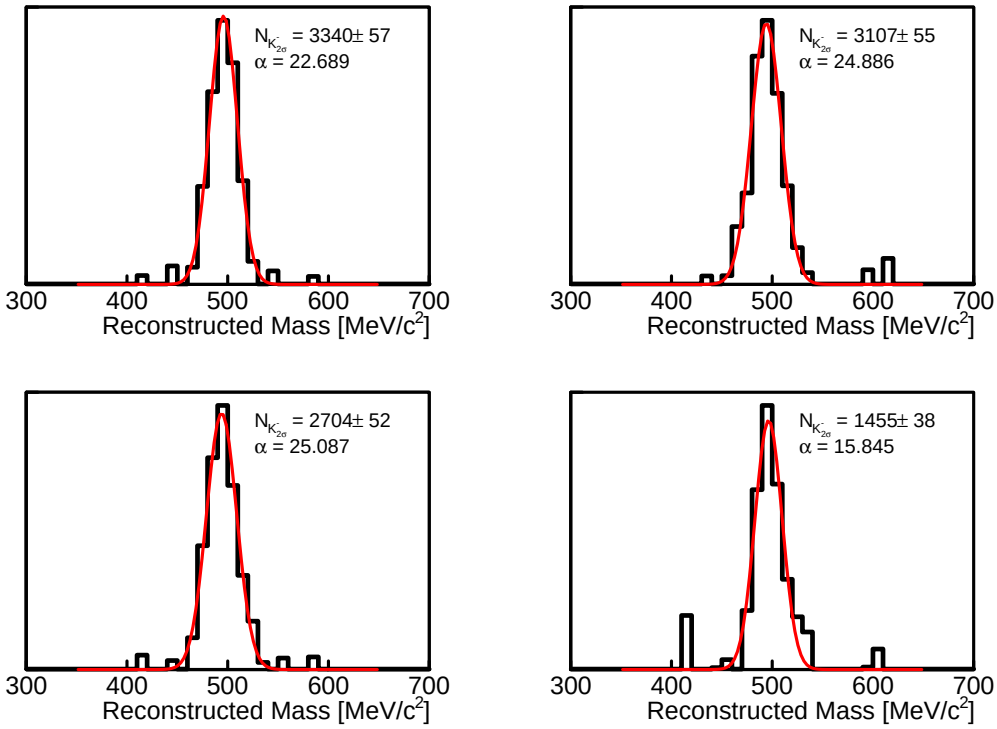

Figure A.22.: Subtracted exemplary RPC K^- mass spectra in the rapidity range $0.72 < y < 0.92$ for the $0 - 10\%$ centrality range.

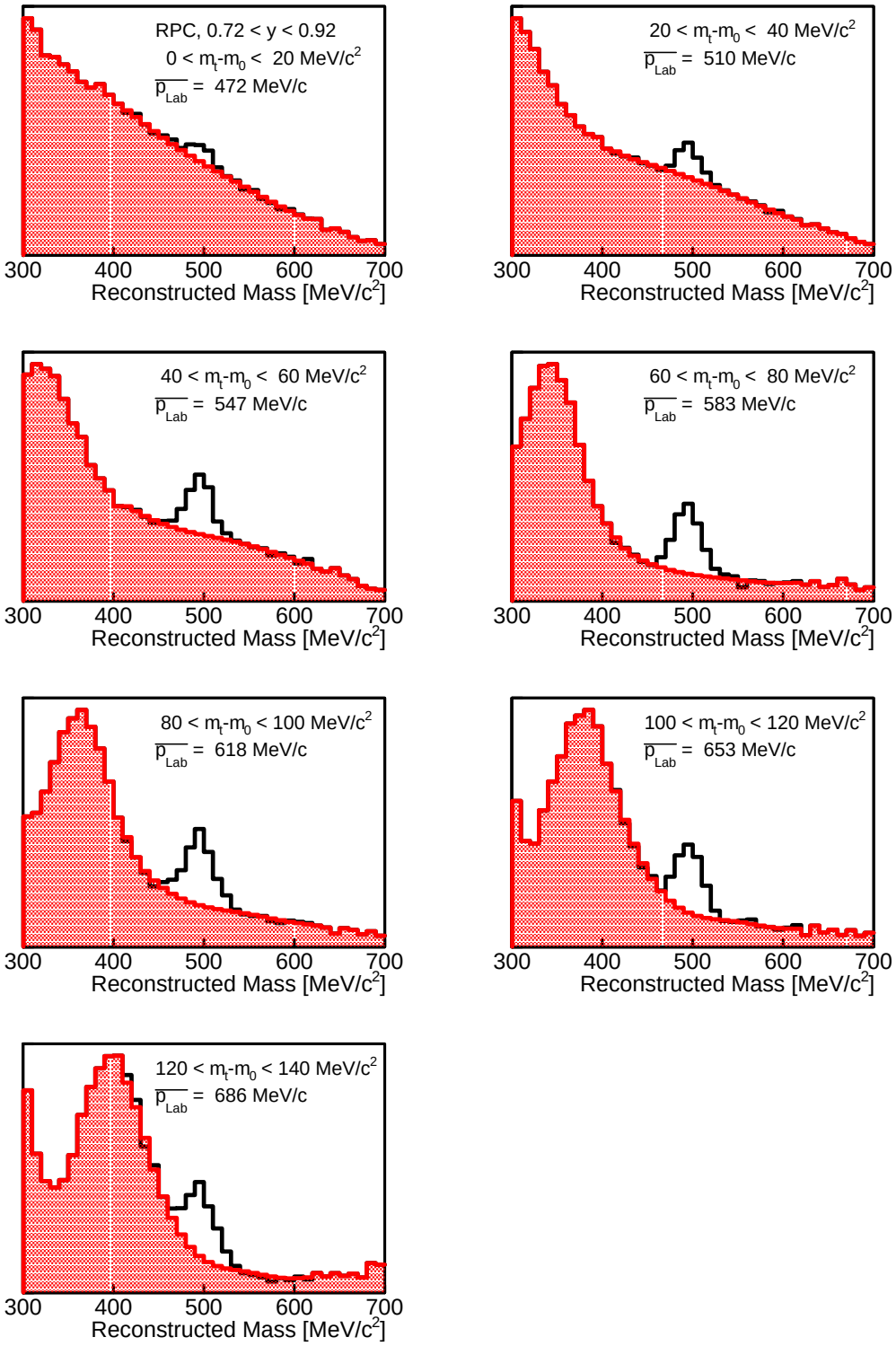

Figure A.23.: Exemplary RPC K^- mass spectra in the rapidity range $0.72 < y < 0.92$ for the $10 - 20\%$ centrality range.

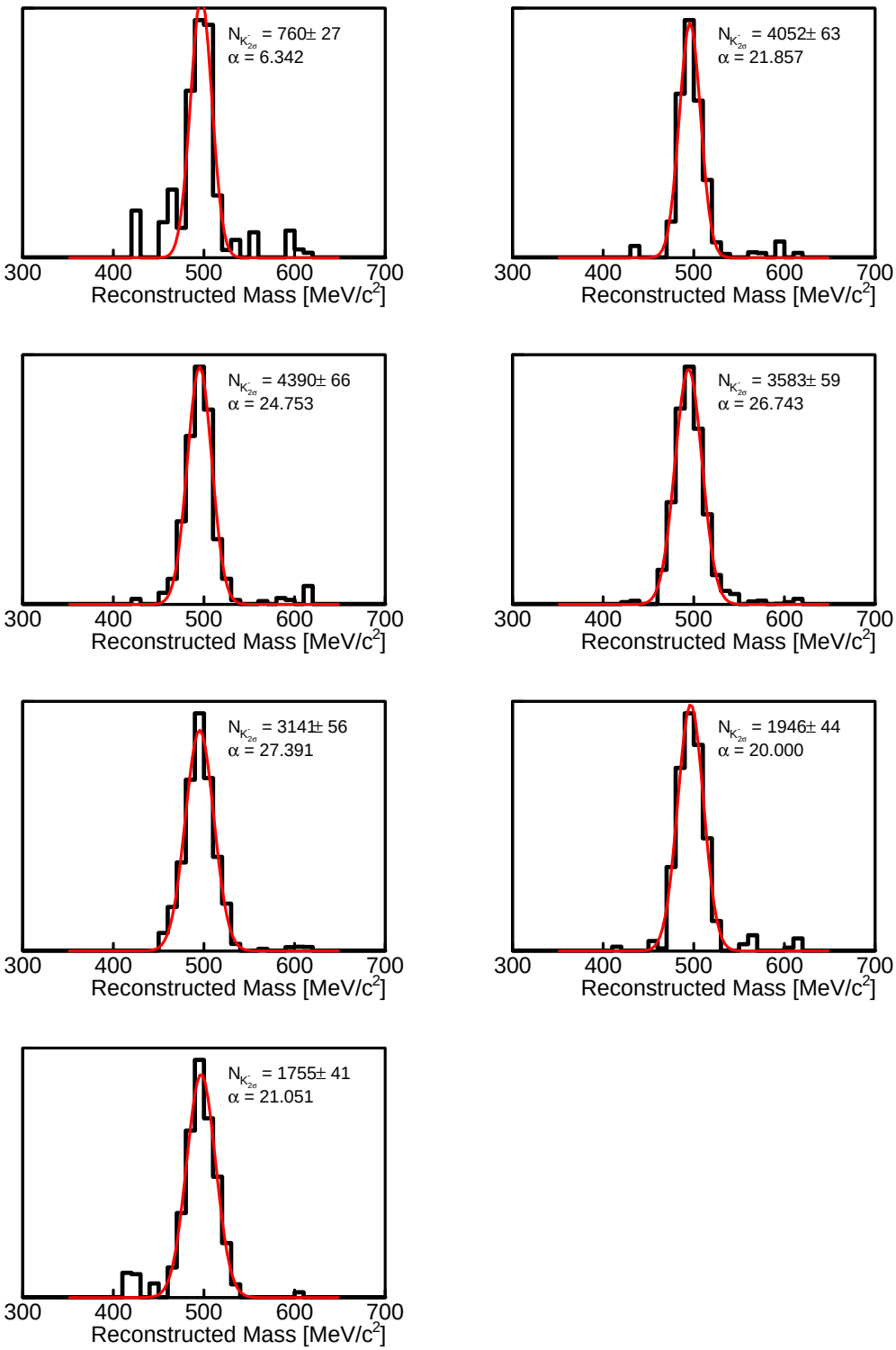

Figure A.24.: Subtracted exemplary RPC K^- mass spectra in the rapidity range $0.72 < y < 0.92$ for the $10 - 20\%$ centrality range.

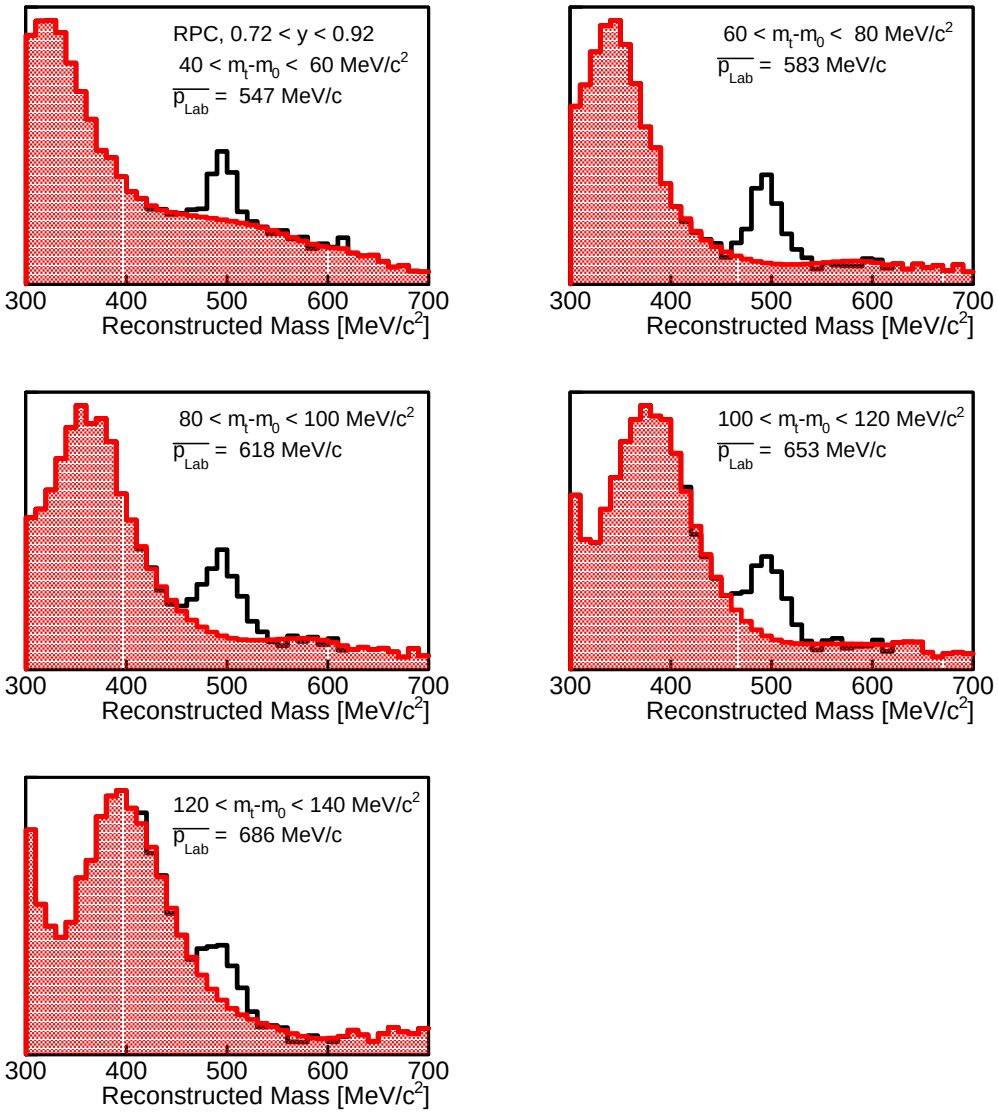

Figure A.25.: Exemplary RPC K^- mass spectra in the rapidity range $0.72 < y < 0.92$ for the $20 - 30\%$ centrality range.

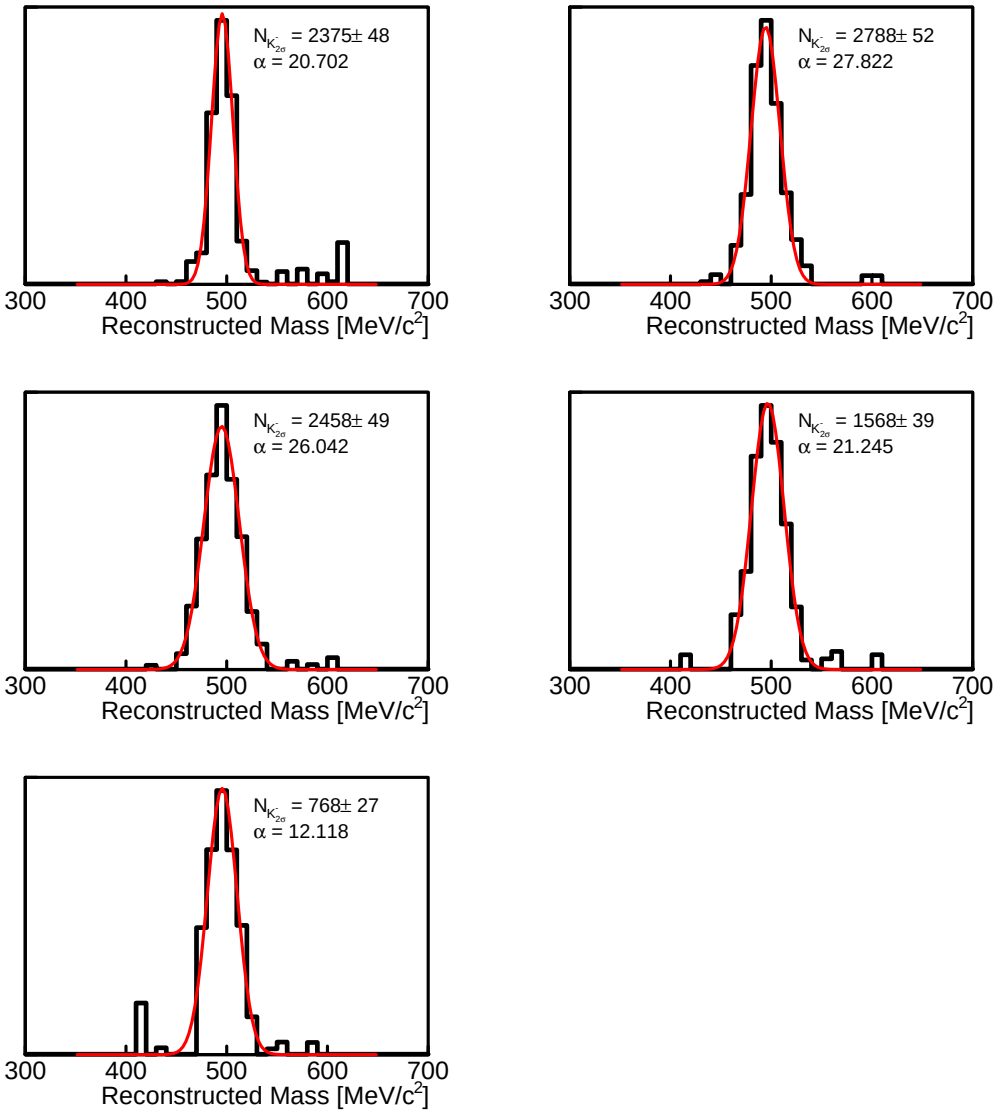

Figure A.26.: Subtracted exemplary RPC K^- mass spectra in the rapidity range $0.72 < y < 0.92$ for the $20 - 30\%$ centrality range.

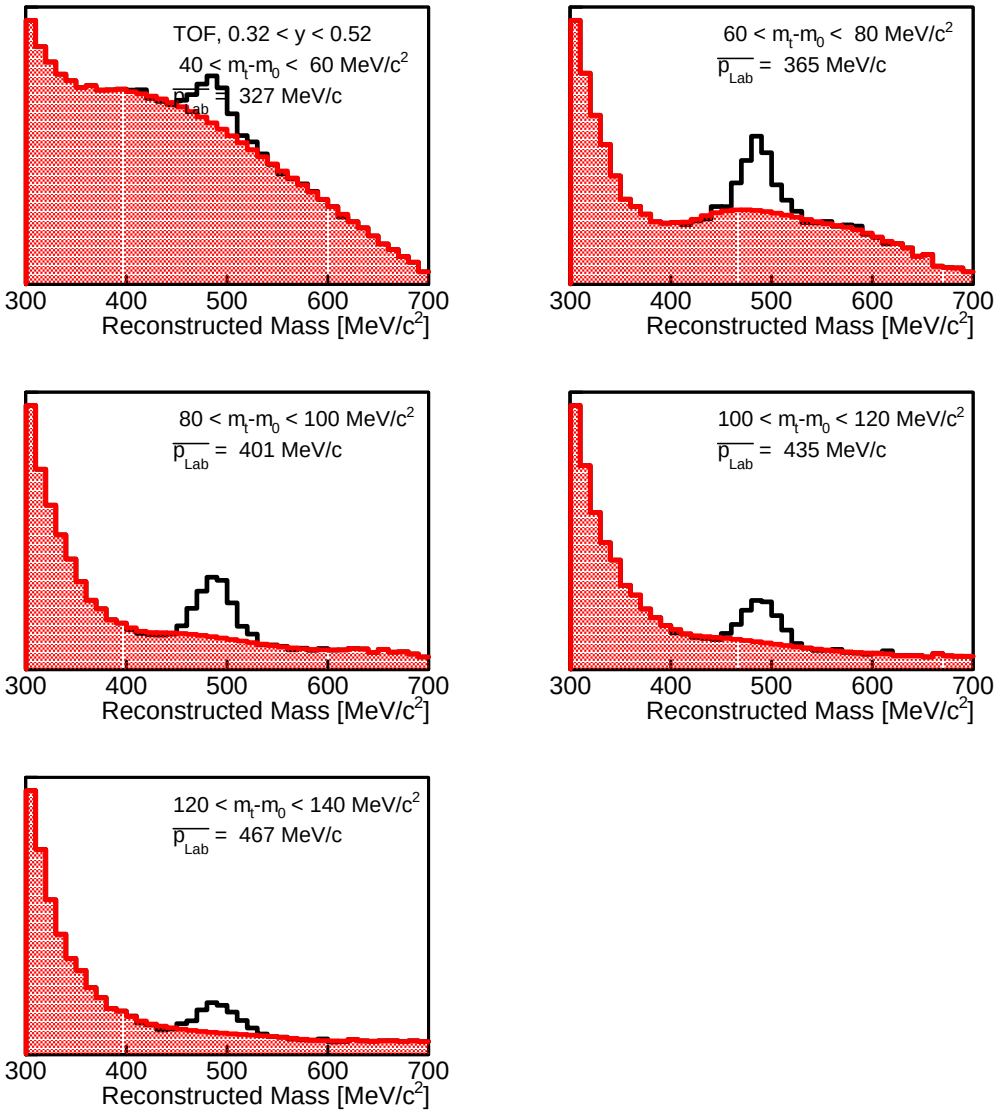

Figure A.27.: Exemplary TOF K^- mass spectra in the rapidity range $0.32 < y < 0.52$ for the $0 - 30\%$ centrality range.

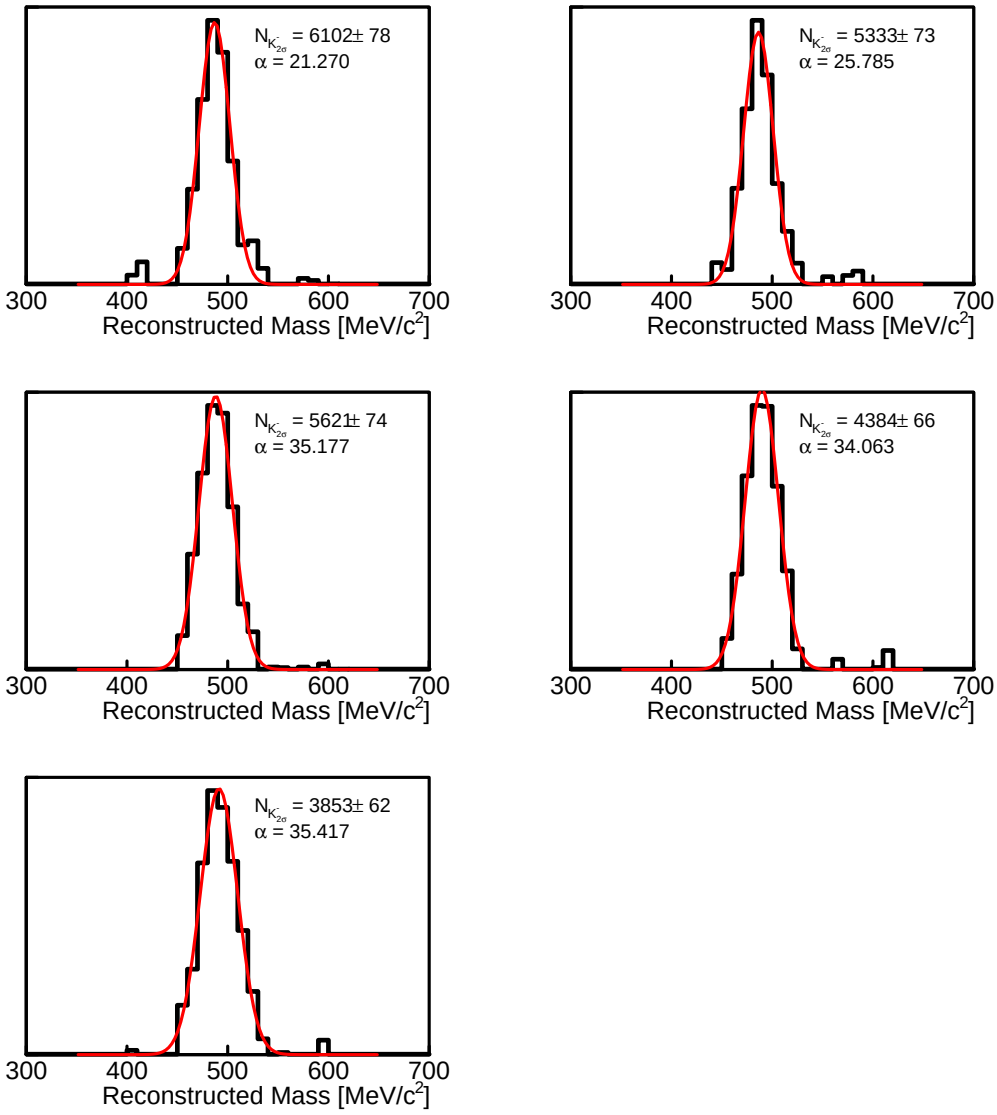

Figure A.28.: Subtracted exemplary TOF K^- mass spectra in the rapidity range $0.32 < y < 0.52$ for the $0 - 30\%$ centrality range.

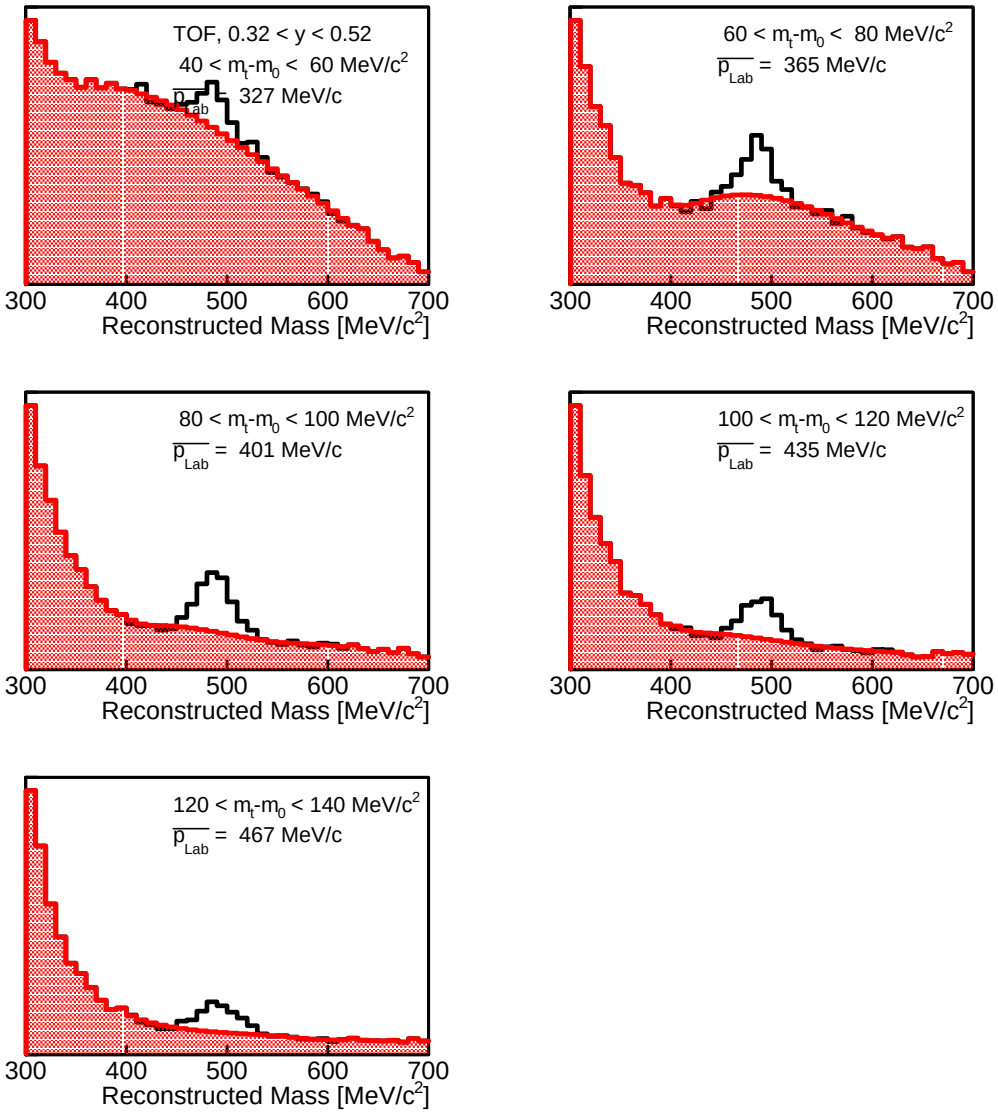

Figure A.29.: Exemplary TOF K^- mass spectra in the rapidity range $0.32 < y < 0.52$ for the $0 - 10\%$ centrality range.

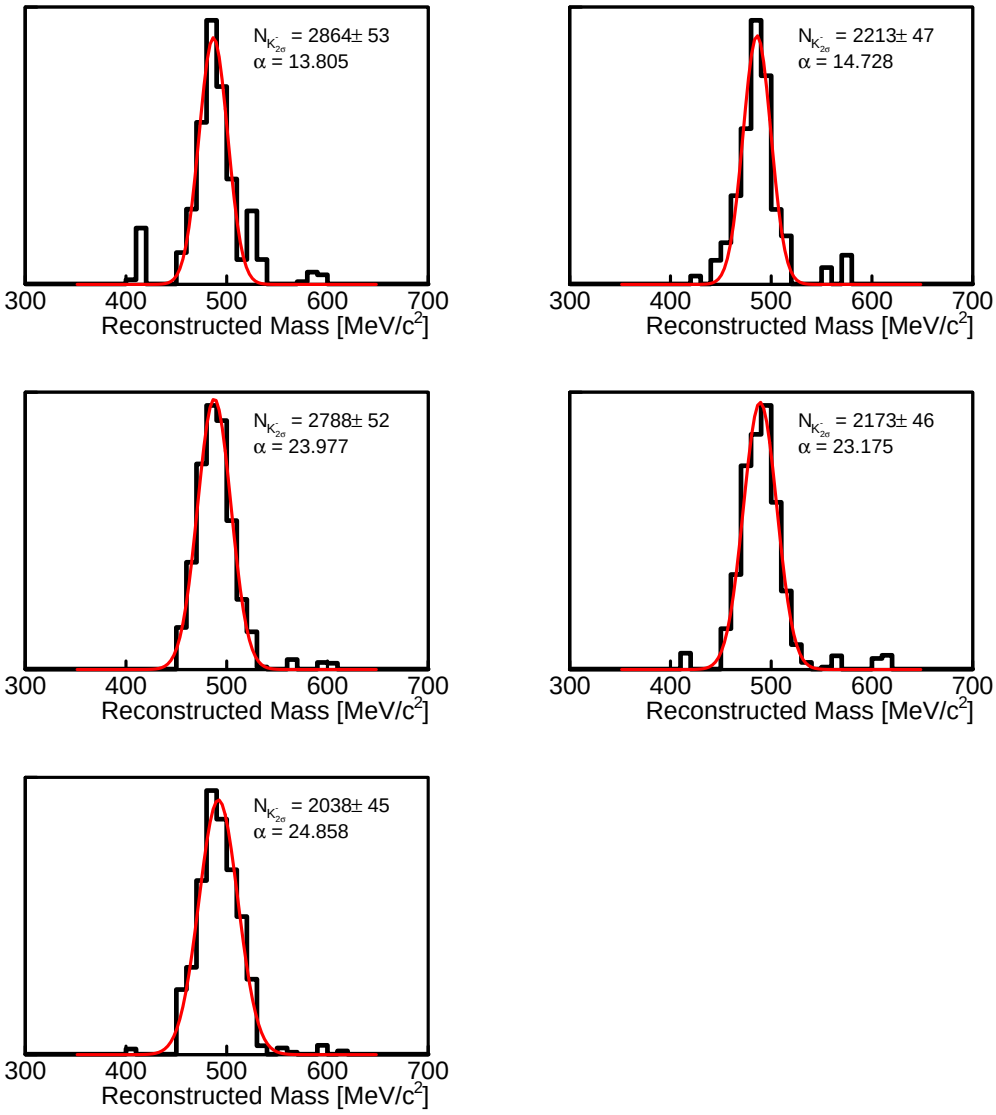

Figure A.30.: Subtracted exemplary TOF K^- mass spectra in the rapidity range $0.32 < y < 0.52$ for the $0 - 10\%$ centrality range.

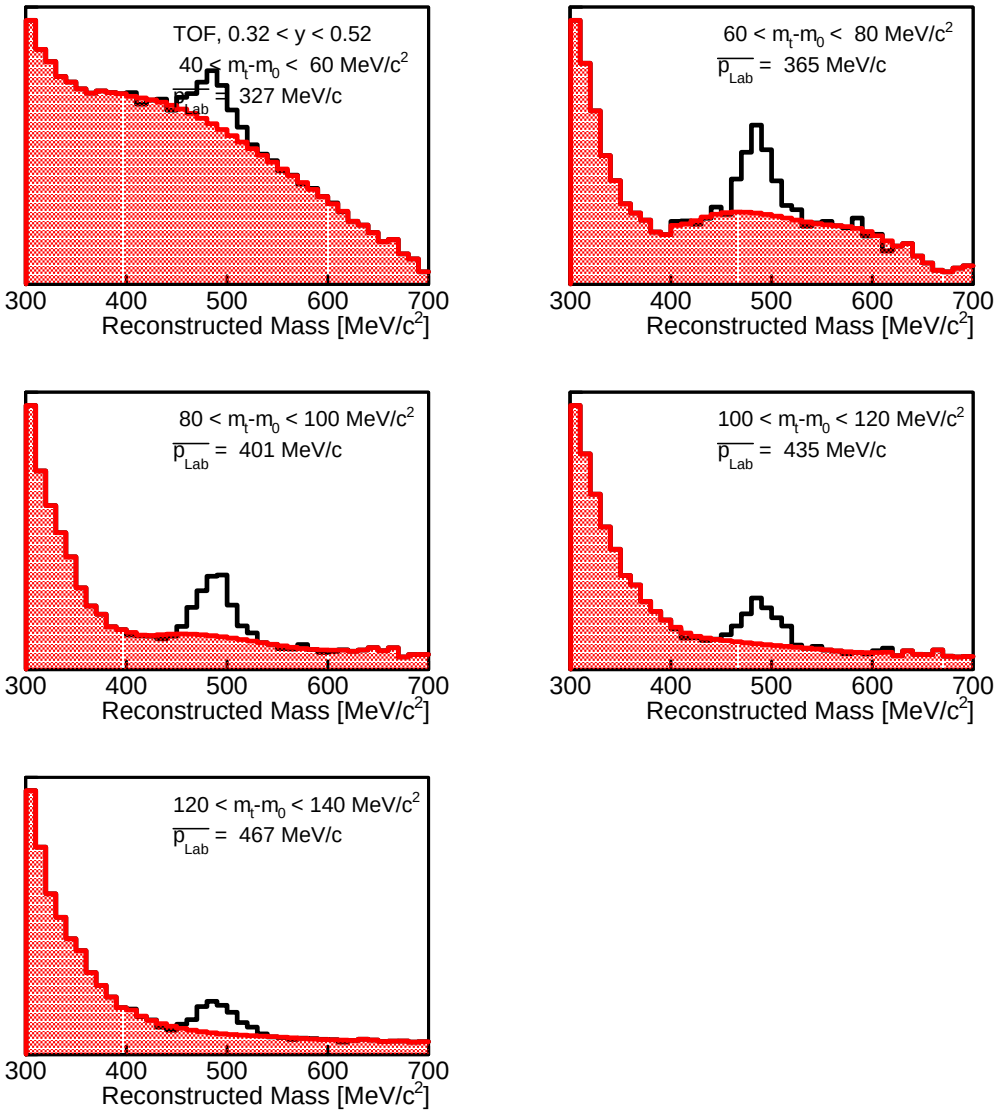

Figure A.31.: Exemplary TOF K^- mass spectra in the rapidity range $0.32 < y < 0.52$ for the $10 - 20\%$ centrality range.

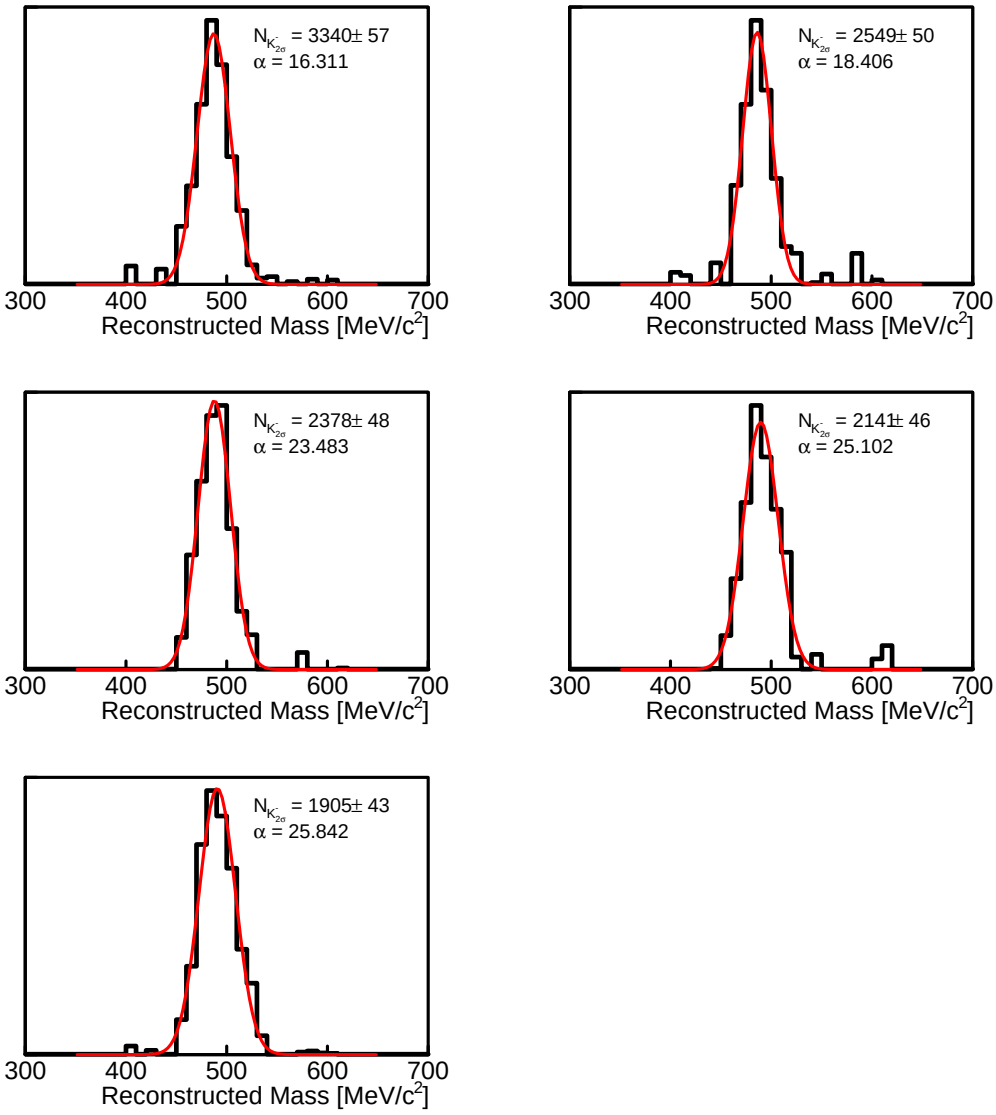

Figure A.32.: Subtracted exemplary TOF K^- mass spectra in the rapidity range $0.32 < y < 0.52$ for the $10 - 20\%$ centrality range.

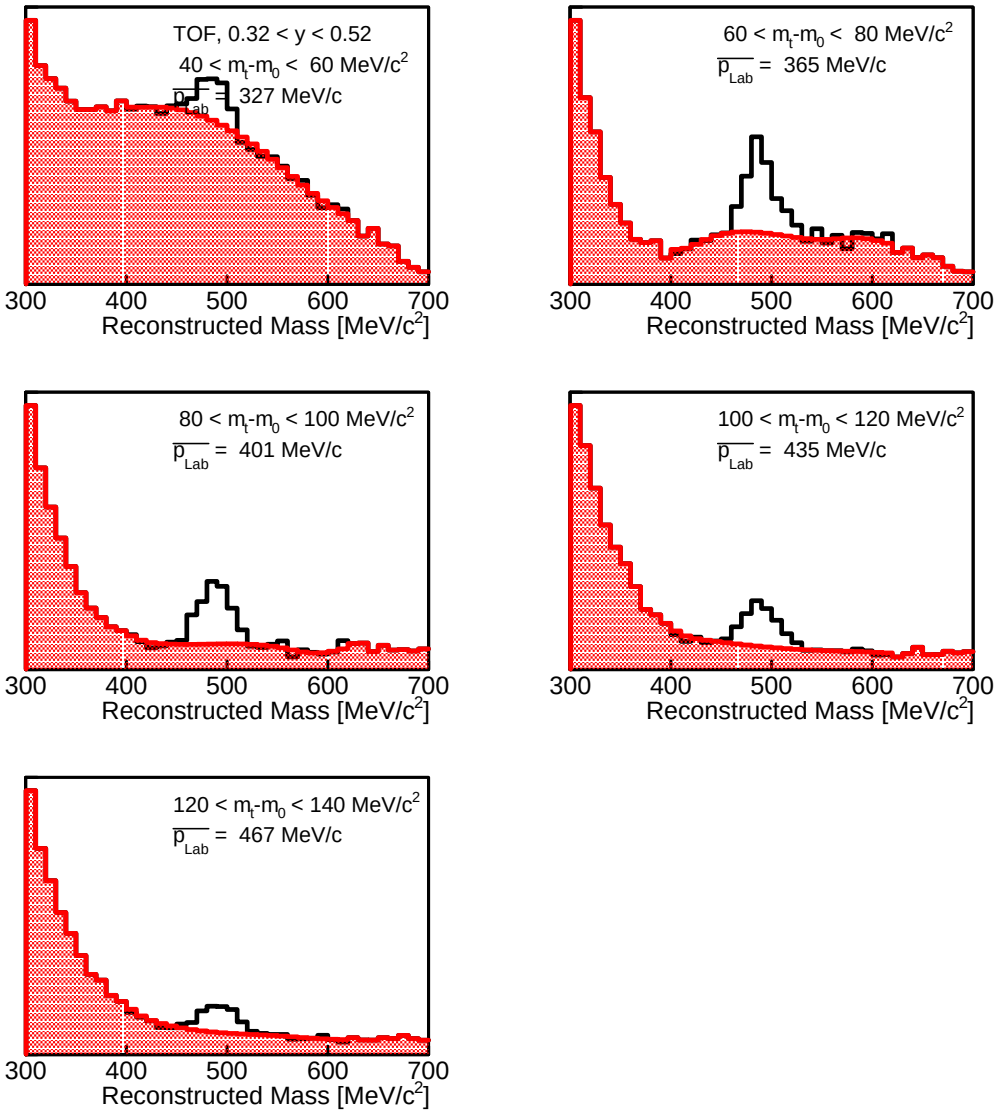

Figure A.33.: Exemplary TOF K^- mass spectra in the rapidity range $0.32 < y < 0.52$ for the $20 - 30\%$ centrality range.

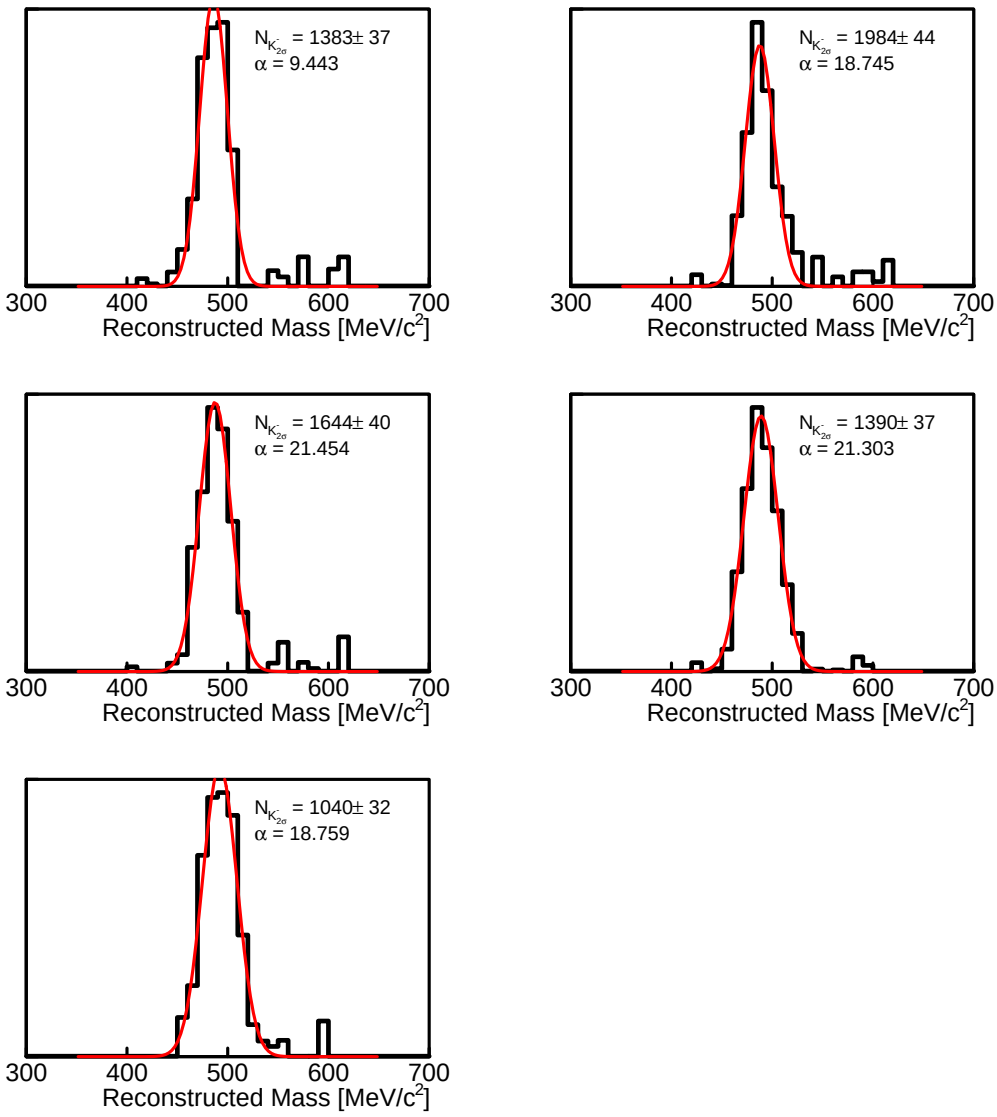

Figure A.34.: Subtracted exemplary TOF K^- mass spectra in the rapidity range $0.32 < y < 0.52$ for the $20 - 30\%$ centrality range.

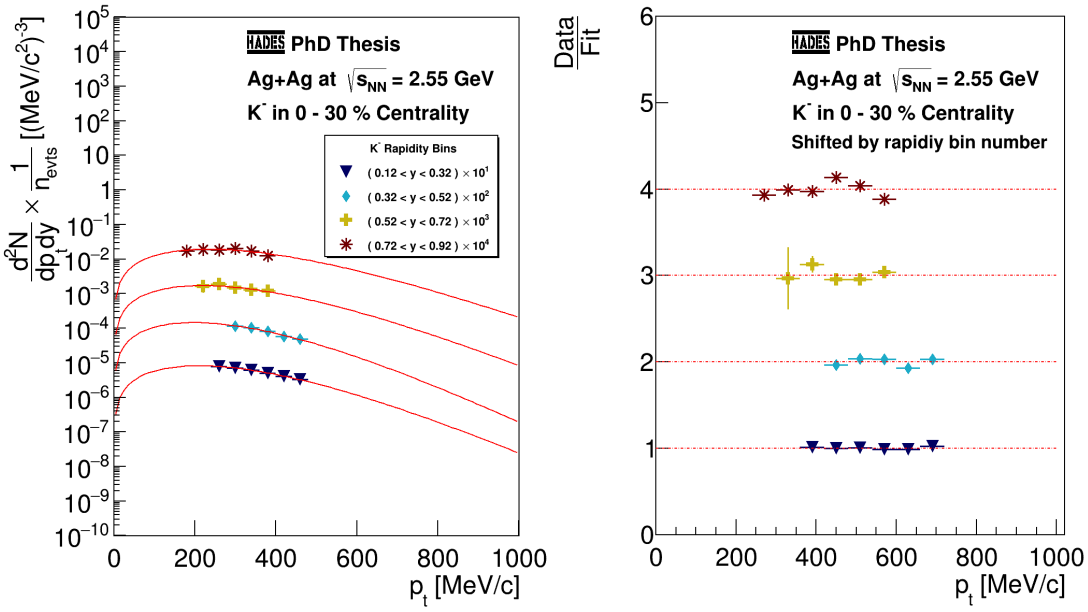

Figure A.35.: Fitted K^- p_t spectra for the $0-30\%$ centrality range.

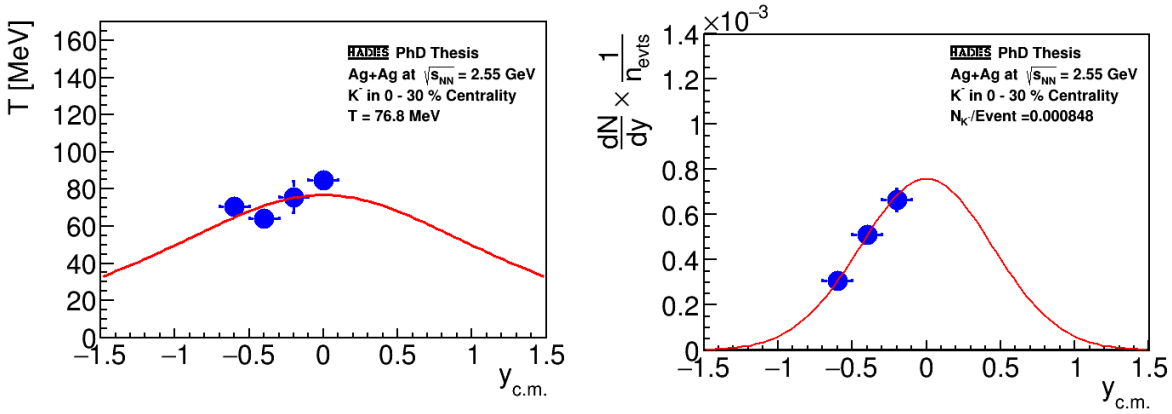

(a) T_{Eff} (b) dN/dy

Figure A.36.: Resulting and fitted K^- T_{Eff} and dN/dy spectra resulting from the transverse momentum analysis for the $0-30\%$ centrality range.

A.5. ϕ-Meson Multidifferential Example Spectra

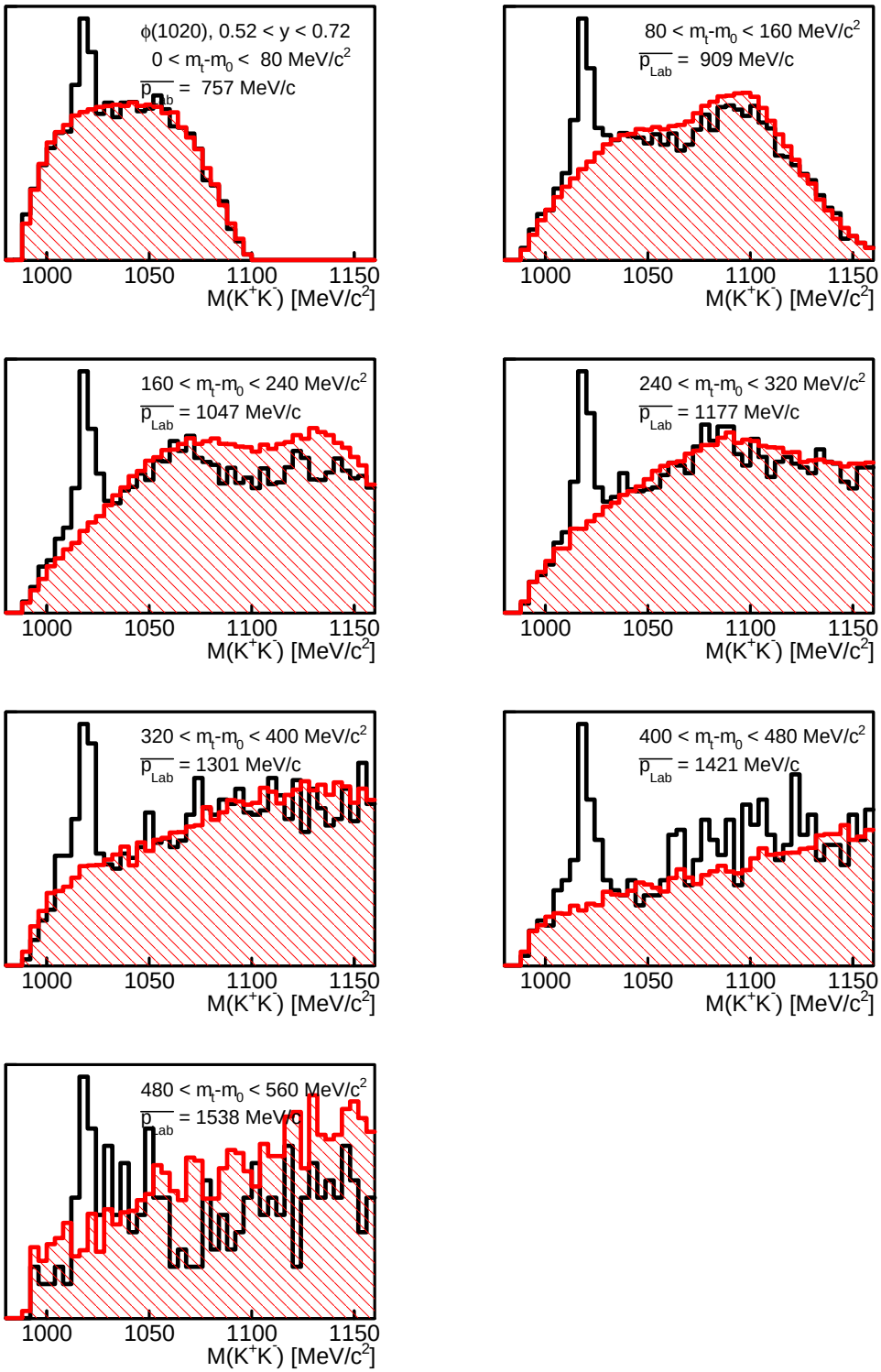

Figure A.37.: Exemplary ϕ-meson invariant mass spectra in the rapidity range $0.52 < y < 0.72$ for the $0 - 30\%$ centrality range.

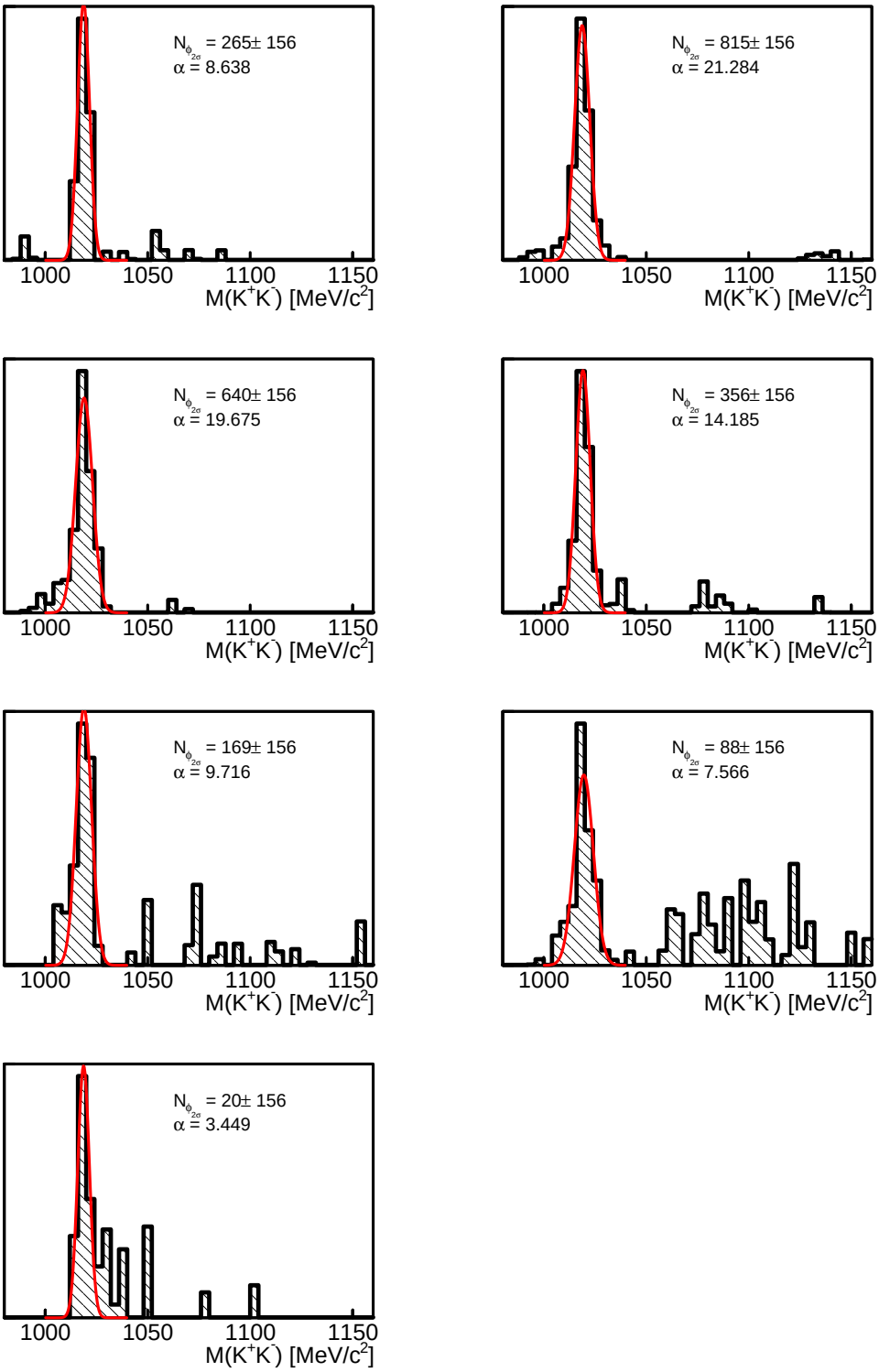

Figure A.38.: Subtracted exemplary ϕ-meson invariant mass spectra in the rapidity range $0.52 < y < 0.72$ for the $0 - 30\%$ centrality range.

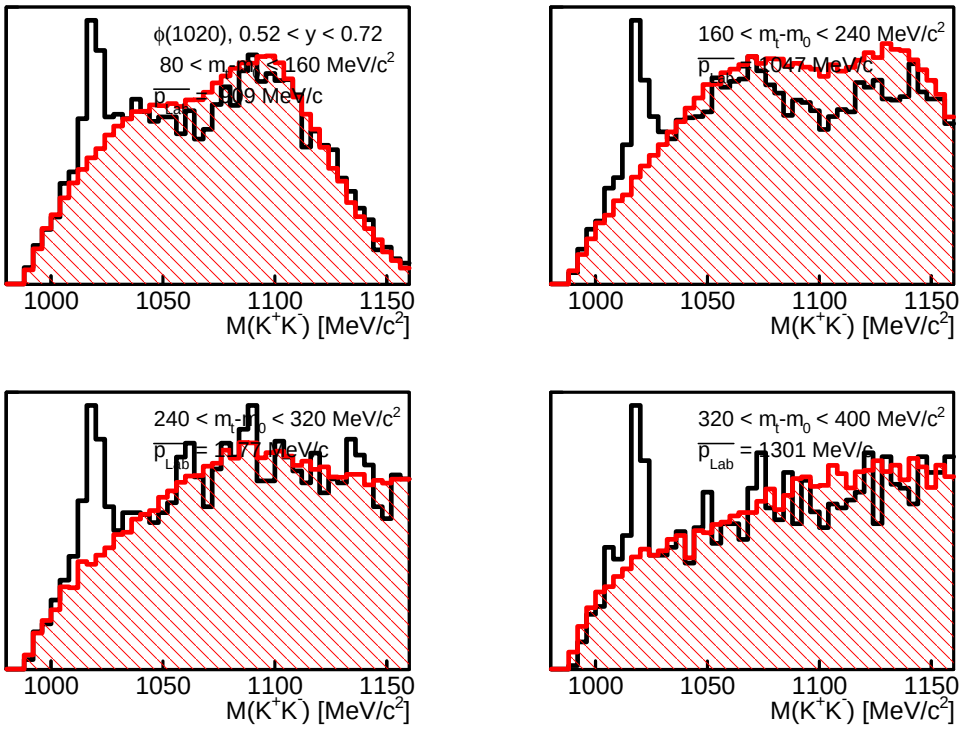

Figure A.39.: Exemplary ϕ-meson invariant mass spectra in the rapidity range $0.52 < y < 0.72$ for the $0 - 10\%$ centrality range.

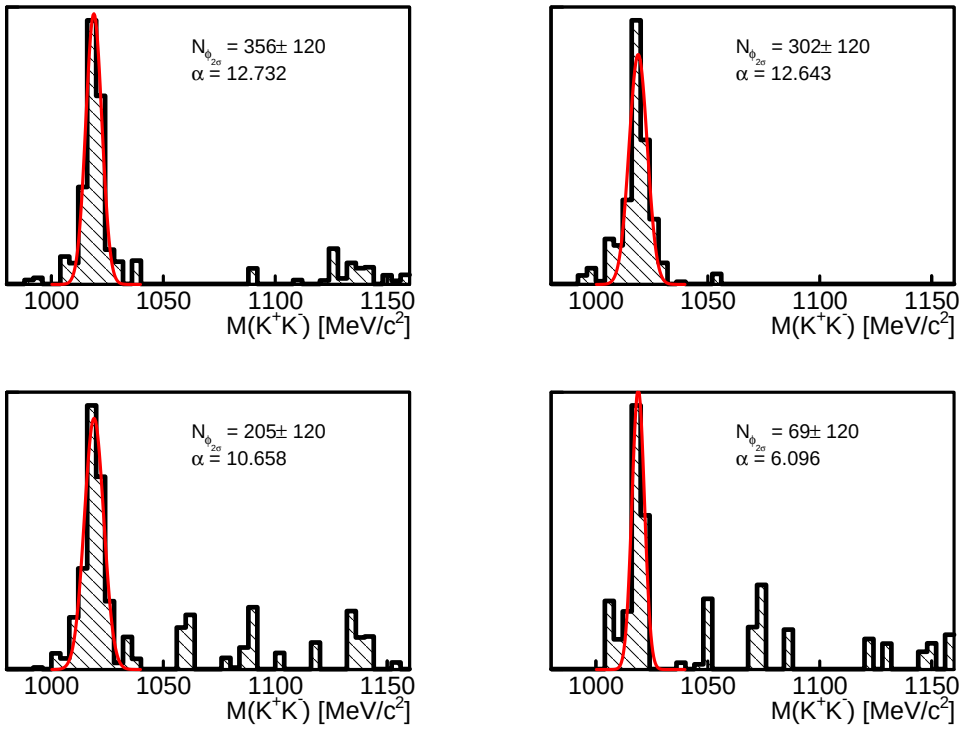

Figure A.40.: Subtracted exemplary ϕ-meson invariant mass spectra in the rapidity range $0.52 < y < 0.72$ for the $0 - 10\%$ centrality range.

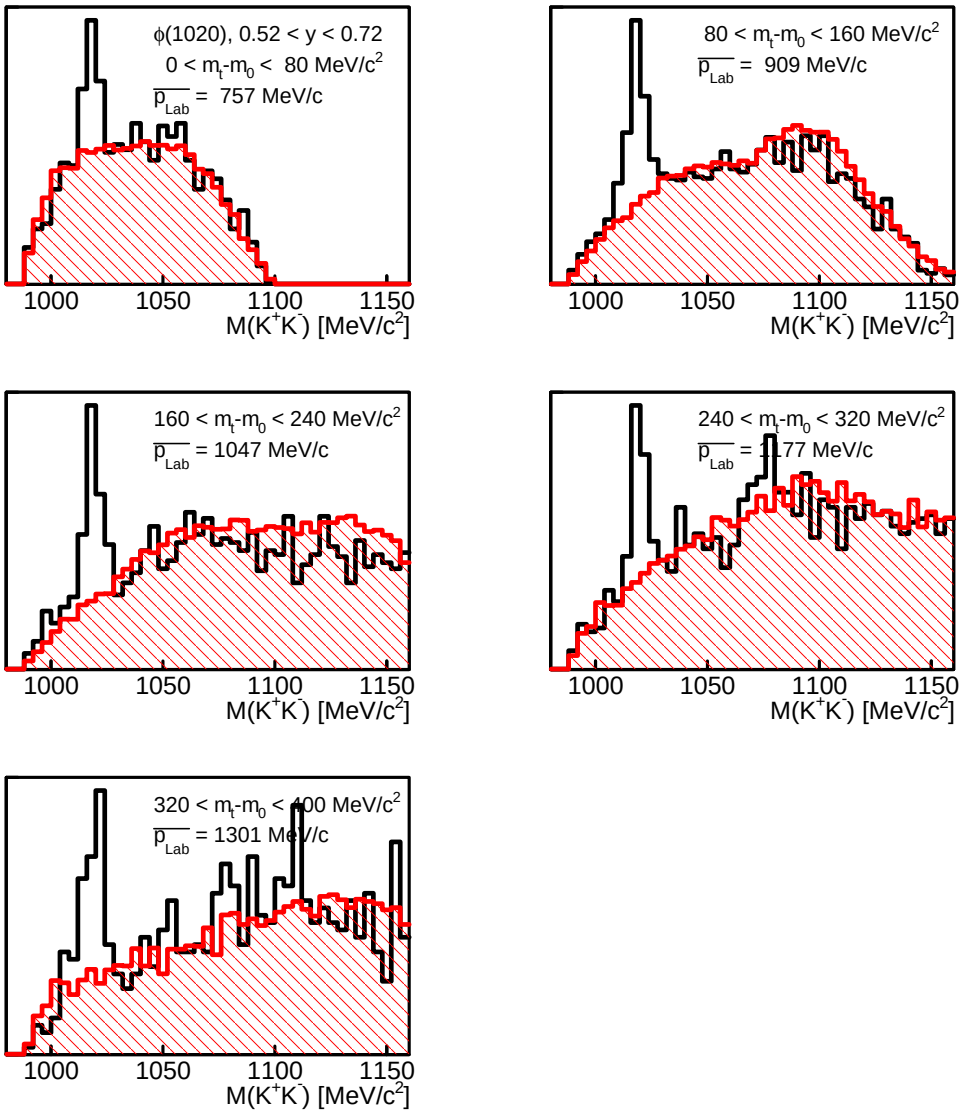

Figure A.41.: Exemplary ϕ-meson invariant mass spectra in the rapidity range $0.52 < y < 0.72$ for the $10 - 20\%$ centrality range.

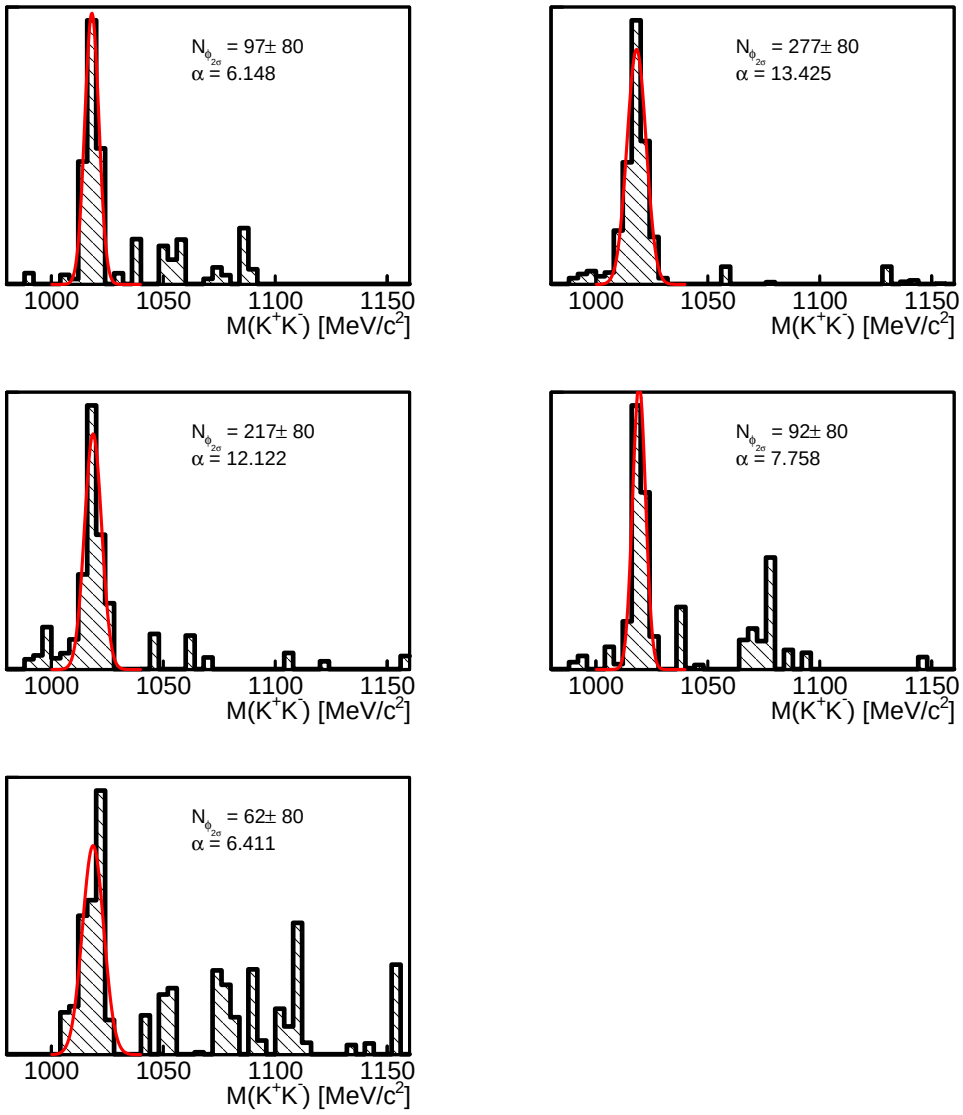

Figure A.42.: Subtracted exemplary ϕ-meson invariant mass spectra in the rapidity range $0.52 < y < 0.72$ for the $10 - 20\%$ centrality range.

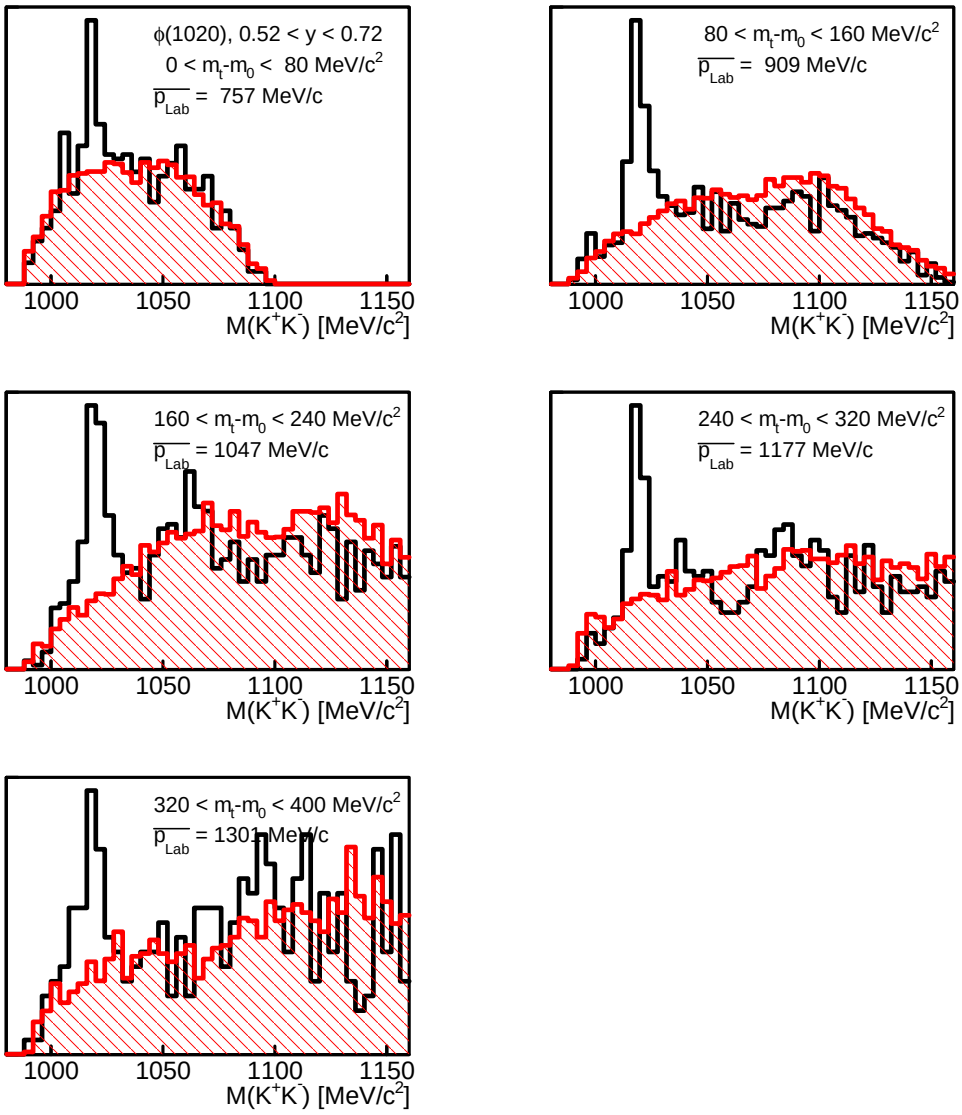

Figure A.43.: Exemplary ϕ-meson invariant mass spectra in the rapidity range $0.52 < y < 0.72$ for the $20 - 30\%$ centrality range.

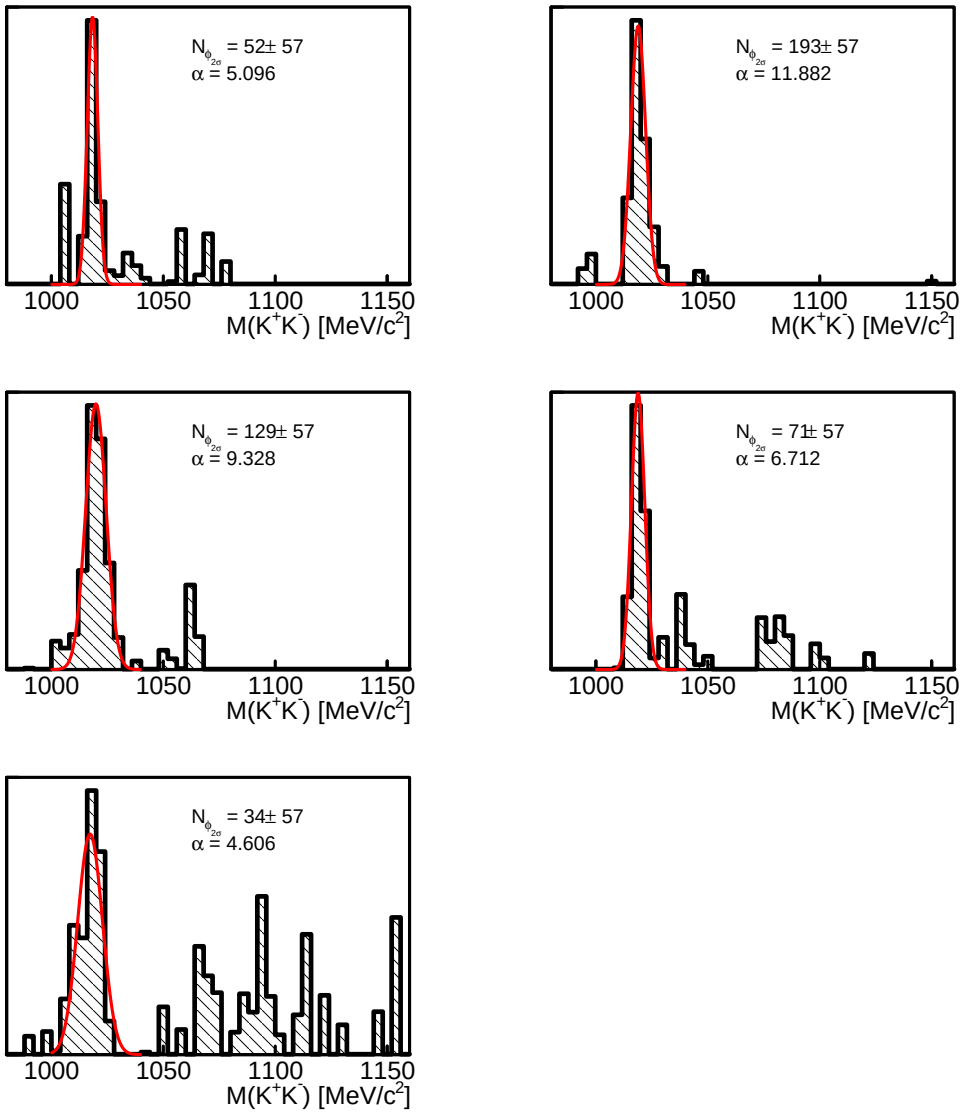

Figure A.44.: Subtracted exemplary ϕ-meson invariant mass spectra in the rapidity range $0.52 < y < 0.72$ for the $20 - 30\%$ centrality range.

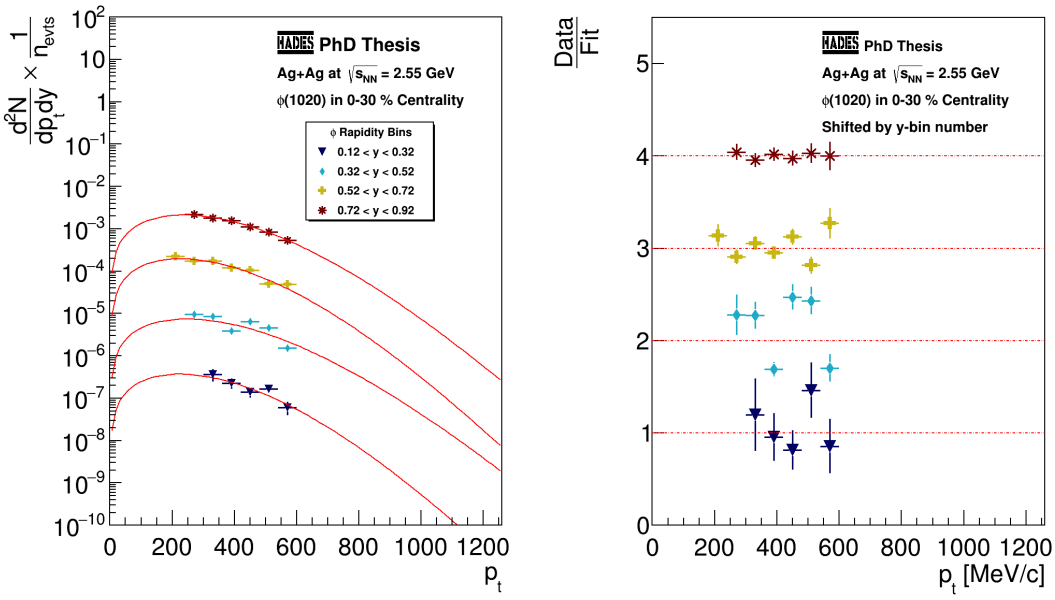

Figure A.45.: Fitted ϕ-meson p_t spectra for the $0-30\%$ centrality range.

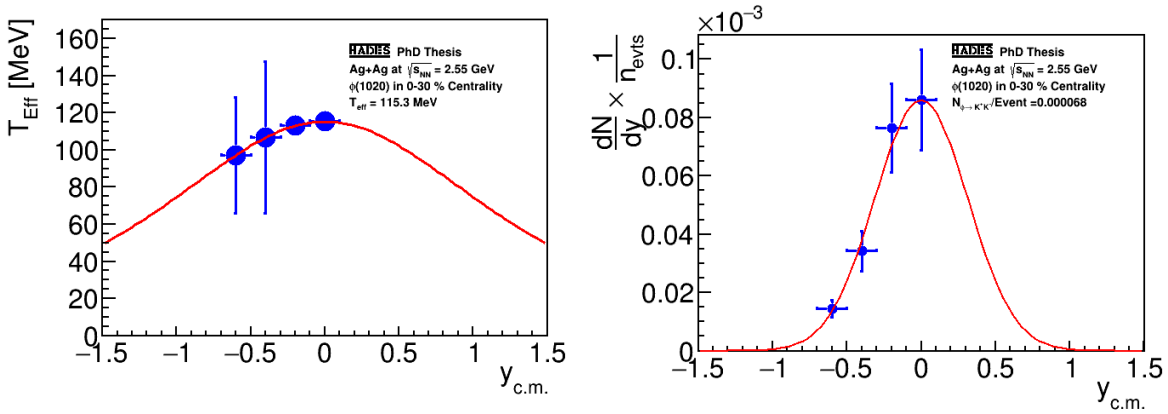

(a) T_{Eff} (b) dN/dy

Figure A.46.: Resulting and fitted ϕ-meson T_{Eff} and dN/dy spectra resulting from the transverse momentum analysis for the $0-30\%$ centrality range.

List of Figures

List of Tables

Bibliography

[1] B. I. Abelev *et al.* [STAR], *Systematic Measurements of Identified Particle Spectra in pp, d^+ Au and Au+Au Collisions from STAR*, Phys. Rev. C **79** (2009), 034909, doi:10.1103/PhysRevC.79.034909, [arXiv:0808.2041 [nucl-ex]]

[2] B. I. Abelev *et al.* [STAR], *Identified particle production, azimuthal anisotropy, and interferometry measurements in Au+Au collisions at s(NN)**(1/2) = 9.2- GeV*, Phys. Rev. C **81** (2010), 024911, doi:10.1103/PhysRevC.81.024911, [arXiv:0909.4131 [nucl-ex]]

[3] M. S. Abdallah *et al.* [STAR], *Probing strangeness canonical ensemble with K−, ϕ(1020) and $\Xi-$ production in Au+Au collisions at sNN=3 GeV*, Phys. Lett. B **831** (2022), 137152 doi:10.1016/j.physletb.2022.137152 [arXiv:2108.00924 [nucl-ex]]

[4] J. Adam *et al.* [STAR], *Strange hadron production in Au+Au collisions at $\sqrt{s_{\rm NN}}$ = 7.7, 11.5, 19.6, 27, and 39 GeV*, Phys. Rev. C **102** (2020) no.3, 034909, doi:10.1103/PhysRevC.102.034909, [arXiv:1906.03732 [nucl-ex]]

[5] J. Adamczewski-Musch *et al.* [HADES], *Centrality determination of Au + Au collisions at 1.23A GeV with HADES*, Eur. Phys. J. A **54** (2018) no.5, 85 doi:10.1140/epja/i2018-12513-7 [arXiv:1712.07993 [nucl-ex]]

[6] J. Adamczewski-Musch *et al.* [HADES], *Probing dense baryon-rich matter with virtual photons*, Nature Phys. **15** (2019) no.10, 1040-1045 doi:10.1038/s41567-019-0583-8

[7] J. Adamczewski-Musch *et al.* [HADES], *Charged-pion production in* $\mathbf{Au + Au}$ *collisions at* $\sqrt{\mathbf{s_{NN}}}$ = 2.4 **GeV***: HADES Collaboration*, Eur. Phys. J. A **56** (2020) no.10, 259 doi:10.1140/epja/s10050-020-00237-2 [arXiv:2005.08774 [nucl-ex]]

[8] J. Adamczewski-Musch *et al.* [HADES], *Impact of the Coulomb field on charged-pion spectra in few-GeV heavy-ion collisions*, Eur. Phys. J. A **58** (2022) no.9, 166, doi:10.1140/epja/s10050-022-00796-6, [arXiv:2202.12750 [nucl-ex]]

[9] J. Adams *et al.* [STAR], *phi meson production in Au + Au and p+p collisions at s(NN)**(1/2) = 200-GeV*, Phys. Lett. B **612** (2005), 181-189 doi:10.1016/j.physletb.2004.12.082 [arXiv:nucl-ex/0406003 [nucl-ex]]

[10] K. Adcox *et al.* [PHENIX], *Centrality dependence of pi+ / pi-, K+ / K-, p and anti-p production from s(NN)**(1/2) = 13-=GeV Au+Au collisions at RHIC*, Phys. Rev. Lett. **88** (2002), 242301, doi:10.1103/PhysRevLett.88.242301, [arXiv:nucl-ex/0112006 [nucl-ex]]

[11] C. Adler *et al.* [STAR], *Kaon production and kaon to pion ratio in Au+Au collisions at s(NN)**1/2 = 130-GeV*, Phys. Lett. B **595** (2004), 143-150, doi:10.1016/j.physletb.2004.06.044, [arXiv:nucl-ex/0206008 [nucl-ex]]

[12] S. S. Adler *et al.* [PHENIX], Identified charged particle spectra and yields in Au+Au collisions at S(NN)**1/2 = 200-GeV, Phys. Rev. C **69** (2004), 034909, doi:10.1103/PhysRevC.69.034909, [arXiv:nucl-ex/0307022 [nucl-ex]]

[13] S. V. Afanasiev *et al.* [NA49], *Production of Phi mesons in p + p, p + Pb and central Pb + Pb collisions at E(beam) = 158-A-GeV*, Phys. Lett. B **491** (2000), 59-66 doi:10.1016/S0370-2693(00)01023-6

[14] S. V. Afanasiev *et al.* [NA49], *Energy dependence of pion and kaon production in central Pb + Pb collisions*, Phys. Rev. C **66** (2002), 054902, doi:10.1103/PhysRevC.66.054902, [arXiv:nucl-ex/0205002 [nucl-ex]]

[15] G. Agakishiev *et al.* [HADES], *Phi decay: A Relevant source for K- production at SIS energies?*, Phys. Rev. C **80** (2009), 025209, doi:10.1103/PhysRevC.80.025209, [arXiv:0902.3487 [nucl-ex]]

[16] G. Agakishiev *et al.* [HADES], *Statistical hadronization model analysis of hadron yields in p + Nb and Ar + KCl at SIS18 energies*, Eur. Phys. J. A **52** (2016) no.6, 178, doi:10.1140/epja/i2016-16178-x, [arXiv:1512.07070 [nucl-ex]]

[17] C. Agodi, A. Bassi, R. Bassini, G. Bellia, M. Benovic, C. Boiano, S. Brambilla, R. Coniglione, L. Cosentino and P. Finocchiaro, *et al. The HADES time-of-flight wall*, Nucl. Instrum. Meth. A **492** (2002), 14-25 doi:10.1016/S0168-9002(02)01004-5

[18] C. Agodi, A. Bassi, R. Bassini, G. Bellia, M. Benovic, C. Boiano, S. Brambilla, R. Coniglione, L. Cosentino and P. Finocchiaro, *et al. The HADES time-of-flight wall*, Nucl. Instrum. Meth. A **492** (2002), 14-25 doi:10.1016/S0168-9002(02)01004-5

[19] L. Ahle *et al.* [E-802], *Kaon production in Au + Au collisions at 11.6-A-GeV/c*, Phys. Rev. C **58** (1998), 3523-3538, doi:10.1103/PhysRevC.58.3523

[20] L. Ahle *et al.* [E866 and E917], *An Excitation function of K- and K+ production in Au + Au reactions at the AGS*, Phys. Lett. B **490** (2000), 53-60, doi:10.1016/S0370-2693(00)00916-3, [arXiv:nucl-ex/0008010 [nucl-ex]]

[21] C. Alt *et al.* [NA49], *Pion and kaon production in central Pb + Pb collisions at 20-A and 30-A-GeV: Evidence for the onset of deconfinement*, Phys. Rev. C **77** (2008), 024903, doi:10.1103/PhysRevC.77.024903, [arXiv:0710.0118 [nucl-ex]]

[22] A. Andronic, P. Braun-Munzinger and J. Stachel, *Hadron production in central nucleus-nucleus collisions at chemical freeze-out*, Nucl. Phys. A **772** (2006), 167-199, doi:10.1016/j.nuclphysa.2006.03.012, [arXiv:nucl-th/0511071 [nucl-th]]

[23] A. Andronic, P. Braun-Munzinger, K. Redlich and J. Stachel, *Statistical hadronization of heavy quarks in ultra-relativistic nucleus-nucleus collisions*, Nucl. Phys. A **789** (2007), 334-356, doi:10.1016/j.nuclphysa.2007.02.013, [arXiv:nucl-th/0611023 [nucl-th]]

[24] A. Andronic, P. Braun-Munzinger, M. K. Köhler, K. Redlich and J. Stachel, *Transverse momentum distributions of charmonium states with the statistical hadronization model*, Phys. Lett. B **797** (2019), 134836, doi:10.1016/j.physletb.2019.134836, [arXiv:1901.09200 [nucl-th]]

[25] A. Andronic, P. Braun-Munzinger, M. K. Köhler, A. Mazeliauskas, K. Redlich, J. Stachel and V. Vislavicius, *The multiple-charm hierarchy in the statistical hadronization model*, JHEP **07** (2021), 035 doi:10.1007/JHEP07(2021)035 [arXiv:2104.12754 [hep-ph]]

[26] I. Angeli and K. P. Marinova, *Table of experimental nuclear ground state charge radii: An update*, Atom. Data Nucl. Data Tabl. **99** (2013) no.1, 69-95, doi:10.1016/j.adt.2011.12.006

[27] Y. Aoki, S. Borsanyi, S. Durr, Z. Fodor, S. D. Katz, S. Krieg and K. K. Szabo, *The QCD transition temperature: results with physical masses in the continuum limit II.*, JHEP **06** (2009), 088, doi:10.1088/1126-6708/2009/06/088, [arXiv:0903.4155 [hep-lat]]

[28] I. C. Arsene *et al.* [BRAHMS], *Kaon and Pion Production in Central Au+Au Collisions at S(NN)**(1/2) = 62.4 GeV*, Phys. Lett. B **687** (2010), 36-41, doi:10.1016/j.physletb.2010.02.078, [arXiv:0911.2586 [nucl-ex]]

[29] J. Bartke, *Introduction to Relativistic Heavy Ion Physics*, World Scientific, 2009

[30] S. A. Bass, M. Belkacem, M. Bleicher, M. Brandstetter, L. Bravina, C. Ernst, L. Gerland, M. Hofmann, S. Hofmann and J. Konopka, *et al.*, *Microscopic models for ultrarelativistic heavy ion collisions*, Prog. Part. Nucl. Phys. **41** (1998), 255-369, doi:10.1016/S0146-6410(98)00058-1, [arXiv:nucl-th/9803035 [nucl-th]]

[31] S. Basu, S. Thakur, T. K. Nayak and C. A. Pruneau, *Multiplicity and pseudorapidity density distributions of charged particles produced in pp, pA and AA collisions at RHIC & LHC energies*, J. Phys. G **48** (2020) no.2, 025103, doi:10.1088/1361-6471/abc05c, [arXiv:2008.07802 [nucl-ex]]

[32] A. Bazavov, T. Bhattacharya, M. Cheng, C. DeTar, H. T. Ding, S. Gottlieb, R. Gupta, P. Hegde, U. M. Heller and F. Karsch, *et al. The chiral and deconfinement aspects of the QCD transition*, Phys. Rev. D **85** (2012), 054503, doi:10.1103/PhysRevD.85.054503, [arXiv:1111.1710 [hep-lat]]

[33] A. Bazavov *et al.* [HotQCD], *Chiral crossover in QCD at zero and non-zero chemical potentials*, Phys. Lett. B **795** (2019), 15-21 doi:10.1016/j.physletb.2019.05.013 [arXiv:1812.08235 [hep-lat]]

[34] I. Bearden *et al.* [NA44], *Strange meson enhancement in Pb Pb collisions*, Phys. Lett. B **471** (1999), 6-12, doi:10.1016/S0370-2693(99)01327-1, [arXiv:nucl-ex/9907013 [nucl-ex]]

[35] I. G. Bearden *et al.* [NA44], *Particle production in central Pb + Pb collisions at 158-A-GeV/c*, Phys. Rev. C **66** (2002), 044907, doi:10.1103/PhysRevC.66.044907, [arXiv:nucl-ex/0202019 [nucl-ex]]

[36] M. Becker, private correspondence

[37] O. Behnke, K. Kröninger, T. Schörner-Sadenius and G. Schott, *Data Analysis in High Energy Physics: A Practical Guide to Statistical Methods*, Wiley-VCH, 2013

[38] R. Bellwied, J. Noronha-Hostler, P. Parotto, I. Portillo Vazquez, C. Ratti and J. M. Stafford, Freeze-out temperature from net-kaon fluctuations at energies available at the BNL Relativistic Heavy Ion Collider, Phys. Rev. C **99** (2019) no.3, 034912, doi:10.1103/PhysRevC.99.034912, [arXiv:1805.00088 [hep-ph]]

[39] D. Belver, A. Blanco, P. Cabanelas, N. Carolino, E. Castro, J. Diaz, P. Fonte, J. A. Garzon, D. Gonzalez-Diaz and A. Gil, *et al.*, *The HADES RPC inner TOF wall*, Nucl. Instrum. Meth. A **602** (2009), 687-690 doi:10.1016/j.nima.2008.12.090

[40] C. A. Bertulani, *Nuclear Physics in a Nutshell*, Princeton University Press, 2007

[41] A. Bialas, *Wounded Nucleons, Wounded Quarks: A Personal Story*, Acta Phys. Polon. B **51** (2020), 1023-1032, doi:10.5506/APhysPolB.51.1023

[42] A. Blanco, D. Belver, P. Cabanelas, J. Diaz, P. Fonte, J. A. Garzon, A. Gil, D. Gonzalez-Diaz, W. Koenig and B. Kolb, *et al.*, *RPC HADES-TOF wall cosmic ray test performance*, Nucl. Instrum. Meth. A **661** (2012), S114-S117 doi:10.1016/j.nima.2010.08.068

[43] A. Blanco *et al*, *Performance of the HADES-TOF RPC wall in a Au + Au beam at 1.25 AGeV* 2013 *JINST* 8 P01004

[44] I. Angeli and K. P. Marinova, Atom. Data Nucl. Data Tabl. **99** (2013) no.1, 69-95 doi:10.1016/j.adt.2011.12.006

[45] W. Blum, L. Rolandi and W. Riegler, *Particle detection with drift chambers*, doi:10.1007/978-3-540-76684-1

[46] C. Blume, *Particle Production at the SPS and the QCD Phase Diagram*, J. Phys. Conf. Ser. **230** (2010), 012003 doi:10.1088/1742-6596/230/1/012003 [arXiv:1007.1114 [nucl-ex]]

[47] C. Blume and C. Markert, *Strange hadron production in heavy ion collisions from SPS to RHIC*, Prog. Part. Nucl. Phys. **66** (2011), 834-879 doi:10.1016/j.ppnp.2011.05.001 [arXiv:1105.2798 [nucl-ex]]

[48] W. H. Bragg M.A. and R. Kleeman B.Sc. (1905) XXXIX., *On the α particles of radium, and their loss of range in passing through various atoms and molecules*, The London, Edinburgh, and Dublin Philosophical Magazine and Journal of Science, 10:57, 318-340, DOI: 10.1080/14786440509463378

[49] E. L. Bratkovskaya, W. Cassing and U. Mosel, *Analysis of kaon production at SIS energies*, Nucl. Phys. A **622** (1997), 593-604, doi:10.1016/S0375-9474(97)80701-4, [arXiv:nucl-th/9703047 [nucl-th]]

[50] P. Braun-Munzinger, V. Koch, T. Schäfer and J. Stachel, *Properties of hot and dense matter from relativistic heavy ion collisions*, Phys. Rept. **621** (2016), 76-126, doi:10.1016/j.physrep.2015.12.003, [arXiv:1510.00442 [nucl-th]]

[51] J. Cleymans, D. Elliott, A. Keranen and E. Suhonen, *Thermal model analysis of particle ratios at GSI Ni-Ni experiments using exact strangeness conservation*, Phys. Rev. C **57** (1998), 3319-3323, doi:10.1103/PhysRevC.57.3319, [arXiv:nucl-th/9711066 [nucl-th]]

[52] J. Cleymans, H. Oeschler, K. Redlich and S. Wheaton, *Comparison of chemical freeze-out criteria in heavy-ion collisions*, Phys. Rev. C **73** (2006), 034905 doi:10.1103/PhysRevC.73.034905 [arXiv:hep-ph/0511094 [hep-ph]]

[53] M. Effenberger and U. Mosel, *Off-shell effects on particle production*, Phys. Rev. C **60** (1999), 051901, doi:10.1103/PhysRevC.60.051901, [arXiv:nucl-th/9906085 [nucl-th]]

[54] H. Elfner and B. Müller, *The exploration of hot and dense nuclear matter: Introduction to relativistic heavy-ion physics*, [arXiv:2210.12056 [nucl-th]]

[55] D. Belver Fernandez, *The Front-End Electronics of the HADEStiming RPCs wall: design, developmentand performances analysis*, PhD Thesis, University of Santiago de Compostela, 2009

[56] S. Floerchinger and C. Wetterich, *Chemical freeze-out in heavy ion collisions at large baryon densities*, Nucl. Phys. A **890-891** (2012), 11-24 doi:10.1016/j.nuclphysa.2012.07.009 [arXiv:1202.1671 [nucl-th]]

[57] W. Florkowski, *Phenomenology of Ultra-Relativistic Heavy-Ion Collisions*, World Scientific, 2010

[58] A. Forster, F. Uhlig, I. Bottcher, D. Brill, M. Debowski, F. Dohrmann, E. Grosse, P. Koczon, B. Kohlmeyer and S. Lang, *et al.*, *Production of K+ and of K- Mesons in Heavy-Ion Collisions from 0.6 to 2.0-A-GeV Incident Energy*, Phys. Rev. C **75** (2007), 024906, doi:10.1103/PhysRevC.75.024906, [arXiv:nucl-ex/0701014 [nucl-ex]]

[59] R. W. Freund, R. H. W. Hoppe, *Stoer/Bulirsch: Numerische Mathematik 1*, 10th edition, Springer Verlag, 2007

[60] I. Frohlich, T. Galatyuk, R. Holzmann, J. Markert, B. Ramstein, P. Salabura and J. Stroth, *Design of the Pluto Event Generator*, J. Phys. Conf. Ser. **219** (2010), 032039 doi:10.1088/1742-6596/219/3/032039 [arXiv:0905.2568 [nucl-ex]]

[61] C. Fuchs, Z. Wang, L. Sehn, A. Faessler, V. S. Uma Maheswari and D. Kosov, *Origin of subthreshold K+ production in heavy ion collisions*, Phys. Rev. C **56** (1997), R606-R609 doi:10.1103/PhysRevC.56.R606 [arXiv:nucl-th/9701065 [nucl-th]]

[62] C. Fuchs, *Kaon production in heavy ion reactions at intermediate energies*, Prog. Part. Nucl. Phys. **56** (2006), 1-103, doi:10.1016/j.ppnp.2005.07.004, [arXiv:nucl-th/0507017 [nucl-th]]

[63] K. Fukushima, T. Kojo and W. Weise, *Hard-core deconfinement and soft-surface delocalization from nuclear to quark matter*, Phys. Rev. D **102** (2020) no.9, 096017, doi:10.1103/PhysRevD.102.096017, [arXiv:2008.08436 [hep-ph]]

[64] J. Förtsch *et al.*, *Fast readout and performance of the upgraded HADES RICH in heavy ion collisions*, JINST **15** C03021, 2020, doi: 10.1088/1748-0221/15/03/c03021

[65] T. Galatyuk, M. Golubeva, F. Guber, A. Ivashkin, A. Kugler, S. Morozov, O. Petukhov, A. Reshetin, A. Rost and A. Shabanov, *et al.*, *Tests of the Electromagnetic Calorimeter for HADES Experiment at GSI*, KnE Energ. Phys. **3** (2018), 162-169, doi:10.18502/ken.v3i1.1739

[66] P. Gasik *et al.* [FOPI], *Strange meson production in Al+Al collisions at 1.9 A GeV*, Eur. Phys. J. A **52** (2016) no.6, 177 doi:10.1140/epja/i2016-16177-y [arXiv:1512.06988 [nucl-ex]]

[67] *GEANT - Detector Description and Simulation Tool*, `https://www.yumpu.com/en/document/read/16462544/geant-manual-writeups-cern`, 21st April 2022

[68] GNU Reference Guide, *Interpolation*, `https://www.gnu.org/software/gsl/doc/html/interp.html`, 13th May 2022

[69] B. Gough, *GNU scientific library reference manual*, Network Theory Ltd., 2009

[70] GSI webpage, `https://www.gsi.de/fileadmin/_processed_/f/5/csm_GSI-MSV_300dpi_Aug_2021_EN_4017c9d5d3.jpg`, 20th November 2021

[71] GSI webpage, `https://www.gsi.de/en/work/beschleunigerbetrieb/beschleuniger/ionenquellen/sources/ion_sources`, 20th November 2021

[72] GSI webpage, `https://www.gsi.de/en/work/beschleunigerbetrieb/beschleuniger/unilac/unilac`, 20th November 2021

[73] GSI webpage, `https://www.gsi.de/en/researchaccelerators/accelerator_facility/ring_accelerator`, 20th November 2021

[74] J. N. Guenther, R. Bellwied, S. Borsanyi, Z. Fodor, S. D. Katz, A. Pasztor, C. Ratti and K. K. Szabó, *The QCD equation of state at finite density from analytical continuation*, Nucl. Phys. A **967** (2017), 720-723 doi:10.1016/j.nuclphysa.2017.05.044 [arXiv:1607.02493 [hep-lat]]

[75] F. Guttner and H. J. Pirner, *Quark Percolation in Nuclei*, Nucl. Phys. A **457** (1986), 555, doi:10.1016/0375-9474(86)90468-9

[76] The HADES Collaboration, *Proposal for experiments at SIS18 during FAIR Phase-0*, `https://hades.gsi.de/sites/default/files/web/media/documents/proposals/HadesSis18_proposal_2018-2019.pdf`

[77] The HADES Collaboration, *The high-acceptance dielectron spectrometer HADES*, Eur. Phys. J. A **41**, 243-277 (2009) doi:10.1140/epja/i2009-10807-5

[78] S. Harabasz, W. Florkowski, T. Galatyuk, ‡. Ma Lgorzata Gumberidze, R. Ryblewski, P. Salabura and J. Stroth, *Statistical hadronization model for heavy-ion collisions in the few-GeV energy regime*, Phys. Rev. C **102** (2020) no.5, 054903, doi:10.1103/PhysRevC.102.054903, [arXiv:2003.12992 [nucl-th]]

[79] C. Hartnack, R. K. Puri, J. Aichelin, J. Konopka, S. A. Bass, H. Stoecker and W. Greiner, *Modeling the many body dynamics of heavy ion collisions: Present status and future perspective*, Eur. Phys. J. A **1** (1998), 151-169, doi:10.1007/s100500050045, [arXiv:nucl-th/9811015 [nucl-th]]

[80] U. W. Heinz, H. Song and A. K. Chaudhuri, *Dissipative hydrodynamics for viscous relativistic fluids*, Phys. Rev. C **73** (2006), 034904, doi:10.1103/PhysRevC.73.034904, [arXiv:nucl-th/0510014 [nucl-th]]

[81] B. Holzman *et al.* [E917], *Systematic study of Au - Au collisions with AGS experiment E917*, Nucl. Phys. A **698** (2002), 643-646 doi:10.1016/S0375-9474(01)01448-8 [arXiv:nucl-ex/0103015 [nucl-ex]]

[82] R. Holzmann, private correspondence

[83] K. Johnson, *The M.I.T. Bag Model*, Acta Phys. Polon. B **6** (1975), 865, MIT-CTP-494

[84] B. Kardan [HADES], *Collective flow and correlations measurements with HADES in Au+Au collisions at 1.23 AGeV*, Nucl. Phys. A **982** (2019), 431-434 doi:10.1016/j.nuclphysa.2018.09.061 [arXiv:1809.07821 [nucl-ex]]

[85] A. Kisiel, T. Taluc, W. Broniowski and W. Florkowski, *THERMINATOR: THERMal heavy-IoN generATOR*, Comput. Phys. Commun. **174** (2006), 669-687, doi:10.1016/j.cpc.2005.11.010, [arXiv:nucl-th/0504047 [nucl-th]]

[86] C. M. Ko, *EFFECT OF FINAL STATE INTERACTIONS ON SUBTHRESHOLD K-PRODUCTION IN HEAVY ION COLLISIONS*, Phys. Lett. B **138** (1984), 361-364, doi:10.1016/0370-2693(84)91917-8

[87] C. M. Ko, V. Koch and G. Q. Li, *Properties of hadrons in hot and dense matter*, Ann. Rev. Nucl. Part. Sci. **47** (1997), 505-539, doi:10.1146/annurev.nucl.47.1.505, [arXiv:nucl-th/9702016 [nucl-th]]

[88] V. Koch, *Introduction to chiral symmetry*, [arXiv:nucl-th/9512029 [nucl-th]]

[89] H. Kolanoski, N. Wermes, *Teilchendetektoren - Grundlagen und Anwendungen*, Springer Spektrum, 2016, doi: 10.1007/978-3-662-45350-6

[90] G. Kornakov, *New Advances and Developments on the RPC TOF Wall of the HADES Experiment at GSI*, PhD Thesis, University of Santiago de Compostela, 2012

[91] G. Kornakov *et al.* [HADES], *Time of flight measurement in heavy-ion collisions with the HADES RPC TOF wall*, JINST **9** (2014) no.11, C11015 doi:10.1088/1748-0221/9/11/C11015

[92] J. Letessier and J. Rafelski, *Hadrons and quark - gluon plasma*, Cambridge University Press, 2002, ISBN 978-0-521-01823-4, 978-0-521-38536-7, 978-0-511-03727-6

[93] D. R. Lide, *CRC Handbook of Chemistry and Physics*, 90th edition, CRC Press 2010

[94] M. Lorenz, *Recent Results from HADES*, Springer Proc. Phys. **250** (2020), 15-20 doi:10.1007/978-3-030-53448-6_2

[95] Y. Maeda *et al.* [ANKE], *Kaon Pair Production in Proton–Proton Collisions*, Phys. Rev. C **77** (2008), 015204, doi:10.1103/PhysRevC.77.015204, [arXiv:0710.1755 [nucl-ex]]

[96] J. Markert, *Untersuchungen zum Ansprechverhalten der Vieldraht-Driftkammern niedriger Massenbelegung des HADES Experimentes*, PhD Thesis, Goethe University Frankfurt am Main, 2005

[97] J. Michel, *Development and Implementation of a New Trigger and Data Acquisition System for the HADES Detector*, PhD Thesis, Goethe University Frankfurt am Main, 2012

[98] E. R. Most, L. J. Papenfort, V. Dexheimer, M. Hanauske, S. Schramm, H. Stöcker and L. Rezzolla, *Signatures of quark-hadron phase transitions in general-relativistic neutron-star mergers*, Phys. Rev. Lett. **122** (2019) no.6, 061101, doi:10.1103/PhysRevLett.122.061101, [arXiv:1807.03684 [astro-ph.HE]]

[99] M. Nabroth, *Emission patterns of charged pions from Ag+Ag collisions at 1.58A GeV*, Master Thesis, Goethe University Frankfurt am Main, 2022

[100] M. Nabroth, private correspondence

[101] D. Ondreka, C. Dimopoulou, H. Hüther, H. Liebermann, J. Stadlmann and R. Steinhagen, *Recommissioning of SIS18 After FAIR Upgrades*, doi:10.18429/JACoW-IPAC2019-MOPTS035

[102] HADES Oracle database for the Mar19 beamtime

[103] J. H. Otto, *Dielectron reconstruction in Ag+Ag collisions at* $\sqrt{s_{NN}} = 2.55$ *GeV with HADES*, PhD-Thesis, Justus Liebig Universität Giessen, 2022, doi:10.22029/JLUPUB-7207

[104] H. Petersen, D. Oliinychenko, M. Mayer, J. Staudenmaier and S. Ryu, *SMASH – A new hadronic transport approach*, Nucl. Phys. A **982** (2019), 399-402, doi:10.1016/j.nuclphysa.2018.08.008, [arXiv:1808.06832 [nucl-th]]

[105] K. Piasecki *et al.* [FOPI], *Influence of* ϕ *mesons on negative kaons in Ni+Ni collisions at 1.91A GeV beam energy*, Phys. Rev. C **91** (2015) no.5, 054904 doi:10.1103/PhysRevC.91.054904 [arXiv:1412.4493 [nucl-ex]]

[106] B. Povh, K. Rith, C. Scholz, F. Zetsche, W. Rodejohann, *Teilchen und Kerne - Eine Einführung in die physikalischen Konzepte*, Springer Spektrum Berlin, Heidelberg, November 2013, doi: 10.1007/978-3-642-37822-5

[107] W.H. Press, S.A. Teukolsky, W.T. Vetterling, B.P. Flannery, *Numerical Recipes - The Art of Scientific Computing*, 3rd Edition, Cambridge University Press, 2007

[108] J. Rafelski and B. Muller, *Strangeness Production in the Quark - Gluon Plasma*, Phys. Rev. Lett. **48** (1982), 1066, [erratum: Phys. Rev. Lett. **56** (1986), 2334], doi:10.1103/PhysRevLett.48.1066

[109] R. Rapp, *Hadro chemistry and evolution of (anti–) baryon densities at RHIC*, Phys. Rev. C **66** (2002), 017901 doi:10.1103/PhysRevC.66.017901 [arXiv:hep-ph/0204131 [hep-ph]]

[110] T. Reichert, A. Elz, T. Song, G. Coci, M. Winn, E. Bratkovskaya, J. Aichelin, J. Steinheimer and M. Bleicher, *Comparison of heavy ion transport simulations: Ag + Ag collisions at E_{lab} = 1.58A GeV*, J. Phys. G **49** (2022) no.5, 055108, doi:10.1088/1361-6471/ac5dfe, [arXiv:2111.07652 [nucl-th]]

[111] H. G. Ritter and R. Stock, *Collective Flow of QCD Matter: a Historical Introduction*, J. Phys. G **41** (2014), 124002 doi:10.1088/0954-3899/41/12/124002 [arXiv:1408.4296 [nucl-ex]]

[112] ROOT Webpage, `https://root.cern/`

[113] ROOT Reference Guide, `https://root.cern/doc/master/index.html`

[114] A. Rustamov, *Exclusive η Meson Reconstruction in Proton-Proton Collisions at 2.2 GeV with the HADES Spectrometer and High Resolution Tracking*, PhD Thesis, Technische Universität Darmstadt, 2006

[115] M. Sánchez, *Momentum reconstruction and pion production analysis in the HADES spectrometer at GSI*, PhD Thesis, University of Santiago de Compostela, 2003

[116] T. Scheib, Λ *and* K^0_s *Production in Au+Au Collisions at 1.23A GeV*, PhD Thesis, Johann Wolfgang von Goethe-Universität Frankfurt am Main, 2017

[117] A. M. Schmah, *Produktion von Seltsamkeit in Ar+KCI Reaktionen bei 1.756 AGeV mit HADES*, PhD Thesis, Johann Wolfgang von Goethe-Universität Frankfurt am Main, 2008

[118] E. Schnedermann, J. Sollfrank and U. W. Heinz, *Thermal phenomenology of hadrons from 200-A/GeV S+S collisions*, Phys. Rev. C **48** (1993), 2462-2475 doi:10.1103/PhysRevC.48.2462

[119] H. Schuldes, *Charged Kaon and φ reconstruction in Au+Au collisions at 1.23 AGeV*, PhD Thesis, Johann Wolfgang von Goethe-Universität Frankfurt am Main, 2016

[120] H. Schuldes [HADES], *Strangeness production in Au(1.23 A GeV)+Au collisions*, Nucl. Phys. A **967** (2017), 804-807, doi:10.1016/j.nuclphysa.2017.04.028

[121] GSI Helmholtzzentrum für Schwerionenforschung GmbH,
GSI Scientific Report 2013, doi:10.15120/GR-2014-1,
GSI Scientific Report 2014, doi:10.15120/GR-2015-1,
GSI Scientific Report 2015, doi:10.15120/GR-2016-1,
GSI Scientific Report 2016, doi:10.15120/GR-2017-1,
GSI Scientific Report 2017, doi:10.15120/GSI-2017-01856,

GSI Scientific Report 2018, doi:10.15120/GSI-2019-00545,
GSI Scientific Report 2019, doi:10.15120/GSI-2020-00416,
GSI Scientific Report 2020, doi:10.15120/GSI-2021-01005

[122] K. Sennhenn, *Identifikation von Helium und Lithium in Au+Au-Kollisionen bei 1.23 AGeV mit HADES*, Bachelor Thesis, Johann Wolfgang von Goethe-Universität Frankfurt am Main, 2020

[123] E. V. Shuryak, *Quark-Gluon Plasma and Hadronic Production of Leptons, Photons and Psions*, Phys. Lett. B **78** (1978), 150, doi:10.1016/0370-2693(78)90370-2

[124] H. J. Specht [NA60], *Thermal Dileptons from Hot and Dense Strongly Interacting Matter*, AIP Conf. Proc. **1322** (2010) no.1, 1-10 doi:10.1063/1.3541982 [arXiv:1011.0615 [nucl-ex]]

[125] S. Spies, *Strange Hadron Production in Ag+Ag Collisions at 1.58A GeV*, PhD Thesis, Johann Wolfgang von Goethe-Universität Frankfurt am Main, 2022

[126] J. Stachel, A. Andronic, P. Braun-Munzinger and K. Redlich, *Confronting LHC data with the statistical hadronization model*, J. Phys. Conf. Ser. **509** (2014), 012019, doi:10.1088/1742-6596/509/1/012019, [arXiv:1311.4662 [nucl-th]]

[127] J. Staudenmaier, N. Kübler and H. Elfner, *Particle production in AgAg collisions at* $E_{kin} = 1.58A$ *GeV within a hadronic transport approach*, Phys. Rev. C **103** (2021) no.4, 044904, doi:10.1103/PhysRevC.103.044904, [arXiv:2008.05813 [hep-ph]]

[128] V. Steinberg, J. Staudenmaier, D. Oliinychenko, F. Li, Ö. Erkiner and H. Elfner, *Strangeness production via resonances in heavy-ion collisions at energies available at the GSI Schwerionensynchrotron*, Phys. Rev. C **99** (2019) no.6, 064908, doi:10.1103/PhysRevC.99.064908, [arXiv:1809.03828 [nucl-th]]

[129] H. Stöcker, *Taschenbuch der Physik*, Verlag Harri Deutsch, 6th Edition, 2010, ISBN: 978-3-8171-1860-1

[130] J.Stoer, R. Bulirsch, *Introduction to Numerical Analysis*, 3rd Edition, Springer Verlag, 2002

[131] P. Tlusty, HADES Collaboration, Private Correspondence

[132] L. Tolos and L. Fabbietti, *Strangeness in Nuclei and Neutron Stars*, Prog. Part. Nucl. Phys. **112** (2020), 103770, doi:10.1016/j.ppnp.2020.103770, [arXiv:2002.09223 [nucl-ex]]

[133] L. Tolos, A. Polls, A. Ramos and J. Schaffner-Bielich, *K- / K+ ratio in heavy ion collisions at GSI with an antikaon selfenergy in hot and dense matter*, Phys. Rev. C **68** (2003), 024903, doi:10.1103/PhysRevC.68.024903, [arXiv:nucl-th/0302082 [nucl-th]]

[134] V. Vovchenko and H. Stoecker, *Thermal-FIST: A package for heavy-ion collisions and hadronic equation of state*, Comput. Phys. Commun. **244** (2019), 295-310, doi:10.1016/j.cpc.2019.06.024, [arXiv:1901.05249 [nucl-th]]

[135] J. Weil, V. Steinberg, J. Staudenmaier, L. G. Pang, D. Oliinychenko, J. Mohs, M. Kretz, T. Kehrenberg, A. Goldschmidt and B. Bäuchle, *et al.*, *Particle production and equilibrium properties within a new hadron transport approach for heavy-ion collisions*, Phys. Rev. C **94** (2016) no.5, 054905, doi:10.1103/PhysRevC.94.054905

[136] S. Wheaton and J. Cleymans, *THERMUS: A Thermal model package for ROOT*, Comput. Phys. Commun. **180** (2009), 84-106, doi:10.1016/j.cpc.2008.08.001, [arXiv:hep-ph/0407174 [hep-ph]]

[137] M. Wiebusch, *Towards new Front-End Electronics for the HADES Drift Chamber System*, PhD Thesis, Johann Wolfgang von Goethe-Universität Frankfurt am Main, 2019

[138] H. Wolter *et al.* [TMEP], *Transport model comparison studies of intermediate-energy heavy-ion collisions*, Prog. Part. Nucl. Phys. **125** (2022), 103962, doi:10.1016/j.ppnp.2022.103962, [arXiv:2202.06672 [nucl-th]]

[139] Y. X. Zhang, Y. J. Wang, M. Colonna, P. Danielewicz, A. Ono, B. Tsang, H. Wolter, J. Xu, L. W. Chen and D. Cozma, *et al.*, *Comparison of heavy-ion transport simulations: Collision integral in a box*, Phys. Rev. C **97** (2018) no.3, 034625, doi:10.1103/PhysRevC.97.034625, [arXiv:1711.05950 [nucl-th]]

[140] Y. Zhou, *Strange Hadron Production in Au+Au Collisions at RHIC Beam Energy Scan*, `https://indico.cern.ch/event/1037821/contributions/4871683/attachments/2461529/4220367/sqm2022_strangeness_production.pdf`, Talk, Strangeness in Quark Matter, 2022

[141] P.A. Zyla *et al.* [Particle Data Group], PTEP **2020** (2020) no.8, 083C01 doi:10.1093/ptep/ptaa104